

LASER SURFACE MODIFICATION OF STEEL

SYARIFAH NUR AQIDA SYED AHMAD
(B.Sc., M.Eng.)

A thesis submitted for the degree of
Doctor of Philosophy

School of Mechanical and Manufacturing Engineering
DUBLIN CITY UNIVERSITY

Supervisors:
Dr Dermot Brabazon
Dr Sumsun Naher

June 2011

I hereby certify that this material, which I now submit for assessment on the programme of study leading to the award of Ph.D. is entirely my own work, that I have exercised reasonable care to ensure that the work is original, and does not to the best of my knowledge breach any law of copyright, and has not been taken from the work of others save and to the extent that such work has been cited and acknowledged within the text of my work.

Signed : _____

(Syarifah Nur Aqida Syed Ahmad)

ID No. : 57115222

Date : June 2011

PREFACE

This thesis presents original work on laser surface modification. The research work has been conducted in the School of Mechanical and Manufacturing Engineering, Dublin City University during the period of January 2008 until March 2011. This work has been disseminated through the following publications and conferences.

Journals:

- i. Aqida, S.N., Brabazon, D., Naher, S., Kovacs, Zs., & Browne, D.J., Laser micro-machining of Cu₄₅Zr₄₈Al₇ bulk metallic glass, *Applied Physics A: Materials Science & Processing*, Vol. 101, No. 2: 357-360, 2010.
- ii. Chikarakara, E., Aqida, S.N., Brabazon, D., Naher, S., Picas, J.A., Punset, M. & Forn, A. Surface modification of HVOF of thermal sprayed WC-CoCr coatings by laser treatment. *International Journal of Material Forming*, Vol. 3 Suppl 1:801-804, 2010.

Conferences:

- i. Aqida, S.N., Naher, S. and Brabazon, D., Laser Surface Modification of H13 Die Steel using Different Laser Spot Sizes, 14th International ESAFORM Conference on Material Forming, Queen's University Belfast, Northern Ireland, United Kingdom, April 27th-29th, 2011, *AIP Conference Proceedings, Volume 1353*, pp. 1081-1086 (2011).
- ii. Aqida, S.N., Brabazon, D. and Naher, S., Designing Pulse Laser Surface Modification of H13 Steel using Response Surface Method, Advances in Materials and Processing Technologies, Paris, France, October 24th-27th, 2010, *AIP Conference Proceedings, Volume 1315*, pp. 1371-1376 (2011).
- iii. Aqida, S.N., Brabazon, D. and Naher, S., Laser Surface Modification of Die Steels, UK-Malaysia- Ireland Engineering Science Conference 2010, Queen's University Belfast, Northern Ireland, United Kingdom, June 23rd-25th, 2010, pp. 4.
- iv. Chikarakara, E., Aqida, S.N., Brabazon, D., Naher, S., Picas, J.A., Punset, M. & Forn, A. Surface modification of HVOF of thermal sprayed WC-CoCr coatings by laser treatment. 13th International ESAFORM Conference on Material Forming, University of Brescia, Brescia, Italy, April 7th-9th, 2010, pp. 439-442.
- v. Aqida, S.N., Brabazon, D., Naher, S., Kovacs, Zs., and Browne, D.J., Laser micro-machining of Cu₄₅Zr₄₈Al₇ bulk metallic glass, 10th International Conference on Laser Ablation at Furama Riverfront Hotel, Singapore, November 22nd-27th, 2009, pp. 245-249.

- vi. Aqida, S.N., Brabazon, D. and Naher, S., Effect of laser parameters on temperature distribution of glazed die steel, Advanced Manufacturing Processes Technology 2009 conference at Legend Hotel, Kuala Lumpur on October 26th-29th, 2009, pp. 233-241.
- vii. Kovacs, Zs., Aqida, S.N., Naher, S., Brabazon, D., Stratton, D., and Browne, D.J., Laser micro-channel inscription on Cu-Zr-based bulk metallic glass, Proc. WPI-INPG-Europe Workshop on Metallic Glass, Grenoble, France, August 25th-28th, 2009, pp. 45-51.
- viii. Aqida, S.N., Brabazon, D. and Naher, S., Thermal stability of glazed die material for semi-solid metal forming, 12th International European Scientific Association for Material Forming (ESAFORM) Conference on Material Forming, University of Twente, Netherlands, April 27th-29th, 2009, pp. 146-152.
- ix. Aqida, S.N., Naher, S., Maurel, M., and Brabazon, D. An overview of laser surface modification of die steels. 25th International Manufacturing Conference Proceedings, Dublin Institute of Technology, Dublin, Ireland, September 3rd-5th, 2008, pp. 120-128.

SYARIFAH NUR AQIDA SYED AHMAD

June 2011

ACKNOWLEDGEMENT

I would like to express my gratitude to my supervisors Dr. Dermot Brabazon and Dr. Sumsun Naher. Their enthusiasm and kindness have inspired me the whole time and were never wasted. They have provided knowledge, guidance, and advice that was invaluable throughout the course of this research. Plus the opportunities given to me during the past years have made my research works more exciting than I have imagined.

I am indebted to Prof. Saleem Hashmi for his support and concern which provides the comfort during my entire study.

I gratefully acknowledge the financial support from the Ministry of Higher Education Malaysia and Universiti Malaysia Pahang.

I thank the laser processing research team, Evans and David, and all technical staff especially Michael May and Martin Johnson for their support. It has been a great and enjoyable working experience. I thank all my officemates Ahmed, Tuty, Joseph, Jack and Shadi for sharing a friendly environment.

A special appreciation to my beloved husband and children, Izwan, Muhammad Afiq Farhan and Sofia Zahrah. Their love has made my PhD journey more meaningful and wonderful.

And last but not least, many thanks to my supportive father, mother, brothers, sisters and in-laws for their never ending support.

ABSTRACT

The presented work is an investigation of the laser surface modification of H13 tool steel using pulse laser processing mode. Initial screening experimental designs conducted lead to more optimised detailed designs. A carbon dioxide (CO₂) laser system with 10.6 μm wavelength was used. In the experimental designs investigated three different sizes of laser spot used were 0.4, 0.2 and 0.09 mm diameter. The other controlled parameters were laser peak power, pulse repetition frequency and pulse overlap. The laser processing was constantly assisted by in line argon gas at 0.1 MPa pressure. H13 samples were roughened and chemically etched prior processing to improve the surface absorbance at the CO₂ laser wavelength. Laser processed samples were prepared for metallographic study and were characterised for physical and mechanical properties. The metallographic study and chemical composition analysis were conducted using scanning electron microscope integrated with energy dispersive x-ray spectroscopy. The crystallinity and phase detection of the modified surface were conducted using an XRD system with Cu Kα radiation and wavelength of 1.54 Å. The surface profile was measured using stylus profilometry measuring systems. The hardness properties of the modified surface were measured by micro-Vickers diamond indentation. A modified surface grain with an ultrafine size of less than 500 nm was observed to be achievable. A modified surface depth which ranged between 35 and 150 μm was developed on the laser processed H13 samples. A reduction of crystallinity was noticeable for the modified H13 surface which was related to the more random distribution of crystallites after laser processing. A minimum modified H13 average surface roughness, Ra, of 1.9 μm was achieved. Another important finding was that at different settings of laser parameters, the modified H13 surface exhibited a range of hardness between 728 and 905 HV_{0.1}. A relationship between thermal simulations findings (heating and cooling rates) and hardness results was established for further understanding of the effects of the laser parameters. These findings are significant to the establishment of surface hardening techniques for wear resistance and thermal barrier coating applications.

LIST OF CONTENTS

PREFACE	iii
ACKNOWLEDGEMENT	v
ABSTRACT	vi
NOMENCLATURE AND ABBREVIATION	x
LIST OF FIGURES	xi
LIST OF TABLES	xviii
CHAPTER 1 Introduction	
1.1 Introduction	1
1.2 Prior Knowledge of Problem	2
1.3 Research Objectives	2
1.4 Thesis Outline	3
CHAPTER 2 Literature Review	
2.1 Laser Surface Modification Techniques	5
2.1.1 Laser Shock Hardening, Transformation Hardening, Alloying and Cladding	7
2.1.2 Laser Glazing	7
2.2 Effects of Laser Parameters	8
2.2.1 Laser Processing Modes - Continuous and Pulse Wave	11
2.2.2 Overlapped Pulse Geometry	14
2.2.3 Materials Surface Absorptance at Laser Wavelength	15
2.3 Laser Modified Surface Properties	18
2.3.1 Modified Surface Depth	18
2.3.2 Hardness Properties	20
2.3.3 Surface Roughness	23
2.3.4 Thermal Fatigue	25
2.4 Rapidly Quenched Alloy	28
2.4.1 Phase Crystallinity and Transformation	30
2.4.2 Hardness	36
2.5 Thermal Modelling of Laser Surface Modification	38
2.5.1 Heating and Cooling Rate in Pulsed Laser Surface Modification	39
2.5.2 Thermal Profile	41
2.6 Dies Failure in Semi Solid Metal Processing	43
2.7 Motivation and Aims of Research	46
2.7.1 Motivation of Research	46
2.7.2 Aims of Research	48

CHAPTER 3 Experimental and Model Set-up

3.1	Materials and Sample Preparation	49
3.1.1	Chemical Etching	49
3.1.2	Surface Absorptance by Roughening	50
3.2	Laser Surface Modification.....	51
3.2.1	Design of Experiment 1 (DOE1)	58
3.2.2	Design of Experiment 2 (DOE2)	60
3.2.3	Design of Experiment 3 (DOE3)	61
3.2.4	Design of Experiment 4 (DOE4)	62
3.2.5	Design of Experiment 5 (DOE5)	62
3.3	Thermal Modelling of Heat Conduction.....	64
3.4	Characterisation Techniques	70
3.4.1	Metallographic Study	70
3.4.2	Micro-hardness Test.....	72
3.4.3	Surface Profilometry	72
3.4.4	Energy Dispersive X-ray Spectroscopy (EDXS).....	73
3.4.5	X-Ray Diffraction Analysis	73

CHAPTER 4 Results

4.1	Introduction	74
4.2	Laser Surface Modification Design of Experiments	76
4.2.1	DOE1	76
4.2.2	DOE2	82
4.2.3	DOE3	91
4.2.4	DOE4	95
4.2.5	DOE5	104
4.2.6	EDXS Analysis	125
4.2.7	XRD Analysis.....	134
4.3	Thermal Modelling Simulations of Laser Surface Modification of H13 Tool Steel.....	142
4.3.1	Temperature Distribution in Modified Surface.....	142
4.3.2	Effect of Heating and Cooling Rate on Hardness Properties	144

CHAPTER 5 Discussion

5.1	Introduction	146
5.1.1	As-received H13 Tool Steel	149
5.2	Laser Surface Modified H13 Tool Steel	149
5.2.1	Metallographic Study	149

5.2.2	Hardness Properties.....	161
5.2.3	Surface Roughness.....	163
5.2.4	Statistical Analysis	164
5.2.5	EDXS Analysis	168
5.2.6	XRD Analysis.....	169
5.3	Thermal Modelling Simulations of Laser Surface Modification of H13 Tool Steel.....	171
CHAPTER 6 Conclusion		
6.1	Conclusion.....	173
6.2	Future Work.....	176
	BIBLIOGRAPHY	177
	APPENDICES	195

NOMENCLATURE AND ABBREVIATION

P_P	peak power
P_{ave}	average power
DC	duty cycle
PRF	pulse repetition frequency
T	pulse period
τ	pulse width
S	traverse speed
ω	circumferential speed
V	linear translation speed
d	laser spot diameter
X_p	length of traverse per pass
n	number of laser spots
T_R	residence time
E_P	laser pulse energy
I	laser irradiance
F	laser fluence
η	overlap
z	distance from focal position
w_R	beam radius at a distance z from the waist
w_{OR}	non-gaussian beam radius at the waist
λ	laser wavelength
M^2	beam quality
N	refractive index
k	surface absorptance coefficient
A	surface absorptance factor
H_T	total energy

LIST OF FIGURES

Figure 2.1: Schematic process map of laser material processing [16].

Figure 2.2: Comparison of industrial high power lasers [20].

Figure 2.3: Calculated surface temperature and cooling rate as a function of laser power and energy density [44].

Figure 2.4: Variations of parameters used in laser surface treatments showing a normal log plot of irradiance versus exposure time [3, 6, 16, 28, 45-50].

Figure 2.5: Beam diameter (spot size) of a Gaussian beam [51].

Figure 2.6: Geometry and intensity of the Gaussian laser beam [54].

Figure 2.7: Mean layer depths produced at different wave pulse frequencies and by a continuous wave [7].

Figure 2.8: The effect of varying laser absorption rate of the solid surface on the resulting melted area of laser-irradiated cast iron [57].

Figure 2.9: Surface roughness measurements for mild steel samples processed using a CO₂ in continuous and pulse laser wave [7].

Figure 2.10: Absorption of a number of metals as a function of laser radiation wavelength [64].

Figure 2.11: Some of the mechanisms which increase the absorptivity of real engineering surfaces: (a) typical cross section of an engineering surface; (b) high (Brewster) angle absorptance and multiple reflections due to surface roughness and (c) multiple reflections within an oxide layer [66].

Figure 2.12: Surface absorptance of Cr-base steel for infrared and green wavelengths at different surface roughness [66].

Figure 2.13: Variations of treated zone width and depth with pulse energy in Ti6Al4V alloy laser treatment (at $\tau=5$ ms, PRF=30 Hz and S=5 mm/s) using Nd:YAG laser [9].

Figure 2.14: Depth of the melted and hardened layers of the laser-treated H13 steel using CO₂ laser system and cross-sectional views of affected microstructures [71].

Figure 2.15: Changes of melted zone depth of laser glazed H13 steel at scan rates of (a) 73.2, (b) 146.4, (c) 219.6, (d) 292.8 and (e) 366.0 mm/s [40].

Figure 2.16: Cross-section micrograph and hardness distribution of laser-processed 6 mm diameter specimen. The H11 tool steel specimen was rotated at constant speed of 5 mm/s while being processed with an Nd:YAG laser at 0.5 kW laser power [73].

Figure 2.17: Effect of laser power density on the average hardness of nickel-coated cast iron [19].

Figure 2.18: Hardness values of stainless steel samples processed at different pulse frequencies [7].

Figure 2.19: Hardness distribution of H13 tool steel at different scan rates [40].

Figure 2.20: Dependence of surface roughness on laser irradiance in laser ablation of cobalt-cemented tungsten carbide using excimer laser at 20 ns pulse width and 450 mJ pulse energy [76].

Figure 2.21: Surface roughness of laser-treated nickel-coated cast iron at varying number of pulses using excimer laser at irradiance range between 120 and 325 MW/cm² and PRF of 30 Hz [19].

Figure 2.22: Changes in surface roughness with pulse width at 20 and 80 ms pulse period in laser processed 316L stainless steel using CO₂ laser [70].

Figure 2.23: Schematic of thermal fatigue test apparatus [82].

Figure 2.24: L-N curve of untreated and laser treated grey cast iron with four different laser treatments [77].

Figure 2.25: Length of fatigue cracks in untreated (smooth) and laser treated (No.1 to 4) gray cast iron samples at 2,500 cycles [85].

Figure 2.26: XRD of powder Fe₄₈Cr₁₅Mo₁₄Y₂C₁₅B₆ samples took from two samples of 2 mm (bottom scan) and 4 mm (top scan) cross-sectional thicknesses. The peaks are consistent with M₂₃C₆ phase [88].

Figure 2.27: XRD peak profiles of the laser treated SAE 52100 steel. The substrate profile presents the same XRD profile as the untreated surface [32].

Figure 2.28: XRD pattern of (a) untreated stainless steel, and treated stainless steel samples at (b) 1.02x10⁹ W/m² and (c) 1.45x10⁹ W/m² power density [94].

Figure 2.29: X-ray diffraction patterns of (a) amorphous and (b) crystalline sheet of twin roll cast Fe_{50.7}Y_{1.5}Cr_{14.5}Mo₁₃C_{14.8}B_{5.5} alloy [89].

Figure 2.30: X-ray diffraction scans of a (100) oriented Fe-Ga single crystal for the slow-cooled and quenched conditions [100].

Figure 2.31: Athermal martensite on grain boundaries of Ti alloy [106].

Figure 2.32: Morphology of ferrite: (a) grain boundary allotriomorph, (b) Widmanstätten plates. (i) primary. (ii) secondary; (c) Widmanstätten sawteeth. (i) primary. (ii) secondary; (d) idiomorphs; (e) intragranular Widmanstätten plate; (f) massive ferrite [114].

Figure 2.33: Grain size dependence of Vickers hardness [125].

Figure 2.34: Relationship between hardness of HAZ and heat input [127].

Figure 2.35: Model of heating and cooling rate versus time on surface for different beam shapes [135].

Figure 2.36: Variations of temperature in surface of work piece relative to the pulse duration [69].

Figure 2.37: Variation of grain radius and laser fluence as a function of undercooling [137].

Figure 2.38: Thermal profile (temperature against time) predicted on top surface by numerical solution during laser surface processing [93].

Figure 2.39: Thermal histories of four points on the surface of laser processed glass sheet [60].

Figure 2.40: (a) Heat checking in die-casting dies and (b) close-up view of heat checks [13].

Figure 2.41: Power as a function of time in pulse processing mode.

Figure 3.1: Surface profile of $2.90 \pm 0.2 \mu\text{m} R_a$ machined sample.

Figure 3.2: Beam delivery path in CO₂ laser system

Figure 3.3: Laser surface modification process setup (A: 9.4 mm diameter H13 sample, B: laser head, C: rotating chuck, and D: linear translation platform.

Figure 3.4: Laser beam diameter as a function of distance from the focal position.

Figure 3.5: Rotational and linear sample movement in laser surface processing where d is the spot diameter and X_2 is the processed longitudinal length of two subsequent passes.

Figure 3.6: Number of laser spots calculated without and with 50% circumferential overlap for a 10 mm diameter rod.

Figure 3.7: PRF as a function of overlap in pulse laser processing for a 10 mm diameter rod, a 0.4 mm spot size and at a rotational speed of 2000 rpm.

Figure 3.8: '3D channel profile simulation' software used for constructing molten pool geometry of laser processed surface.

Figure 3.9: Three-dimensional surface viewer software interface.

Figure 3.10: Planar isotherm software interface.

Figure 3.11: Outline of characterisation techniques for as-received and laser modified samples.

Figure 3.12: Image J software interface with 'Analyze Particles' pull-down menu.

Figure 4.1: Back scatter detector SEM micrograph of as received H13 tool steel.

Figure 4.2: Modified layer depth in DOE1 samples at residence time and irradiance of (a) 0.38 ms and 3,973 W/mm² (b) 0.38 ms and 5,576 W/mm² (c) 0.34 ms and 3,951 W/mm² (d) 0.34 ms and 5503 W/mm² (e) 0.31 ms and 3,881 W/mm², and (f) 0.31 ms and 4,607 W/mm² respectively.

Figure 4.3: Modified layer depth measurements in sample 12 with residence time and irradiance of 0.24 ms and 4,607 W/mm².

Figure 4.4: Three dimensional plot of laser irradiance and residence time effect on the modified surface depth with spot size focused on the sample surface.

Figure 4.5: Micrographs of samples 23 and 23b processed at defocused beam of (a) +2.6 mm and (b) -2.6 mm respectively, where A is laser modified zone, B is heat affected zone and C is substrate.

Figure 4.6: The effect of focal position on modified layer depth at (a) and (b) 0.38 ms; (c) and (d) 0.31 ms; and (e) and (f) 0.29 ms.

Figure 4.7: Modified layer depth as a function of residence time at positive and negative focal position.

Figure 4.8: Molten pool geometry of sample E14 given by molten pool depth, **a**, molten pool gap, **b**, molten pool width, **c**, and modified layer height, **h**.

Figure 4.9: Surface absorptance measurements from molten pool width variations for different samples. Difference in levels was largely due to the differences in pulse energy, E_p . Pulse energy for set 1 ranged from 0.18 to 0.24 J and for set 2 from 0.15 to 0.17 J.

Figure 4.10: Modified surface cross section of samples processed at 10% overlap, and (a) 0.23 J (sample E8) and (b) 0.24 J (sample E6) pulse energy respectively.

Figure 4.11: Modified surface cross section of samples processed at 30% overlap, and (a) 0.17 J (sample E14) and (b) 0.20 J (sample E15) pulse energy respectively.

Figure 4.12: Modified surface cross section of samples processed at 50% overlap, and (a) 0.16 J (sample E26) and (b) 0.19 J (sample E27) pulse energy respectively.

Figure 4.13: Back scattered detector micrograph of sample E27 cross section where A represents the laser modified layer, B is heat affected zone, and C is substrate.

Figure 4.14: Grain composition of laser modified sample E26 produced in DOE2, processed at 85% duty cycle, 50% overlap and 4000 Hz PRF.

Figure 4.15: Three-dimensional plot of micro-hardness for DOE2 samples.

Figure 4.16: Three-dimensional plot of average surface roughness for DOE2 samples at the different settings of overlap and duty cycle.

Figure 4.17: Contour plot of processing parameters in DOE2 corresponding to design desirability.

Figure 4.18: Surface morphology of overlapped pulses on DOE3 samples at 10% overlap for sample N10 (a) plan view, (b) cross sectional view; and 50% overlap for sample N24 (c) plan view, (d) cross sectional view.

Figure 4.19: Grain composition of laser modified sample N12 processed by DOE3.

Figure 4.20: Micrographs of DOE4 samples at different peak powers and (a) to (c) 0%; (d) to (f) 10%; and (g) to (i) 30% overlap.

Figure 4.21: Contour plot of modified layer depth for DOE4 samples corresponding to overlap and power settings.

Figure 4.22: Back scattering image of grain density variation of sample X4 processed at 0.09 mm spot size.

Figure 4.23: Nano-size sub-grains, amorphous and quasi-crystalline phase formation in the laser modified sample X4.

Figure 4.24: Hardness range of DOE4 samples.

Figure 4.25: Two-dimensional surface profile of DOE4 samples at (a) 1515 W, (b) 1138 W and (c) 760 W power settings.

Figure 4.26: Contour plot of DOE4 sample surface roughness at different overlap and laser power settings.

Figure 4.27: Micrographs of DOE5 samples processed at 0.12 J pulse energy and residence time of (a) 0.08 (sample F2), (b) 0.09 (sample F9), (c) 0.12 (sample F11) and (d) 0.16 ms (sample F1).

Figure 4.28: Micrographs of DOE5 samples processed at 0.10 J pulse energy and residence time of (a) 0.06 (sample F6), (b) 0.07 (sample F8), (c) 0.08 (sample F13), (d) 0.11 (sample F5) and (e) 0.14 ms (sample F7).

Figure 4.29: Micrographs of DOE5 samples processed at 0.08 J pulse energy and residence time of (a) 0.05 (sample F4), (b) 0.06 (sample F10), (c) 0.08 (sample F12) and (d) 0.10 ms (sample F3).

Figure 4.30: Normal probability plot of the studentized residuals for the modified surface depth response.

Figure 4.31: Predicted against actual plot of modified surface depth response.

Figure 4.32: Contour plot for DOE5 samples (F1, F3, F15, F2 and F4) modified layer depth corresponds to PRF and power settings at 0% overlap.

Figure 4.33: Contour plot of modified layer depths for DOE5 samples (F1, F9, F11 and F2) corresponding to overlap and power settings at 2300 Hz PRF.

Figure 4.34: Contour plot of modified layer depths for DOE5 samples (F1, F5, F7 and F3) corresponding to overlap and PRF settings at 760 W peak power.

Figure 4.35: Normal probability plot of the studentized residuals for hardness properties response.

Figure 4.36 Predicted against actual plot for hardness properties response.

Figure 4.37: Contour plot of PRF and power effect on hardness at minus 10% overlap. Design points shown are for sample F5, F9, F10 and F6.

Figure 4.38: Contour plot of overlap and power effect on hardness at 2300 Hz PRF. Design points shown are for samples F1, F9, F11 and F2.

Figure 4.39: Contour plot of overlap and PRF effect on hardness at 1515 W power. Design points shown are for samples F2, F6, F8 and F4.

Figure 4.40: Normal probability plot of the studentized residuals for surface roughness response.

Figure 4.41: Predicted against actual plot for surface roughness response.

Figure 4.42: Contour plot of PRF, peak power and surface roughness relationship at minus 10% overlap. Design points are shown for samples F5, F9, F10 and F6.

Figure 4.43: Contour plot of the insignificant effect of overlap and peak power on surface roughness response at 3500 Hz PRF. Design points are shown for samples F3, F10, F12 and F4.

Figure 4.44: Selected area in H13 tool steel substrate.

Figure 4.45: EDXS area analysis in H13 tool steel substrate with elements distribution (as-labeled).

Figure 4.46: EDXS qualitative analysis spectrum of phases for H13 tool steel substrate.

Figure 4.47: EDXS area analysis in sample E8 with elements distribution (as labeled).

Figure 4.48: Nickel elements distribution in sample E8.

Figure 4.49: EDXS qualitative analysis spectrum of phases for sample E8.

Figure 4.50: (a) Micrograph shows line spectrum measurements across sample E27 cross section and (b) EDXS qualitative spectrum analysis of phases indicates presence of primarily eight elements in sample E27.

Figure 4.51: (a) Micrograph shows line spectrum measurements and (b) EDXS qualitative analysis spectrum of phases indicates presence of eight elements in sample F11 cross section.

Figure 4.52: X-ray diffraction pattern of as received H13 tool steel.

Figure 4.53: X-ray diffraction patterns of (a) E15 and (b) E8 sample from DOE2 processed at 0.4 mm spot size.

Figure 4.54: X-ray diffraction patterns of (a) N4 and (b) N12 sample of DOE3 processed at 0.2 mm spot size.

Figure 4.55: X-ray diffraction patterns of (a) X5 and (b) X2 sample from DOE4 processed at 0.09 mm spot size.

Figure 4.56: Reflection of martensite phase in (a) E18, (b) E15, (c) E21 and (d) E27 sample of DOE2 processed at 0.4 mm spot size.

Figure 4.57: A close up of (110) α -Fe peak reflected from as-received H13 surface.

Figure 4.58: Metastable phase peaks reflected from sample (a) F1, (b) F6 and (c) F10.

Figure 4.59: Nominal temperature distribution simulation in modified surface of sample X2 along depth, at (a) $Z = 20 \mu\text{m}$, (b) $Z = 40 \mu\text{m}$, (c) $Z = 80 \mu\text{m}$, (d) $Z = 100 \mu\text{m}$ and (e) $Z = 120 \mu\text{m}$.

Figure 4.60: Modified layer [A] formed on substrate [B] after laser surface modification in sample F13.

Figure 4.61: Nominal temperature as a function of time at $Y=70.6 \mu\text{m}$ position for various depths.

Figure 4.62: Micro-hardness of the modified surface corresponding to nominal heating and cooling rate of molten pool in the modified surface of sample F13 along the depth.

Figure 5.1: Outline of order of results discussion presented in this chapter.

Figure 5.2: (a) Theoretical [169] and (b) experimental division of a Gaussian beam into regions on sample E8 modified surface cross section.

Figure 5.3: Micrographs of laser modified H13 samples processed at (a) 0.09, (b) 0.2 and (c) 0.4 mm spot size corresponding to the laser irradiance and residence time settings.

Figure 5.4: Molten pool width and thickness of samples processed at 0.4 mm (a), (b) and 0.2 mm (c), (d) and 0.09 mm (e), (f) spot size. Micrographs (a), (b) represent sample E26; (c), (d) represent sample N12; and (e), (f) represent sample F8.

Figure 5.5: Grain measurement layout at (a) required selection and (b) threshold adjustment stages of analysis using Image J software. This micrograph was captured from the sample processed with a 0.2 mm spot size, N12.

Figure 5.6: Average Feret's diameter distribution for 12 different samples processed at three different spot sizes

Figure 5.7: Two-dimensional model of a nano-structured material. The atoms in the centres of the crystals are indicated in black [171].

Figure 5.8: Increase of indentation mark diameter from modified surface [A] to substrate material [B] for sample F11.

LIST OF TABLES

Table 2.1: Estimated surface absorptance for AISI H13 tool steel at two beam widths and different laser power input [65].

Table 2.2: Properties of die materials at room and elevated temperatures.

Table 2.3: Properties of surface modified tool steels and Fe-based alloys.

Table 3.1: Chemical composition of AISI H13 tool steel.

Table 3.2: Properties of H13 tool steel at room temperature.

Table 3.3: Specifications of Rofin DC-015 diffusion-cooled CO₂ slab laser system.

Table 3.4: DOE1 processing parameter settings at constant peak power of 760 W.

Table 3.5: Laser parameter settings for samples at two different focal positions and 50% overlap.

Table 3.6: DOE2 parameter settings for nital etched samples processed at negative focal position.

Table 3.7: Processing parameter for DOE3 samples.

Table 3.8: Parameter settings for DOE4 samples at constant pulse energy of 0.095 J, average power of 274 W and PRF of 2900 Hz.

Table 3.9: DOE5 laser parameters for process optimisation.

Table 4.1: Overview of sample preparation, parameters settings and surface characterisation for five DOEs.

Table 4.2: The resulting molten pool geometry and estimated total energy, H_T , for different processing parameters.

Table 4.3: Processing parameter settings in DOE2 based on high desirability.

Table 4.4: Processing parameters and cooling period for DOE3 samples.

Table 4.5: The average hardness of modified surface in DOE3 samples.

Table 4.6: The average surface roughness of DOE3 samples.

Table 4.7: Parameter settings, heating rate and cooling period for DOE4 samples.

Table 4.8: Processing parameters and characterisation results from DOE5 samples.

Table 4.9: ANOVA results for modified surface depth response using quadratic model.

Table 4.10: ANOVA results for modified surface depth response (after stepwise elimination).

Table 4.11: ANOVA results for hardness properties response using quadratic model.

Table 4.12: ANOVA results for surface roughness response using cubic model (after stepwise elimination).

Table 4.13: Constraints in design optimisation with hardness and modified layer depth were in range and surface roughness was minimised

Table 4.14: Design solutions in DOE5 to minimise surface roughness with range of hardness and modified layer depth.

Table 4.15: Constraints in design optimisation with hardness and modified layer depth were maximised and surface roughness was minimised.

Table 4.16: Design solutions in DOE5 to minimise surface roughness with maximising hardness and modified layer depth.

Table 4.17: Chemical composition of the H13 tool steel substrate analysed from selected area.

Table 4.18: Chemical composition of sample E8 from selected area analysis.

Table 4.19: Chemical composition of modified layer in DOE2 samples cross section.

Table 4.20: Chemical composition comparison for DOE5 samples at different processing parameters.

Table 4.21: Contrast of x-ray diffraction values for as-received H13 steel and laser modified H13 steel surface.

Table 5.1: Summary of laser parameters setting ranges and characterisation results for the laser modified H13 tool steel samples.

Table 5.2: Processing parameters for H13 tool steel samples at three beam spot sizes.

Table 5.3: Range of modified H13 grain size processed at three beam spot sizes.

Table 5.4: Hardness properties of as-received and laser modified H13 tool steels at a range of heating rate and cooling periods.

Table 6.1: Summary of metallographic study findings of as-received and laser modified H13 tool steel for the different DOE.

Table 6.2: Surface roughness of laser modified H13 tool steel from different DOE.

CHAPTER 1

Introduction

1.1 Introduction

For many years, research work has been conducted to enhance the surface properties of materials to better endure high temperature, wear and friction through coating or surface modification. Although various advanced materials with significant properties have been developed, nevertheless when it concerns a particular surface engineering application, a materials' physical properties are among other factors that need to be considered, which include practicality, cost and time consumption. For instance, die casting is increasingly operated to produce cast metal parts due to the high surface quality of product, low manufacturing cost, and large quantity production capability. In spite of these advantages, a major problem lies in the costly dies preparation which includes tool design, material selection, its heat treatment, and development of casting process parameters, with the aim of maintaining the surface properties and prolonging the life cycle [1, 2]. Even high temperature, using H13 tool steel in die applications necessitates die replacement after thousands of cycles of aluminium castings or even fewer cycles for brass castings.

Various researches indicate that surface treatment and coating are the most effective methods to protect die surfaces from thermal fatigue and extend die life by reducing the damage at contact surfaces [3]. Due to the high temperature and cyclic running, failures of die-casting dies used in the metal casting industry occur excessively. These severe conditions will eventually lead to surface damage and die failures due to some combination of thermal fatigue, heat checking, erosion, stress corrosion, and soldering [3, 4]. Due to the rapid advancement in the field of surface engineering, conventional techniques for surface treatment like carburizing and flame hardening have been replaced by techniques using advanced heat sources such as plasma, laser, ion, and electron. Currently, high power lasers have become increasingly accepted as tools for many applications from cutting to welding to surface modification methods. Laser processing has also been proven to be capable of producing adherent, hard, wear, corrosion, fatigue and fracture resistant coatings on a diverse range of materials [5]. In other words, the crystal structure of metals' surfaces can actually be modified into very fine non-equilibrium microstructures as a result of rapid solidification via laser surface modification [6].

1.2 Prior Knowledge of Problem

Laser surface modification has been studied as a way of die surface hardening, in order to overcome the premature failure of the die during casting by developing a layer of high hardness on the substrate surface. Coating techniques are currently implemented to improve die life though it is difficult to meet the many coating requirements of excellent bonding, adequate thickness, absence of flaws, suitable mechanical properties, thermal shock resistance and high temperature stability [3]. Previous works of laser surface modification were conducted using continuous laser operation mode [3, 6]. However, many reviews indicate the problem of using the continuous laser mode compared to the pulsed laser operation mode. Though both continuous and pulsed wave lasers may be employed for surface modification, defects such as porosity, bubbles or depressions, occur easily with a continuous wave laser [7, 8]. Meanwhile, in contrast to the continuous wave operation, pulsed beam offers several challenges owing to the higher number of operating variables and the complexity of optimizing the process parameters [9].

The cyclic temperature changes due to the use of pulsed laser sources was established in several fields such as welding, laser sintering and laser surface treatment [10], but very few papers have dealt with the influence of pulse frequency on the final material mechanical properties and microstructure; and these have not been found to be consistent [7]. Therefore the great potential of cyclic temperatures in laser hardening has not yet been realised [10]. To overcome this, experimental investigation and thermal mathematical modelling would be necessary to determine the temperature distribution in achieving the optimum properties of laser glazed die surfaces [11-14].

1.3 Research Objectives

The main objectives of the thesis were to modify H13 tool steel surface using CO₂ laser for semi-solid processing die applications in order to produce a modified surface layer with enhanced hardness properties and minimum surface roughness. To meet the main objectives, the thesis addresses six separate goals:

- i. To investigate the effects of laser processing parameters and surface absorptance on the modified surface.
- ii. To design the experiments with three processing factors and to optimise the processing parameters.
- iii. To produce a maximum modified layer depth with a reduction of grain size.

- iv. To identify the crystallinity of the modified surface.
- v. To simulate the temperature distribution in laser surface modification process.

1.4 Thesis Outline

Chapter 1 Introduction

In this chapter, a brief research background was presented including the introduction of surface modification, followed by prior knowledge of problem and objectives.

Chapter 2 Literature Review and Theoretical Background

This chapter presents previous works on laser surface modification of tool steel and alloys. The literature review includes laser surface modification, controlled parameters and their formulas in laser processing, parameters effects on surface properties, materials surface absorptance, overlapping pulse effect on modified surface, mechanical and physical properties of rapidly quenched alloy, thermal modelling of laser surface modification, and die failures in semi-solid processing.

Chapter 3 Methodology

The research methodology is presented in Chapter 3 and comprises: materials and sample preparation, laser surface modification process, five design of experiments, characterisation techniques and thermal modelling. The thermal modelling simulation parameter settings used in a developed thermal model in LabVIEW software are also given.

Chapter 4 Results

This chapter presents the characterisation results of the as-received H13 tool steel and laser modified samples. The modified samples results were presented according to the sequence of design of experiments conducted and presented in Chapter 3. At the end of each design of experiment results section, a brief summary of results achievement is presented. The results of EDXS, XRD analysis and thermal modelling conclude the chapter.

Chapter 5 Discussion

Results of DOE1, DOE2, DOE3 and DOE4 were discussed in chapter 5 according to the characterisation method. The DOE5 results were discussed in a statistical manner with

design optimisation. The EDXS, XRD analysis and thermal modelling findings were discussed for selected laser modified samples and compared with the as-received H13 tool steel.

Chapter 6 Conclusion

The thesis was completed with research findings conclusion and recommendations for future work. Overall significance of the findings of metallographic study, hardness properties, phase analysis, surface roughness, and design optimisation, for wear resistance and semi-solid processing applications are highlighted.

CHAPTER 2

Literature Review

2.1 Laser Surface Modification Techniques

The laser has been developed for many different scientific applications including materials processing, spectroscopy, photochemistry, microscopy, lunar laser ranging and nuclear fusion. These applications are a result of the coherency and mono-chromaticity of the electromagnetic radiation beam that can propagate in a straight line with negligible divergence and which can be generated in a wide range of wavelengths, energies and beam-modes [15, 16]. Application of laser technology in metal surface modification takes advantage of heat energy from the laser beam to alter the materials' surface properties. Laser processing has more advantages over the conventional methods which include local heating of the surface without changing the substrate material properties, precision and high speed of operation, and low cost [11].

There are several methods of laser surface modification, namely laser alloying, transformation hardening, surface amorphisation, shock hardening, cladding and glazing. These methods are different in terms of the composition changes on the material's surface and energy absorption rate as shown in Figure 2.1. In comparing to other conventional methods for selective surface hardening, the benefits of laser surface processing technique include fine-grained and homogeneous microstructures, low thermal damage to the underlying substrate, reduced grain growth and distortion, non-equilibrium and amorphous structures, and extension of the solid solubility of alloying elements [3, 6, 17]. These benefits in turn can be used to enhance the tribological and other mechanical properties, including hardness, strength, toughness, fatigue and corrosion resistance while the bulk properties remain unaltered.

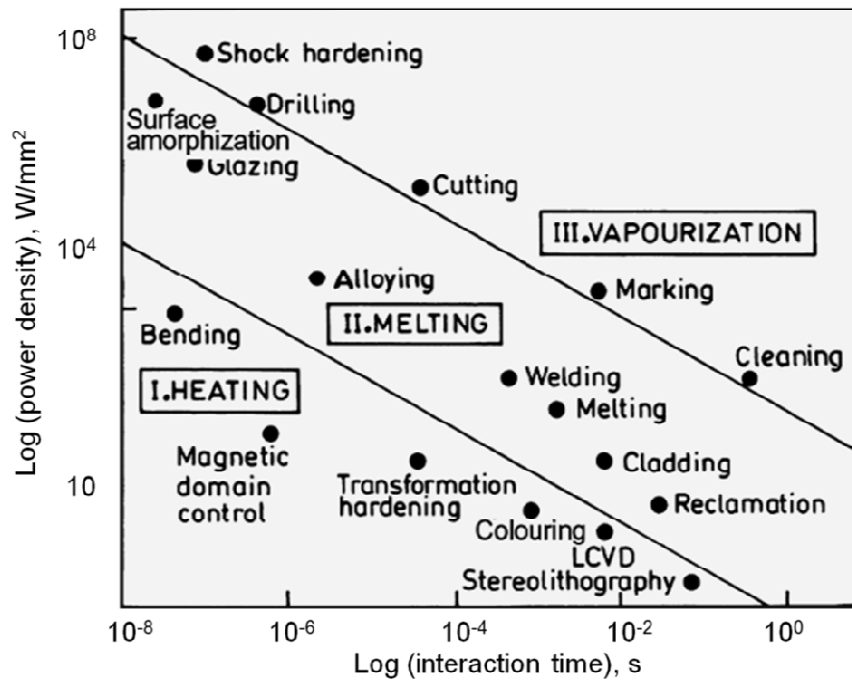


Figure 2.1: Schematic process map of laser material processing [16].

Though several types of laser have been used in surface processing to date, infrared lasers like CO₂ have advantages over excimer lasers such as large beam size, higher laser efficiency, ease of operation, use of non-toxic gases and lower cost [18, 19]. Figure 2.2 compares the most popular industrial high power lasers in terms of power, beam quality, wavelength, footprint and ownership costs. Among these, the ownership cost of the laser system is often of greatest practical significance when considering for the surface modification of high cost dies surface. While fiber lasers are presented as the best in many reviews, the use of CO₂ lasers especially in continuous mode is widespread for cutting, drilling, surface melting, welding, material removal, annealing and cladding applications.

	Power	Beam quality	Wavelength	Maintenance	Footprint	Ownership costs
Fiber laser	●	●	●	●	●	●
CO ₂ (gas)	◐	◐	◐	◐	○	◐
Lamp-pumped Nd:YAG (solid-state)	◐	◐	◐	◐	◐	◐
Diode-pumped Nd:YAG (solid-state)	◐	◐	◐	◐	◐	◐
Disk lasers Yb:YAG (solid-state)	◐	◐	◐	◐	◐	◐

Figure 2.2: Comparison of industrial high power lasers [20].

2.1.1 Laser Shock Hardening, Transformation Hardening, Alloying and Cladding

For laser shock hardening processes which need vaporisation to occur, the Nd:YAG laser has commonly been used to process 6061-T6 aluminium alloy and brass for wear, friction and hardness improvement [21, 22]. In transformation hardening, surface heating of materials like carbon steel, martensitic high nitrogen stainless steels, chromium-molybdenum alloy steel and cold forging tools use of CO₂ or diode laser systems are widespread to increase the wear and hardness properties [10, 23-25]. Transformation hardening was achieved by heating a metal above a critical temperature with unfocused beam and then rapidly quenching it rather than allowing equilibrium phases to form by slow cooling [26]. The power density in the hardening process was 100 W/cm² which generates low thermal distortion such that refinishing of the part can be eliminated [27]. The alloying and cladding processes involve introducing additional elements to the laser melted surface. The elements can be in the form of gases, powder, wire or sheet. In alloying, the composition of the surface changes while in cladding, only bonding with minimal mixing of the additional elements and melted surface is involved. However, a similar power density level of about 10⁴ W/cm² is used for both processes. Without additional elements, surface melting such as during glazing can be preferred to homogenize and harden the material's surface.

2.1.2 Laser Glazing

Glazing is a process to produce a thin amorphous or nano-crystalline layer on top of the substrate material in which the surface material of a solid is melted using a focused laser beam, and then rapidly cooled [3, 28, 29]. The laser energy absorbed into the surface melts the material to a depth determined by the quantity of transferred energy and the material thermal properties [30]. Glazing is conducted at a high power density and with short laser-material interaction time which could create a nano-crystalline or amorphous structure with excellent mechanical properties compared to conventional crystalline alloys [31]. Due to the enhanced properties, laser glazed surfaces can meet the demands of many wear resistant and high temperature applications such as die casting dies, thermal barrier coatings, rail road rails and other bearings components [3, 6, 32, 33].

Laser glazing has the potential to seal the heat checks formed on the die surfaces and allow relaxation of surface stresses [3]. In thermal barrier coatings, sprayed composite coatings are very porous and a treatment with a high power CO₂ laser has been applied to improve their wear properties [33]. The composite coating density and metallurgical

bonding between the substrate and the coatings have also been improved [34]. Glazing of railroad rails has resulted in a 40% decreased of friction coefficient when measured at prototypic rail service loads [6]. The cross section of laser glazed railroad rail surface consisted of glazed, transition and base metal regions. The transition zone showed an intimate bonding between the glazed zone and the base metal which provided for a micro-hardness gradient between the glazed zone and base metal [6]. In addition to the applications above, laser modified bearings have exhibited martensitic microstructure with high hardness and wear resistance and a residual compressive stress has been noted at the surface of austempered SAE 52100 steel with a bainitic microstructure [32]. This treatment developed a superior bearing assembly with a tougher core and a harder surface with higher fatigue and wear resistance. Several type of lasers have been employed (Nd:YAG, CO₂, excimer, and fiber lasers) for the surface melting (glazing, alloying and cladding) of high speed steel, martensitic high-nitrogen steel, aluminium alloys, austenitic stainless steel, aluminium aerospace alloys, Ni-base on Al-Mg-Si alloy and H13 tool steel [35-41].

2.2 Effects of Laser Parameters

The formation of a modified layer is determined by the laser processing parameters settings. Some laser parameters are, laser beam wavelength, temporal pulse power (pulse length, peak power and pulse shape), repetition rate, beam energy distribution, and beam geometry including focal spot size and depth of focus [42]. Control of parameter settings also yields different effects on the modified surface properties. Though several types of laser have been used in laser surface processing, the laser power and scan speed or material-laser interaction time were observed to have a strong influence on the resulted temperature profile, modified layer depth, and mechanical, corrosion and tribological properties of the processed surface [10, 43]. Reducing the laser power affects the melt depth, changing the beam size affects the melt pool dimensions, and changing the scanning speed affects the coverage rate [25]. The effect of laser power and energy density on the cooling rate and surface temperature during laser processing of EN18 steel is shown in Figure 2.3. The surface temperature and cooling rate linearly increase with increasing laser power or energy density. Increasing the laser power increases the surface temperature which influences the molten surface solidification rate. While high cooling rate is necessary to refine the grain structures, a high power density (irradiance) and short interaction time (exposure time) combination is generally preferred to allow for a faster cooling rate to be achieved.

Figure 2.4 shows irradiance versus exposure time plot used in laser glazing work from previous researchers. Though surface processing at high power density can cause melting and oxidation, inert gas flow such as with like argon, is used to protect the surface during the entire process [28].

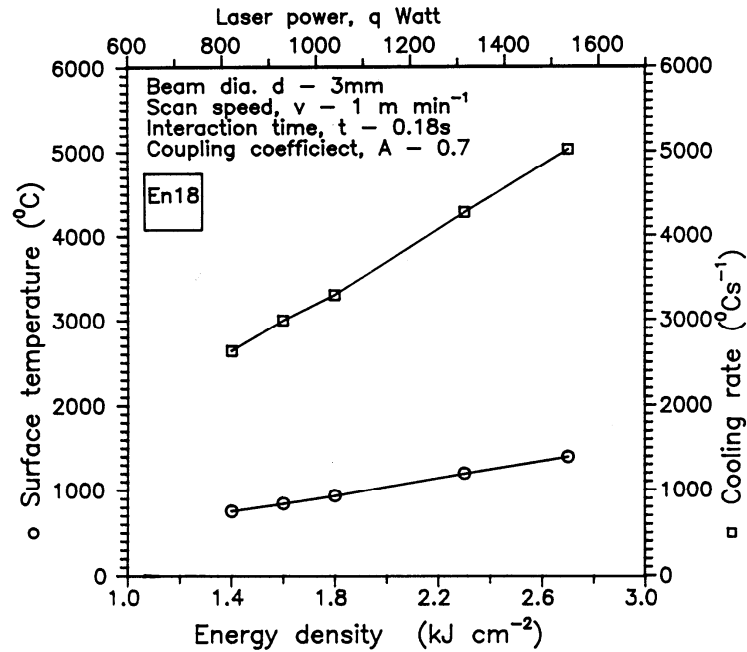


Figure 2.3: Calculated surface temperature and cooling rate as a function of laser power and energy density [44].

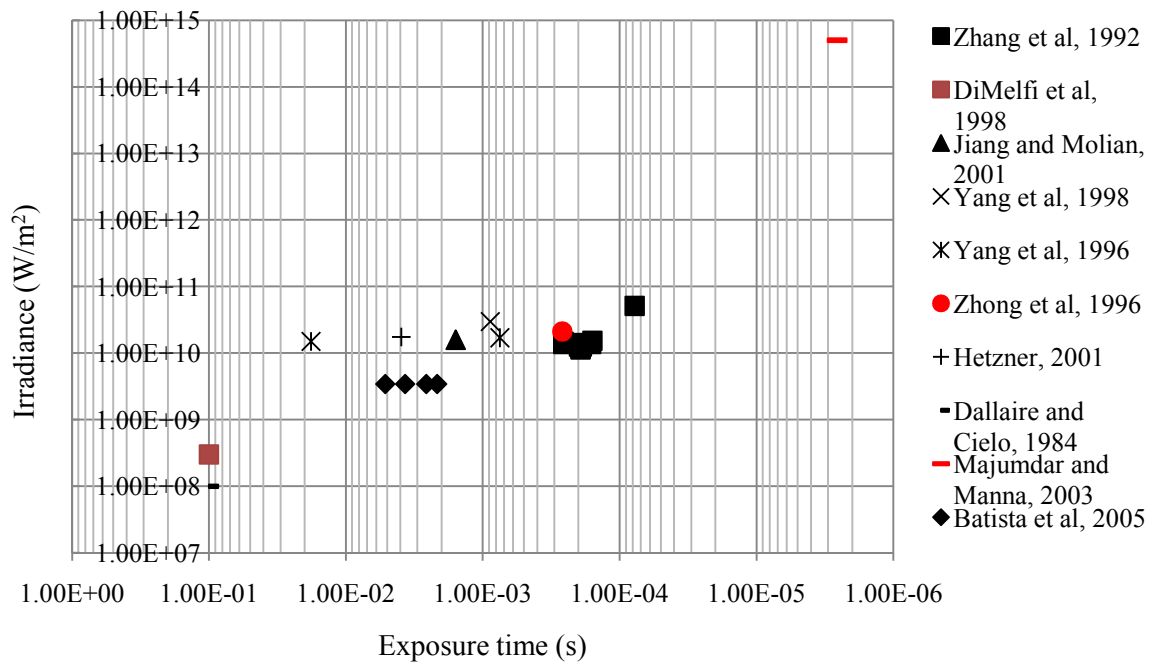


Figure 2.4: Variations of parameters used in laser surface treatments showing a normal log plot of irradiance versus exposure time [3, 6, 16, 28, 45-50].

The power density or irradiance of a laser beam is determined by the power of the laser beam used and the diameter of its focal spot. The diameter of the beam which contains almost 86.5% of the total laser power is defined by $1/e^2$ of the peak intensity [51]. Though levels of surface hardening are achieved with a TEM_{01} intensity distribution, circular laser spot profiles produced by the TEM_{00} mode are generally more suitable for most laser applications. Furthermore, the melt pool formed by the TEM_{00} mode has the greatest depth and width, and develops more quickly during processing compared to other modes [52]. Figure 2.5 shows the Gaussian mode beam diameter and spot size produced by TEM_{00} laser systems. The shape of this curve is Gaussian; therefore, TEM_{00} laser beams are called Gaussian beams.

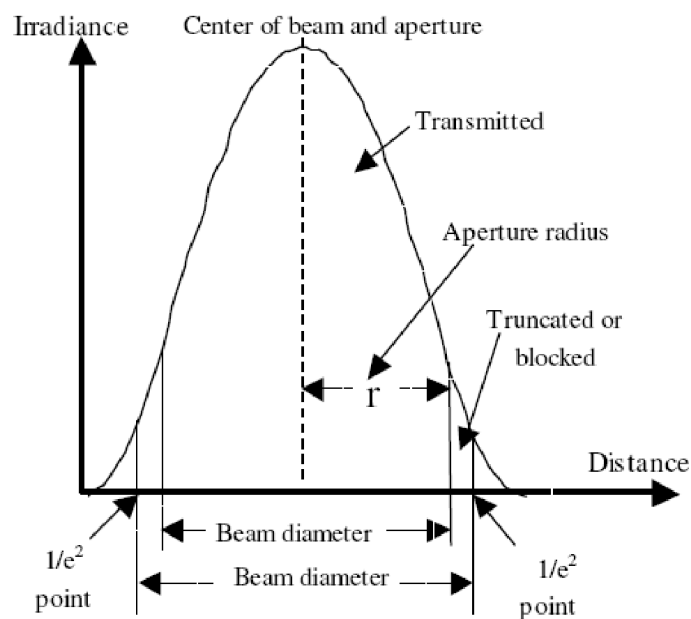


Figure 2.5: Beam diameter (spot size) of a Gaussian beam [51].

When processing with a Gaussian laser beam, the focal position determines the spot size. Most works on laser surface modification have used defocused laser beams to process the metal surface in order to achieve a larger spot size [32, 50, 53]. At the same distance from the focal distance, the laser beam produces a similar spot diameter either above or below the materials surface as shown in Figure 2.6. Though a similar diameter of spot size can be achieved both above and below the focal position, the choice of which position the surface is placed affects the heat input. Thus, the modified area width and depth vary due to a change in amount of laser energy absorbed into the materials surface [40, 53]. The heat absorption has been shown in one case to be 10% larger when the focal position, z , was moved downward into the materials surface (-) compared to above the material surface (+) [53].

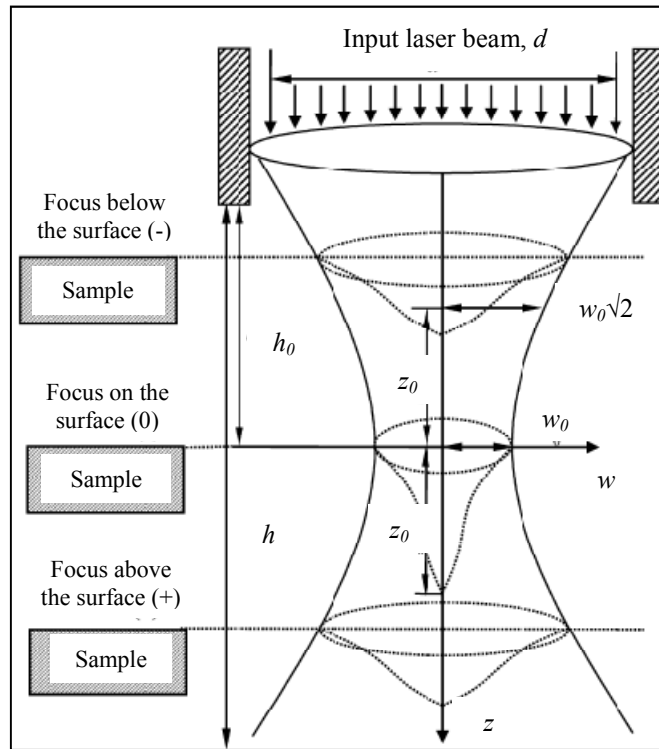


Figure 2.6: Geometry and intensity of the Gaussian laser beam [54].

2.2.1 Laser Processing Modes - Continuous and Pulse Wave

Laser surface modification has been carried out previously using both continuous and pulsed wave lasers [28, 40, 55, 56]. Compared to pulse laser, an advantage of using continuous laser beam is that the modified layer or amorphous state can be obtained in a continuous process [28, 55, 56]. Figure 2.7 shows the mean modified layer depth measured from samples processed with continuous and pulse laser modes. The mean depths of 316L steel sample processed with pulsed mode CO_2 laser were dependant on the pulse frequency. Whereas the mean depths of the sample processed with continuous laser mode were consistent at approximately 0.5 mm which is higher than the maximum depth measured from pulsed laser processing route.

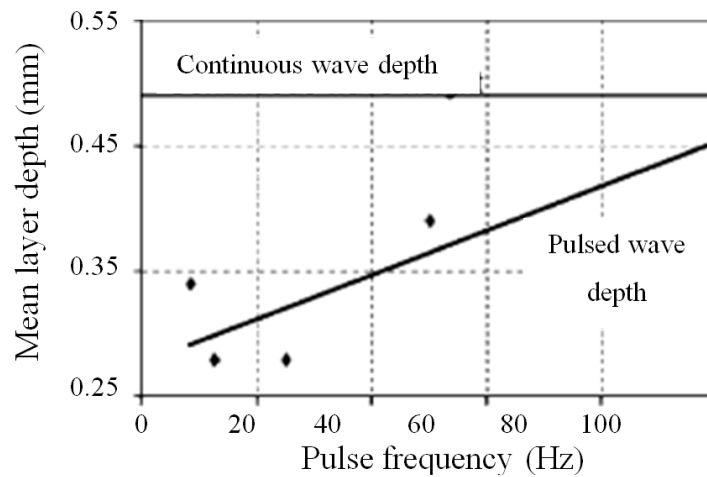


Figure 2.7: Mean layer depths produced at different wave pulse frequencies and by a continuous wave [7].

On the other hand defects such as cracks, porosity, bubbles or depressions, occur easily with continuous wave laser processing [7, 8]. Surfaces processed by continuous laser mode are characterised by reduced laser absorption compared to the surface processed with pulse mode [57]. In Figure 2.8, at an average power of 400W from Nd:YAG laser and scanning rate of 4 mm/s, the given pulse conditions produced a more uniform melted area on the cast iron compared to the continuous laser. An inconsistent melted area formed in the continuous laser processing due to varying laser absorption rates between 28% and 52%. In the continuous mode, to increase the absorption rate will necessitate increase of laser power or irradiance. In the pulse mode, a higher absorption rate can be achieved by changing the duty cycle as the resulting peak power will produce a deeper penetration into a material's surface. A larger width dimension of processed region was also measured from the surface processed by pulse mode.

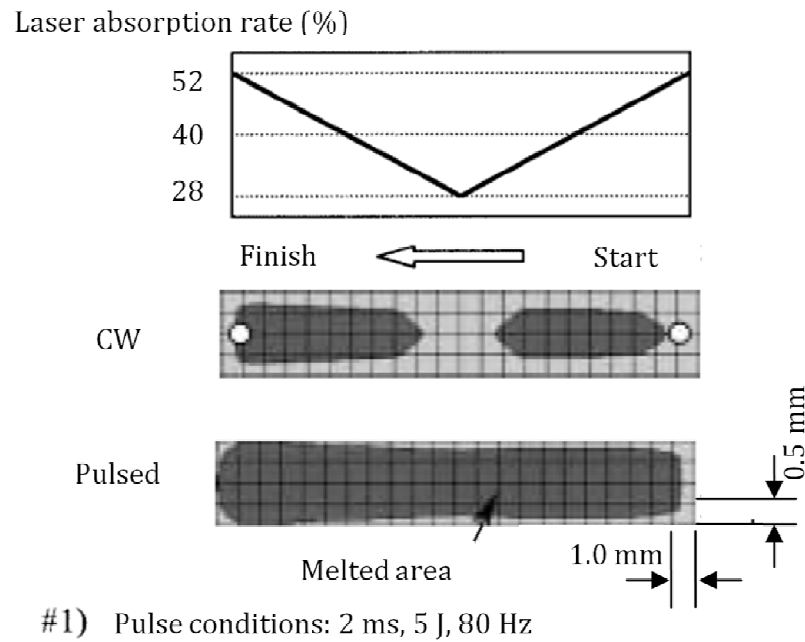


Figure 2.8: The effect of varying laser absorption rate of the solid surface on the resulting melted area of laser-irradiated cast iron [57].

In contrast to the continuous wave operation, pulsed beam offers several challenges owing to the higher number of operating variables and the complexity of optimizing the process parameters [9]. The cyclic temperature changes due to the use of pulsed laser sources was established in several fields such as welding, laser sintering and laser surface treatment [10], but very few papers have dealt with the influence of pulse frequency on the final material mechanical properties and microstructure; and these have not been found to be consistent [7]. Therefore the great potential of precise cyclic temperatures application in laser surface modification has not yet been realised [10]. A high-quality modified layer on plasma sprayed $(\text{ZrO}_2\text{-}12\text{wt.}\%\text{Y}_2\text{O}_3)/(\text{Ni-}22\text{wt.}\%\text{Cr-}10\text{wt.}\%\text{Al-}1\text{wt.}\%\text{Y})$ thermal barrier coatings has been successfully produced using a CO_2 pulsed laser [8]. The advantages of pulsed mode in laser processing are mainly [42]:

- i. temporal control of energy coupling to the target, resulting in a limited depth of heat conduction into the surface, often resulting in more control of energy deposition and in reduced heating of the work piece, and thus in higher quality.
- ii. high pulse peak power and thereby high intensity, obtainable, resulting in improved light coupling in some materials, especially metals and thereby enabling or improving the processing.

Pulsed laser mode has been shown to have an influence on final material properties where samples processed by pulse laser exhibited lower surface roughness than samples processed using continuous wave mode [7]. In wear-resistant applications, a sound surface finish is crucial. For example, the allowable average surface roughness of high pressure die can vary between 0.2 and 5.0 μm [58]. Figure 2.9 contrasts the surface roughness measurements of samples processed using continuous and pulse laser. Using a continuous wave laser, the sample surface roughness is constant with a measurement of at least 10 μm higher than the sample processed by pulsed laser. While at certain pulse frequency settings in pulse laser processing, the surface roughness was reduced which suggests the benefit of pulse laser in surface modification. Despite having excellent hardness surface properties from high energy beam surface processing, controlling the surface roughness is still a challenge.

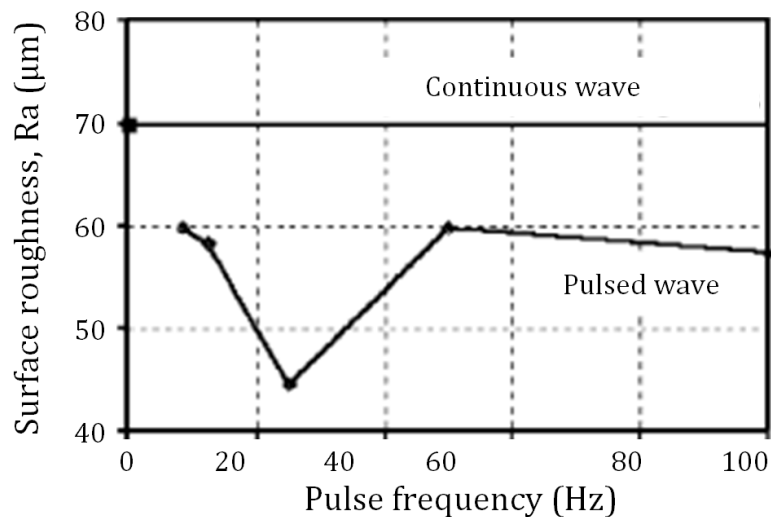


Figure 2.9: Surface roughness measurements for mild steel samples processed using a CO_2 in continuous and pulse laser wave [7].

2.2.2 Overlapped Pulse Geometry

In pulse processing mode the pulse repetition frequency of the laser controls the overlapping between laser spots, while the extent of overlapping is influenced by the scan rate and pulse width [9, 59]. The overlapping technique with multipass is an effective method to enlarge the processed area of the laser glazing treatment, but the sample surface roughness has also been seen to increase with increased crack density, as a consequence of increased beam scanning speed and overlap [28, 53]. Increasing pulsing frequency and decreasing scan rate increase the overlapping area [9]. At a constant scan speed, the overlap increases with increasing frequency, see Appendix A1.

Morphological defects on the laser glazed surface can be avoided by studying the laser process parameters. The rate at which the laser pulses are delivered to the sample greatly affects the morphology of the ablated zone [60]. The pulse energy is inversely proportional to PRF. Low PRFs tend to produce high pulse energies and hence can result in higher surface stresses due to thermal cycling and thermal shocks. The result is that the material cracks and flakes on a microscopic scale. Therefore, by adjusting the number of laser pulses, the amount of thermal energy deposited per unit area or volume can be controlled with great precision. Consequently, the properties such as hardness and surface roughness can be improved for any given material/laser system combination.

2.2.3 Materials Surface Absorptance at Laser Wavelength

Metals' properties like surface reflectivity, thermal diffusivity, melting point, and phase behaviour are significant to determine the effects of the laser in the surface modification process [29]. A major disadvantage of the CO₂ laser is the very high light reflectivity at 10.6 μm which makes the absorption of the laser energy difficult for metals including steels [19, 61]. However, high energy CO₂ laser systems are easy to fabricate, maintain and are relatively common so are widely used for most processing despite their low efficiency. Surface absorptance, the fraction of the incident laser light which is absorbed, varies with laser properties, temperature, material type and the material's surface finish. Material surfaces can readily absorb shorter wavelength lasers like Nd:YAG (1064 nm) and ruby (694.3 nm) compared to longer wavelength laser systems.

Figure 2.10 shows the absorption factor of metals at different laser wavelengths. Most metal surfaces including steel can absorb less than 15% of the energy when processed with the CO₂ laser wavelength. In laser glazing, sufficient material absorbance at a particular laser wavelength is important in order to melt the surface efficiently. Although the surface absorption can increase as much as 40% during processing at high temperature, most steels have high surface reflectivity when processed with CO₂ laser wavelength at room temperature [62]. It was found that the reflectivity of AISI 4340 steel for CO₂ lasers decreased from 93.1% to 88.3% as the surface temperature was increased from 20 to 500°C with an argon atmosphere in place [63]. In contrast to the CO₂ laser, die steels have a 0.35 absorption factor when processed with an Nd:YAG laser [61]. Besides laser wavelength, for H13 tool steel surface absorptance varies with the input laser power as given in Table 2.1. Laser surface treatments performed in an oxidizing atmosphere like in air experience increased surface oxidation during processing and enhanced absorptance.

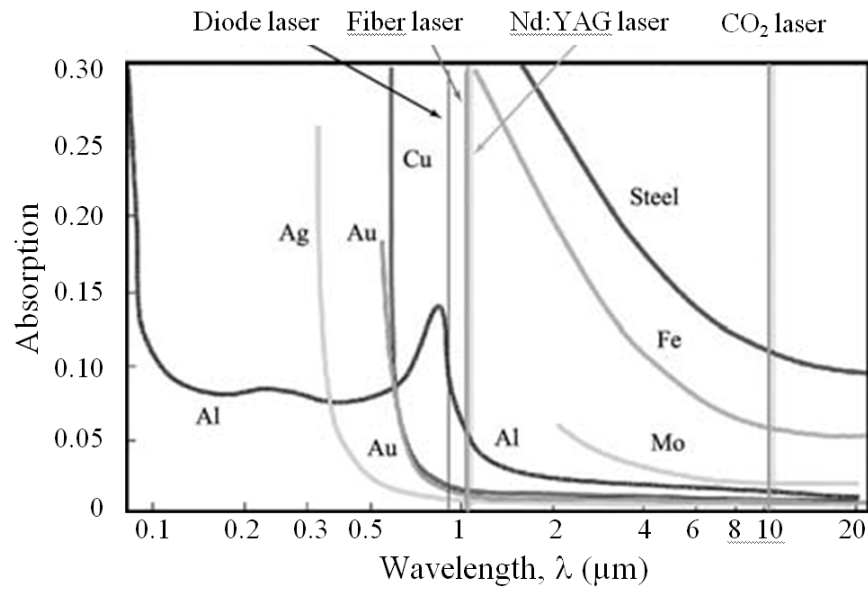


Figure 2.10: Absorption of a number of metals as a function of laser radiation wavelength [64].

Table 2.1: Estimated surface absorptance for AISI H13 tool steel at two beam widths and different laser power input [65].

Beam width, w (mm)	4			2		
Laser power (W)	1300	1200	1000	720	660	600
Absorptance (%)	65.4	60.8	58.0	45.1	43.7	40.0

Useful techniques like absorptive coating, chemical etching and surface roughening improve steel surface absorption at infrared laser wavelengths [44]. Figure 2.11 indicates the photon absorption into different types of surfaces. For engineering surfaces in Figure 2.11 (a), such a surface has a characteristic roughness and is generally covered by an oxide layer that helps photon absorption into the surface. In Figure 2.11 (b), roughness on surface can result in multiple reflections, which also involve multiple absorptions. Surface roughnesses that present more opportunity for incident angle less than or equal to Brewster angle allow for very high local absorptance levels while Figure 2.11 (c), the oxide layer may be absorbing or responsible for multiple reflections [66].

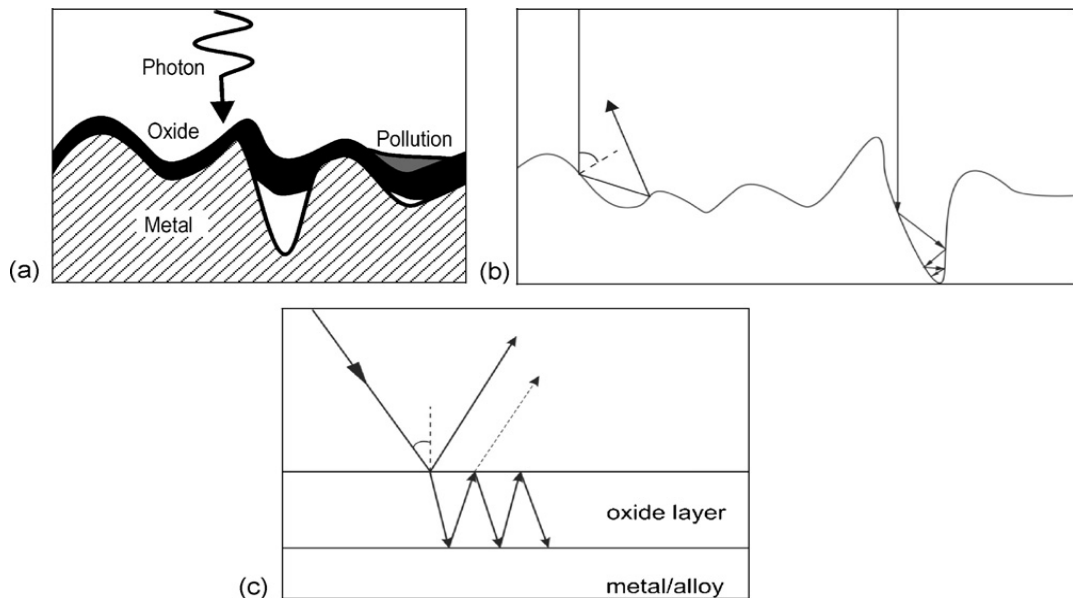


Figure 2.11: Some of the mechanisms which increase the absorptivity of real engineering surfaces: (a) typical cross section of an engineering surface; (b) high (Brewster) angle absorptance and multiple reflections due to surface roughness and (c) multiple reflections within an oxide layer [66].

Samples coated with absorptive layers on their surface have not been made into an amorphous state through laser processing because some carbon grain impurities were mixed in the molten cell when the surface was melted locally [46]. However, preparing samples through grinding, cleaning with alcohol and etching with nital was also seen to be effective to reduce the laser beam reflectivity [67]. Compared to smoother surfaces, a sand blasted sample surface at certain roughness levels can reduce the reflectivity of the laser beam for different materials [39, 44]. Without an absorptive coating, an increase in average surface roughness to approximately $3.0\ \mu\text{m}$ for H13 tool steel has been seen to increase surface absorptivity with CO_2 laser wavelength by as much as 60% [68].

Figure 2.12 shows absorptance as a function of surface roughness for stainless steel samples. The surface absorptance was increased from 40% to approximately 60% with increased surface roughness. This trend was similar for both infrared and green wavelengths. Improving surface absorptance allows efficient CO_2 laser processing and more accurate estimation of total energy required in the process.

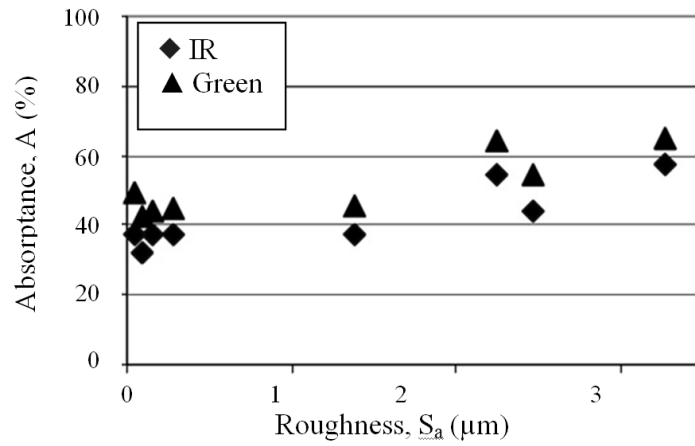


Figure 2.12: Surface absorbance of Cr-base steel for infrared and green wavelengths at different surface roughness [66].

2.3 Laser Modified Surface Properties

2.3.1 Modified Surface Depth

The laser processing parameters have been previously varied to obtain treated layers of different depths [67]. In pulsed laser treated surfaces, the properties are controlled by several independent laser parameters; peak power, pulse energy, pulse width, frequency and scan rate [9, 59]. The laser peak power is more important than the average power, where changing the peak power with pulse width and frequency at constant average power the surface properties will vary [59]. The pulsed laser ‘off’ state provides the cooling periods, while in the continuous laser mode a continuous heating is provided to the material surface and cooling only happens when the laser radiation is switched off [14]. Pulse energy or pulse energy density (fluence) and interaction time at the surface determine the temperature profile and also both width and depth of hardening as shown in Figure 2.13 and Figure 2.14. From these findings, it can be seen that the pulse energy determines the average and peak power settings in laser processing of titanium alloy and H13 steel. In other words, as the pulse energy increases both the average and peak power increases, increasing the treated zone dimensions, see Appendix A2.

A linear relationship between laser treated zone depth and three (PRF, scan rate and pulse width) processing parameters was established in Ti-6AL-4V samples, processed using Nd:YAG laser system, see Appendix A3(a) [9]. The maximum treated zone depth was achieved at higher frequency, lower scan rates and lower pulse widths. Similar findings were found in st14 steel treated using Nd:YAG laser system where the heat penetration depth decreased with increasing pulse width, see Appendix A3(b) [69]. When the pulse

width equals to pulse period the laser operates as continuous wave and a constant modified layer depth is formed [70]. Generally, in the short pulsing range (1-50 μ s) the heat conduction limits the processed surface depth to a few micrometers per pulse and makes the short pulse lasers applicable for marking and surface layer removal, while longer pulse lengths (i.e. in the range of 50-5000 microseconds) are applied for industrial cutting, surface treatment and welding [42]. Though shorter pulses are more efficient they may also lead to unwanted vaporisation [49].

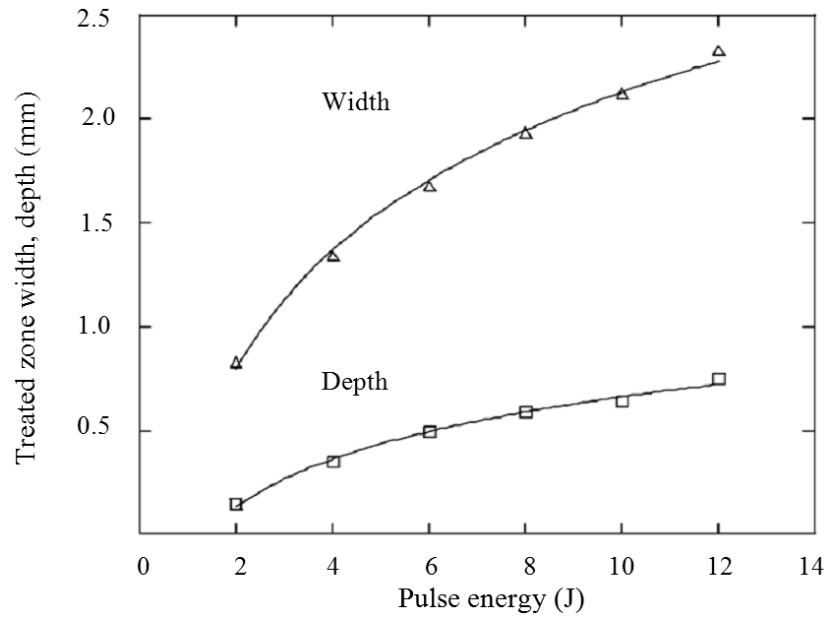


Figure 2.13: Variations of treated zone width and depth with pulse energy in Ti6Al4V alloy laser treatment (at $\tau=5$ ms, PRF=30 Hz and S=5 mm/s) using Nd:YAG laser [9].

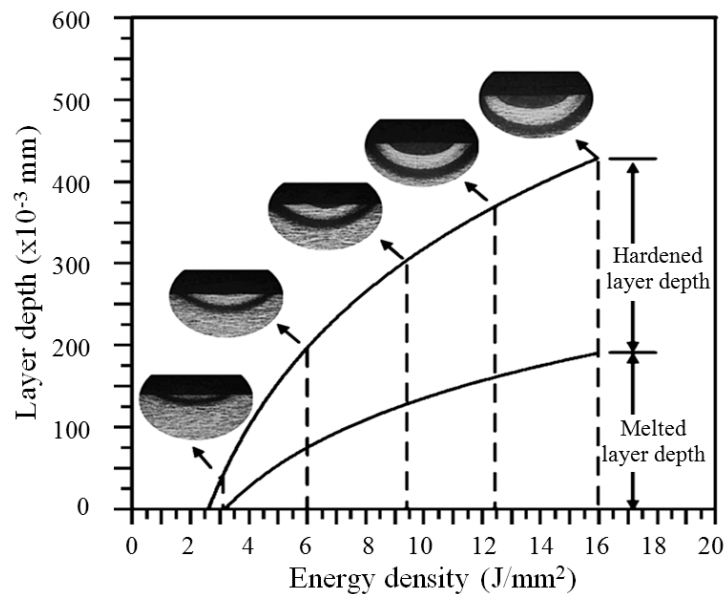


Figure 2.14: Depth of the melted and hardened layers of the laser-treated H13 steel using CO_2 laser system and cross-sectional views of affected microstructures [71].

The effect of scan rate on the modified layer depth is shown in Figure 2.15. The cross section of laser glazed H13 steel surface shows glazed surface depths at five different processing speeds. In laser surface modification processes, increasing the processing speed decreases the melted zone depth [40, 47]. Lower scan speed allows longer material-laser interaction and increased heat input and energy penetration into the materials surface. The increase of heat input is due to the increased amount of laser beam energy absorption on the surface of the specimen [53]

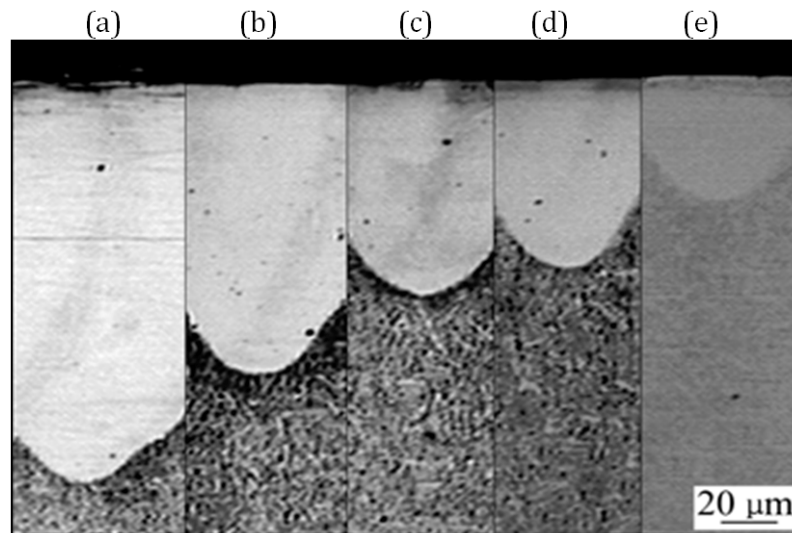


Figure 2.15: Changes of melted zone depth of laser glazed H13 steel at scan rates of (a) 73.2, (b) 146.4, (c) 219.6, (d) 292.8 and (e) 366.0 mm/s [40].

2.3.2 Hardness Properties

The laser beam has been utilised for surface treatment to enhance the mechanical properties, by surface modification of AISI H13, structural steels, and alloy steels [55, 56]. By laser processing, a steel surface can be rapidly melted (above austenite temperature) and rapidly quenched. The treated layer could exhibit high hardness due to the formation of finer grains, secondary carbide and hard non-equilibrium microstructures that are intimately bonded to the substrate and the modified region itself [6, 72].

The laser modified surface consists of three zones namely the melted zone, heat affected zone (HAZ) and base metal or substrate which are shown in Figure 2.16. In the melted zone, the hardness properties increased due to brittle martensite structure formation during rapid cooling and can be more than 200% harder than the substrate [3, 56, 73]. The hardness of laser glazed H13 steel surface decreased the deeper into the surface the measurement was taken [3]. A decrease of hardness properties also occurred when the

laser modified surface was heat treated at 500°C and 600°C as a result of tempered martensite processing.

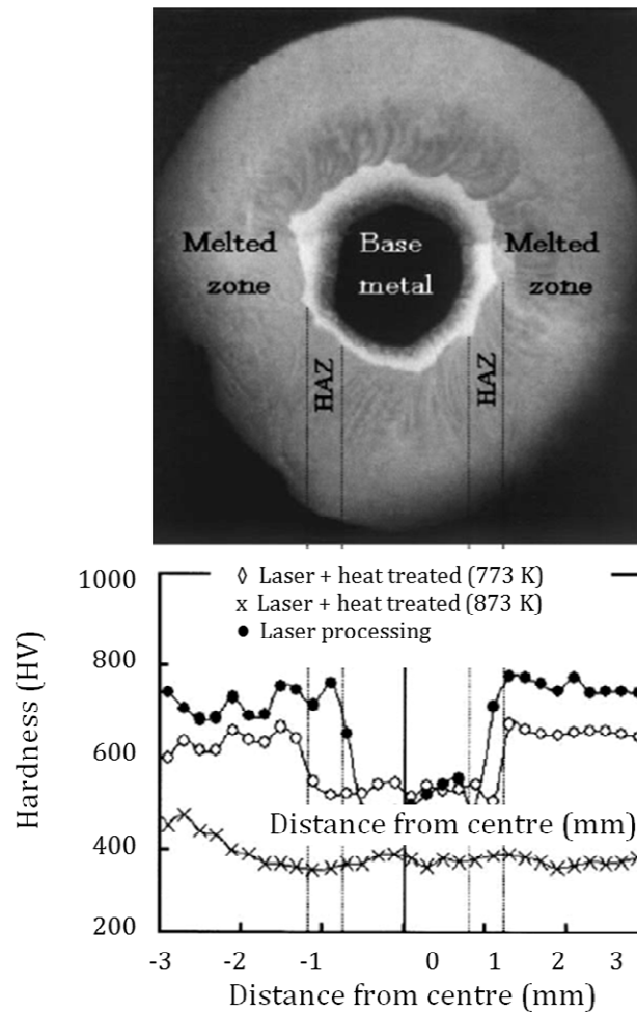


Figure 2.16: Cross-section micrograph and hardness distribution of laser-processed 6 mm diameter specimen. The H11 tool steel specimen was rotated at constant speed of 5 mm/s while being processed with an Nd:YAG laser at 0.5 kW laser power [73].

Laser parameters like power density, pulse repetition frequency and scan rate affect the hardness properties. In Figure 2.17, the average hardness of laser processed nickel-coated cast iron samples increased with increasing power density. At high power density, formation of solid solutions between iron and nickel caused an increase in nickel average hardness as the solid solutions produced were harder and stronger than the pure metals [19]. For metal samples processed at different pulse repetition frequency, the hardness properties increased with increasing pulse frequency. At higher pulse frequency, the pulse energy was lower and caused a faster cooling rate. The overall findings also indicated that

the continuous laser produced a modified surface with lower hardness as shown in Figure 2.18.

The effect of scan rate on the hardness distribution of laser modified H13 steel is shown in Figure 2.19. In the melted zone, the hardness was increased at least two times that of the base metal which occurred at each scan rate. High scan rates of 219.6 mm/s and more exhibited higher hardness measurements due to the fast material-laser interaction time. Faster interaction times yield higher surface cooling rates.

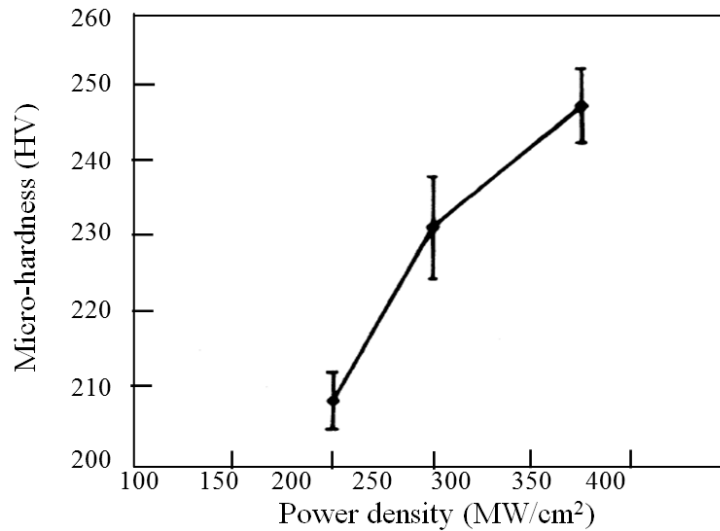


Figure 2.17: Effect of laser power density on the average hardness of nickel-coated cast iron [19].

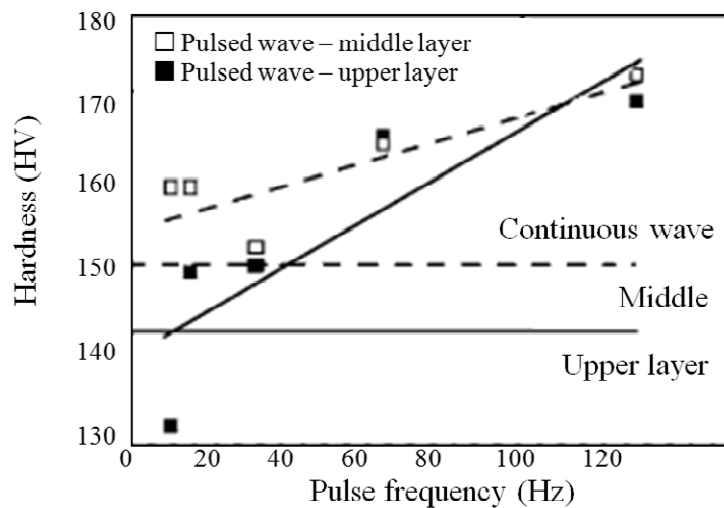


Figure 2.18: Hardness values of stainless steel samples processed at different pulse frequencies [7].

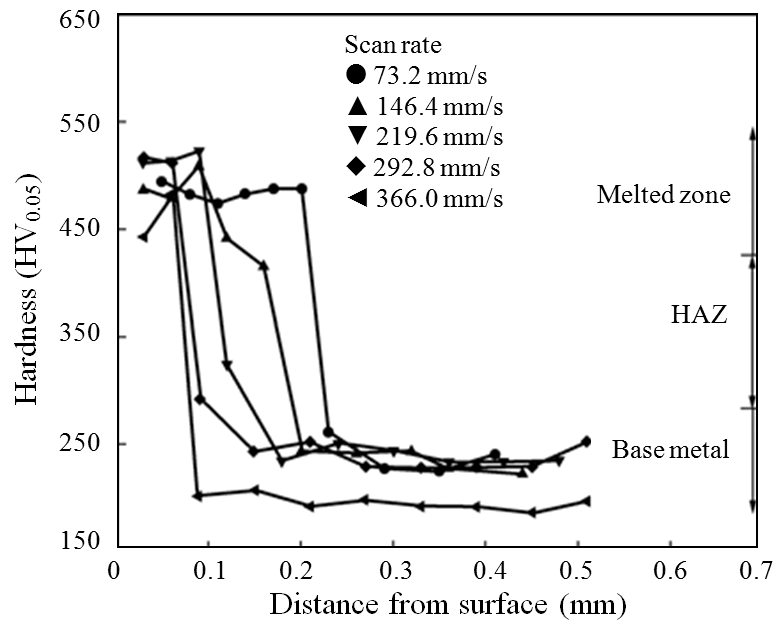


Figure 2.19: Hardness distribution of H13 tool steel at different scan rates [40].

2.3.3 Surface Roughness

The effect of surface roughness on analytical precision was found to be dependent on laser beam energy [74]. The beam energy can be controlled by varying laser irradiance, number of pulses or pulse repetition frequency, and pulse duration. The experimental results in Figure 2.20, Figure 2.21 and Figure 2.22 indicate surface roughness as a function of laser irradiance, number of pulses, pulse width and pulse period. In Figure 2.20, a nonlinear relationship was achieved between surface roughness the increment of laser irradiances. A significant rate of increase of surface roughness was measured at low irradiance range of 80 and 200 MW/cm² and high irradiances of more than 500 MW/cm². High irradiance produced high pulse energy which ablated the material's surface especially when processed at a slow scan rate. By increasing beam scanning speed and overlap, the surface roughness is consequently increased [3, 50]. Referring to the advantage in reducing the surface roughness for thermal barrier coatings, successful results of the laser glazing process have been noted in one work as an improvement from 9 μm to 4 μm R_a [75].

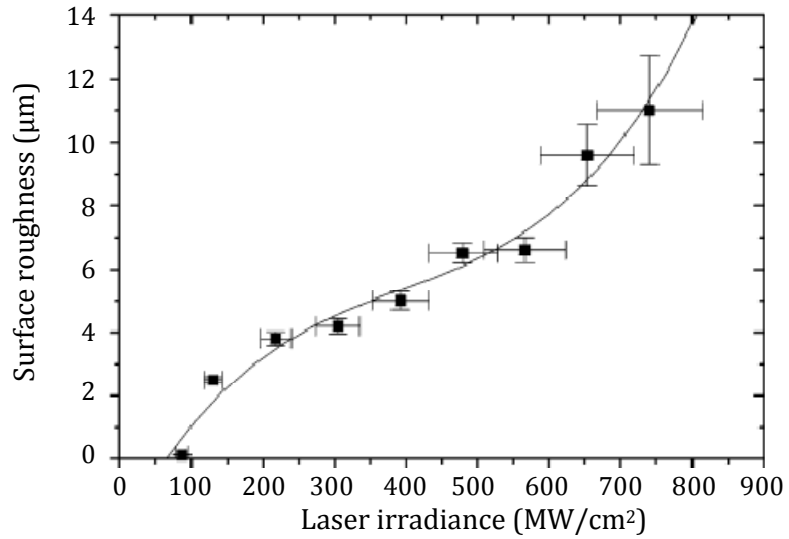


Figure 2.20: Dependence of surface roughness on laser irradiance in laser ablation of cobalt-cemented tungsten carbide using excimer laser at 20 ns pulse width and 450 mJ pulse energy [76].

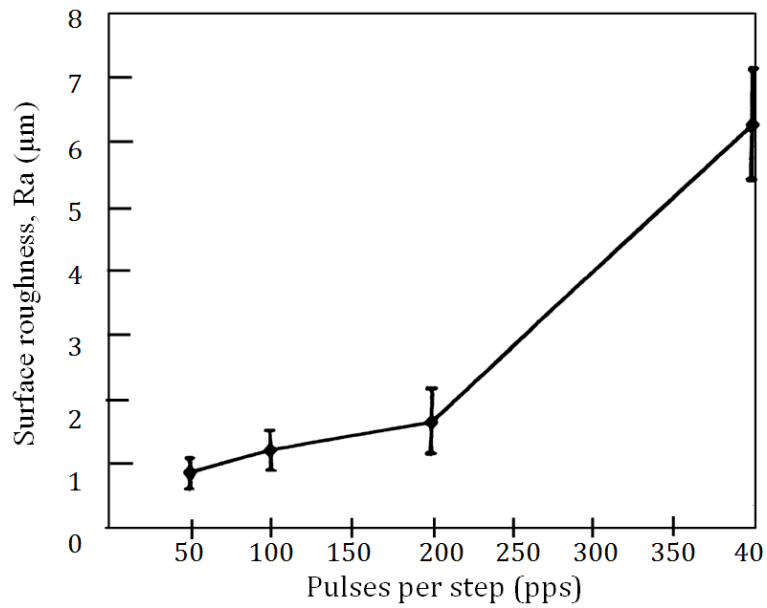


Figure 2.21: Surface roughness of laser-treated nickel-coated cast iron at varying number of pulses using excimer laser at irradiance range between 120 and 325 MW/cm² and PRF of 30 Hz [19].

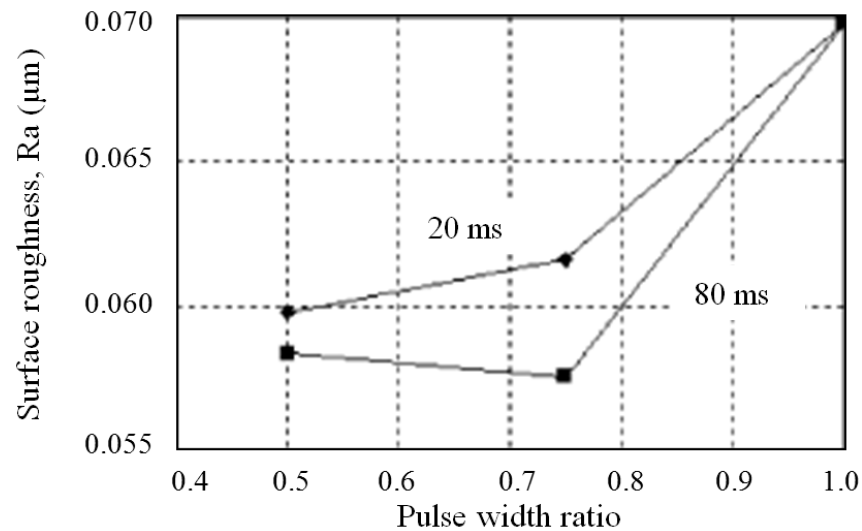


Figure 2.22: Changes in surface roughness with pulse width at 20 and 80 ms pulse period in laser processed 316L stainless steel using CO₂ laser [70].

Figure 2.21 shows increasing surface roughness with increasing number of pulses for nickel-coated cast iron surface processing. Increasing the number of pulses per step increased the interaction time which leads to higher laser energy absorption by the nickel surfaces. When more laser energy was absorbed the surface temperature increased and formed more irregular surface geometries.

Surface roughness dependence on pulse width and pulse period was reviewed with laser processing of 316L steel by Pinkerton and Li [70]. At 20 ms pulse period, the surface roughness was higher than measured from the 80 ms pulse period processing. The pulse width ratio indicates the duty cycle setting during processing, where at 0.5 pulse width ratio the material-laser interaction time was 50% of the fixed pulse period. At higher ratios, the surface roughness increased as the sample surface was more irradiated for longer interaction times. The surface roughness achieved for samples processed at 100% duty cycle for both pulse periods was the maximum value recorded of 0.07 µm. A low surface roughness range was achieved in the study due to a large beam spot size of 1.7 mm and low beam intensity of 198 W/mm² used.

2.3.4 Thermal Fatigue

Engineering parts like brake drums, gas turbines, moulds and dies experience alternate heating and cooling to their working surface at elevated temperatures and mechanical loads [4, 13, 77-79]. Thermal stresses developed from cycling temperature causes thermal fatigue failure on part surfaces. Friction on brake drums in a braking system can generate

temperature up to 900°C which initiate and propagate cracks [77]. In semi solid metal forming, a lot of work has been undertaken to improve die life by surface treatment and coatings with thermal barrier effects. The thermal fatigue failure in semi solid metal forming is due to die cyclic exposure to molten metal at high temperature for thousands of cycles. Increasing surface hardness can enhance the thermal fatigue properties of engineering parts exposed in high temperature applications [77]. From previous work, laser surface treatment using an Nd:YAG laser at 100 W power and 0.88 mm/s traverse speed was shown to be effective to protect surfaces from premature thermal fatigue failure [77].

In thermal fatigue testing, the sample surface expands during heating and shrinks during cooling [80]. Thermal stresses from temperature gradients between the sample outer and inner surface initiates cracks which are further aided by material strength reduction which occurs at higher temperatures [1, 80, 81]. Several methods of high temperature heating and cooling have been implemented in thermal fatigue testing including use of pulsed laser to heat up the surface, magnetic induction heating and silicon oil cooling, vacuum chamber heating, and Joule effect resistive heating with water cooling sprays [4, 78, 79]. However, to simulate the thermal fatigue failure in the semi solid metal forming process environment, a thermal fatigue test apparatus as shown in Figure 2.23 is often used. Specimens are subjected to cyclic heating in bath of molten aluminium alloy (e.g. at 690°C) and cooling in bath of water-based lubricant where the specimens are also continuously internally cooled with cold water [82-84]. The cyclic heating and cooling effect on the exterior and internal surfaces produce high temperature gradients in the specimens, and controlled thermal fatigue [82].

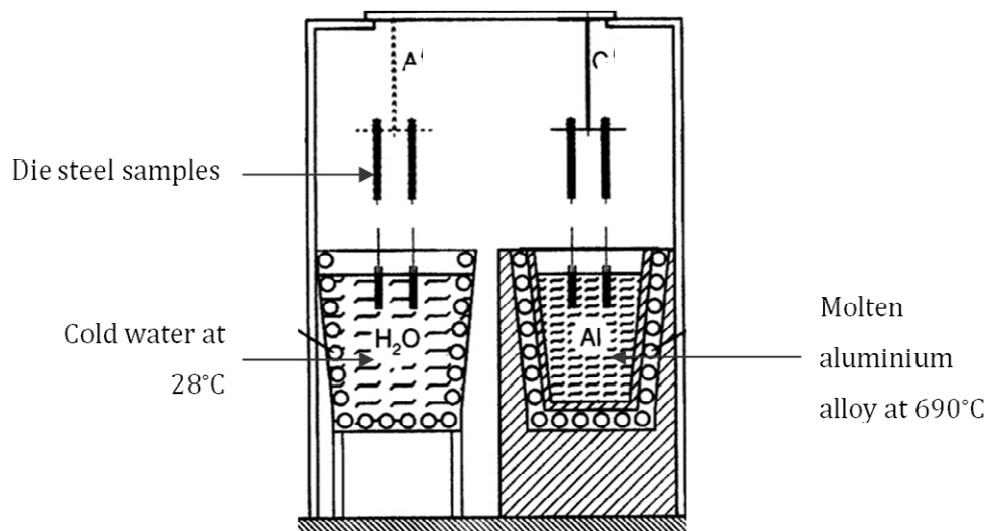


Figure 2.23: Schematic of thermal fatigue test apparatus [82].

Figure 2.24 shows the thermal fatigue performance of untreated and laser treated cast iron samples from 200 to 1300 cycles as measured from crack propagation rate tests. In Figure 2.24 untreated sample with smooth surface produced the highest crack length compared with the other four laser treated samples. Cracks on the untreated sample surface initiate as early as 200 cycles, while the laser treated samples started to crack at 400 cycles. The treated samples surface was harder than the untreated sample and the sample base due to the refined grains and the arising of eutectic carbides caused by the induced high cooling rate [77]. Consequently, cracks also were observed more in the untreated sample. The treated sample no. 4 with maximum hardness exhibited the lowest crack length range compared to other treated samples with lower surface hardness which suggests the importance of surface hardness in increasing thermal fatigue resistant. More findings related to comparison of crack measurement length in untreated and laser treated cast iron samples are shown in Figure 2.25. Thermal fatigue tests were conducted at 2,500 cycles and resulted in a similar trend found in the work of Zhou et al. and Tong et al. [77, 80].

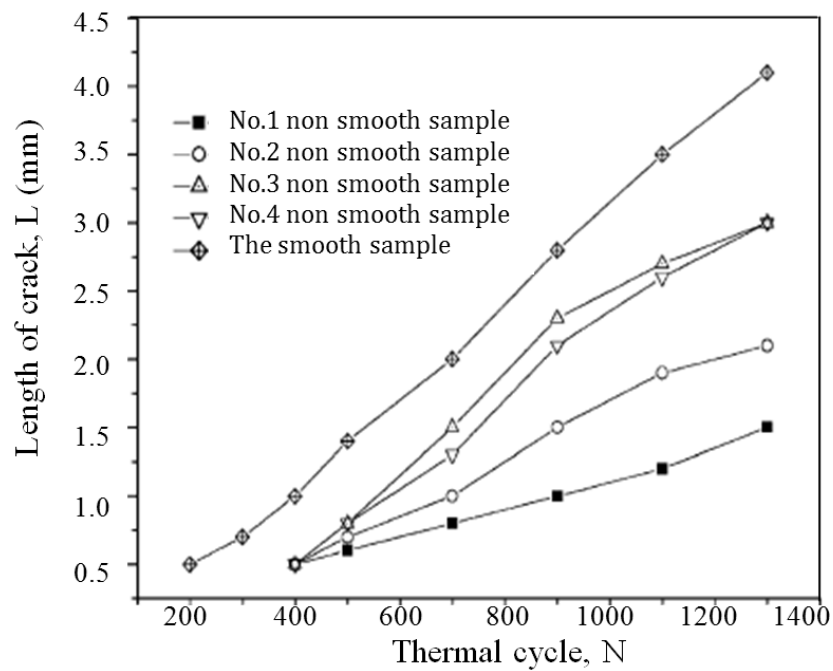


Figure 2.24: L-N curve of untreated and laser treated grey cast iron with four different laser treatments [77].

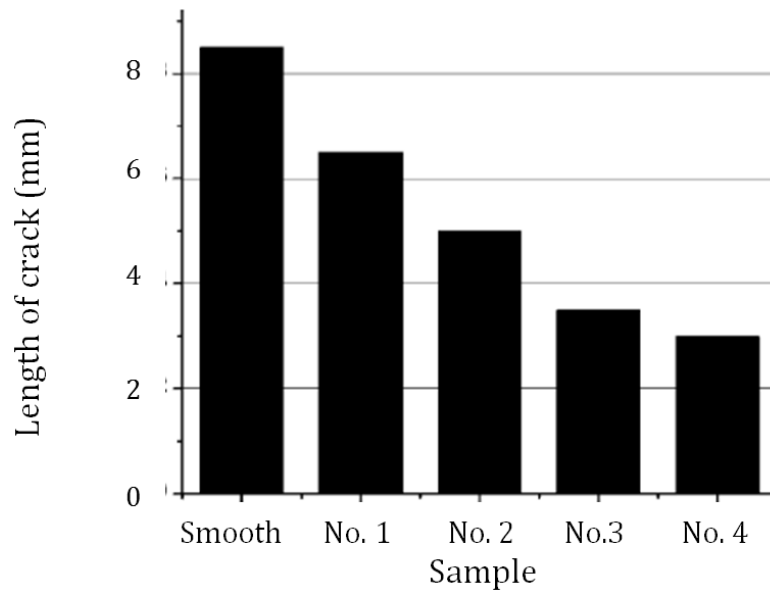


Figure 2.25: Length of fatigue cracks in untreated (smooth) and laser treated (No.1 to 4) gray cast iron samples at 2,500 cycles [85].

2.4 Rapidly Quenched Alloy

In rapid-solidification processing of metallic alloys, a thin surface layer of amorphous or nano-crystalline material can be produced with increased chemical homogeneity, extended solid solubility and metastable phase structure [86]. Based on the starting material from which nano-materials are made, they can be crystallized from amorphous solid or nano-materials can be made from other surface modification methods where the starting material is usually crystalline [87]. Different types of processing and mechanisms to produce rapid quenched alloys include thermal spray processing, drop casting, vacuum die casting, twin roll casting and laser surface processing [5, 88, 89]. At high heating and cooling rate, the alloys are in droplets, ribbons, rods or wedge form with varying dimensions typically from 20 to 30 μm thickness and 40 to 80 mm long [5, 88]. The effect of thickness on amorphous phase formation in rapidly quenched iron based alloy is shown by a broad diffraction halo from an XRD scan, see Figure 2.26. At 2 mm thickness, the sample was more rapidly solidified and crystallisation was fully avoided.

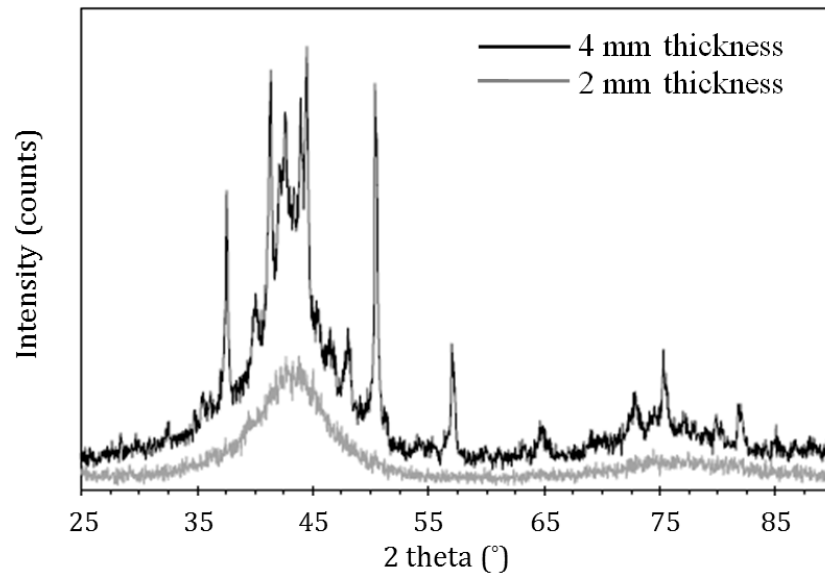


Figure 2.26: XRD of powder Fe₄₈Cr₁₅Mo₁₄Y₂C₁₅B₆ samples taken from two samples of 2 mm (bottom scan) and 4 mm (top scan) cross-sectional thicknesses. The peaks are consistent with M₂₃C₆ phase [88].

To avoid or hinder crystallisation in rapidly quenched alloys, the alloying elements atomic radii are varied, while fourth or fifth elements can be added to the basic ternary alloys [90]. Among the many amorphous alloys developed, iron-based alloys are the most difficult to make amorphous where high cooling rates of 10^5 to 10^6 K/s are typically necessary, and alloys are limited to a maximum of 50% Fe content composed in the alloy [91]. However, by increasing the glass forming ability of Fe-based alloys through addition of element like Nb, a higher content of Fe can be alloyed. In Fe-based alloys, Cr addition in a large amount tends to decrease the glass forming ability since the liquidus temperature significantly increases with an increase of Cr content [92]. Some examples of rapidly quenched cast Fe-based alloys composition with five or more elements are, Fe₄₈Cr₁₅Mo₁₄Y₂C₁₅B₆, [(Fe_{0.5}Co_{0.5})_{0.75}B_{0.20}Si_{0.05}]₉₆Nb₄, Fe_{69.9-x}C_{7.1}Si_{3.3}B_{5.5}P_{8.7}Cr_xMo_{2.5}Al_{2.0}Co_{1.0} (x=0.0,2.3,12.3); and Fe_{50.7}Y_{1.5}Cr_{14.5}Mo₁₃C_{14.8}B_{5.5} [88, 89, 91, 92].

In surface modification of steels where crystalline surfaces are processed, usually more than ten elements are present in the alloy which aid prevention of crystallisation. Materials with typically fine grained structure tend to produce amorphous structure more easily in the laser surface modification process. As grain size influences various properties, the mechanical and physical properties of rapidly quenched Fe-based alloy differed from conventionally cooled alloys. The properties reviewed here were for both bulk Fe-based alloys and for thin layer Fe-based substrates. The properties investigated include grain composition, phase crystallinity and lattice distortion, hardness and thermal fatigue properties.

2.4.1 Phase Crystallinity and Transformation

The crystallinity of a metal surface changes when treated with high energy beam processing such as laser, ion and electron [40, 59, 70, 93-97]. In conventional alloys, sharp fine XRD peaks with high intensity indicate high crystallinity. When the alloy surface is laser processed, the crystalline phase is disrupted and the diffracted peak intensities decrease and other phase compositions are formed as shown in Figure 2.27. The diffracted peaks in the substrate material indicated mainly ferrite peaks along with a small volume fraction of carbide, while after the sample was laser treated, the presence of carbide and retained austenite were reflected at the melted surface, with martensite and small amount of carbide reflected at a depth of 45 μm below the surface [32].

Rapid solidification from laser processing usually results in supercooled or undercooled melt and phase transformation in metal alloys [96, 98, 99]. Figure 2.28 shows untreated and laser treated stainless steel diffraction patterns. The stainless steel samples experienced a decrease of $\alpha\text{-Fe}$ peak intensity and typical martensite-austenite phase transformation after laser treatment at a power density of $1.02 \times 10^9 \text{ W/m}^2$ whereas, full transformation to austenite phase occurred when processed at $1.45 \times 10^9 \text{ W/m}^2$ power density [94]. A similar effect occurred in a laser melted high chrome steel surface where fast quenching of the laser melted sample yielded austenite phase, see Appendix A4(a) [99].

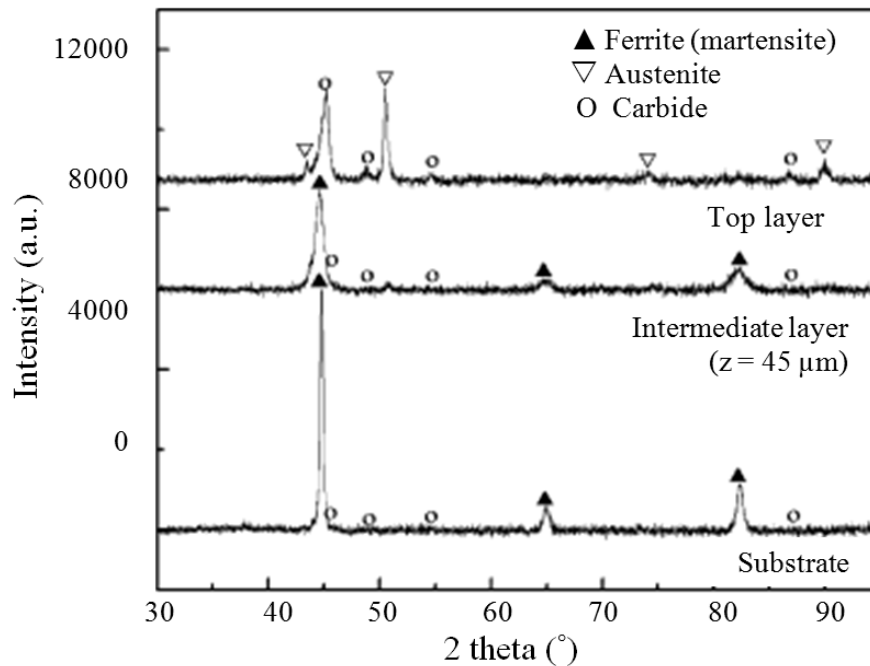


Figure 2.27: XRD peak profiles of the laser treated SAE 52100 steel. The substrate profile presents the same XRD profile as the untreated surface [32].

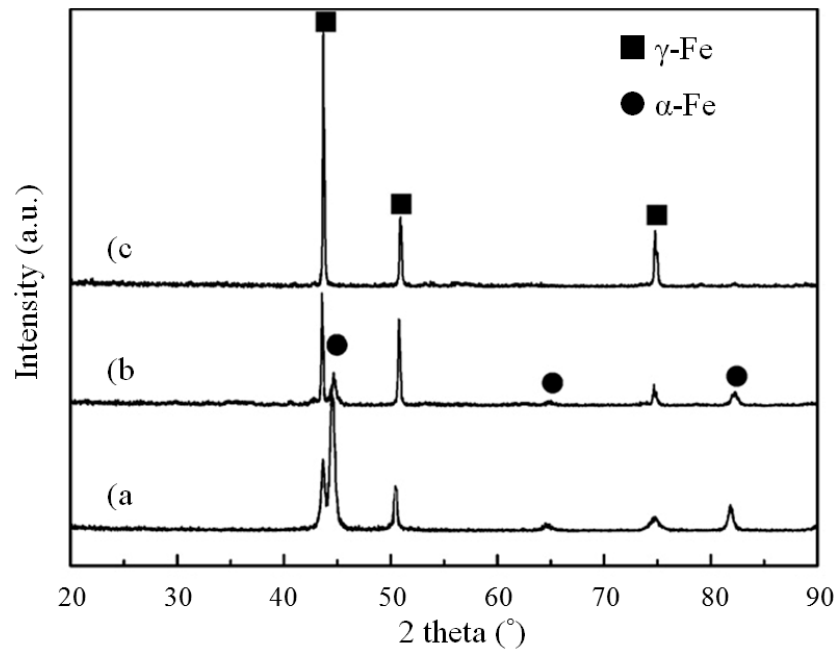


Figure 2.28: XRD pattern of (a) untreated stainless steel, and treated stainless steel samples at (b) 1.02×10^9 W/m² and (c) 1.45×10^9 W/m² power density [94].

Another effect of laser surface modification is the crystalline to amorphous phase transformation. In rapid quenched $\text{Fe}_{48}\text{Cr}_{15}\text{Mo}_{14}\text{Y}_2\text{C}_{15}\text{B}_6$ alloy, the amorphous phase formation competes with nucleation and growth of an $\text{M}_{23}(\text{B,C})_6$ type crystalline phase during continuous cooling [88]. Figure 2.29 (a) and (b) respectively show the amorphous and crystalline pattern of cast $\text{Fe}_{50.7}\text{Y}_{1.5}\text{Cr}_{14.5}\text{Mo}_{13}\text{C}_{14.8}\text{B}_{5.5}$ alloy. The Bragg peaks in the crystalline sample are consistent with M_{23}C_6 and M_6C phases. The presence of amorphous phase is known through the broad maxima curve at lower angles of the scan, see Figure 2.29 (a). Peak broadening has also been attributed to the existence of fine grain size and stress on the materials surface in stainless steel samples [94]. Though none of the samples contained a fully amorphous layer, a considerable volume fraction of amorphous phase was detected from the broad maximum. The presence of the amorphous pre-peak at 2θ of about 8° in $\text{Mg}_{65}\text{Cu}_{25}\text{Mn}_{10}$ alloy showed that the amorphous phase has a high chemical short-range order, Appendix A4(b) [98].

The effect of quenching temperature and cooling rate is shown in Figure 2.30 where a (100) single crystal was cooled at different rates. In quenched samples, the crystalline peak at 31° Bragg's angle observed in slowly cooled samples was suppressed at higher cooling rates [100]. This indicates how variations of quenching temperature and solidification rate affect the peak intensity. As cooling rate was decreased the peaks became sharper and more intense [101].

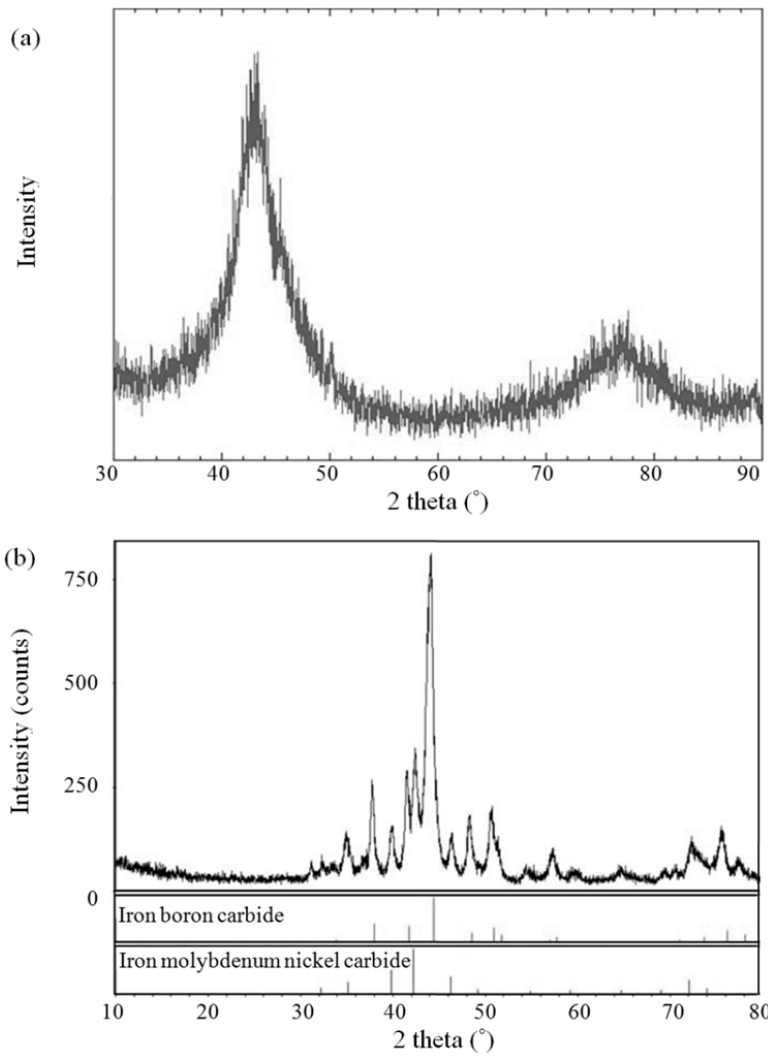


Figure 2.29: X-ray diffraction patterns of (a) amorphous and (b) crystalline sheet of twin roll cast $\text{Fe}_{50.7}\text{Y}_{1.5}\text{Cr}_{14.5}\text{Mo}_{13}\text{C}_{14.8}\text{B}_{5.5}$ alloy [89].

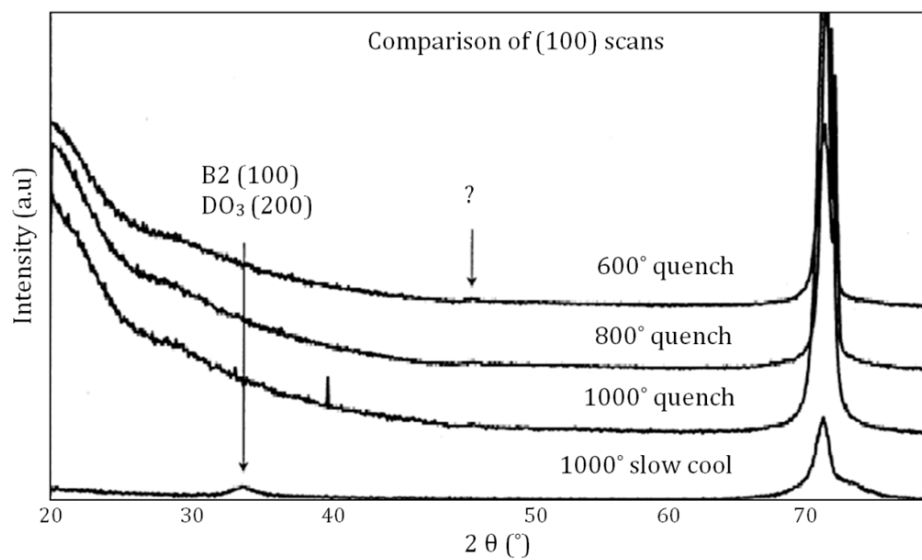


Figure 2.30: X-ray diffraction scans of a (100) oriented Fe-Ga single crystal for the slow-cooled and quenched conditions [100].

Metastable Phase Formation

Amorphous, quasicrystals and martensite are all metastable phases found in metal alloys as a result of solubility extension of the solute atoms at high cooling rate [94, 102]. Amorphous alloys are characterised by critical cooling rates, usually higher than 10^5 K/s and often have thickness below $60\ \mu\text{m}$ [103]. The amorphous phase has a non-crystalline structure with unique properties that combine high strength, stiffness and hardness.

The quasicrystalline state is a metastable state between the amorphous and the crystalline phases with high mechanical properties like hardness and stiffness [102, 104]. In contrast to the amorphous state, the quasicrystalline phase has long range rotational order but a lack of long range translational order and is not truly periodic [102]. In rapidly solidified cast $\text{Al}_{92}\text{Fe}_3\text{Cr}_2\text{Mn}_3$ alloy, the presence of nearly quasi-crystalline phase was observed at a cooling rate of approximately 10^2 to 10^3 K/s [101]. At higher cooling rates of 10^4 to 10^5 K/s, the quasi-crystalline phase was developed.

Martensite structure develops from a diffusionless motion of atoms across an interface which can cause a shape change in the solidified part [105]. In the Fe-based alloy systems, the phase transformation occurs from FCC to a different structure of martensitic or quasi-martensite. For the Fe-C, Fe-Ni-C, Fe-Cr-C and Fe-Mn-C systems, the structural change involves transition from FCC to BCT. The Fe-Ni system martensitic transformation involves FCC to BCC while in Fe-Mn and Fe-Cr-Ni system, the structure change is from FCC to HCP. The martensitic transformation is dependent on the stress, strain, time and temperature which results in athermal and isothermal martensite structure. The athermal martensite is an orthorhombic stress induced phase which is found in steel and Ti-based alloys [106, 107]. Isothermal martensite transformation occurs at low temperature and is stress-assisted [108]. Transformation in Fe-Cr alloy begins in grain boundary areas of significant Cr-depletion, where the chemical driving force is highest [107]. Figure 2.31 shows the athermal martensite observed on grain boundaries of Ti-based alloy. The laser processed Fe-based alloys which undergo rapid austenitizing followed by quenching may develop a unique microstructure consisting of ultrafine-grained martensite and a little retained austenite [99]. Steep temperature gradient and high cooling rate produce ultrafine grained martensite with a high density of dislocations [99]. Retained austenite can significantly decrease the mechanical properties of steels and the service life of steel components [109]. The amount of martensite and retained austenite in steels has previously been examined using XRD techniques [110].

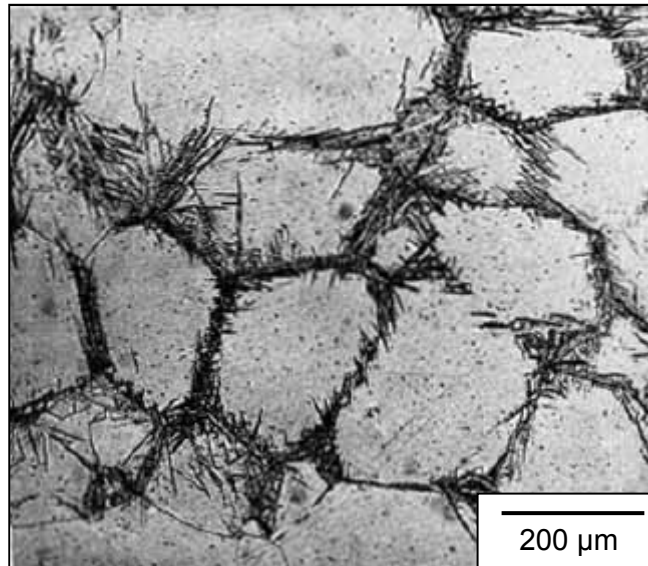


Figure 2.31: Athermal martensite on grain boundaries of Ti alloy [106].

Grain Refinement

In thermo-mechanical processing (strain induced), undercooled austenite transforms to ultrafine ferrite ranging from 1 to 3 μm or less with enhanced strength and ductility [111]. The initial austenite grain size has significant effect on the ferrite characteristics where ferrite grain size distribution is more uniform for the fine prior austenite grain size than for the coarse austenite [111]. In low-carbon steels, the classification of the microstructures is described by the ferritic shapes, such as polygonal ferrite, massive ferrite and bainitic [112]. Austenite decomposition products depend on the amount of carbon redistribution, interface coherence, and undercooling, where morphologies such as allotriomorphic ferrite (grain boundary ferrite), Widmanstätten ferrite, massive ferrite, bainite, or martensite can develop from the parent austenite [113]. Figure 2.32 shows the morphology of ferrite colonies developed at different undercoolings.

At small undercooling, pro-eutectoid ferrite forms as grain boundary allotriomorphs, which generally nucleate at austenite grain boundaries. Allotriomorphic ferrite does not have regular boundaries with the parent austenite grains, but rather is usually equiaxed or lenticular (lentic-like) in shape since it tends to grow preferentially along the grain boundary on which it was nucleated [114]. At larger undercoolings a greater tendency was observed for ferrite to grow into the parent grains as plates. Primary and secondary Widmanstätten ferrites in plate forms grow both from clean austenite grain boundaries and from protuberances on pre-existing colonies of grain boundary ferrite [114].

Massive ferrites occur at large undercoolings and grow very rapidly through the movement of high energy boundaries. The transformation exhibits nucleation and growth characteristics and produces large patches of grains with irregular boundaries surrounded by areas with a mixture of planar and curved boundaries. Since massive transformations occur so rapidly, they are not found in medium or high carbon steels, in which there is insufficient time for enough carbon to diffuse out of the austenite to prevent the formation of martensite [112, 114].

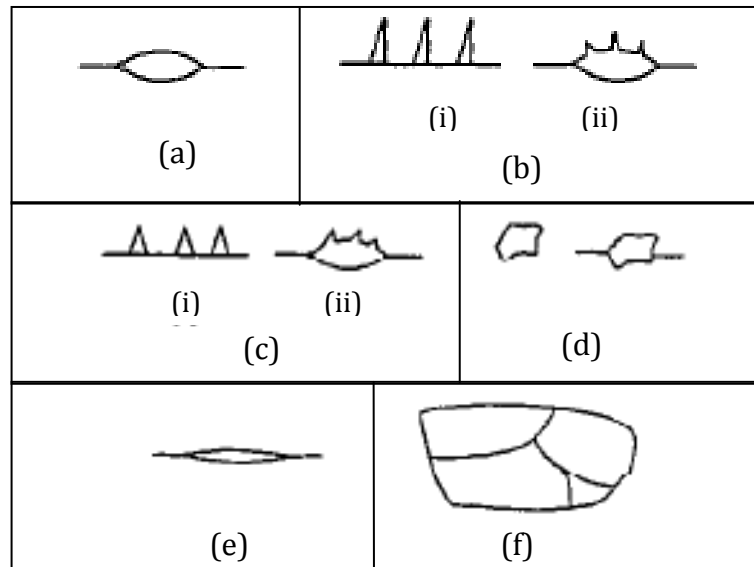


Figure 2.32: Morphology of ferrite: (a) grain boundary allotriomorph, (b) Widmanstätten plates. (i) primary. (ii) secondary; (c) Widmanstätten sawteeth. (i) primary. (ii) secondary; (d) idiomorphs; (e) intragranular Widmanstätten plate; (f) massive ferrite [114].

Nano-scale structures have been observed in crystalline and quasicrystalline materials. Martensitic transformations in steels are known to produce nano-scale structures and very high strengths. The ultrafine-grained materials yield excellent mechanical properties compared with conventional fine-grained materials as well as coarse-grained materials [115, 116]. The refinement of grains can occur either by formation of strain-induced martensites from austenite or martensitic transformation from ϵ (HCP) to α (BCC) which makes the grain sizes of α smaller than ϵ [117]. The nano-scale structures in Fe-based alloys including grains, subgrains and particles can be developed through severe plastic deformation and transformation processes [118]. Severe plastic deformation involves material deformation at ferrite temperatures like ball milling and large strain deformation processes. The transformation processes in Fe-based alloys that can produce nano-scale structures require heating to γ phase followed by rapid cooling [118]. Nano-crystal $M_{23}C_6$ particles in laser modified high chrome steels are only observed from TEM and undetected

in XRD patterns due to its low volume [99]. Pulsed laser treatment of stainless steel at $1.02 \times 10^9 \text{ W/m}^2$ irradiance can rid the steel of the α -Fe phase and produce 4 to 10 nm sized nano-structures and amorphous phase [94]. When processed at a higher irradiance of $1.45 \times 10^9 \text{ W/m}^2$, the amorphous phase re-crystallised and formed 50 to 100 nm grains [94].

In nano-crystalline materials, excess volume of grain boundaries associated with vacancies, and dislocations can lead to lattice strain which modifies the physical properties [119]. Grain refinement is measurable as observed through SEM and XRD analysis [89, 120]. From the Williamson-Hall method, line broadening of a Bragg reflection (h k l) indicates lattice strain or small crystallite size. The crystallite size can be determined using the Scherrer equation:

$$D = \frac{0.9 \lambda}{\beta \cos\theta} \quad \text{Equation 2.1}$$

where D is the crystallite size, λ is the wavelength, β is the broadening (radians), and θ is the diffraction angle.

Many types of nano-quasicrystalline alloys have been developed with a microstructure with nanometer sized icosahedral particles [121]. Some examples of nano quasi-crystalline materials developed recently are Al-Cu-Fe-Bi, Al-Si, and $\text{Fe}_{48}\text{Cr}_{15}\text{Mo}_{14}\text{C}_{15}\text{B}_6\text{TM}_2$ [122, 123]. Nano quasi-crystalline alloys exhibit higher mechanical strength in contrast to nanocrystalline and conventional alloys at high temperature [121]. Due to the need for a high cooling rate of at least 106 K/s, the nano-structured quasi-crystals are produced on different substrates via laser processing [122].

2.4.2 Hardness

Mechanical properties like hardness and yield stress of metals and alloys are affected by their grain size. Decreasing the grain size leads to an increase the mechanical strength [124]. In Fe-based alloys, the nano-scale structures can produce very strong materials with strengths exceeding 3 GPa [118]. The grain size effect relationship of a polycrystalline metal is given by the Hall-Petch equation. Equation 2.2 is based on the fundamental concept that grain boundaries act as barriers to dislocation motion. The grain size dependence of hardness in mild steel samples is shown in Figure 2.33. The grain size changing from 30 μm to 200 nm corresponds to an increase in micro-hardness, which is consistent with the Hall-Petch relationship. Hall-Petch behaviour can be observed for

low-carbon steels with grain size changing from micron to submicron, despite production method and is valid for grain size change over two magnitude orders [125].

$$\sigma_0 = \sigma_i + k_Y D^{-1/2} \quad \text{Equation 2.2}$$

where σ_0 and σ_i are the yield stress of single crystal and polycrystalline metals respectively, k_Y is the experimental constant, and D is the mean grain size. Another equation (Equation 2.3) for metallic crystalline solid deformation due to dislocation motion is given by the relationship of hardness, H , and yield strength, σ_Y , or known as Tabor's equation.

$$H = K\sigma_Y \quad \text{Equation 2.3}$$

where K is a constraint factor which depends on indenter shape and mechanical properties of the indented metal or alloy [126].

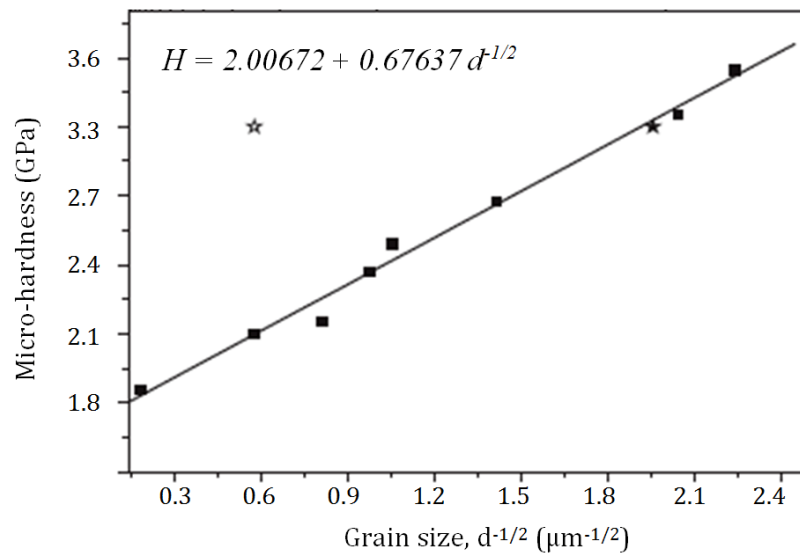


Figure 2.33: Grain size dependence of Vickers hardness [125].

In Figure 2.34, the hardness of heat affected zone shows dependency on the heat input in the processing of low-carbon steels. With different initial grain sizes, the samples yield a similar decreasing hardness trend with increasing heat input. Coarse grain size in specimen 1 and 2 experienced a large decrease of hardness in the heat affected zone (HAZ) when the heat input was increased from 0.5 to 1.0 kJ/mm, compared to finer grain size in specimen 3. Change in strength as a function of grain size is much larger for Fe compared to other structural metals and a reduction in ferrite grain size to the order of 1 μm will significantly strengthen Fe [111]. Hardness decrease was also seen to be due to the

formation ferrite and pearlite structure in the HAZ while the presence of martensite structure contributes to high hardness.

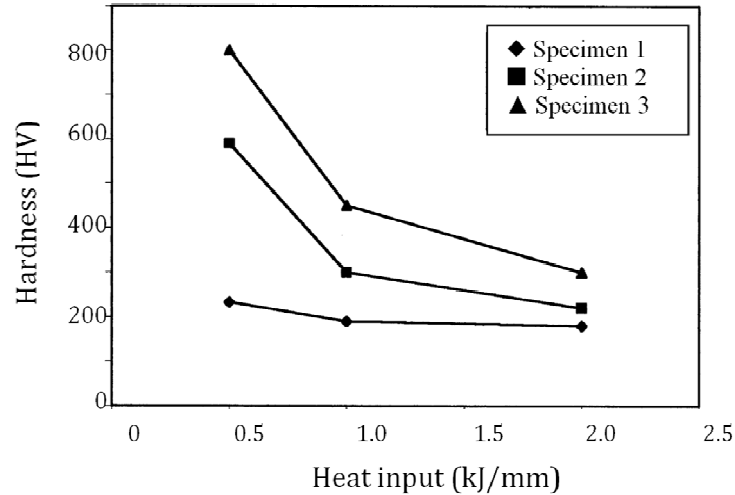


Figure 2.34: Relationship between hardness of HAZ and heat input [127].

2.5 Thermal Modelling of Laser Surface Modification

The physical phenomena corresponding to low and intermediate laser power is simple and predictable in the laser surface modification processing. However, when processing at high power, it is more complicated as the surface temperature becomes overheated and vaporization can occur. Thermal model simulations have been implemented to investigate the relative importance of various laser parameters, the laser heating of surfaces and the thermal stress development at different processing parameters [128-131]. However, most of the studies were largely focused on ceramic coatings and only a few on H13 steel laser surface modifications [129, 130, 132]. The modelling of the laser heating process minimizes the experimental cost and gives insight into the physical processes pertinent to laser surface heating [11, 14]. Modelling of heat conduction in laser heating can be solved using either analytical or numerical methods. Analytical methods provide an effective study of heat source effect whereas numerical solutions focus on the effect of material properties [131]. The advantages of an analytical approach is well known where the temperature of a particular point can be determined without calculating the complete temperature field, the boundary conditions can be fast and easy to implement, as well as useful for studying different heat source geometries [131]. At constant material properties, it is possible to solve analytically the three-dimensional heat conduction with a moving heat source. Both Fourier and kinetic theories were shown in one case to predict similar surface temperature profiles for the same pulse intensities [133]. The well-known

heat conduction differential equation governing the laser heating is given in Equation 2.4. When the medium is moving with a constant velocity, U , parallel to the x -axis, Equation 2.5 applies.

$$\rho C_p \frac{\partial T}{\partial t} = \alpha \left(\frac{\partial^2 T}{\partial x^2} + \frac{\partial^2 T}{\partial y^2} + \frac{\partial^2 T}{\partial z^2} \right) \quad \text{Equation 2.4}$$

$$\frac{\partial T}{\partial t} + U \frac{\partial T}{\partial x} = \alpha \left(\frac{\partial^2 T}{\partial x^2} + \frac{\partial^2 T}{\partial y^2} + \frac{\partial^2 T}{\partial z^2} \right) \quad \text{Equation 2.5}$$

In formulating the heat conduction process with a time-dependant heat source like a pulsed laser beam, some useful assumptions are made including [60, 132, 134]:

- a. the melt pool diameter is equal to the laser beam diameter,
- b. the initial temperature is equal to the ambient temperature $T(x,y,z,0)=T_o$,
- c. the medium is a slab of two parallel planes and heat enters from one plane at $z=0$,
- d. the size of the laser spot is small (fraction of a millimetre), and absorption depth is too small (micrometre depth) compared to the work piece thickness. Therefore, the depth of melt pool, z , is solved using one dimensional heat conduction, and there is no heat losses by any mean from the medium at its two planes; $\partial T/\partial z = 0$.
- e. thermal properties of the work piece are assumed to be independent of temperature,
- f. the latent heat of fusion is small compared to the total energy required for processing; $Q_F \ll Q_L$, and
- g. the work piece is a semi-infinite material where the temperature variations in the region of interest do not affect the temperatures in regions considered to be far away from it, such as the bottom plane.

The absorption factor in the thermal modelling of the laser surface modification process measures incident laser energy absorbed by the surface and transferred to the underlying metal. Absorptance factor depends on surface type, laser power, scan speed and material chemistry. The absorption factor is often assumed constant in order to determine the thermal profile, and thus investigate the phase transformations occurring during surface hardening [44, 133].

2.5.1 Heating and Cooling Rate in Pulsed Laser Surface Modification

Heating and cooling rates in laser surface melting are both significant to determine the mechanical properties of the modified surface. Each laser processing applies different

rates. Despite the fact that laser processing offers rapid heating and cooling, a few milliseconds faster or slower can result in very different grain sizes, microstructures and phases. Molten surfaces experience undercooling where the cooling occurs below the transformation temperature and without phase transformation. A heating and cooling rate model for different laser beam profiles is shown in Figure 2.35. Though different beams produce different rates, the time period for each beam to reach the maximum and minimum temperature was approximately between 1.7 and 1.9 seconds for heating and between 2.5 and 2.7 seconds for cooling. The heating rate was the highest when the circular or rectangular beam shapes were used [135].

At the same pulse energy, the surface experiences a higher temperature when processed with a short pulse in contrast to longer pulses due to high power intensity of the short pulse [136]. In Figure 2.36 the surface temperature decrease with increasing pulse duration is shown. Short pulses result in high fluence which affects the heating and cooling rate. Figure 2.37 indicates the results from solidification theory where cooling rate reduced as the fluence was increased. At lower fluence, the cooling rate was higher and caused more undercooling [137]. The grain size was dependant on the undercooling where smaller sized grains were formed at high undercooling.

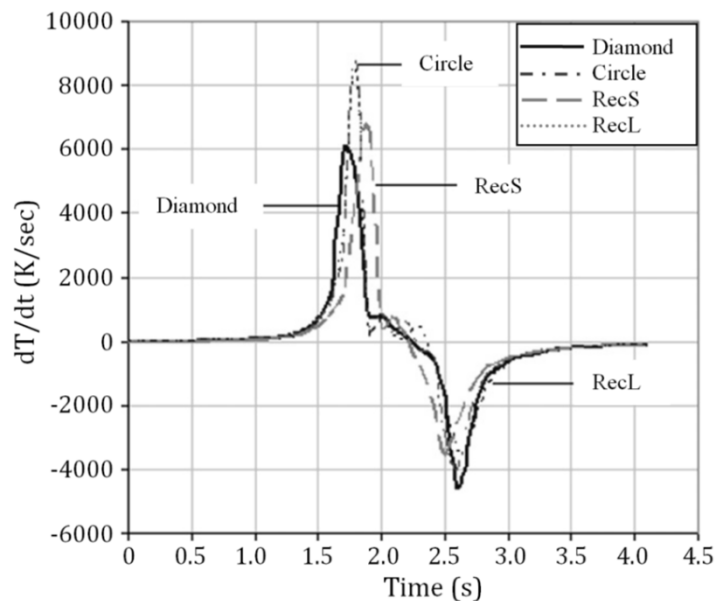


Figure 2.35: Model of heating and cooling rate versus time on surface for different beam shapes [135].

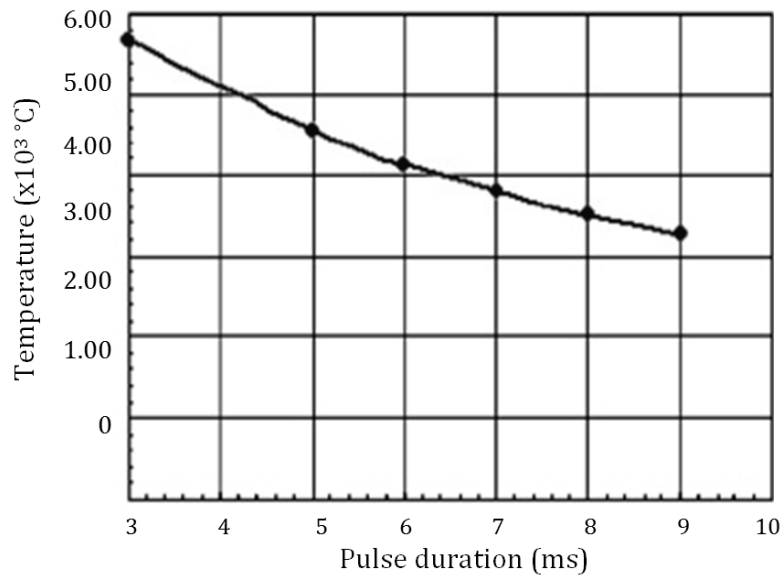


Figure 2.36: Variations of temperature in surface of work piece relative to the pulse duration [69].

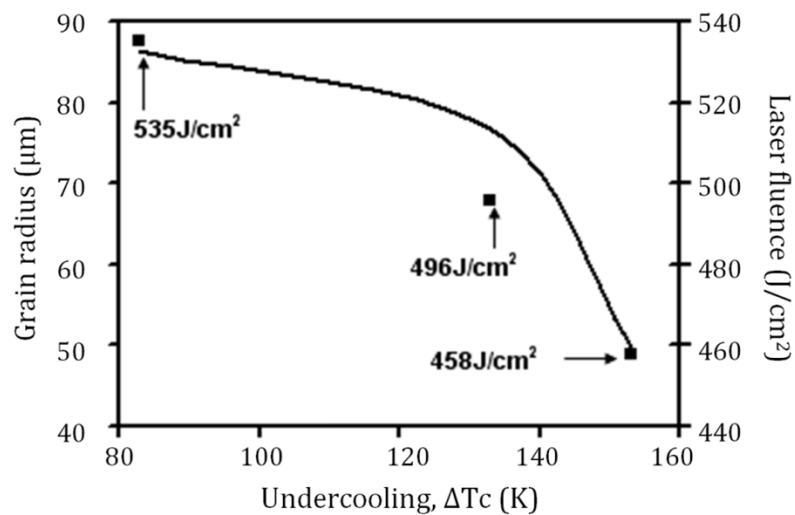


Figure 2.37: Variation of grain radius and laser fluence as a function of undercooling [137].

2.5.2 Thermal Profile

The laser processing thermal history influences the melt pool behaviour, thermal stresses and microstructure [60, 138]. Thermal history determines the final properties of the processed surface like strength, elongation, fatigue behaviour and hardness [131]. It is useful in monitoring how the temperatures change over a period of time which exceeds the pulse duration, and enables study of the heating and cooling rates [60]. Changing the processing parameters effects the surface temperature distribution as shown by Figure 2.38. The thermal profile was predicted for four samples with two processing powers and

scan speeds for a total time of 100 msec. At the higher power of 2.0 kW and lower scan speed of 2.5 m/min, the maximum surface temperature was at 2000°C while at higher speed of 3.5 m/min, the temperature was approximately 1800°C. At lower power of 1.5 kW, a similar trend was plotted where lower surface temperature was achieved when sample was processed at the higher speed of 3.5 m/min. However, the maximum temperature was reached faster when processed at higher speed. It was noted that cooling rates are different for all four samples and can be used to predict the resulting microstructure.

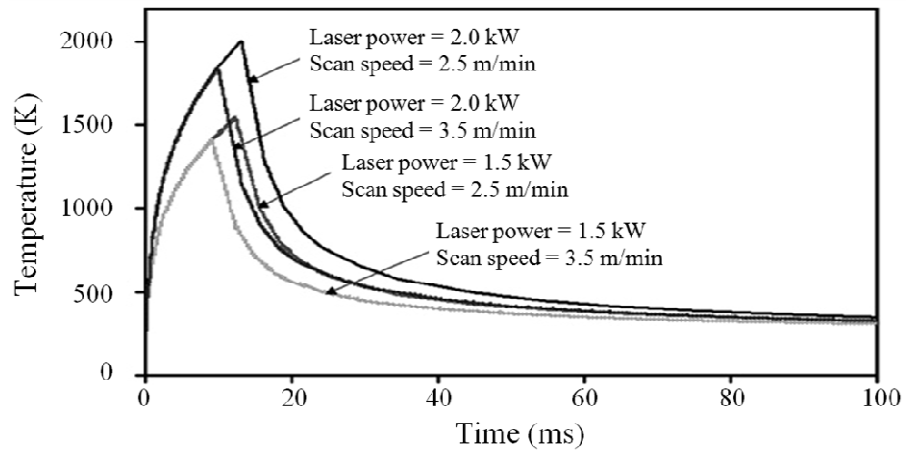


Figure 2.38: Thermal profile (temperature against time) predicted on top surface by numerical solution during laser surface processing [93].

Thermal history can also be plotted for different sample location coordinates where sample temperature changes with respect to distance from spot central position. In Figure 2.39, the thermal histories of four points along the molten pool depth Y direction were measured for a total time of 2 sec. The initial x-coordinate was set to cross the laser point source. Time changes for the coordinate to reach the maximum temperature indicates that substantial time duration is required for the heat to diffuse for points far from the heat source [60]. The temperature distribution also affects the cooling rate which results in microstructure variation along the modified surface region.

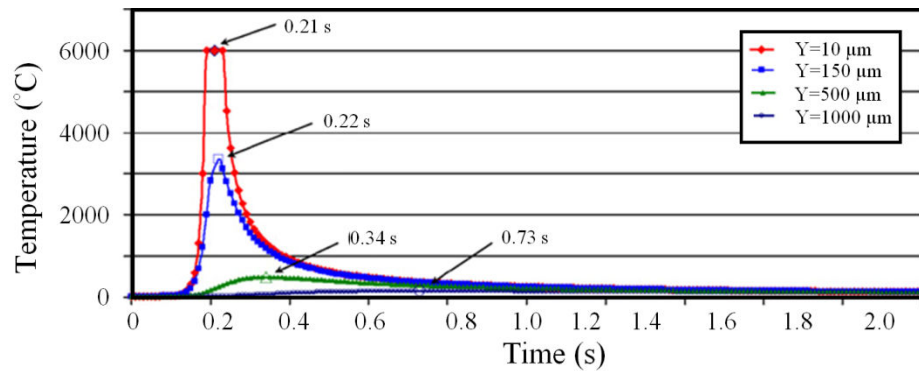


Figure 2.39: Thermal histories of four points on the surface of laser processed glass sheet [60].

2.6 Dies Failure in Semi Solid Metal Processing

In semi-solid metal processing, the forming temperatures are considerably lower than in liquid metal die-casting. Though die material like AISI H13 steel is able to withstand high working temperatures, above 600°C the die easily wears such that the die life at high temperature is not sufficiently long [13, 139, 140]. The cyclic high temperature conditions along with exposure to high viscosity molten metal in semi-solid forming causes the die to wear and crack and causes huge loss due to downtime, die repair and replacement [84]. Wear mechanisms are common in tool steel dies [13, 141], including:

- a. erosion or washout from high velocity and molten metal,
- b. heat checking or thermal cracking affected by thermal fatigue causes heat checks on the surface of the die, and
- c. soldering and corrosion was due to chemical interaction of casting alloy and die material during filling and solidification.

Figure 2.40 shows the heat checking in die casting dies. In forging, cracks appear in the die fillets and some oxides layers are formed on corners which could occur after less than 10,000 forging cycles which usually ends the dies service life at 30,000 cycles [142].

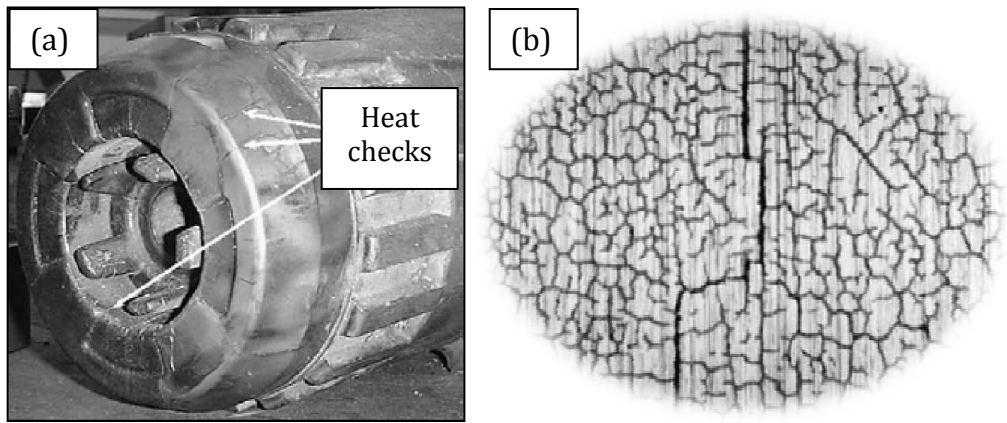


Figure 2.40: (a) Heat checking in die-casting dies and (b) close-up view of heat checks [13].

Die materials have been designed to withstand the temperature, pressure, abrasion, and thermal cycling associated with various hot working operations. Dies are used almost exclusively in extrusion, die casting, plastic injection moulding, hot pressing of copper alloys and steel forging [143, 144]. The properties of die materials are given in Table 2.2 in which the density and thermal properties can be seen to change at higher temperatures. In high temperature applications, the die properties and dimensions change after thousands of processing cycles and often cause non-conformity of final shape [142].

Table 2.2: Properties of die materials at room and elevated temperatures.

Properties	AISI H11	AISI H13	Maraging steel	Reference
Density (kg/m ³)				
20°C		7760		[71]
400°C		7700		(Orvar supreme)
600°C		7600		
Liquidus temperature (°C)		1454/1483		[141]/[71]
Solidus temperature (°C)		1315		[141]
Modulus of elasticity (GPa)	210	210	191*	[1]
20°C		210		(Orvar supreme)
400°C		180		
600°C		140		
Tensile strength (MPa)	1410	1430	1763* 1000**	[1] [145]
Yield strength (MPa)	1170	1230	1688* / 950**	[1] / [145]
Hardness (HRC)		46		[146]
Forged		49		[144]
<i>As-quenched</i>		50		
<i>Tempered at 500°C</i>		53.3		[141]
<i>Tempered at 630°C</i>		39.6		
Heat treated	46			[147]
Solution annealed			30-35**	[148]
Coefficient of thermal expansion (x10 ⁻⁶ °C ⁻¹)				
20-400°C	13.2	12.5	10**	[1]
20-600°C	13.7	13.1	5.6**	
Thermal conductivity (W/m°C)				
20°C	25	25	28**	[1]
500°C	28.5	28.5	32**	
600°C	29.3	29.3	33**	
Specific heat (J/kgK)		447		[141]
Latent heat of fusion (J/kg)		2.8x10 ⁵		[141]
Thermal diffusivity (mm ² /s)		5.35		[71]

Note: *14%Ni maraging steel, **18% Ni maraging steel.

To improve die materials resistance, among the preferable and effective methods are surface modification and coating. Other surface treatments like ion-nitriding, gas-carburizing and thermo-reactive diffusion carburising were reviewed to reduce soldering, increase surface hardness and wear resistance respectively in die steels [149-151]. Both surface treatment and coating were also previously examined to protect tool steels [40, 72, 84, 151, 152]. Coatings of TiC/TiN/Al₂O₃ system were magnetron-sputtered on nitrided tool steel [153]. Coatings can be done in mono-layer, duplex or triple layers with several types of coating materials like ceramics and rare earth elements, and through different methods such as, chemical vapour deposition (CVD), physical vapour deposition (PVD), sputtering process, and thermal spray processes. Examples of coating materials used in die materials are nano-structured CrAlSiN system and triple layers of the Ti/TiAlN/oxide system, [13, 84]. Though various coating technologies were implemented for thermal barrier purposes, the effective coating requirements have proven difficult to meet which makes laser surface modification a useful potential alternate surface properties enhancement method.

2.7 Motivation and Aims of Research

2.7.1 Motivation of Research

In high temperature metal forming, hot work tool steels (AISI Group H series) are used exclusively to withstand the high working temperatures [154]. Hot work steels were chemically designed for good toughness, resistance to high temperature softening, high temperature corrosion and wear properties with low carbon content (0.4 wt.%), medium chromium content (5 wt.%), 1 wt.% Si and small molybdenum and vanadium additions (about 1%) [144]. In spite of these capabilities, above 600°C, these dies easily wear due to high velocity and thermal gradients from injected molten or semi-solid metal. Therefore, die material sustainability has motivated the development of the surface hardening study. Continuous efforts have been undertaken to increase die durability especially through coating and heat treatment technologies [2, 3, 6, 155]. Typical hardness for die casting dies is in the range of 436 to 513 HV (44 to 50 HRC) [140]. Most previous studies have been directed at improving the surface properties of die-casting dies to minimize heat checking, erosion, stress corrosion, and soldering [73, 156]. In this study, the research direction was to develop a modified layer on H13 tool steel substrate by utilising CO₂ laser surface processing. Table 2.3 summarises the previous work on surface modification of hot work tool steels and Fe-based alloy.

Table 2.3: Properties of surface modified tool steels and Fe-based alloys.

Materials	Process/ Laser type (laser mode)	Layer thickness (µm)	Micro-structure/ Composition/ Phase	Surface hardness	Surface roughness (µm)	Reference
H13 tool steel	Laser surface hardening/ fiber laser (PM)	200	-	480-500 HV _{0.1}	-	[40]
DF-2 cold work tool steel	Laser glazing/ Nd:YAG laser (PM)	111	Martensite with retained austenite	1414 HV _{0.1}	R _q = 0.80	[72]
AISI 1045 steel	Laser melting/ picoseconds Nd:YAG lasers (PM)	-	Laser wavelengths cause damage of the steel in the central zone of irradiated area	-	-	[157]
Stainless steel	Laser melting/ Nd:YAG lasers (PM)	-	α-Fe and γ-Fe, or only γ-Fe in amorphous phase and nanograins of 4-100 nm	-	-	[94]
H13 tool steel	Laser glazing/ CO ₂ laser (CW)	150	-	700 HV _{0.1}	-	[55]
H13 tool steel	Laser transformation hardening/ CO ₂ laser (CW)	300	-	510 HV _{0.1} (5 GPa)	-	[65]
X38CrMoV5-3 hot work steel	Laser melting/ diode laser (CW)	100-570	-	698 HV _{0.1} (60 HRC)	R _a = 0.42-0.72	[158]
H13 tool steel	Laser surface hardening/ CO ₂ laser (CW)	-	Martensite within the metallic carbides precipitation	-	-	[71]
H13 tool steel	Laser glazing/ CO ₂ laser (CW)	650	Fine grains and secondary carbides	795 HV _{0.1} (780 kgf/mm ²)	-	[3]
M1 high speed steel	Laser glazing/ CO ₂ laser (CW)	-	Fine carbides formation	-	-	[48]
AISI 1080 steel	Laser glazing/ Nd:YAG laser (PM)	<100	-	655-800 HV _{0.1}	-	[6]
FeCrPC alloy	Laser glazing/ CO ₂ laser (CW)	-	Amorphous	-	-	[28]
AISI P20 mold steel	Laser hardfacing/ CO ₂ laser (CW)	-	Tempered martensite	350 HV _{0.1}	-	[159]
304L stainless steel	Laser melting/ CO ₂ laser (CW)	-	Chemical compositional changes	-	-	[160]

2.7.2 Aims of Research

The aims of this work were:

- a. Development of design of experiments (DOEs) for H13 tool steel laser surface modification using pulsed laser mode to investigate the influence of the processing parameters of laser irradiance (W/mm^2), materials-laser interaction time (ms), and overlapping (%). The range of each parameter was designed, iterated and improved after sample characterisation. Identification of factors affecting modified surface properties from characterisation. Thus, samples were processed at three different laser beam sizes to reduce surface roughness.
- b. Improvement of H13 tool steel surface absorptance for CO_2 laser wavelength through chemical etching and surface roughening.
- c. Characterisation of samples by scanning electron microscopy, crystallinity and phase analysis, hardness testing, and surface profilometry. Specimen preparation for metallographic study, XRD analysis, hardness testing and surface profilometry.
- d. Development of an optimised parameters design for H13 tool steel surface modification.
- e. Thermal modelling simulations of pulsed laser surface modification at varied laser parameters to investigate the effect of surface absorption on the modified region dimensions, the effect of laser parameters on temperature distribution, and to establish a relationship between modified surface properties, structure, and the heating/cooling rate.

CHAPTER 3

Research Methodology

3.1 Materials and Sample Preparation

The material investigated in this study was AISI H13 tool steel with chemical composition given in Table 3.1. The chemical composition was measured using Spectro Max CCD-LMX03 spark light emission spectroscopy. The as-received rods supplied by Special Steels Ireland were in the annealed condition with 280 HV (27 HRC) maximum hardness. The H13 tool steel properties are listed in Table 3.2.

Table 3.1: Chemical composition of AISI H13 tool steel.

Material	Elements (wt%)										
	C	Mn	Si	Cr	Ni	Mo	V	Cu	P	S	Fe
H13	0.32-0.45	0.20-0.50	0.80-1.20	4.75-5.50	0.30	1.10-1.75	0.80-1.20	0.25	0.03	0.03	Bal.

Table 3.2: Properties of H13 tool steel at room temperature.

H13 tool steel	Properties	Reference
Density	7000 kg/m ³	[141]
Hardness	annealed	285 HV
	tempered	544 HV
Liquidus temperature	1454°C	[141]
Thermal conductivity	28 W/mK	[140]
Specific heat	447 J/kgK	[141]
Latent heat of fusion	2.8 x 10 ⁵ J/kg	[141]
Heat transfer coefficient	40 N/s/mm/°C	[140]

As-received 10 mm diameter H13 tool steel cylindrical rods were sectioned into 120 mm length samples. The samples were cleaned with ethanol prior to processing. Samples were laser processed in the as-received condition, after chemically etching the surface, and after surface roughening to 2.90 ± 0.2 μm average roughness, R_a , and chemical etching.

3.1.1 Chemical Etching

Materials surface absorptance in laser surface processing is crucial since most metals are very reflective to CO₂ laser wavelength. The H13 tool steel surface absorptance was enhanced by chemical etching. Samples were immersed in nital (8-10%) solution for 10 minutes before laser processing. Nital (8-10%) solution was prepared by mixing 8 to 10 ml nitric acid with 90 to 92 ml methanol under fume hood ventilation. Nital etchant

reacted with the surface and darkened the as-received surface of the H13 sample. The darkened surface reduced reflectivity upon laser beam-material interaction.

To generate some idea on the heating energy required for surface modification, a calculation of the energy required to melt the surface was performed. The absorption factor, A , was calculated using Equation 3.1 and only 2.2% of energy was absorbed by the as-received steel surface during surface processing.

$$A = \frac{4N}{[(N+1)^2 + k^2]} \quad \text{Equation 3.1}$$

where N and k are the refractive index and absorption coefficient. For iron samples processed at 10.6 μm laser wavelength, the N and k values are 5.97 and 32.2 respectively [62].

The heat conduction calculation in Equation 3.2 was used to estimate the total amount of energy, H_T , needed in the surface modification of H13 steel. The amount of energy to process the surface is given by the total amount of energy required to raise the surface temperature to the melt temperature. The specific heat capacity and latent heat of fusion properties of H13 tool steel that were used are given in Table 3.2. By multiplying the absorbance factor of as-received H13 steel with the total calculated energy, the resulted energy to melt the surface was calculated. Improvements in the surface absorbance were achieved by conducting design of experiments.

$$H_T = [C_p \times (T_L - T_o) \times m] + [H_{\text{fusion}} \times m] \quad \text{Equation 3.2}$$

where C_p , T_L and H_{fusion} are respectively the specific heat capacity (J/kgK), liquidus temperature (K) and latent heat of fusion (J/kgK) of H13 steel, T_o is room temperature (K) and m is the mass of material melted (kg). The mass of material was calculated from area, depth and H13 steel density.

3.1.2 Surface Absorptance by Roughening

The H13 tool steel surface absorptance was improved by surface roughening. The as-received 10 mm diameter and 120 mm length H13 tool steel samples surfaces were machined using Computer Numerical Controlled (CNC) turning machine to produce a $2.90 \pm 0.2 \mu\text{m}$ average R_a surface roughness. The final diameter of the samples after roughening was 9.4 mm. Figure 3.1 shows the machined sample surface profile as measured with TR-200 two-dimensional surface profilometer. Five measurements taken

at different parts of the sample length resulted in a consistent average roughness reading of 2.90 μm . The machined surface was then chemically treated using Nital (8-10%).

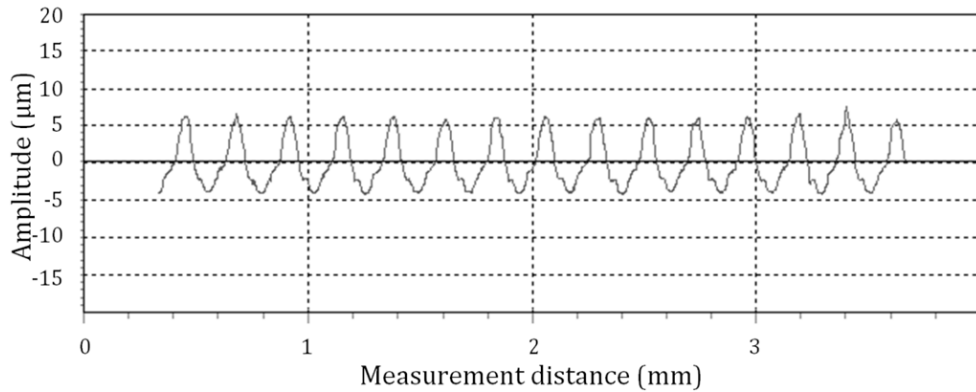


Figure 3.1: Surface profile of $2.90 \pm 0.2 \mu\text{m}$ R_a machined sample.

3.2 Laser Surface Modification

A Rofin DC-015 diffusion-cooled CO_2 slab laser system with 10.6 μm wavelength was used to modify the steel surface. The system specifications are given in Figure 3.2. The laser system was focusable to a minimum laser spot size of 90 μm on the sample surface. The focused spot diameter can be calculated using Equation 3.3. The beam delivery path in this CO_2 laser system is shown in Figure 3.2. During laser processing, a constant flow of Argon gas at 0.1 MPa (1 bar) pressure was maintained to avoid oxidation of the sample surface.

Table 3.3: Specifications of Rofin DC-015 diffusion-cooled CO_2 slab laser system.

Laser parameters	Specifications
Wavelength, λ	10.6 μm
Maximum power, P_{max}	1520 W
Operation mode	Continuous and pulse
Pulse repetition frequency	2 to 5000 Hz
Pulse width, τ	0.026 to 125 ms
Beam spatial mode	TEM_{00}
Beam quality factor, K	>0.9
Beam propagation parameter, M^2	1.11

$$\text{Focused spot diameter, } d = \frac{\lambda f x M^2}{\pi x D} \quad \text{Equation 3.3}$$

where, λ is the laser wavelength, f is the focal length of the lens (127 mm), M^2 is the beam quality (1.11) and D is the beam diameter (22 mm).

Figure 3.3 shows the laser surface modification process setup. The sample was attached in a chuck to a translation stage. The sample surface was set normal to the laser head. The sample circumferential surface was treated by rotating it perpendicular to the laser firing direction. The sample was also linearly translated in order to process a pre-defined overlapping helix pattern longitudinally which allowed for complete processing of the surface area. The maximum circumferential speed and linear translation speed were 3,000 rpm and 5,000 mm/min (83.33 mm/s) respectively.

Controlled processing parameters were laser peak power, duty cycle, pulse repetition frequency, linear speed and rotational translation speed. The sample was rotated by using a DC motor (Bodine® Small Motor type-32A5BEPM with 2500 rpm) which was fixed to a customised laser platform moving perpendicular to the laser firing direction. Sample rotational translation speed was set by the voltage input controllers while the linear translation speed and laser processing parameters were set at the Rofin laser controller. The laser parameter settings resulted in the modified surface grain size, mechanical properties, surface morphology, phase and structure composition. The independent parameters were computed to produce relationships of two or more laser parameters. Parameters derived from the chosen settings such as pulse period, pulse width, residence time, average power, pulse energy, fluence and irradiance allow accurate control of the laser processing.

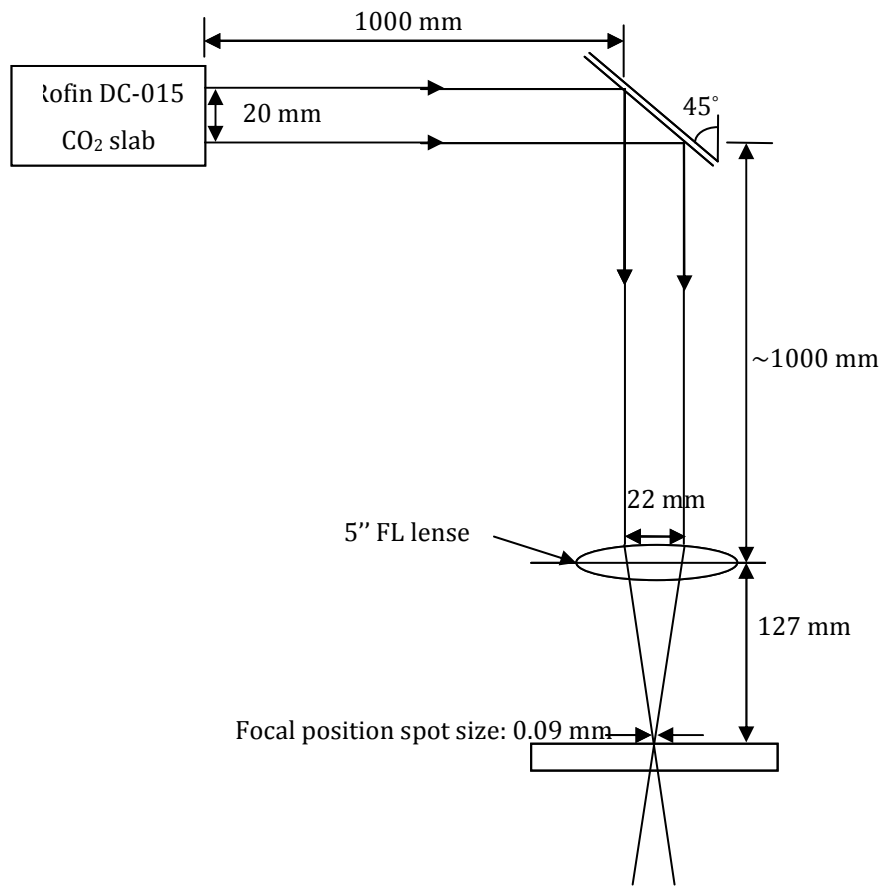


Figure 3.2: Beam delivery path in CO₂ laser system

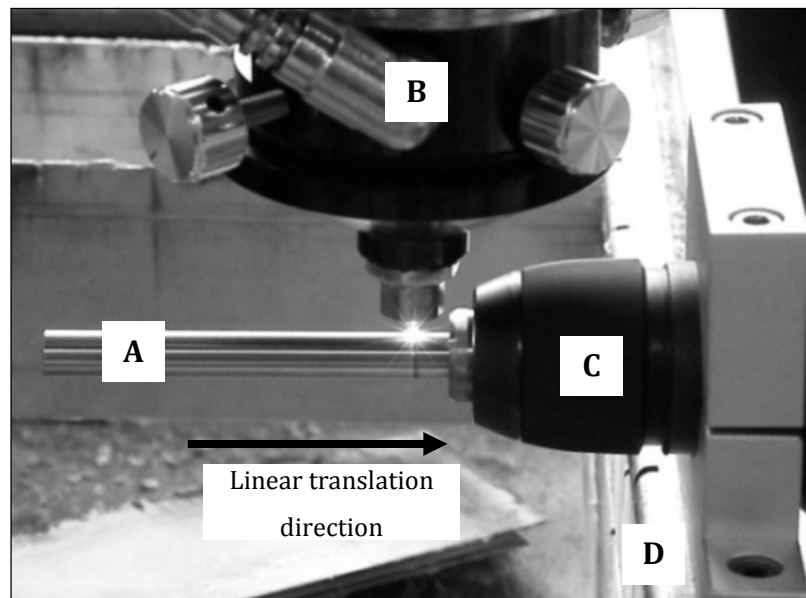


Figure 3.3: Laser surface modification process setup (A: 9.4 mm diameter H13 sample, B: laser head, C: rotating chuck, and D: linear translation platform).

Laser Spot Size, w_R and Focal Distance, z

In the experimental design of laser processing, the laser beam was focused to the sample surface with 0.09 mm, 0.2 mm and 0.4 mm spot size. The processing focal position was set at two different distances between sample surface and the focal position to produce spot sizes of 0.2 mm and 0.4 mm. The focal distance was calculated using Equation 3.4. Figure 3.4 shows the laser beam diameter plot against focal distance as calculated from Equation 3.4.

$$w_R(z) = w_{OR} \left[1 + \left(\frac{z \lambda M^2}{\pi w_{OR}^2} \right)^2 \right]^{1/2} \quad \text{Equation 3.4}$$

where, w_{OR} is the radius of a real (non-Gaussian) beam at the waist, w_R is the radius of the beam at a distance z from the waist, λ is the laser wavelength and M^2 is the beam quality.

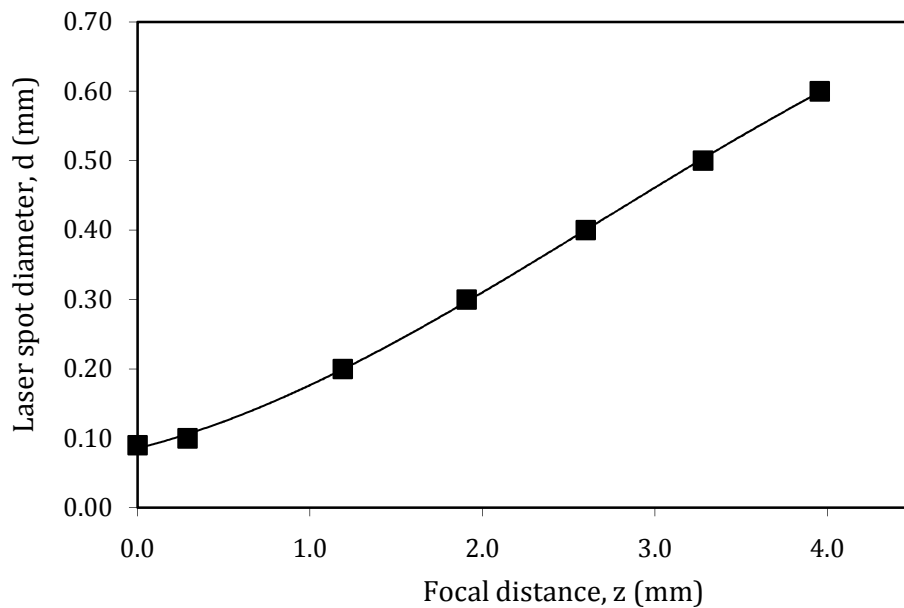


Figure 3.4: Laser beam diameter as a function of distance from the focal position.

Linear Translation Speed, V

Figure 3.5 shows the relationship of rotational and translational speed in order for consecutive laser passes to overlap and form a continuous processed region. For a given length traversed per pass, X_p , the speed for the sample to move in x -direction is given by Equation 3.5.

$$V = (X) \cdot (\omega) \text{ [mm/s]} \quad \text{Equation 3.5}$$

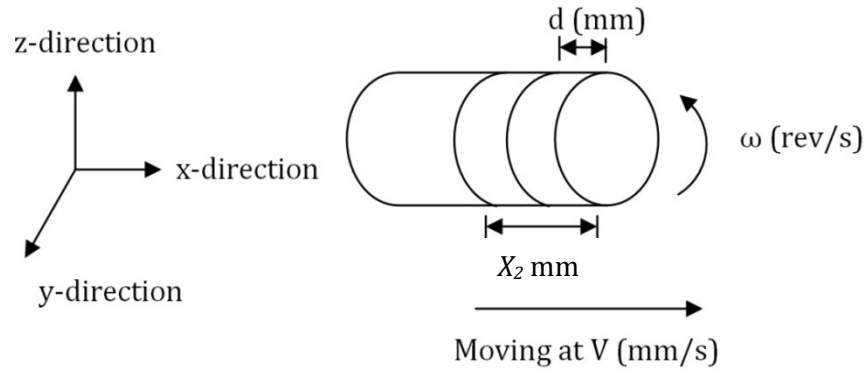


Figure 3.5: Rotational and linear sample movement in laser surface processing where d is the spot diameter and X_2 is the processed longitudinal length of two subsequent passes.

PRF Correlation with Pulse Overlap

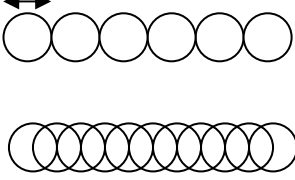
The number of pulses frequency and translational speed processed along a sample length determined the circumferential and longitudinal overlap percentage. The circumferential and longitudinal overlaps were designed to be the same. The overlap, η , can be calculated from Equation 3.6

$$\eta = \left(1 - \frac{\Delta}{d}\right) \cdot 100\% \quad \text{Equation 3.6}$$

where, $\Delta = (X_2 - d)$, is the overlap distance between passes and X_2 is the longitudinal length of two subsequent passes.

The laser PRF required to process the sample surface was determined using the basic principle which counts the number of laser spots diameters, n , in a single pass of the sample circumference. The circumference of the 10 mm diameter sample calculated was 31.42 mm and for the roughened diameter of 9.4 mm was calculated as 29.53 mm. Referring to Figure 3.6, when the laser spot diameter, d was 0.4 mm, the number of laser spots or pulses, n , required to process the sample without overlap between the spots, can be calculated using the relation of sample circumference divided by laser beam spot diameter. In the preliminary design where overlaps were 10, 30 and 50%, the number of circumferential laser spots used were 86, 102 and 118 respectively.

$d=0.4 \text{ mm}$



Without overlap, $n = \frac{2\pi \times 10 \times 10^{-3}}{0.4 \times 10^{-3}} = 78.5$

At 50% overlap, $n = \left(78.5 \cdot \frac{50}{100}\right) + 78.5 = 117.8$

Figure 3.6: Number of laser spots calculated without and with 50% circumferential overlap for a 10 mm diameter rod.

The PRF was calculated from the number of laser spots, n divided by the time taken to laser process one full rotation. In this calculation, a linear relationship was established between PRF and overlap as shown in Figure 3.7. Using the rotational speed, the time required to complete the process in one full rotation is given by Equation 3.7. To calculate the linear translation speed with a 30% longitudinal overlap, the stage was set to move at a speed of seven tenths of the laser spot diameter per revolution.

$$t = \frac{1}{\omega} [s] \quad \text{Equation 3.7}$$

In this formulation, the circumferential speed was constant at any overlap percentage. As the PRF increased with increases overlap percentage, shorter pulse period and pulse width were required. Thus, the amount of energy per pulse also decreased with increasing frequency or overlap.

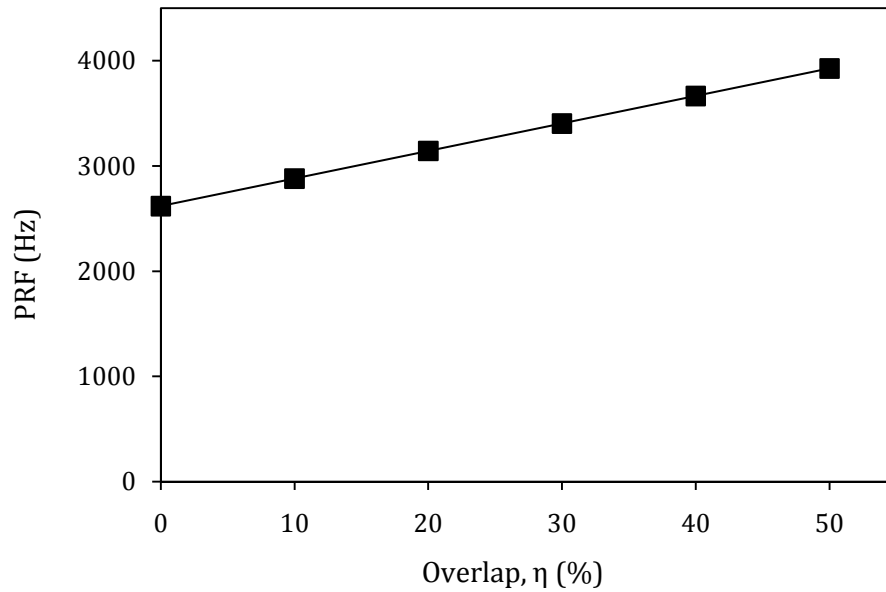


Figure 3.7: PRF as a function of overlap in pulse laser processing for a 10 mm diameter rod, a 0.4 mm spot size and at a rotational speed of 2000 rpm.

Designing Pulse Overlap at Constant PRF

Besides increasing the PRF at constant traverse speed to obtain the number of required pulses, the overlap pulses was also calculated using a different approach. In order to keep most of the laser parameters at constant values, the effective pulse energy required for H13 tool steel surface processing was determined. For example, when the PRF was fixed at a constant value of 2900 Hz, constant pulse energy, pulse period and pulse width were achievable at any overlap percentage. In this case, to produce overlapped pulses, the rotational speed was adjusted instead of increasing the number of laser spots, as shown in Figure 3.6. The overlap was increased by decreasing rotational speed. The overlap percentage can be calculated from the residence time to pulse width ratio. The pulses were not overlapped when the residence time was equal to pulse width.

Surface Absorptance and Overlap

The pulse overlap was designed by taking into account surface absorptance percentage. The surface absorptance, A , was calculated from molten pool geometry processed by a single laser pulse as given in Equation 3.8.

$$A = \frac{c}{d} \cdot 100 [\%] \quad \text{Equation 3.8}$$

where c is the molten pool width and d is the laser spot diameter. This equation was only applied to samples processed at 0.4 mm diameter spot size.

3.2.1 Design of Experiment 1 (DOE1)

The primary goal in DOE1 was to produce a modified surface layer with depth of modification dependant on the laser parameter settings. Table 3.4 shows the laser processing parameter for samples in DOE1. Cylindrical 10 mm diameter as-received H13 tool steel was sectioned to 120 mm long samples which were processed at different settings of duty cycle, overlap and PRF. Laser processed samples were prepared for metallographic study. Micrographs of laser modified surface cross section were recorded for measuring the processed surface depth. Phase analysis of laser modified surface was conducted to measure the phase transformation in the processed surface. These initial characterisation results were focused on obtaining a maximum depth of the laser modified layer and reducing the α -Fe phase peak intensity as measured from metallographic and XRD analysis respectively.

In DOE1, H13 samples were processed using a full factorial design of 3^3 , with a constant peak power of 760 W. Three different levels of overlap (10, 30 and 50%), duty cycle (70, 85 and 100%) and circumferential speed (2000, 2222 and 2500 rpm) were designed, see Table 3.4. The overlap was calculated from the traverse speed which in turn provided the PRF settings, see Figure 3.7. Three levels of duty cycle of 70, 85 and 100% were set which resulted in average powers of 532, 646 and 760 W respectively. The H13 surface was processed in the as-received condition. The laser beam was defocused to 0.4 mm size. The laser irradiances and residence times resulting from these parameter settings were in the range of 3,872 to 5,576 W/mm² and 0.22 to 0.38 ms respectively.

Table 3.4: DOE1 processing parameter settings at constant peak power of 760 W.

Sample	Set parameters				Outcome parameters				
	DC (%)	η (%)	ω (rpm)	PRF (Hz)	P_A (W)	τ (ms)	I (W/mm ²)	T_R (ms)	E_p (J)
1	70	10	2500	3636	532	0.19	5,313	0.22	0.15
2	85				646	0.23	5,304	0.27	0.18
3	100				760	0.28	5,269	0.32	0.21
4	70		2222	3200	532	0.22	5,547	0.24	0.17
5	85				646	0.27	5,547	0.29	0.20
6	100				760	0.31	5,503	0.34	0.24
7	70		2000	2857	532	0.25	5,570	0.27	0.19
8	85				646	0.30	5,540	0.33	0.23
9	100				760	0.35	5,576	0.38	0.27
10	70	30	2500	4211	532	0.17	4,626	0.22	0.13
11	85				646	0.20	4,517	0.27	0.15
12	100				760	0.24	4,607	0.31	0.18
13	70		2222	3810	532	0.18	4,608	0.24	0.14
14	85				646	0.22	4,631	0.29	0.17
15	100				760	0.26	4,589	0.35	0.20
16	70		2000	3333	532	0.21	4,760	0.27	0.16
17	85				646	0.26	4,793	0.32	0.19
18	100				760	0.30	4,798	0.38	0.23
19	70	50	2500	5000	532	0.14	3,872	0.22	0.11
20	85				646	0.17	3,881	0.27	0.13
21	100				760	0.20	3,881	0.31	0.15
22	70		2222	4444	532	0.16	3,946	0.24	0.12
23	85				646	0.19	3,946	0.29	0.15
24	100				760	0.23	3,948	0.35	0.17
25	70		2000	4000	532	0.18	3,959	0.27	0.13
26	85				646	0.21	3,951	0.34	0.16
27	100				760	0.25	3,973	0.38	0.19

Focal Position of Defocused Laser Beam

DOE1 was conducted using defocused beam to 0.4 mm diameter spot size. In order to gain a defocused spot size of 0.4 mm, the focal position was set to be 2.6 mm above the sample surface. Although most of the samples were processed with a positive focal position offset, some of the samples of DOE1 were processed at negative offset where the beam was focused 2.6 mm below the sample surface. In order to investigate the effect of focal position, six samples were processed at the parameter settings given in Table 3.5. The laser parameter settings were set as per sample 21, 23 and 27 in Table 3.4.

Table 3.5: Laser parameter settings for samples at two different focal positions and 50% overlap.

Sample	Set parameters			Outcome parameters		
	DC (%)	Focal position (mm)	PRF (Hz)	T _R (ms)	I (W/mm ²)	E _P (J)
21	100	+2.6	5000	0.31	3,881	0.15
21b	100	-2.6				
23	85	+2.6	4444	0.29	3,946	0.15
23b	85	-2.6				
27	100	+2.6	4000	0.38	3,973	0.19
27b	100	-2.6				

3.2.2 Design of Experiment 2 (DOE2)

An experimental design, DOE2, was developed with parameters given in Table 3.6. DOE2 parameters combinations were selected from DOE1. Selected parameters were based on the modified surface depth findings produced in DOE1 samples. The parameters were designed for nital etched samples at a negative focal position of -2.6 mm, beam spot size of 0.4 mm diameter, constant peak power of 760 W, and with four residence times. Duty cycle was set at 85 and 100% to produce average power of 646 and 760 W respectively, while overlap was set at the three levels of 10, 30 and 50%. The overlap percentage was calculated from the traverse speed which in turn provided the PRF settings, see Figure 3.7. The samples were labelled with 'E' to indicate etched samples and were also 10 mm diameter and 120 mm long.

Table 3.6: DOE2 parameter settings for nital etched samples processed at negative focal position.

Sample	Set parameters				Outcome parameters			
	DC (%)	η (%)	ω (rpm)	PRF (Hz)	P _A (W)	I (W/mm ²)	T _R (ms)	E _P (J)
E6	100	10	2222	3200	760	5,510	0.34	0.24
E8	85		2000	2857	646	5,548	0.32	0.23
E9	100		2000	2857	760	5,592	0.38	0.27
E14	85	30	2222	3810	646	4,618	0.29	0.17
E15	100		2222	3810	760	4,631	0.34	0.20
E18	100		2000	3333	760	4,774	0.38	0.23
E12	100		2500	4211	760	4,475	0.32	0.18
E24	100	50	2222	4444	760	3,958	0.34	0.17
E26	85		2000	4000	646	3,971	0.32	0.16
E27	100		2000	4000	760	3,971	0.38	0.19
E21	100		2500	5000	760	3,745	0.32	0.15

3.2.3 Design of Experiment 3 (DOE3)

In DOE3, the effect of surface roughening and chemical etching was investigated at different laser parameters settings. Laser processing experiments were also designed to increase the surface cooling rate using a smaller spot size of 0.2 mm. A focal distance offset of -1.2 mm was set to produce this spot size. Samples 120 mm long were processed at constant PRF of 2900 Hz. The samples for DOE3 were machined to $2.9 \pm 0.2 \mu\text{m}$ average R_a surface roughness and chemical etched prior to processing. The sample diameter after roughening was 9.4 mm.

DOE3 design consists of four processing settings which compared three levels of peak power as shown in Table 3.7. An additional setting with 10% overlap was conducted at 760 W peak power to investigate the effect of constant PRF on overlap geometry. Duty cycle in DOE3 was designed to be dependent on the peak power in order to control the average power. The residence time varied due to these duty cycle and overlap percentage settings.

Table 3.7: Processing parameter for DOE3 samples.

Sample	Set parameters			Outcome parameters			
	P _P (W)	DC (%)	η (%)	P _A (W)	I (W/mm ²)	T _R (ms)	E _p (J)
N4	507	49	50	249	10,930	0.25	0.09
N10	760	36	10	274	22,139	0.14	0.10
N24	760	36	50	274	16,388	0.19	0.10
N12	1313	23	50	305	28,184	0.12	0.11

Sample Heating Rate and Cooling Period

During processing, samples surface was heated up from room temperature to its liquidus temperature. The heating rate, H_R , of the surface can be calculated using Equation 3.9. Cooling period, $t_{cooling}$, of the samples was determined from the 'off' state duration of the laser pulse, see Equation 3.10. Hence the cooling rate, C_R , can be calculated as per Equation 3.11.

$$H_R = \frac{\Delta T}{T_R} \quad \text{Equation 3.9}$$

$$t_{cooling} = \frac{1}{PRF} - T_R \quad \text{Equation 3.10}$$

$$C_R = \frac{\Delta T}{t_{cooling}} \quad \text{Equation 3.11}$$

where ΔT is temperature deviation from room temperature to the liquidus temperature and T_R is the residence time.

3.2.4 Design of Experiment 4 (DOE4)

In DOE4, a 3^2 factorial design was developed which produced nine sets of processing parameters. Two factors, peak power and overlap were designed at three levels as shown in Table 3.8. Duty cycles were set at three levels dependant on the peak powers and resulted in a constant average power of 274 W for each setting. The processing parameters were conducted using a minimum spot size of 0.09 mm diameter. Due to the very small affected area and high laser irradiance, the residence time was set to lower levels, see Table 3.8. Samples were roughened chemical and etched as previously described. The pulse energy and PRF were constant at 0.095 J and 2900 Hz respectively for each experiment. The outcome pulse width calculated from equation 1 (see Appendix B) was at the three levels of 0.06, 0.08 and 0.12 ms.

Table 3.8: Parameter settings for DOE4 samples at constant pulse energy of 0.095 J, average power of 274 W and PRF of 2900 Hz.

Sample	Set parameters			Outcome parameters			
	P_P (W)	DC (%)	η (%)	I (W/mm ²)	T_R (ms)	S (mm/s)	τ (ms)
X1	760	36		238,087	0.06		0.06
X2	1138	24	0	178,761	0.08	261	0.08
X3	1515	18		119,436	0.12		0.12
X4	760	36		216,524	0.07		0.06
X5	1138	24	10	162,572	0.09	237	0.08
X6	1515	18		108,619	0.14		0.12
X7	760	36		183,282	0.08		0.06
X8	1138	24	30	137,613	0.11	201	0.08
X9	1515	18		91,943	0.16		0.12

3.2.5 Design of Experiment 5 (DOE5)

Optimisation of H13 Tool Steel Laser Surface Modification

DOE5 parameter settings were developed based on the Box-Behnken design Response Surface Methodology (RSM) design using the Design Expert 7.1.4 software for results analysis. RSM is a collection of mathematical and statistical techniques that are useful for the modelling and analysis of problems in which a response of interest which is influenced by several variables can be analysed [161]. Experiments were conducted and characterisation results were analysed using regression analysis to obtain a significant model for the response to the independent input variables. The surface depth and

roughness response models were performed with a step-wise regression method which automatically eliminates the insignificant model terms. The sequential F-test and lack of fit test were carried out using the software to evaluate the model. The range of each parameter was determined from the four previous DOEs presented. Effects of each laser parameter from analysis of the characterisation results from the previous DOEs were established to determine suitable parameter settings for DOE5. For DOE5, three independent parameters (P_p , η and PRF) were varied at three different levels which resulted in a total of 17 parameter settings as given in Table 3.9.

Table 3.9: DOE5 laser parameters for process optimisation.

Sample	Set parameters				Outcome parameters			
	P_p (W)	DC (%)	η (%)	PRF (Hz)	I (W/mm ²)	T_R (ms)	E_p (J)	S (mm/s)
F1	760	36	0	2300	119,297	0.16	0.12	207
F9	1138	24	-10	2300	198,959	0.09	0.12	230
F11			10		162,398	0.12		188
F2	1515	18	0	2300	237,809	0.08	0.12	207
F5	760	36	-10	2900	132,686	0.11	0.10	290
F7			10		108,582	0.14		237
F13	1138	24	0	2900	178,700	0.08	0.10	261
F14								
F15								
F16								
F17								
F6	1515	18	-10	2900	264,499	0.06	0.10	290
F8			10		216,449	0.07		237
F3	760	36	0	3500	119,459	0.10	0.08	315
F10	1138	24	-10	3500	198,631	0.06	0.08	350
F12			10		162,593	0.08		286
F4	1515	18	0	3500	238,133	0.05	0.08	315

In Table 3.9 the duty cycles were dependant to the peak power settings. Five of the parameter settings were repetitions and were labelled F13 to F17. The peak powers used were 760, 1138 and 1515 W. The lower peak power of 760 W was combined with 36% duty cycle while the higher peak power of 1138 and 1515 W were set at 24% and 18% duty cycle respectively. The combinations of peak power and duty cycle were used to ensure a constant resulting average power of 274 W during processing. Three levels of PRF were set at 2300 Hz, 2900 HZ and 3500 Hz. The spot size was 0.09 mm diameter to reduce the laser affected area which would increase the surface temperature heating and cooling rates. At the very small spot size of 0.09 mm, the overlap was set at minus 10, 0 and 10%. The minus 10% overlap was to allow a 10% gap between the consecutive laser spots. However, the irradiance produced by the 0.09 mm spot size caused a larger heat affected area which therefore still produced modified overlapped regions at this setting. Sample surfaces were roughened and chemical etched as previously described.

Analysis of variance (ANOVA) and data optimisation were conducted with significant terms in the model. Model reduction can be performed when non-significant terms exist. Non-significant terms were eliminated using an algorithmic technique which was the step-wise regression method. In this method, a factor was added, eliminated or exchanged at each step. Alpha in and out values, associated with each model term, were used in the model reduction to indicate the terms that were allowed into the model. Each term must have a p-value smaller than or equal to alpha values in order to be kept in the model at each iteration step. The model reduction started with the algorithm adding the single new factor that exhibited the highest correlation with the response. Then, factors were added, eliminated, exchanged or the procedure stopped. With two or more terms in the model, terms having a p-value less than the specified alpha in requirement was added to the model. The terms having probability values greater than the specified alpha out were then removed by the algorithm one at a time. The procedure stops when no further improvement. Data distribution was assured by regression findings, which were predicted R^2 , actual R^2 and adjusted R^2 .

At the end of experiments and characterisation, the design settings were optimised for the three significant factors which were laser peak power, PRF and overlap percentage. This optimisation process involved combining the factors with set desired goals, for each response, into an overall desirability function. In this design the numerical optimization was conducted to minimize surface roughness and maximize hardness and modified layer depth responses. The optimization criteria for peak power, overlap and PRF factors was set as 'in range'. To maximize or minimize the response, a lower and upper limit was set at values achieved from experimental findings and overall desirabilities were selected.

3.3 Thermal Modelling of Heat Conduction

Thermal modelling simulation was performed to investigate the effect of laser parameters and surface absorptance factor on the molten pool geometry. The thermal conduction model used for simulation of the laser induced thermal field had previously been developed [60, 134, 162]. The main objective of this part of the project was to employ the existing thermal model and investigate the temperature distribution in laser modified AISI H13 tool steel surfaces. A specific absorptance factor of 60% was added in the model to suit the experimental surface modification process carried out in this work.

The thermal model used is based on a point source solution. The area of the heat affected zone was determined in the surrounding radial region from the point heat source. In this

case, the laser fluence rather than spot size was related to the resulting thermally affected region from laser processing. The other main assumptions in this model include that the thermal properties of H13 are independent of temperature and that phase changes only account for a small percentage of overall energy input [60]. This latter assumption can be accounted for to some degree in this work due to the fact that the same material H13 was processed in all comparison tests.

Mathematical Model

An analytical mathematical model of the heat field generated during the laser surface modification was used to predict the temperature distribution in the surface and hence dimensions of the treated region of microstructure phase change or melt pool formation. The general heat conduction equation is given in Equation 3.12 where the sample is considered to be moving at constant traverse speed, U , in the x -direction. Equation 3.13 gives the three-dimensional temperature distribution within the surface which was solved from the general heat conduction equation, previously presented by Issa et. al [60]. By taking the surface preparation into account, a 60% surface absorptance factor was used. This absorptance factor was similar to that was used in the previous works of Bergström (2007) and Bhushan (1991) [66, 68].

$$\frac{\partial T}{\partial t} + U \frac{\partial T}{\partial x} = \alpha \left(\frac{\partial^2 T}{\partial x^2} + \frac{\partial^2 T}{\partial y^2} + \frac{\partial^2 T}{\partial z^2} \right) \quad \text{Equation 3.12}$$

$$T(x, y, z, t) = T_o + \frac{P(t)}{2\pi kr} \exp \left[i\omega t + \frac{U}{2\alpha} \left(x - r \sqrt{1 + \frac{4\alpha\omega i}{U^2}} \right) \right] \quad \text{Equation 3.13}$$

where $P(t)$ is the time dependent laser power input (W), ω is the fundamental frequency of the power input (equal to $2\pi PRF$, Hz), r is the radial distance from the power source $= \sqrt{x^2 + y^2 + z^2}$ (m), ρ is the density (kg/m^3), C_p is the heat capacity ($J/kg^\circ C$), k is the thermal conductivity ($W/m^\circ C$), α is the thermal diffusivity of the material (m^2/s) equal to $k/\rho C_p$, and U is traverse speed (m/s). Physical and thermal properties of the H13 tool steel used for the modelling are given in Table 3.2.

The mathematical model of heat conduction in the laser surface modification of H13 was previously developed using LabVIEW 8.0 software [60]. In this simulation, the significant input parameters are the laser processing parameters (power, PRF, pulse duration and traverse speed, U_x), the materials thermal conductivity and the diffusivity. Figure 3.8 shows the '3D channel profile simulation' software interface, which was used to simulate

the heated region geometry affected during the laser surface processing. In this software, the thermal field was calculated and the simulation was truncated at 1454°C such that the coordinates for material which reached this temperature were stored for subsequent viewing. Using this point of truncation temperature, the thermal model was calculated which resulted in a data set with the geometry of the molten region. The simulation data was directly saved in *.txt file format for three-dimensional viewing and analysis. A '3D channel viewer' software was used to plot the molten region geometry dataset as shown by Figure 3.9. The data source file was entered and processed at the given PRFs and traverse speeds used in the simulation. The geometry can also be simulated for any number of pulses. Besides the three-dimensional geometry viewing, the dataset of the molten geometry was extracted to produce separate plots of temperature distribution at specific locations.

Figure 3.10 shows the planar thermal profile simulation with two-dimensional temperature distribution profile along the sample translation axis. It generates a new simulation and shows the temperature profile in the x and y directions for a given selected depth (z). This simulated data was also saved in a (*.txt) file. The planar isothermal simulation code depicts the temperature distribution on H13 laser processed surface for a given number of pulses. In Figure 3.10, the number of pulse set was one and the time duration of the process plotted on x-axis was 0.34 ms. In this software, the truncation temperature was set at 20,000°C to allow presentation of all simulation results [60].

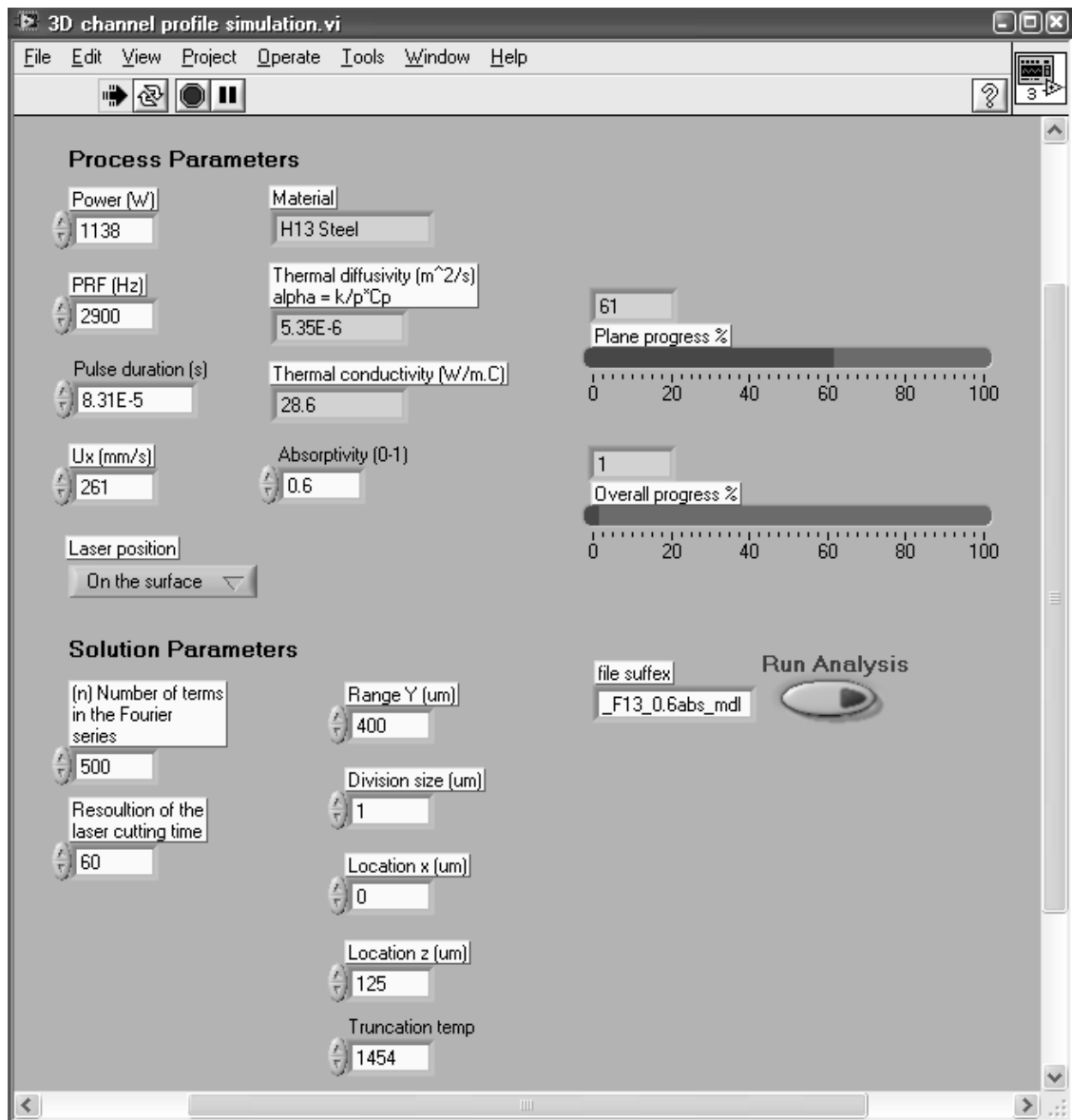


Figure 3.8: '3D channel profile simulation' software used for constructing molten pool geometry of laser processed surface.

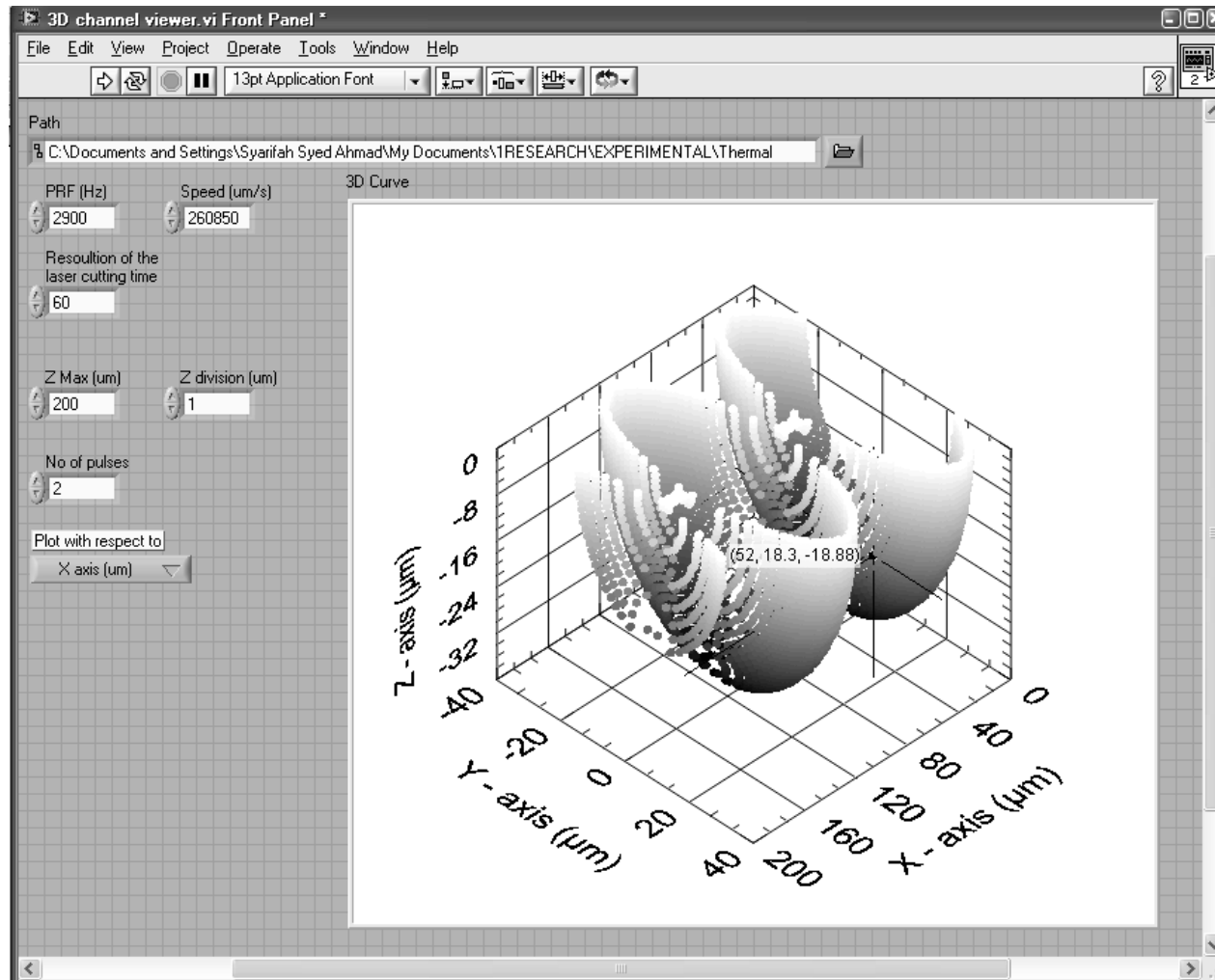


Figure 3.9: Three-dimensional surface viewer software interface.

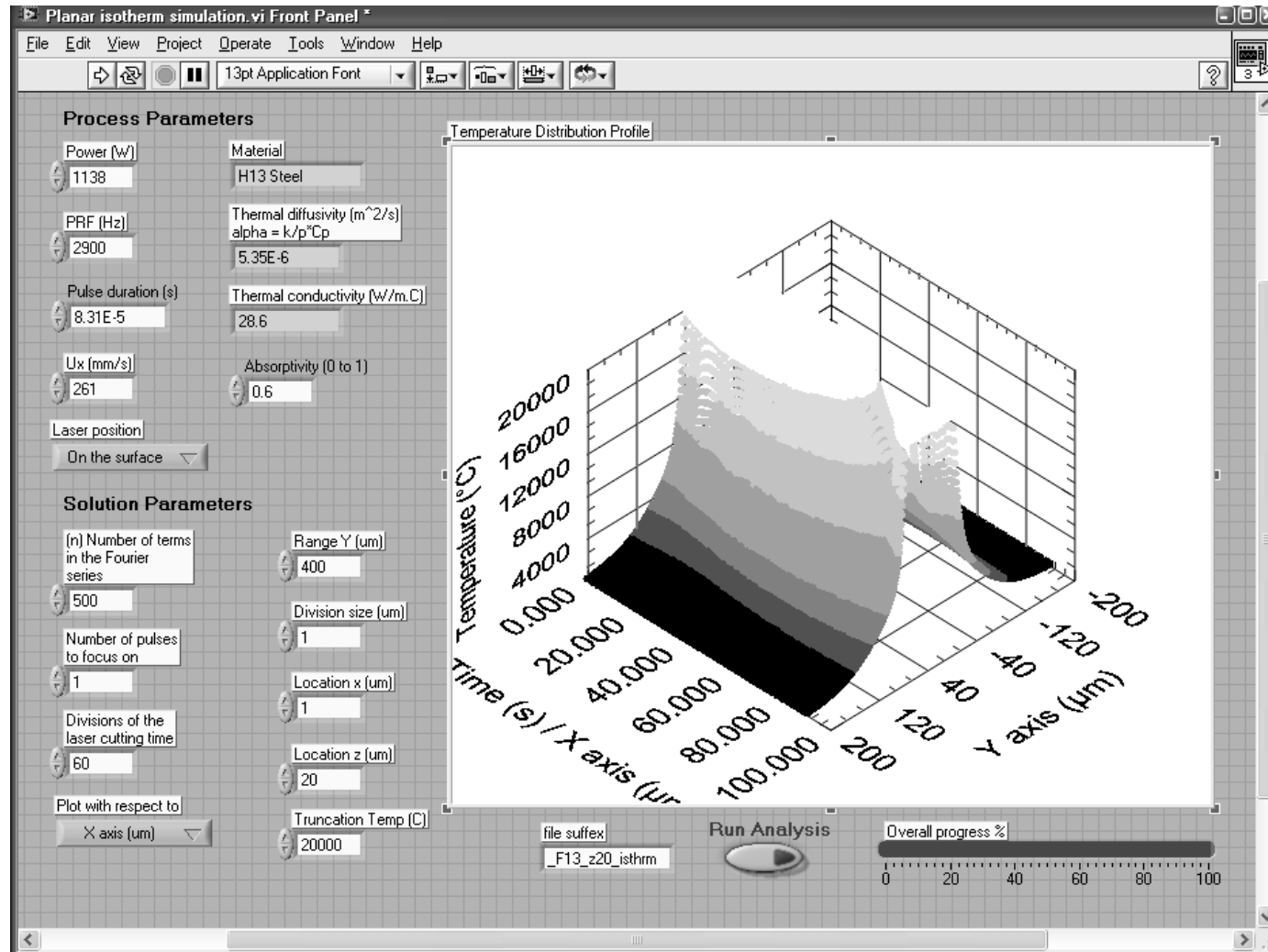


Figure 3.10: Planar isotherm software interface.

Temperature Distribution in Modified Surface

The temperature distribution through the modified surface depths was simulated using 'planar isotherm' software. These profiles were recorded at 20 µm depth intervals from 0 to 120 µm beneath the surface. The processing parameters were 1138 W peak power, 2900 Hz PRF, 24% duty cycle and 261 mm/s traverse speed. Similar processing parameters were plotted in the '3D channel profile simulation' software to obtain temperature data at different coordinates. The temperature data was used to plot the heating and cooling rates of each point in the modified surface. A relationship between the heating/cooling rate ratio and hardness properties was then established.

3.4 Characterisation Techniques

Laser processed samples were prepared for different types of testing and analysis. Figure 3.11 shows the techniques used to characterise the laser processed samples. The characterisation techniques comprised of metallography, micro-hardness testing, surface profilometry, energy dispersive X-ray spectroscopy (EDXS) and x-ray diffraction (XRD) analysis. The metallography, micro-hardness tests and EDXS were conducted on the samples cross-sections. The XRD analysis and surface profilometry were studied to investigate the processed surface crystallinity and morphology respectively.

CHARACTERISATION TECHNIQUES				
Metallographic study	Micro-hardness test	Surface profilometry	EDXS analysis	XRD analysis
<ul style="list-style-type: none">• Modified layer dimension• Grain size• Phase identification	<ul style="list-style-type: none">• Modified layer hardness• Heat affected zone hardness• Substrate hardness	<ul style="list-style-type: none">• Two-dimensional surface profile• Average surface roughness	<ul style="list-style-type: none">• Chemical composition	<ul style="list-style-type: none">• Phase identification• Crystallinity

Figure 3.11: Outline of characterisation techniques for as-received and laser modified samples.

3.4.1 Metallographic Study

Metallographic samples were sectioned using an alumina Buehler 254 mm diameter, 1.78 mm thick cut off wheels flooded with coolant to prevent tempering. Samples were then mounted in Bakelite resin using Buehler Simplimet 2000 Mounting Press hot mounting machine. Mounted samples were ground sequentially with 240, 600, 800 and 1200-grit

size silicon carbide (SiC) papers for 5 minutes, at 0.1 MPa (1 bar) pressure and at 250 rpm grinding wheel speed. Ground samples were polished using Textmet 1000 cloths with 6 μ and 3 μ size diamond paste, and also micro-cloth with 0.05 μ size alumina polishing suspension for 4 minutes each, at a polishing speed of 150 rpm. Both grinding and polishing were done using Buehler Motopol 2000 grinder/polisher machine. Polished samples were washed with continuously running tap water and rinsed with acetone solution to prevent water stain. Samples were dried and chemically etched in a 2% nital solution for approximately 15 seconds. Samples were rinsed using water and dried before microstructural observations.

Microstructural observations were performed using a Reichart ME F2 microscope with Beuhler Omnimet Enterprise image analyser software at 400x magnification. Detailed characterisation of the laser modified surface depth and dimensions, and grain size was done using a Carl-Zeiss EVO-LS15 scanning electron microscope (SEM) integrated with SmartSEM software. An average depth for the laser modified surface was taken from at least five measurements. The back-scattered detector (BSD) at high vacuum was used to view contrasted phase on the sample cross-sectional surfaces. A high voltage level of 20 kV and spot size range of 440 to 560 pm at high level of BSD gain were used to produce the back-scattered micrographs. Micrographs were captured at high contrast to show the grain phases. The degree of steel surface absorptance at the CO₂ laser wavelength, the laser parameter settings and the sample surface properties were determined from the micrographs.

Grain Size Measurement Using Image Analyser

Grain size measurement was determined by Feret's diameter using Image J software [163-166]. Feret's diameter is the greatest distance between two parallel lines touching opposite sides of the grain [165, 166]. This measurement was performed with the 'analyze particles' menu as shown in Figure 3.12. Measurement started with scale setting on the micrograph, thresholding and background subtraction. The number of grains was measured from high contrast micrographs which was adjusted using the image threshold menu. The type of measurement (e.g. Feret's diameter, area and standard deviation) was set before each image analysis. The number of grains resulted from the particle analysis was also indicated by highlighted grains on the micrograph and distribution of grain sizes was presented in histogram format.

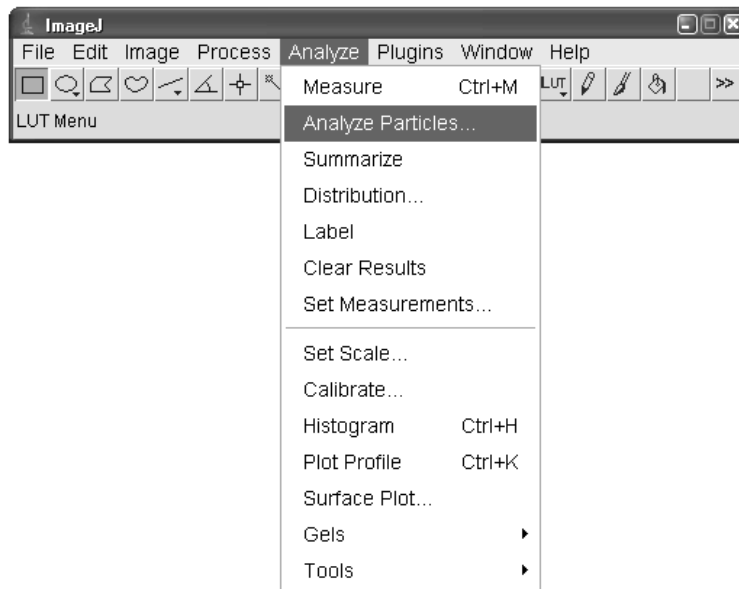


Figure 3.12: Image J software interface with 'Analyze Particles' pull-down menu.

3.4.2 Micro-hardness Test

The micro-hardness properties on the laser modified cross-sectional surface were measured using a Leitz mini-load tester with 981 mN force and Vickers diamond indenter. Samples cross-sectional surface were prepared to be at least of $0.03 \mu\text{m } R_a$ to ensure measurement accuracy. Measurements were recorded from five indentations at different locations within the modified surface cross section. Referring to ISO 14577 standard, indents should be kept at least three diameters (indentation diameter) away from a free surface or interface and at least five diameters of the largest indent from each other to avoid interference [167].

3.4.3 Surface Profilometry

Two-dimensional surface profilometry was done using a TR-200 measuring system integrated with TIME software to record the surface profile. Cylindrical laser modified samples were mounted on the high precision measuring stage. Measurements were complied according to the ISO standard. The range of measurement used was $\pm 80 \mu\text{m}$ to ensure measurement of the maximum average roughness of the samples. The significant surface roughness measurement recorded from the software for comparison purposes was the arithmetic average, R_a .

3.4.4 Energy Dispersive X-ray Spectroscopy (EDXS)

The chemical composition of the laser modified H13 tool steel was measured quantitatively using Oxford Instruments - Inca x-act and micro-analysis suit EDXS. The samples were observed using the scanning electron microscope while the EDXS detector was used to collect composition data from the sample. The focusing distance was set less than 14 mm to allow the EDXS detector to collect the information from the sample surface. Identification of elements on the sample cross-sectional surfaces was carried out using the integrated software.

3.4.5 X-Ray Diffraction Analysis

X-ray diffraction patterns of the samples were recorded using a Bruker D8 XRD system with $\text{CuK}\alpha$ radiation and wavelength, λ , of 1.540598 Å. The system was integrated with XRD Commander software which controlled the power and scanning parameter inputs. Cylindrical laser modified samples were cleaned with alcohol before mounting on the scanning stage. The scanning stage position was between the x-ray source and the detector. A fixed detector slit size of 0.2 mm wide and 12 mm long was used throughout the experiments. A z scan was used to position a sample at the correct height on the z drive, and was performed for each sample before the XRD measurement. Using the height value from the z-scan, the diffraction patterns were recorded in the 2 theta range of 20° to 100° using locked coupled scan type. The locked coupled scan is a standard XRD scan of any 2 theta values. The scan rate was set at 5 seconds/step with 0.1 steps increment. The diffraction pattern produced was plotted on a graph with intensity plotted against the 2 theta axis.

The XRD analysis was done to measure the crystallinity of the laser modified surface and identify the formation of martensite and metastable phases in the modified layer during processing. The effect of sample absorptance, surface temperature, laser pulse energy and processing spot size of 0.4 mm, 0.2 mm and 0.09 mm on the diffracted peak intensities were investigated. The effect of laser processing on the surface crystallinity was measured at Bragg's angles between 30 to 70°.

CHAPTER 4

Results

4.1 Introduction

An outline of the characterisation results and discussion presented is given in Table 4.1. The results presentation starts with those for the as-received AISI H13 tool steel grain composition and hardness properties. The laser surface modification designs are then presented sequentially from DOE1 to DOE5. From DOE1, the effect of laser parameters on the modified surface depth are presented. For DOE2, results presented are the effect of an etched surface on the modified surface depth and the overlapped geometry produced from a 0.4 mm diameter spot size. The grain composition, hardness and surface roughness properties are presented in DOE2. From DOE3, the effect of roughened and etched samples surface on the modified surface depth is presented. The overlapped geometry results from DOE3 with 0.2 mm spot size and constant PRF settings are shown. The effect of the 0.2 mm spot size on grain composition, hardness and surface roughness properties was also presented. From DOE4 results, the effects of a 0.09 mm diameter spot size on the surface properties of modified depth, hardness, roughness and phase analysis are presented. Optimised parameters examined from DOE5 included characterisation of modified layer depth, hardness properties and minimum average surface roughness. Comparison of as-received H13 tool steel XRD results with those for the modified surface samples is presented. This analysis included investigation of surface crystallinity, and diffraction of martensite and metastable phases in the modified layer surface. XRD results analysed and presented included the data collected from samples processed at 0.09 mm, 0.2 mm and 0.4 mm spot size.

Table 4.1: Overview of sample preparation, parameters settings and surface characterisation for five DOEs.

DOE	Sample condition prior processing	Set parameters				Outcome parameters				Surface properties	
		Spot size /Beam focal position (mm)	P _p (W)	DC (%)	η (%)	PRF (Hz)	I (W/mm ²)	T _R (ms)	E _p (J)		P _A (W)
DOE1	As-received samples	0.40 /+2.6 & -2.6	760	70 85 100	10 30 50	2857 to 5000	3,872 to 5,576	0.22 to 0.38	0.11 to 0.27	532 646 760	<ul style="list-style-type: none"> • modified layer depth
DOE2	Nital etched surface	0.40 /-2.6	760	85 100	10 30 50	2857 to 5000	3,569 to 5,592	0.29 to 0.38	0.15 to 0.27	646 760	<ul style="list-style-type: none"> • modified layer depth & morphology • hardness • surface roughness • phase crystallinity • chemical composition
DOE3	Surface roughened and nital etched	0.20 /-1.2	507 760 1313	49 36 23	10 50	2900	10,930 to 28,184	0.12 to 0.25	0.09 0.10 0.11	249 274 305	<ul style="list-style-type: none"> • modified layer depth & morphology • hardness • surface roughness • phase crystallinity
DOE4	Surface roughened and nital etched	0.09 /On surface	760 1138 1515	36 24 18	0 10 30	2900	91,943 to 238,087	0.06 to 0.16	0.10	274	<ul style="list-style-type: none"> • modified layer depth & morphology • hardness • surface roughness • phase crystallinity
DOE5	Surface roughened and nital etched	0.09 /On surface	760 1138 1515	36 24 18	-10 0 10	2300 2900 3500	108,582 to 264,499	0.05 to 0.16	0.08 0.10 0.12	274	<ul style="list-style-type: none"> • modified layer depth • hardness • surface roughness • phase crystallinity • chemical composition • design optimisation

As-received AISI H13 Tool Steel

The back-scatter detector micrograph of Figure 4.1 depicts the α -ferrite and martensite phase composition of the as-received H13 tool steel with $M_{23}C_6$ and M_7C_3 carbide (M=Cr, Fe) dispersion. The carbides are seen in white spheroidal form, while the α -ferrite and martensite phases were respectively identified in grey and black shade regions. From the micrograph, it can be seen that the as-received H13 tool steel grain size was between approximately 3 and 9 μm . The average hardness of the as-received H13 tool steel measured was 280 $\text{HV}_{0.1}$.

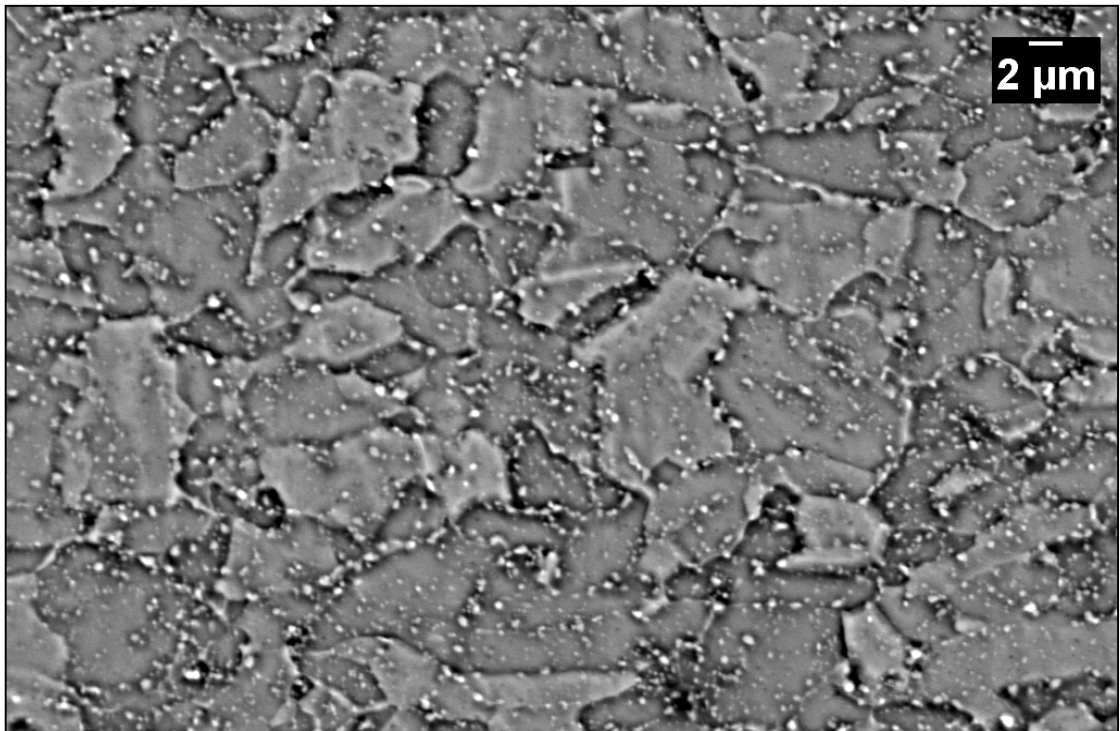


Figure 4.1: Back scatter detector SEM micrograph of as received H13 tool steel.

4.2 Laser Surface Modification Design of Experiments

4.2.1 DOE1

In DOE1, the metallographic study was performed to analyse the modified layer depth formed on the H13 tool steel substrate at different parameter settings. The effects of pulse laser mode, laser irradiance, residence time, and laser spot focal position on the modified surface depth were determined from this work.

Metallographic Study

(a) The Effects of Laser Irradiance and Residence Time

The effect of laser irradiance and residence time on the modified layer depth was observed. Three regions of modified layer zone, heat affected zone and substrate zone are seen from the micrographs in Figure 4.2. The modified layer depth increased with increasing laser irradiance as shown in Figure 4.2 (a) to (f). Figure 4.2 (a) and (b) show the samples processed at high residence time of 0.38 ms; micrographs in Figure 4.2 (c) and (d) are from samples processed at 0.34 ms; while micrograph in Figure 4.2 (e) and (f) are from samples processed at 0.31 ms residence time. The sample with minimum effect of melting was observed in Figure 4.2 (e) as expected at the lowest residence time and irradiance. Micrograph in Figure 4.3 shows the cross section of sample 12 from DOE1 where modified layer depths were measured.

The modified layer depths as measured from the micrographs are plotted in a three-dimensional graph corresponding to the laser irradiance and residence time as shown in Figure 4.4. The range of modified layer depth produced in the 27 laser modified samples was between 0 and 29 μm . Modified layer was not achievable in samples processed at a residence time less than 0.31 ms. Residence time was seen to have the largest contribution to the modified layer depth. At any given laser irradiance setting, a higher residence time increased the modified layer depth.

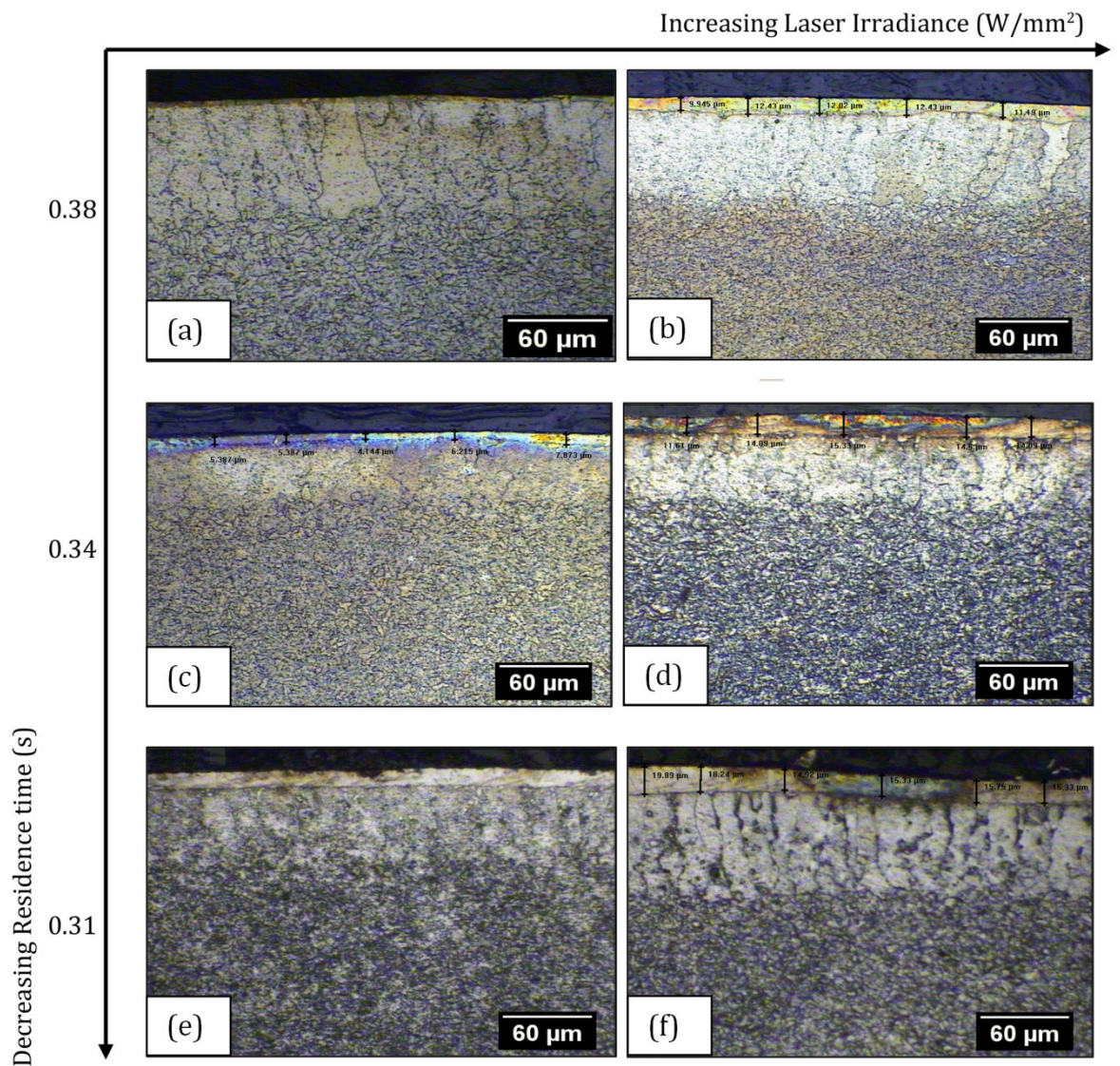


Figure 4.2: Modified layer depth in DOE1 samples at residence time and irradiance of (a) 0.38 ms and $3,973 \text{ W}/\text{mm}^2$ (b) 0.38 ms and $5,576 \text{ W}/\text{mm}^2$ (c) 0.34 ms and $3,951 \text{ W}/\text{mm}^2$ (d) 0.34 ms and $5,503 \text{ W}/\text{mm}^2$ (e) 0.31 ms and $3,881 \text{ W}/\text{mm}^2$, and (f) 0.31 ms and $4,607 \text{ W}/\text{mm}^2$ respectively.

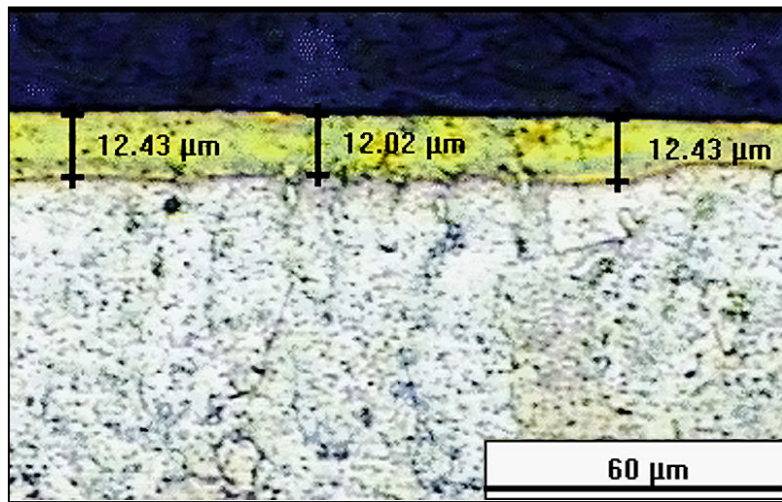


Figure 4.3: Modified layer depth measurements in sample 12 with residence time and irradiance of 0.24 ms and 4,607 W/mm².

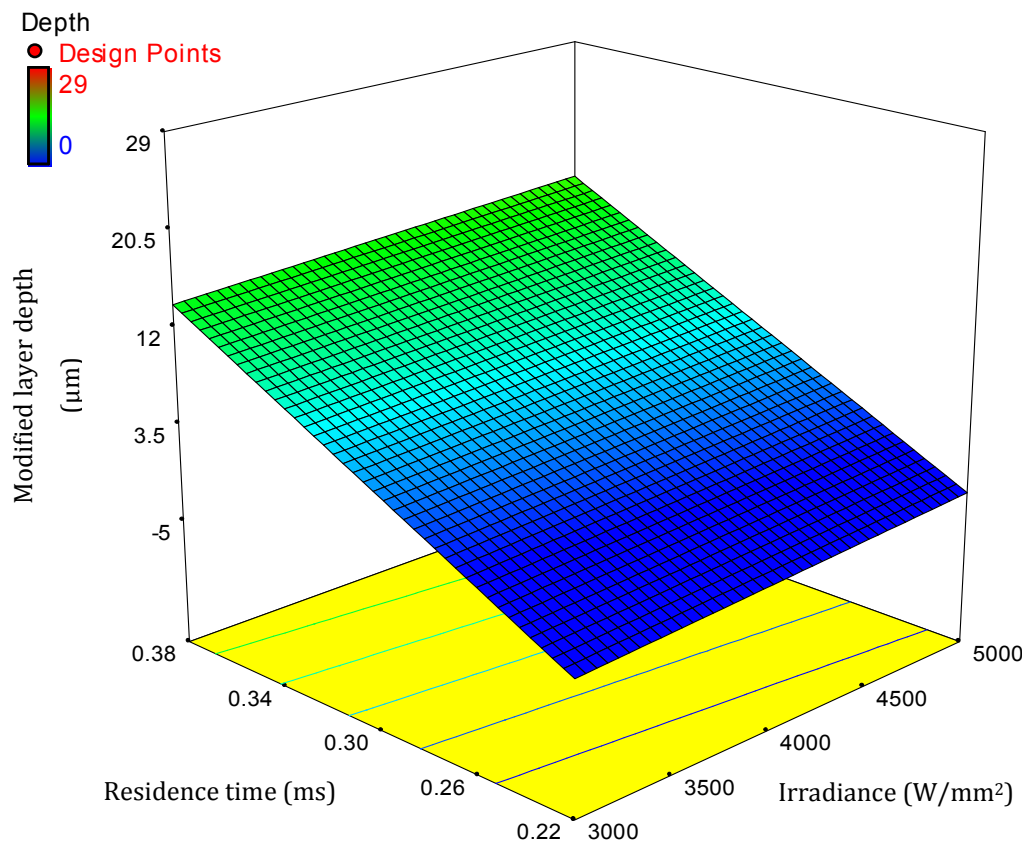


Figure 4.4: Three dimensional plot of laser irradiance and residence time effect on the modified surface depth with spot size focused on the sample surface.

(b) The Effect of Focal Position

For a focal position of -2.6 mm and +2.6 mm the laser spot size on the sample surface was 0.4 mm. At negative focal position, the sample surface is above the focal length position whereas it is below the focal length position at positive focal position. Figure 4.5 shows the effect of focal position on samples processed at a residence time of 0.29 ms and laser irradiance of 3,946 W/mm². The micrographs of the laser modified sample cross sections indicated three important zones, namely a 'glazed zone', heat affected zone and substrate or non affected zone. The micrograph shown in Figure 4.5 (a) indicates only two main layers: the heat affected zone and substrate resulting from processing at a positive focal position. The micrograph in Figure 4.5 (b) shows a distinct modified layer observed with heat affected zone and substrate in this sample processed at negative focal position. The area indicated by A represents the laser modified zone, B represents the heat affected zone and C represents the substrate.

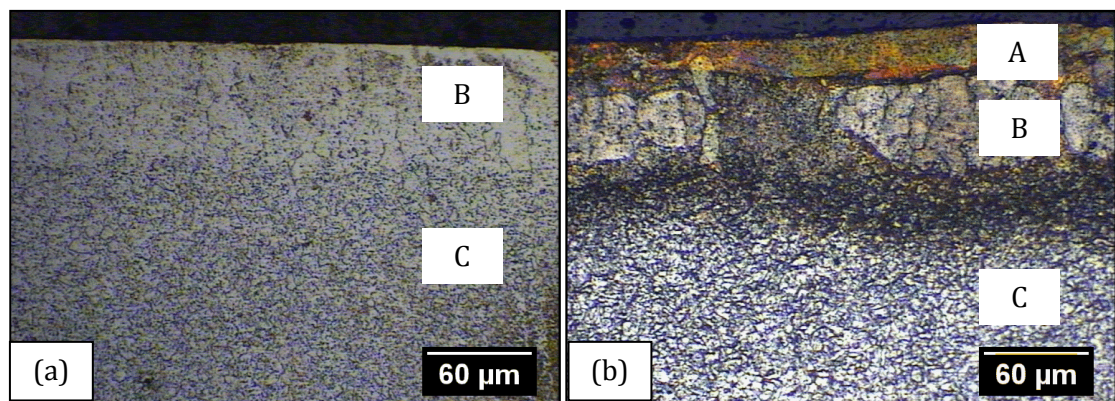


Figure 4.5: Micrographs of samples 23 and 23b processed at defocused beam of (a) +2.6 mm and (b) -2.6 mm respectively, where A is laser modified zone, B is heat affected zone and C is substrate.

Samples investigated at different residence time for these two focal positions are shown by micrographs in Figure 4.6. These samples were processed at laser irradiances of 3881, 3946 and 3973 W/mm² and at residence times of 0.31, 0.29 and 0.38 ms respectively with constant 50% overlap. Figure 4.6 (a) (c) and (e) show the micrographs of laser modified samples processed at -2.6 mm focal position. Micrographs in Figure 4.6 (b), (d) and (f) are cross section of samples processed at the same laser parameter settings except that the beam was focused at the +2.6 mm focal position.

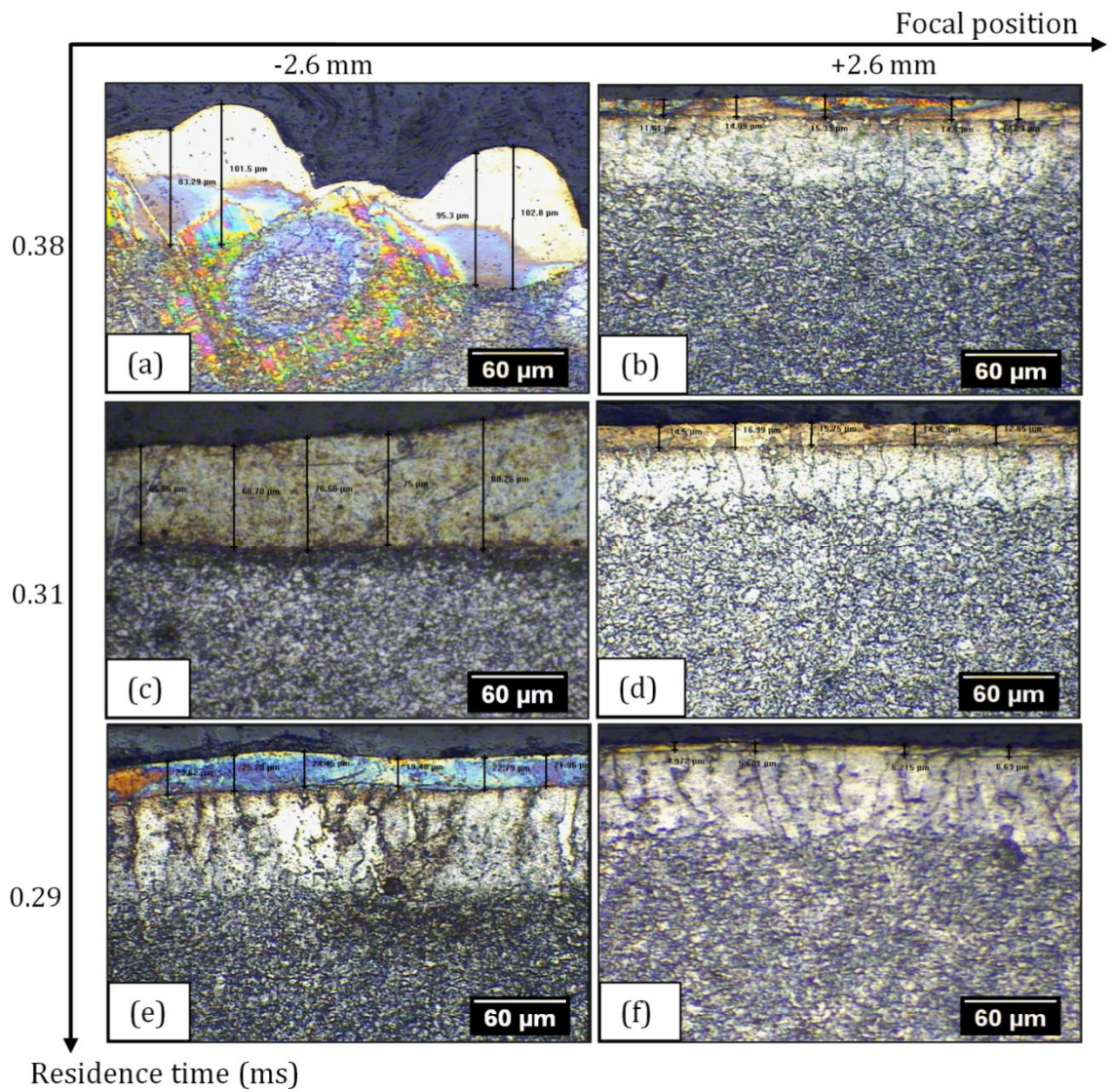


Figure 4.6: The effect of focal position on modified layer depth at (a) and (b) 0.38 ms; (c) and (d) 0.31 ms; and (e) and (f) 0.29 ms.

Figure 4.7 shows a comparison of maximum depths of the modified surfaces processed at irradiances of 3881, 3946 and 3973 W/mm² and different residence times and focal positions as given in Table 3.5. Samples processed at focal position of -2.6 mm produced three to eight times deeper modified layer than samples processed at focal position of +2.6 mm. The modified surface depth increased with the residence time. The modified surface depth difference between the two focal positions also increased with increasing residence time.

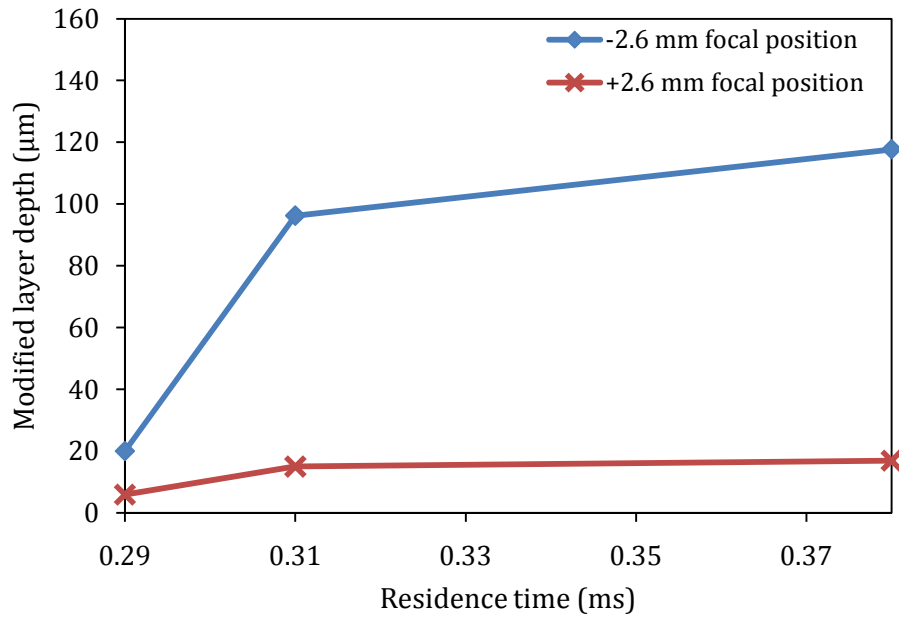


Figure 4.7: Modified layer depth as a function of residence time at positive and negative focal position.

4.2.2 DOE2

In DOE2, the metallography and hardness properties were investigated to analyse the modified layer depth formed on the chemically etched H13 tool steel surface at different laser parameter settings. Overlap geometry of the modified surface using the 0.4 mm spot size is shown in the micrographs. The effect of chemical etching on the modified layer depth, grain composition and hardness is presented for the different laser irradiances, overlaps and residence times.

Metallographic Study

(a) The Effects of Chemical Etching on Steel Surface Absorptance

The estimation of sample surface absorptance was initially calculated from molten pool geometry dimension. Figure 4.8 shows the molten pool geometry produced by a single laser pulse of 0.17 J pulse energy and 0.29 ms residence time achieved with 3810 Hz PRF, 85% duty cycle and 646 W average power. The geometry measurements were molten pool depth, **a**, molten pool gap, **b**, molten pool width, **c**, and modified layer height, **h**. The depth of molten pool, **a**, measured from the surface indicates the magnitude of laser pulse energy penetration.

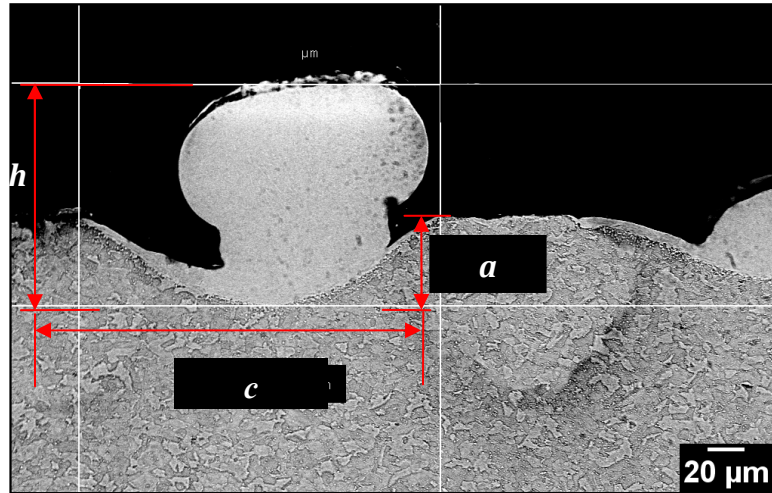


Figure 4.8: Molten pool geometry of sample E14 given by molten pool depth, a , molten pool gap, b , molten pool width, c , and modified layer height, h .

Table 4.2 shows the resulting molten pool geometries measured from the nital etched samples. With improved surface absorptance, the modified layer average height, h , ranged from 46 to 180 μm . A comparison was made between the 0.4 mm laser beam diameter and the resulted molten pool width, c . The measurement difference between the beam diameter and the molten pool width was to determine the surface absorptance percentage. The modified layer height, h , was also measured to indicate the maximum layer thickness resulting from the process.

The surface absorptances measured from the ratios of molten pool widths, c , variations to laser spot diameters were plotted. Figure 4.9 shows that the absorptance varied between 59% and 72% for samples processed at pulse energy, E_p , ranging from 0.18 to 0.24 J. Details of the processing parameters of the samples can be seen in Table 4.2. At lower pulse energy, the surface absorptance ranged from 44% to 53%. Energy difference from the theoretically calculated energy to melt the surface, and the laser energy provided during processing was also calculated to measure the actual energy absorptance. The total energy, H_T , calculated using Equation 3.2 as being required to produce a molten pool on the H13 steel surface of the measured pool mass is given in Table 4.2. The theoretical total energy, H_T , required to melt the region was calculated using the measured modified layer height, h , values, spot diameter and density to calculate the mass melted. The designed laser pulse energy was higher than the theoretically calculated required energy to melt the surface at 100% surface absorptance. The surface absorptance percentages calculated from the molten pool geometry and the theoretical calculated pulse energy, H_T , values were used during settings of all subsequent DOEs. These values were useful in order to

improve the surface absorptance of subsequent samples and to reduce and refine the laser pulse energy range in subsequent DOEs.

Table 4.2: The resulting molten pool geometry and estimated total energy, H_T , for different processing parameters.

Sample	I (W/mm ²)	η (%)	τ (ms)	T_R (ms)	E_p (J)	H_T (J)	Average h (μ m)	Average c (μ m)
E6	5510	10	0.31	0.34	0.24	0.11	164	257
E8	5548	10	0.30	0.32	0.23	0.07	86	211
E9	5592	10	0.35	0.38	0.27	0.14	175	245
E12	4475	30	0.24	0.32	0.18	0.09	153	271
E14	4618	30	0.22	0.29	0.17	0.05	46	189
E15	4631	30	0.26	0.34	0.20	0.08	161	269
E18	4774	30	0.30	0.38	0.23	0.13	180	275
E21	3745	50	0.20	0.32	0.15	0.13	142	199
E26	3971	50	0.21	0.32	0.16	0.03	48	192
E27	3971	50	0.25	0.38	0.19	0.04	169	193

During processing, the H13 surface was melted at its liquidus temperature of 1454°C and vaporisation was avoided. The amount of energy required to raise the H13 tool steel from room temperature to its melting temperature was estimated at 640,104 J/kg.

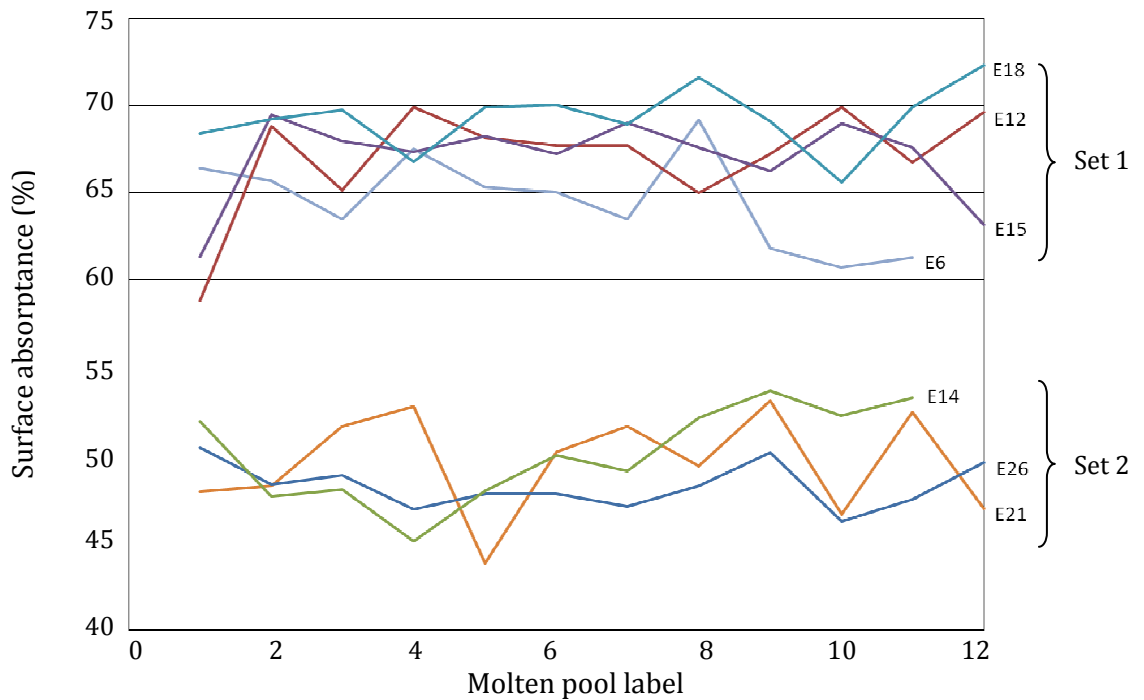


Figure 4.9: Surface absorptance measurements from molten pool width variations for different samples. Difference in levels was largely due to the differences in pulse energy, E_p . Pulse energy for set 1 ranged from 0.18 to 0.24 J and for set 2 from 0.15 to 0.17 J.

Improvement of laser energy absorptance within the nital etched surface is presented in micrographs of Figure 4.10, Figure 4.11 and Figure 4.12. Figure 4.10 (a) and (b) depict the cross section of laser modified samples processed at 10% overlap and at two different pulse energies of 0.23 J (85% DC) and 0.24 J (100% DC). At 10% overlap, gaps were observed between the molten pools. For the 0.1 J increase in pulse energy an increased modified surface thickness was formed, see Figure 4.10 (b) compared to sample in Figure 4.10 (a).

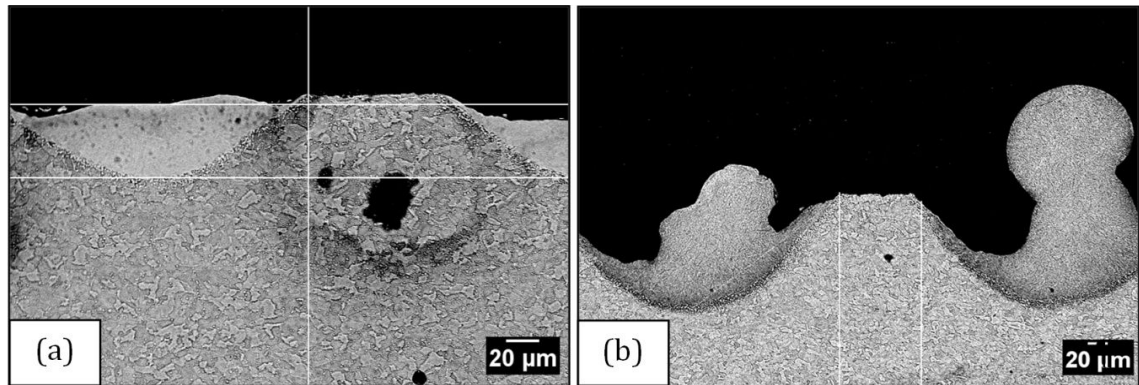


Figure 4.10: Modified surface cross section of samples processed at 10% overlap, and (a) 0.23 J (sample E8) and (b) 0.24 J (sample E6) pulse energy respectively.

Micrographs of Figure 4.11 (a) and (b) were processed at 30% overlap with 0.17 J and 0.20 J pulse energy respectively. The small pulse energy difference of 0.03 J between the samples provided increased modified surface thickness and caused cracks in the modified surface of sample in Figure 4.11 (b).

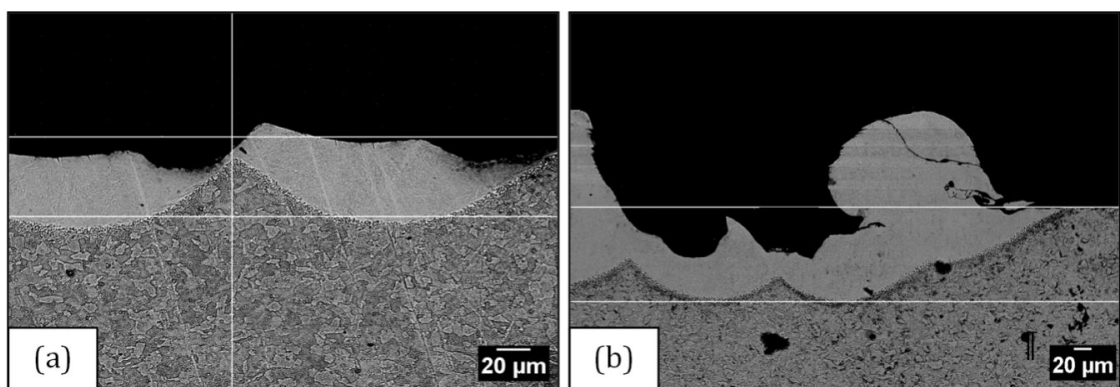


Figure 4.11: Modified surface cross section of samples processed at 30% overlap, and (a) 0.17 J (sample E14) and (b) 0.20 J (sample E15) pulse energy respectively.

For 50% overlap with pulse energies of 0.16 J and 0.19 J, the resulting micrographs are shown in Figure 4.12 (a) and (b). Though the modified surface thickness increased at 0.19

J pulse energy, more cracks were observed, see Figure 4.12 (b). The sample processed at 0.16 J, shown in Figure 4.12 (a), produced well overlapped molten pools and a crack-free relatively smooth modified surface.

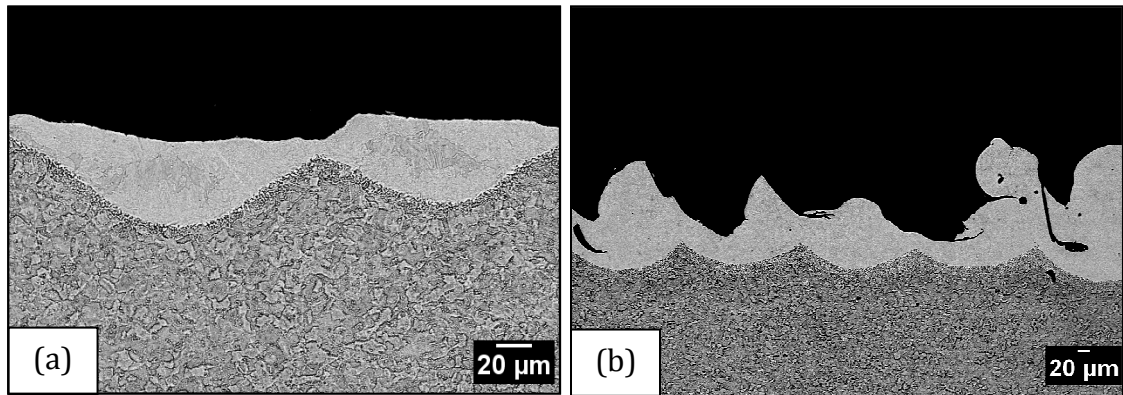


Figure 4.12: Modified surface cross section of samples processed at 50% overlap, and (a) 0.16 J (sample E26) and (b) 0.19 J (sample E27) pulse energy respectively.

(b) Grain Morphology

A micrograph of the laser modified surface where two subsequent pools meet with the substrate on the H13 tool steel is given in Figure 4.13. This shows the region where two subsequent molten pools solidified in sample E27 which processed at 100% duty cycle, 50% overlap, 4000 Hz PRF and 0.38 ms residence time. Three layers produced after this laser processing were A, B and C which represents the modified zone, heat affected zone and substrate respectively. The laser modified layer was separated by a heat affected zone from the substrate. Grain size decreased in both heat affected zone and laser modified layer relative to the substrate grain size. A similar α -Fe and martensite phase composition with a spherical carbide dispersion was observed in both the heat affected zone and substrate. In Figure 4.13, the laser modified zone was found to consist of α -Fe phase with well defined grain boundaries.

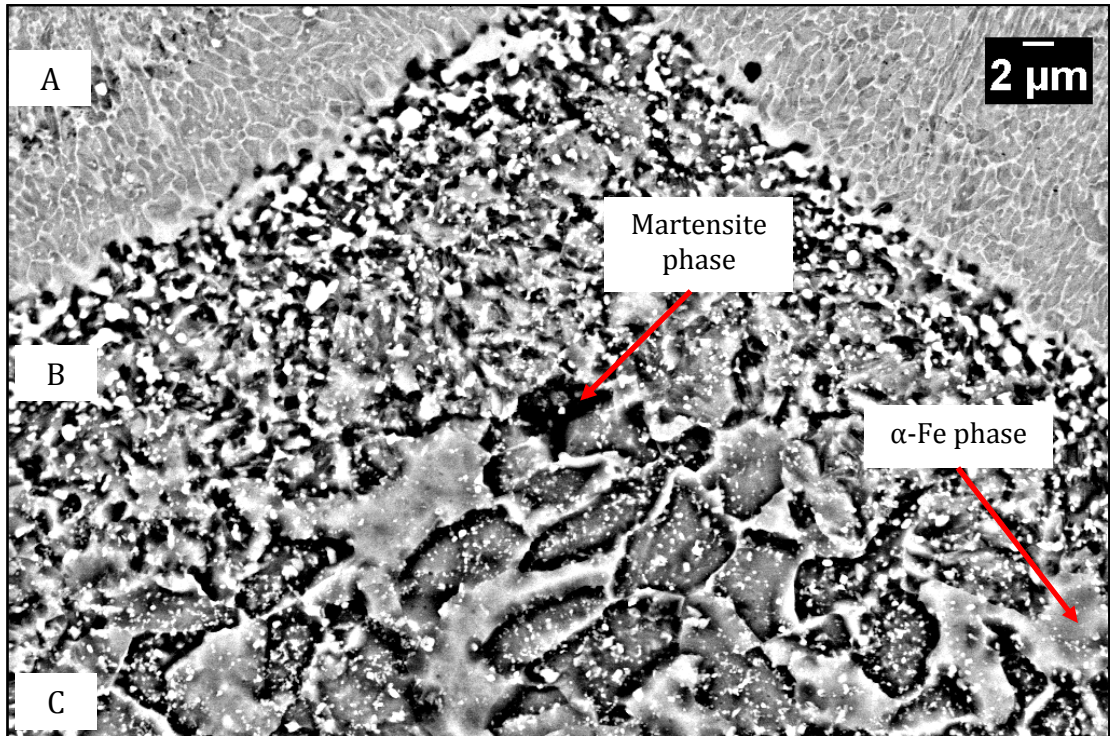


Figure 4.13: Back scattered detector micrograph of sample E27 cross section where A represents the laser modified layer, B is heat affected zone, and C is substrate.

In Figure 4.14 a mixture of coarse and fine grains was observed along with ultrafine subgrains. The dark shaded regions within the grains indicates martensite phase which was blended among the α -Fe phase. Spherical form carbides shaded in white and other black spots were examined using EDXS. Nano-sized grains were observed near and within the grain boundaries as pointed to in Figure 4.14. Several indistinct grain boundaries were observed for some of the micron-size grains.

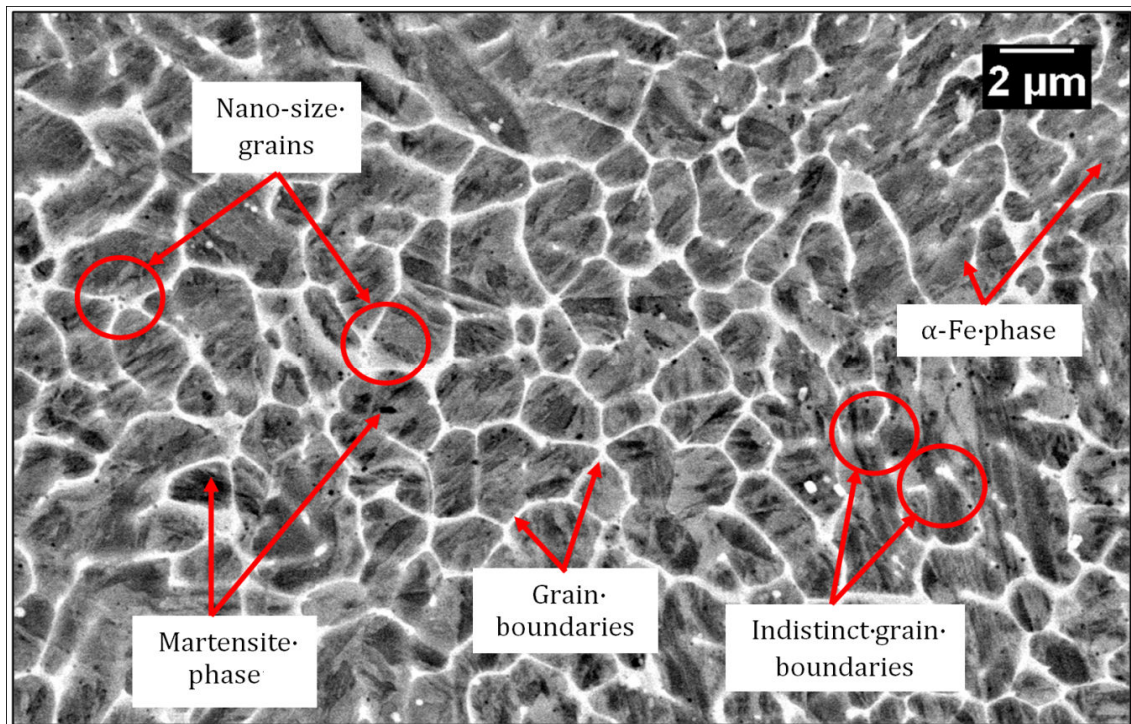


Figure 4.14: Grain composition of laser modified sample E26 produced in DOE2, processed at 85% duty cycle, 50% overlap and 4000 Hz PRF.

Hardness Properties

Figure 4.15 shows the measured hardness of the modified layer for DOE2 samples. The maximum and minimum hardness were 1017 and 724 HV_{0.1} respectively. At low duty cycle range, the maximum hardness was achieved between 10 and 20% overlap, whereas at high duty cycle, the hardness properties were maximum between 40 and 50% overlap. The average hardness for each sample in DOE2 is given in Appendix C1.

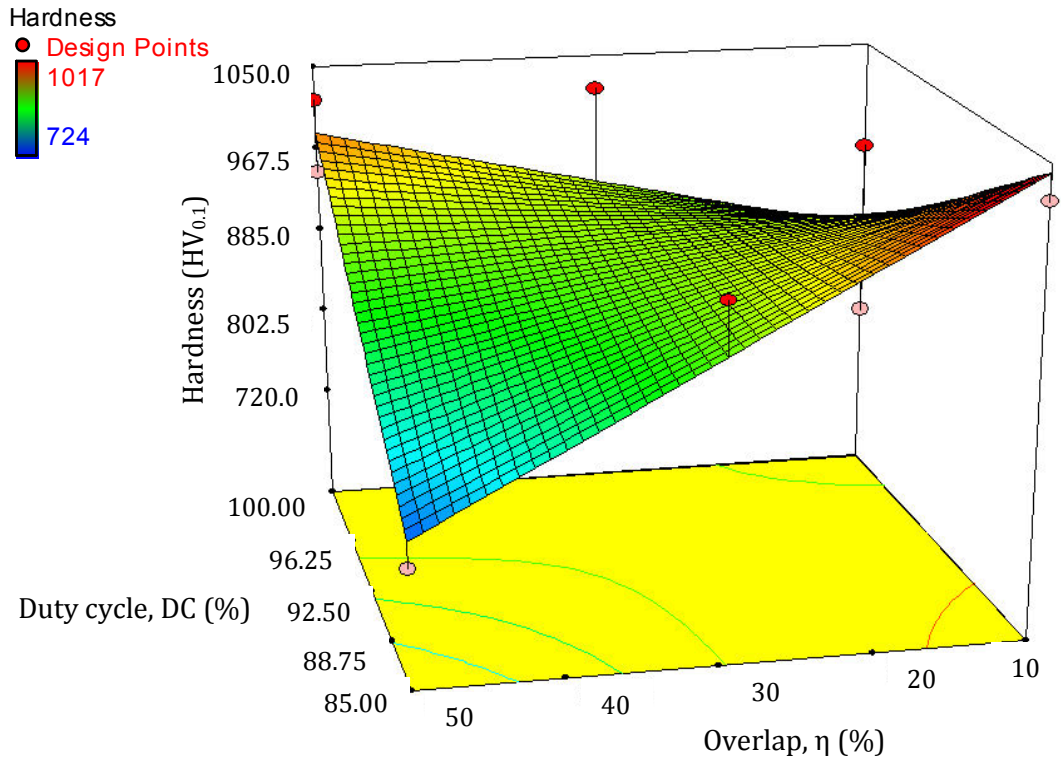


Figure 4.15: Three-dimensional plot of micro-hardness for DOE2 samples.

Surface Roughness

A linear relationship was found between duty cycle, overlap and average surface roughness as given by Equation 4.1. The average surface roughness of DOE2 samples for the various overlaps and duty cycle percentages is plotted in Figure 4.16. The average surface roughness ranged between 3.5 and 38.2 μm . The average surface roughness of the samples at 10, 30 and 50% overlap, and 85% and 100% duty cycle with 95% confidence intervals are given in Appendix C2. The minimum surface roughness of 3.5 μm was achieved in the samples processed at 10% overlap and 85% duty cycle. At maximum duty cycle and overlap, the surface roughness was highest, 38.2 μm R_a . The following equation can be used to calculate R_a from the results of DOE2 within the bounds of tested parameters.

$$R_a = 20.68 + 9.61A + 4.25B \quad \text{Equation 4.1}$$

where A represents duty cycle and B represents overlap.

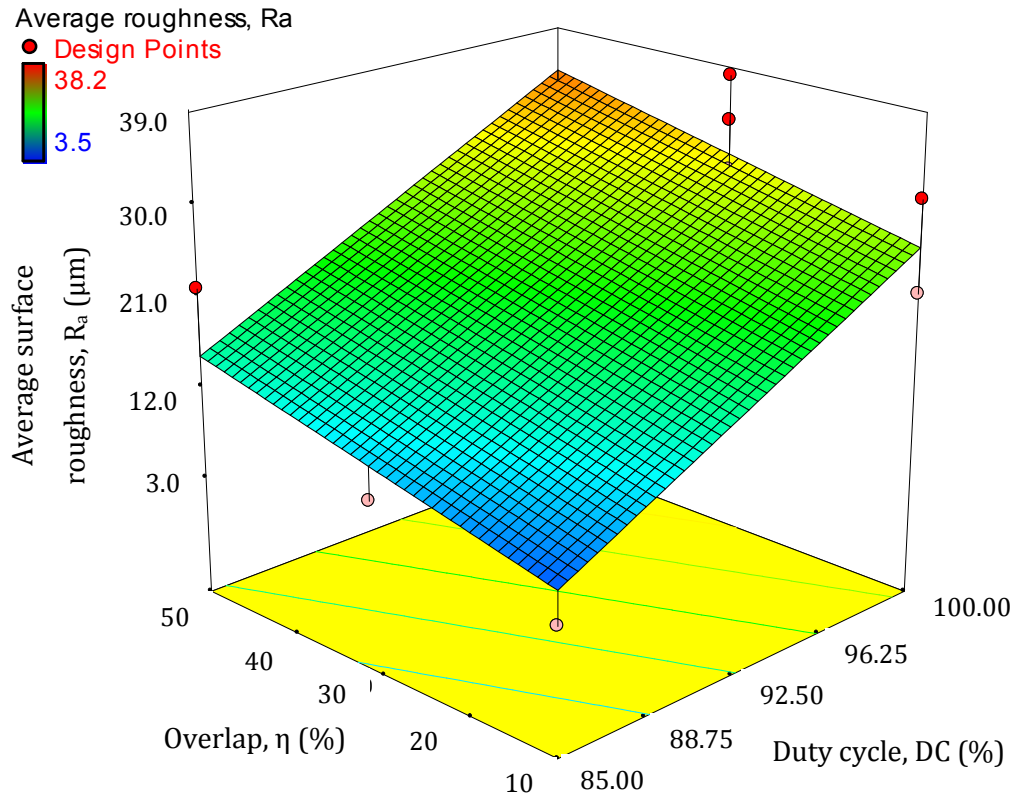


Figure 4.16: Three-dimensional plot of average surface roughness for DOE2 samples at the different settings of overlap and duty cycle.

DOE2 Significance and Summary

Optimisation analysis was conducted for DOE2 within the given range of duty cycle and overlap settings, with a view to maximise hardness properties and minimise average surface roughness. The resulting parameter setting solutions, the average hardness and average surface roughness are listed in Table 4.3. The highest and lowest desirability are represented by 1 and 0 values respectively. The highest desirability was set to produce maximum hardness and minimum average surface roughness. The parameter solutions were at 85% duty cycle and overlap ranged between 10.00 and 14.46% overlap. The model predicted the highest desirability from DOE2 of 0.951 with a combination of maximum hardness of 1042 HV_{0.1} and surface roughness of 6.8 μm R_a. The actual experimental values determined at these duty cycles and overlap values were 1017 HV_{0.1} and 3.5 μm R_a which indicates a level of inaccuracy in absolute value terms from the optimisation model. The predicted desirability of 0.951 is shown in the contour plot of Figure 4.17 and in Table 4.3. The desirability factor decreased as the duty cycle and overlap increased.

Table 4.3: Processing parameter settings in DOE2 based on high desirability.

Solution	DC (%)	η (%)	Hardness (HV) _{0.1}	R _a (μ m)	Desirability
1	85	10.00	1042	6.8	0.951
2	85	10.29	1040	6.9	0.950
3	85	10.82	1036	7.0	0.948
4	85	11.65	1030	7.2	0.946
5	85	14.46	1010	7.8	0.925

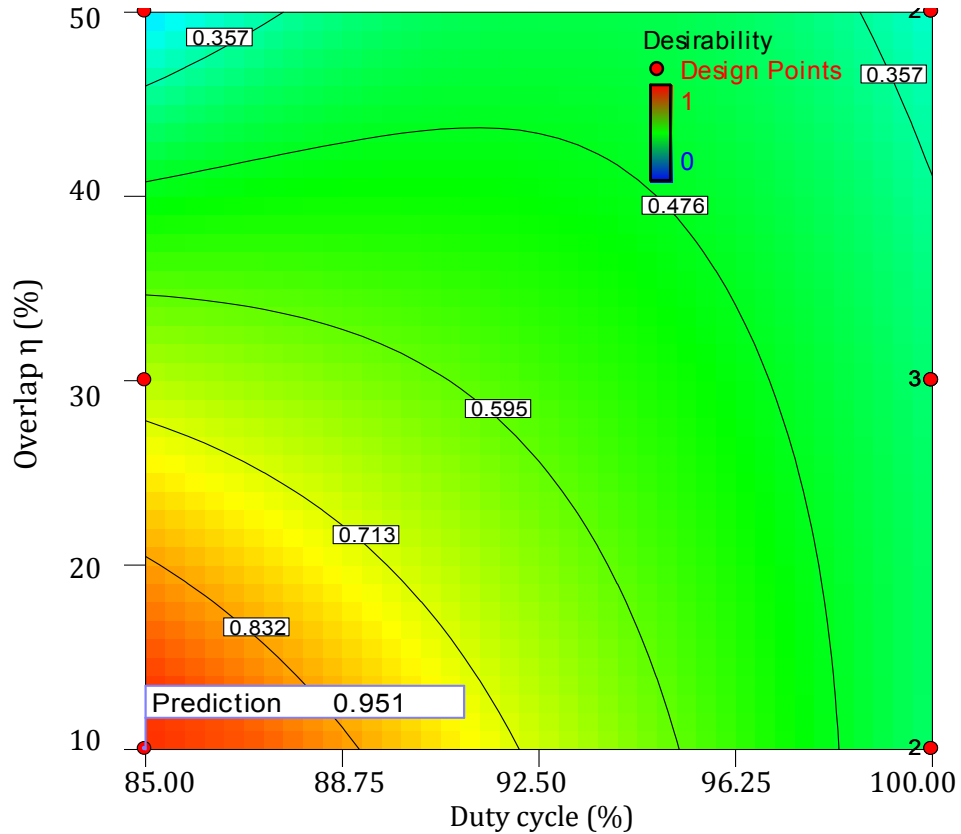


Figure 4.17: Contour plot of processing parameters in DOE2 corresponding to design desirability.

4.2.3 DOE3

From DOE3, the effects from two different power settings with constant 2900 Hz PRF and overlap, 10% and 50% on the modified surface depth and R_a are presented for the etched and roughened pre-treated samples. The pulse energy effect was observed from molten pool height measurements. A spot size of 0.2 mm diameter was used in this DOE. Surface roughness and hardness property results are also presented.

Metallographic Study

(a) The Effects of Constant PRF on Overlapped Melt Pool Geometry

Micrographs in Figure 4.18 show the surface morphology and cross section of samples processed with the 0.2 mm spot size. Details of the processing parameters of the samples can be seen in Table 4.4. The most beneficial processing design solutions from DOE2 indicated use of a 10 to 14% overlap range, however the DOE3 processing was performed at both 10% and 50% overlap to investigate the effect of a more continuous molten pool. Samples N10 and N24 were processed at 2900 Hz PRF, 0.12 ms pulse width, 0.10 J pulse energy and 760 W peak power. The residence time for 10% overlap was set at 0.14 ms while for 50% overlap it was set at 0.19 ms. As the residence time was higher for the higher % overlap, the irradiance used to process the sample in Figure 4.18 (a) 22,139 W/mm² was higher than in Figure 4.18 (c) 16,388 W/mm². This can be seen to have resulted in the rougher surface and modified layer depth Figure 4.18 (d) compared to Figure 4.18 (b)

Table 4.4: Processing parameters and cooling period for DOE3 samples.

Sample	I (W/mm²)	η (%)	τ (ms)	PRF (Hz)	T_R (ms)	E_p (J)	t_{cooling} (ms)
N4	10,930	50	0.17	2900	0.25	0.09	0.094
N10	22,139	10	0.12		0.14	0.10	0.208
N24	16,388	50	0.12		0.19	0.10	0.160
N12	28,184	50	0.08		0.12	0.11	0.226

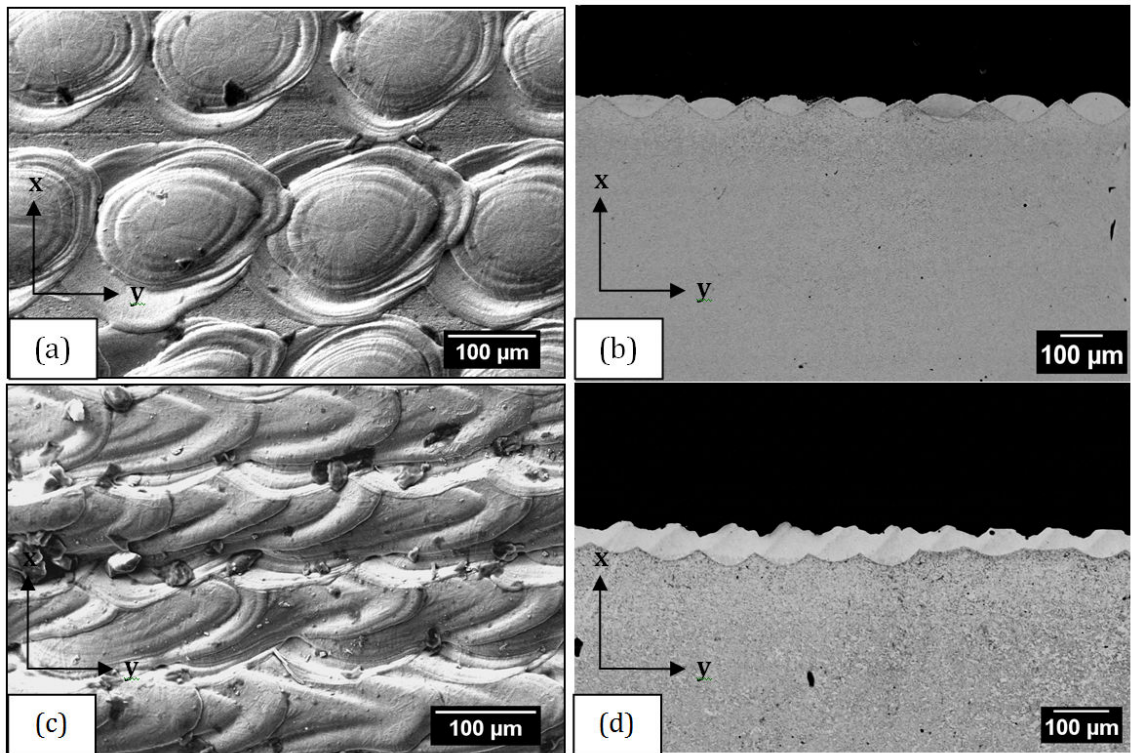


Figure 4.18: Surface morphology of overlapped pulses on DOE3 samples at 10% overlap for sample N10 (a) plan view, (b) cross sectional view; and 50% overlap for sample N24 (c) plan view, (d) cross sectional view.

(b) Grain Morphology

The grain morphology of the laser modified sample N12 processed by DOE3 at 0.2 mm spot size is shown in the micrograph of Figure 4.19. The micrograph was characterised by α -Fe phase amongst the high volume fraction of grain boundaries. The grains observed were homogeneously shaped with the presence of ultrafine size subgrains with approximate minimum diameter of 560 nm. The micrograph of Figure 4.19 can be compared to the laser modified sample in Figure 4.14. A higher volume of grain boundary and more ultrafine sized grains were in general evident from the DOE3 samples compared to DOE2 samples. Similar indistinct grain boundaries found for some grains in the micrograph of Figure 4.14 are evidenced in the micrograph of Figure 4.19.

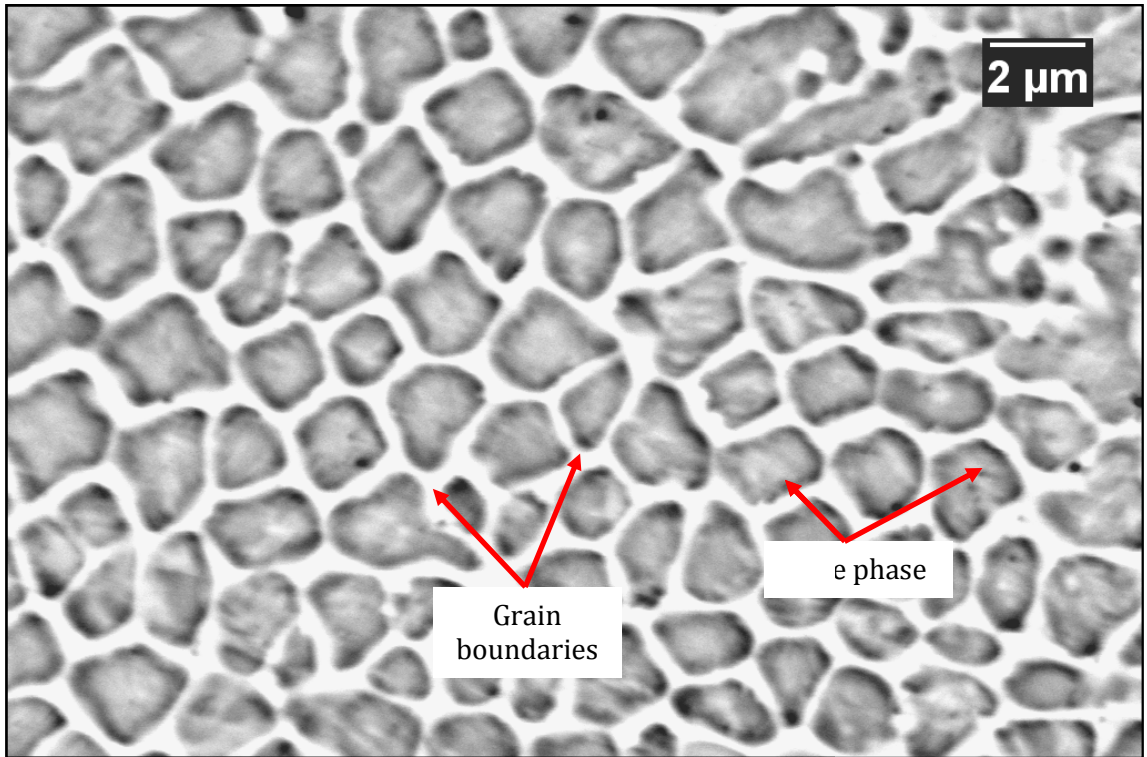


Figure 4.19: Grain composition of laser modified sample N12 processed by DOE3.

Hardness Properties

The processing parameters and hardness properties measured in DOE3 samples are given in Table 4.5. The hardness properties measured in the modified layer were at least 1.5 times higher than the substrate hardness. The sample processed at 0.09 J exhibited the lowest peak hardness of 435 HV_{0.1} with a 5.61x10⁶ K/s heating rate and 0.094 ms cooling period as calculated by Equation 3.9 and Equation 3.10 presented in § 3.2.3. Comparing the hardnesses measured for samples N10 (10% overlap) and N24 (50% overlap), the higher hardness was obtained in the modified layer of the N24 sample processed at 50% overlap. At 10% overlap, the heating rate and cooling period were 10.30x10⁶ K/s and 0.208 ms respectively. The N24 sample with 50% overlap was melted at a 7.61x10⁶ K/s heating rate and solidified within a 0.160 ms cooling period. At maximum pulse energy of 0.11 J, a maximum peak hardness of 996 HV_{0.1} was measured, with 11.8x10⁶ K/s heating rate and 0.226 ms cooling period.

Table 4.5: The average hardness of modified surface in DOE3 samples.

Sample	η (%)	E_p (J)	H_R (10^6 K/s)	$t_{cooling}$ (ms)	Distance from surface (μm)	Average hardness ($HV_{0.1}$)
N4	50	0.09	5.61	0.094	20	435
					40	297
					60	282
					80	282
					100	283
N10	10	0.10	10.30	0.208	20	772
					40	807
					60	711
					80	293
					100	282
N24	50	0.10	7.61	0.160	20	903
					40	824
					60	888
					80	464
					100	293
N12	50	0.11	11.80	0.226	20	996
					40	863
					60	789
					80	435
					100	293

Surface Roughness

The average measurement of surface roughness for the sample processed at 0.09 J pulse energy was 3.1 μm as shown in Table 4.6. At higher pulse energy of 0.11 J, the average surface roughness of sample N12 was 6.2 μm . An effect of overlap on surface roughness can be seen between measurements for sample N10 and N24 (at 10% and 50% overlap respectively) where lower average surface roughness of 5.5 μm was measured from the 10% overlap sample.

Table 4.6: The average surface roughness of DOE3 samples.

Sample	η (%)	E_p (J)	Average surface roughness, R_a (μm)
N4	50	0.09	3.1
N10	10	0.10	5.5
N24	50	0.10	7.9
N12	50	0.11	6.2

4.2.4 DOE4

From DOE4, results presented were the effect of power and overlap on the modified surface properties where a 0.09 mm spot size was used. Results of modified surface depth, grain morphology, hardness and surface roughness are presented corresponding to the constant PRF of 2900 Hz and 0.09 J pulse energy settings. Parameter interaction

investigated is presented for each surface property. Table 4.7 shows the laser parameters settings and corresponding heating rate and cooling period used in DOE4.

Table 4.7: Parameter settings, heating rate and cooling period for DOE4 samples.

Sample	Set parameters			Outcome parameters				
	P _p (W)	DC (%)	η (%)	I (W/mm ²)	T _R (ms)	τ (ms)	H _R (10 ⁶ K/s)	t _{cooling} (ms)
X1	760	36	0	238,087	0.06	0.06	22.50	0.282
X2	1138	24		178,761	0.08	0.08	16.90	0.262
X3	1515	18		119,436	0.12	0.12	11.28	0.220
X4	760	36	10	216,524	0.07	0.06	20.46	0.276
X5	1138	24		162,572	0.09	0.08	15.37	0.254
X6	1515	18		108,619	0.14	0.12	10.26	0.208
X7	760	36	30	183,282	0.08	0.06	17.32	0.264
X8	1138	24		137,613	0.11	0.08	13.01	0.237
X9	1515	18		91,943	0.16	0.12	8.68	0.183

Metallographic Study

(a) The effect of Peak Power on Modified Surface Depth

The micrographs of DOE4 samples processed at 0, 10, 30% overlap are shown in Figure 4.20. At the 0.09 mm spot size, the effect of overlaps investigated at three different peak powers is presented. At low power of 760 W, the molten pool mounted up after four pulses and formed a bulging geometry. Similar effects were observed at the other overlap percentages for this power setting. At this lower power of 760 W, the maximum depth was measured from the bulged molten pool, α , as described in Figure 4.8, § 4.2.2. At higher powers of 1138 W and 1515 W the overlapped pulses produced a uniform modified layer. Without overlap, the modified layer depth was smaller at 1515 W peak power compared to samples processed at 760 and 1138 W peak powers.

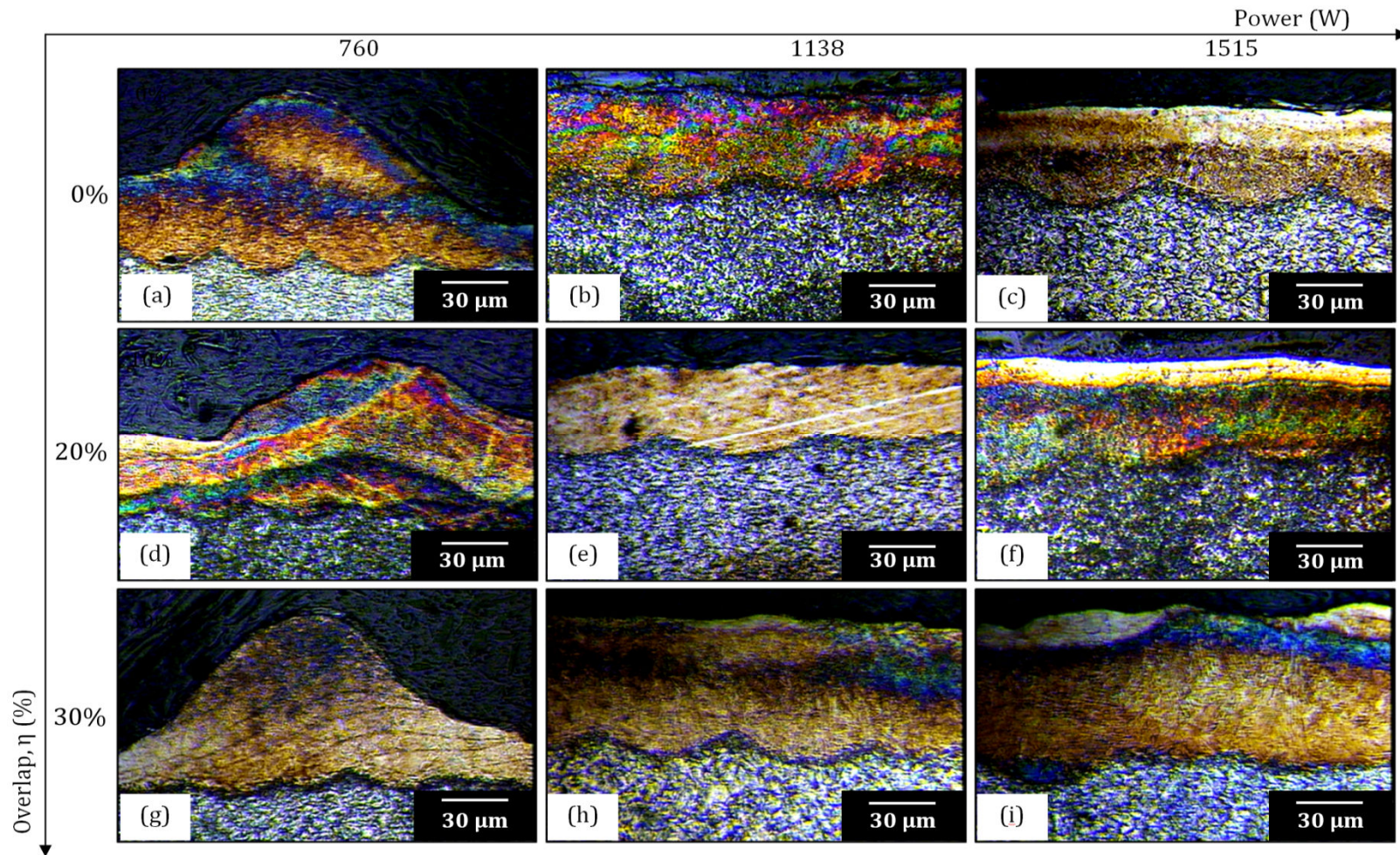


Figure 4.20: Micrographs of DOE4 samples at different peak powers and (a) to (c) 0%; (d) to (f) 10%; and (g) to (i) 30% overlap.

Figure 4.21 shows a contour plot of the response surface generated for modified layer depths for the overlap and power settings used for DOE4 samples. The maximum modified layer depth of 87.5 μm was measured in the samples processed at 760 W peak power. From the contour plot, Figure 4.21, at constant pulse energy of 0.095 J and average power of 274 W, the design model indicates that a relatively uniform modified surface depth of approximately 51.4 μm was achieved in samples processed at peak powers of more than 1090 W and overlaps of less than 19%. At peak power settings between 996 and 1090 W, the modified surface depth was approximately 58.6 μm . At high overlap of 30%, the laser-material interaction time was longer compared to samples processed at 0 or 10% overlap which on average increased the modified layer depth. The modified surface depths for each sample in DOE4 are given in Appendix D1.

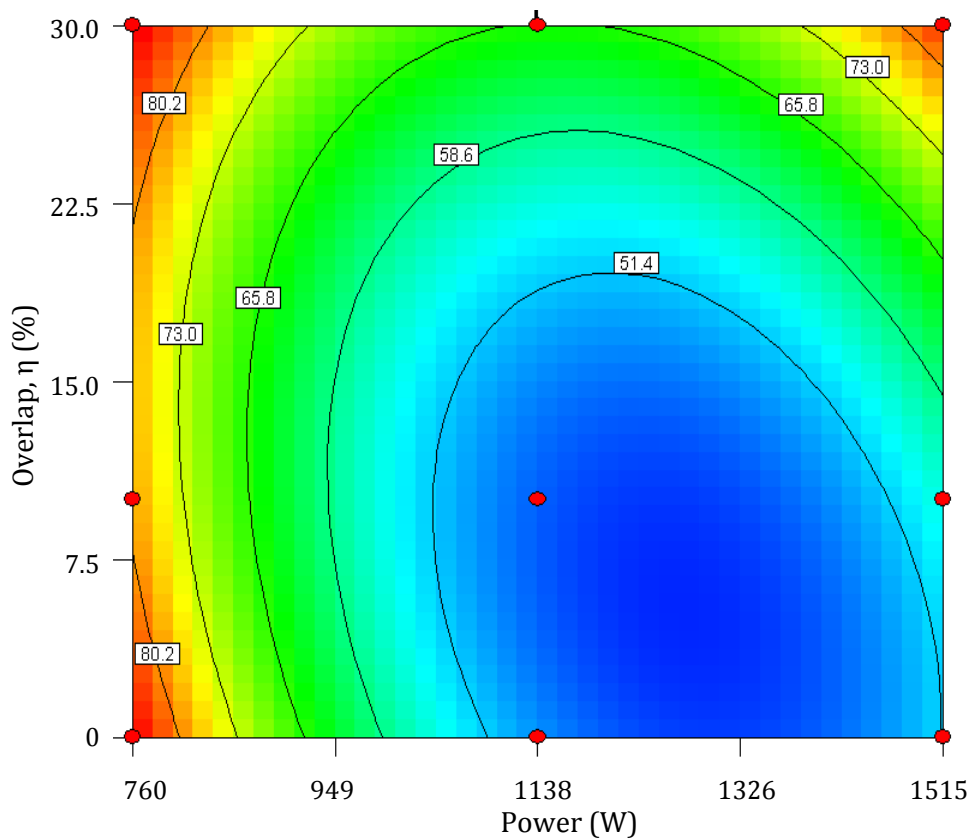


Figure 4.21: Contour plot of modified layer depth for DOE4 samples corresponding to overlap and power settings.

(b) Grain Morphology

In Figure 4.22, the grain morphology of the sample processed with 0.09 mm spot size can be seen to be comprised of a high volume fraction of grain boundary. Nano-size sub-grains were observed among the micron-size grains. Several regions appeared to be an amorphous phase as grain boundaries were absent. In Figure 4.23, amorphous and quasi crystalline resembling phases were observed amongst the crystalline phase structures. The quasi-crystalline phase observed depicted 'flower-like' grains.

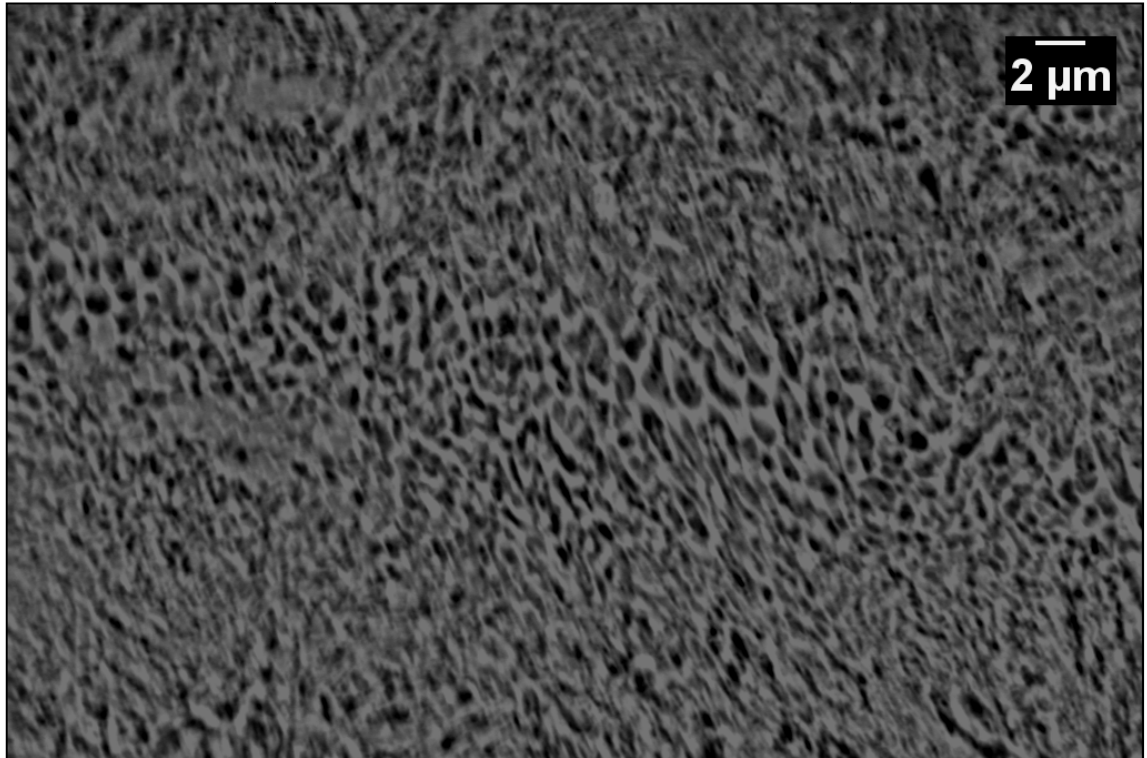


Figure 4.22: Back scattering image of grain density variation of sample X4 processed at 0.09 mm spot size.

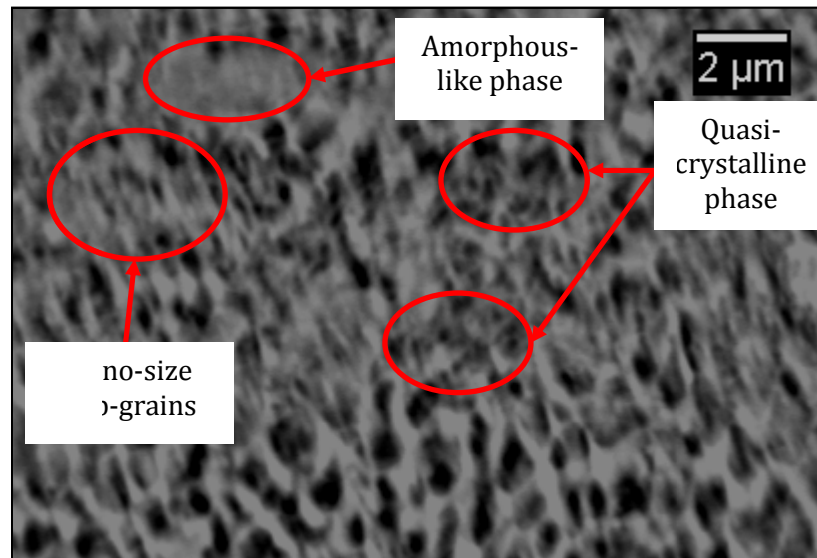


Figure 4.23: Nano-size sub-grains, amorphous and quasi-crystalline phase formation in the laser modified sample X4.

Hardness Properties

The effect of 0.09 mm spot size on hardness properties at different settings of peak power and overlap is plotted in Figure 4.24. The hardness properties were consistent where the average hardness measured from the nine samples of DOE4 was 800 HV_{0.1}. This hardness value is 2.86 times higher than measured in the as-received H13 tool steel sample (280 HV_{0.1}). The average hardness of the modified layer measured was independent of the overlap settings. The maximum hardness achieved at 1138 W peak power and 13.01x10⁶ K/s heating rate was 976 HV_{0.1} in sample X8. The minimum hardness was 670 HV_{0.1} measured in sample X2 with peak power of 1138 W and 16.9x10⁶ K/s heating rate calculated using Equation 3.9 in § 3.2.3.

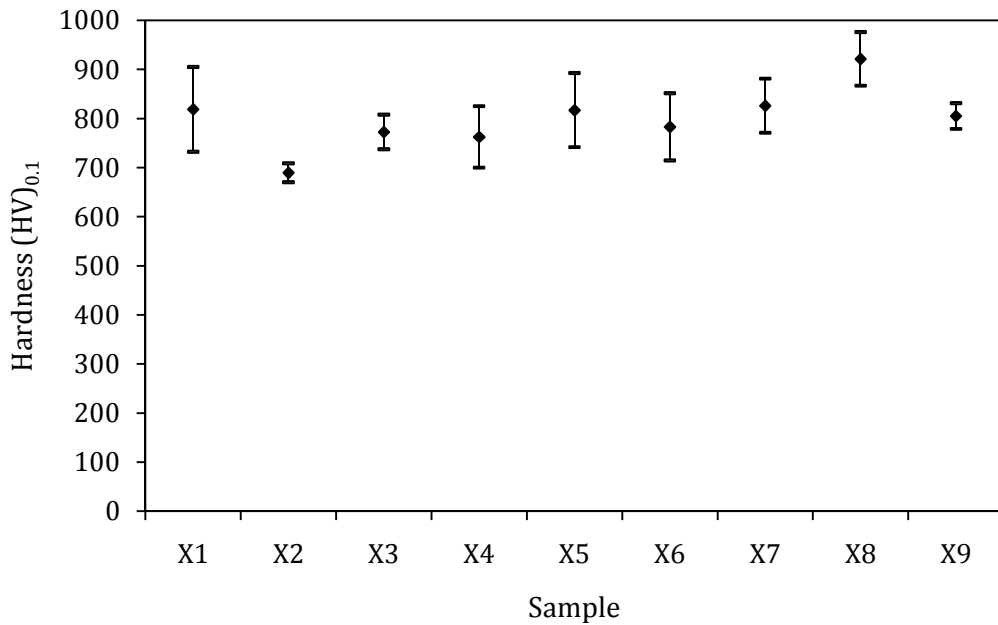


Figure 4.24: Hardness range of DOE4 samples.

Surface Profile and Roughness

The surface roughness profile of DOE4 samples at 0% overlap are given in Figure 4.25. The investigated surface roughness profile is given in green coloured curves (lower lines) while the red coloured curves (upper lines) represent the unfiltered profile with surface waviness included. In Figure 4.25 (a), the sample profile was produced from 1515 W (18% duty cycle). Profiles for samples processed at 1138 W and 760 W, shown in Figure 4.25 (b) and (c) respectively, were processed at 24% and 36% duty cycle respectively. The duty cycle determines the pulse width and thus impacts on modified surface amplitude. The highest amplitude range for the green (lower) curve was between -30 to 20 μm as shown in Figure 4.25 (c). Samples processed at lower duty cycles of 18% and 24% in Figure 4.25 (a) and (b) produced lower amplitudes between -14 and 20 μm and -12 and 10 μm respectively.

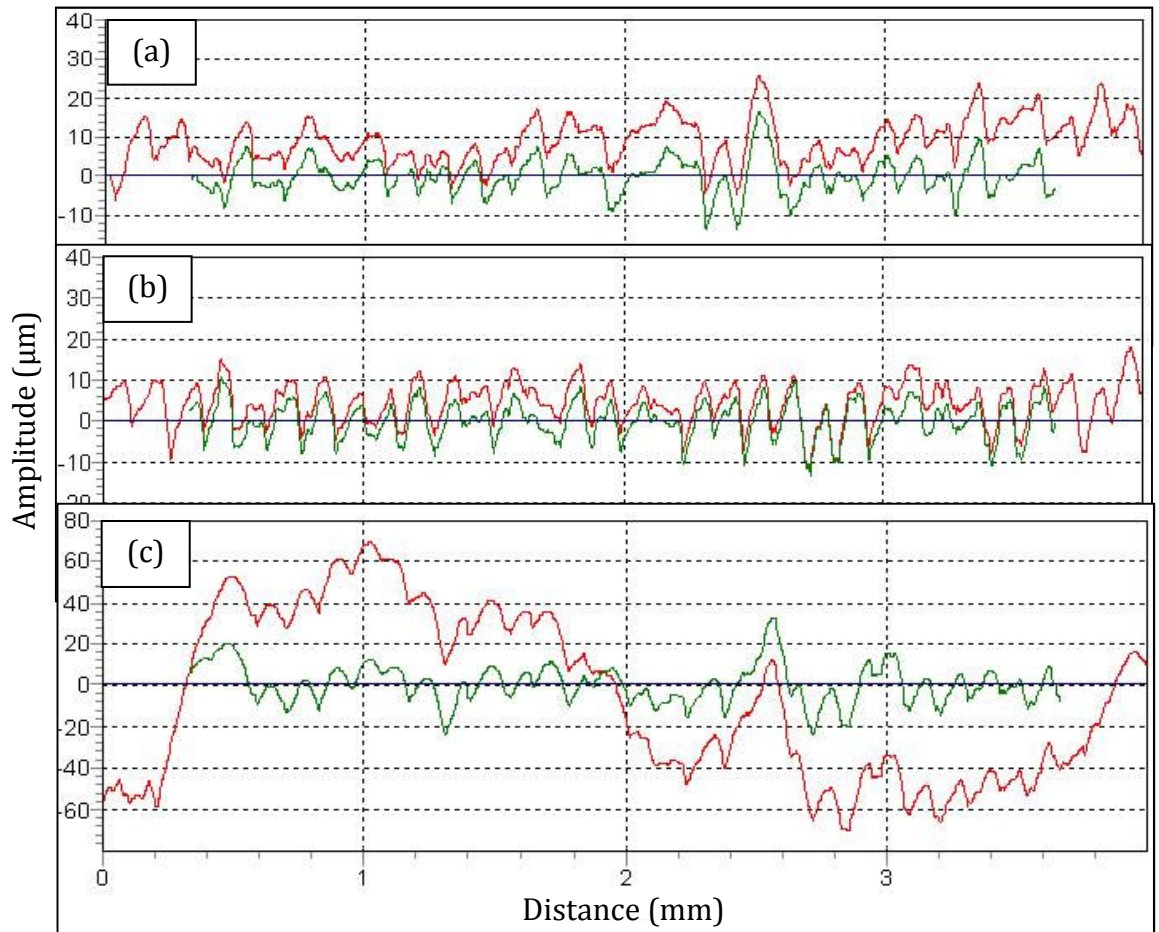


Figure 4.25: Two-dimensional surface profile of DOE4 samples at (a) 1515 W, (b) 1138 W and (c) 760 W power settings.

In Figure 4.26, the resulting surface roughness was plotted in a contour graph to show the parameter-surface property relationship. The average surface roughness range was between 3.2 and 9.5 μm . The highest average surface roughnesses were measured in samples processed between 760 and 810 W power and 15 to 30% overlap. Increasing the laser power reduced the surface roughness. At powers above approximately 1044 W the roughness measured was at the minimum value of 3.2 μm . In samples processed at power settings of less than 1044 W, the surface roughness increased with increasing overlap percentage.

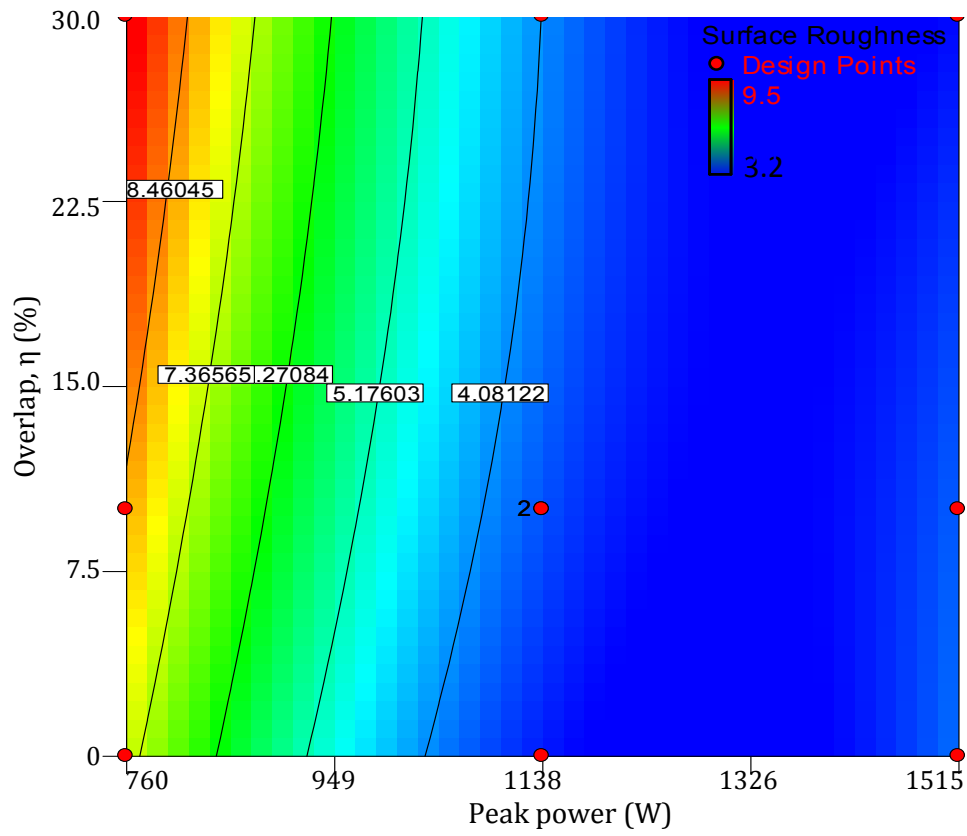


Figure 4.26: Contour plot of DOE4 sample surface roughness at different overlap and laser power settings.

4.2.5 DOE5

From DOE5, the findings on the process optimisation of the H13 tool steel surface modification are presented. The metallographic study presented indicates the presence of a continuous modified surface on the H13 tool steel substrate for each processed sample. Variations of pulse energy effects on the modified surface geometry and depth were observed. The characterisation and statistical analysis results corresponding to the three different levels of peak power, overlap and PRF factors are presented. These results which comprised of modified layer depth, hardness and surface roughness are given in Table 4.8.

Table 4.8: Processing parameters and characterisation results from DOE5 samples.

Sample	I (W/mm ²)	T _R (ms)	τ (ms)	H _R (10 ⁶ K/s)	t _{cooling} (ms)	Modified layer depth (μm)	Hardness (HV) _{0.1}	R _a (μm)
F1	119,297	0.16	0.16	8.94	0.278	150	868	22.4
F9	198,959	0.09	0.10	14.92	0.341	66	861	3.6
F11	162,398	0.12	0.10	12.18	0.319	90	871	4.1
F2	237,809	0.08	0.08	17.83	0.356	72	905	5.0
F5	132,686	0.11	0.12	12.54	0.233	47	772	6.1
F7	108,582	0.14	0.12	10.26	0.208	73	894	5.5
F13	178,700	0.08	0.08	16.90	0.262	49	824	2.2
F14						45	823	2.8
F15						47	840	2.9
F16						48	830	3.2
F17						49	840	2.6
F6	264,499	0.06	0.06	25.00	0.289	39	841	3.0
F8	216,449	0.07	0.06	20.46	0.276	52	816	3.9
F3	119,459	0.10	0.10	13.62	0.183	53	821	2.0
F10	198,631	0.06	0.07	22.67	0.224	43	728	1.8
F12	162,593	0.08	0.07	18.55	0.210	55	820	2.6
F4	238,133	0.05	0.05	27.17	0.234	37	787	2.0

Metallographic Study

The effect of residence time investigated in samples processed at 0.12 J pulse energy is depicted by the micrographs in Figure 4.27. Increasing residence time resulted in waviness and roughness of the modified layer surface. In Figure 4.27 (a), sample F2 shown was processed at highest peak power of 1515 W, low residence time of 0.08 ms and without overlap as given in Table 3.9. Figure 4.27 (b) and (c) are respectively from samples F9 and F11 which were processed at 1138 W peak power and overlap of minus 10 and plus 10% respectively. Sample F1 at lowest peak power of 760 W, longest residence time of 0.16 ms and without overlap in Figure 4.27 (d) shows bulging geometry in the modified surface as found in some of the DOE4 samples.

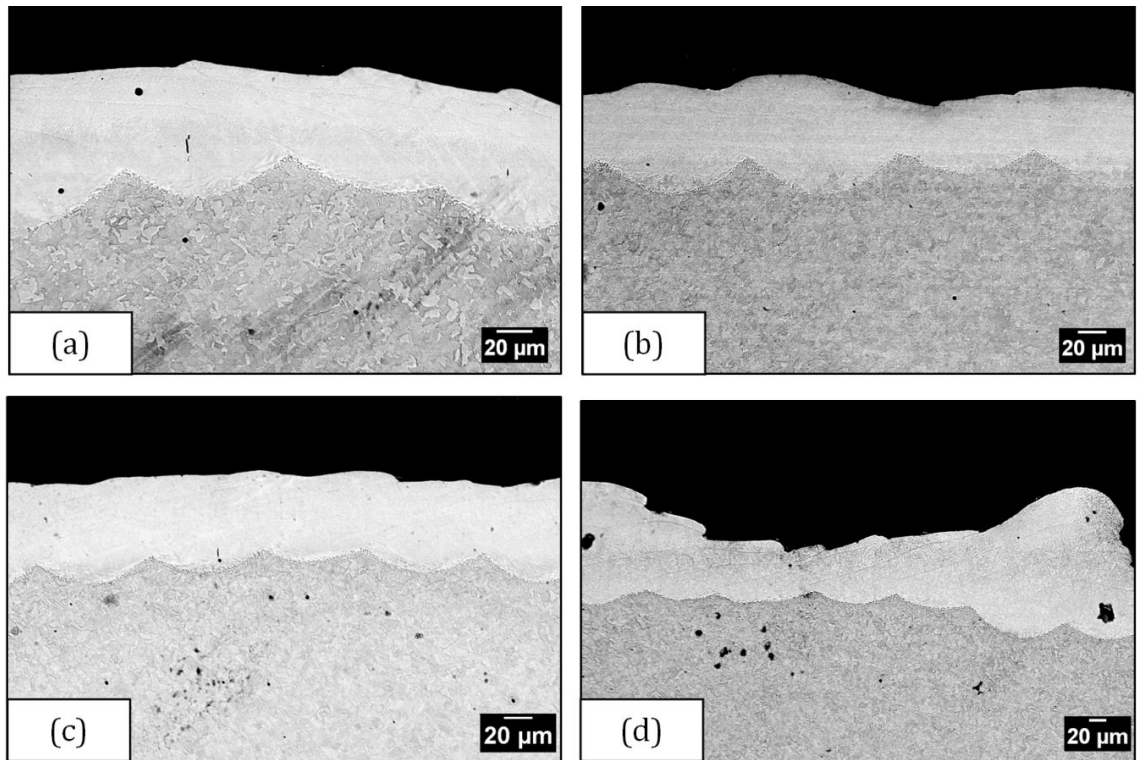


Figure 4.27: Micrographs of DOE5 samples processed at 0.12 J pulse energy and residence time of (a) 0.08 (sample F2), (b) 0.09 (sample F9), (c) 0.12 (sample F11) and (d) 0.16 ms (sample F1).

Decreasing the pulse energy to 0.10 J in samples of Figure 4.28, decreased the waviness and roughness of the surface geometry. Figure 4.28 (a) and (b) are respectively sample F6 and F8; processed at the highest peak power of 1515 W and overlap of -10 and 10% respectively where increased overlap or residence time increased the modified surface depth. Sample F13 in Figure 4.28 (c) was processed at 1138 W without overlap but increased residence time resulting in deeper modified layer than in Figure 4.28 (a) and (b). At higher residence times of 0.11 and 0.14 ms and peak power of 760 W, the upper part of the modified surface in Figure 4.28 (d) and (e) respectively, show waviness-type of geometry.

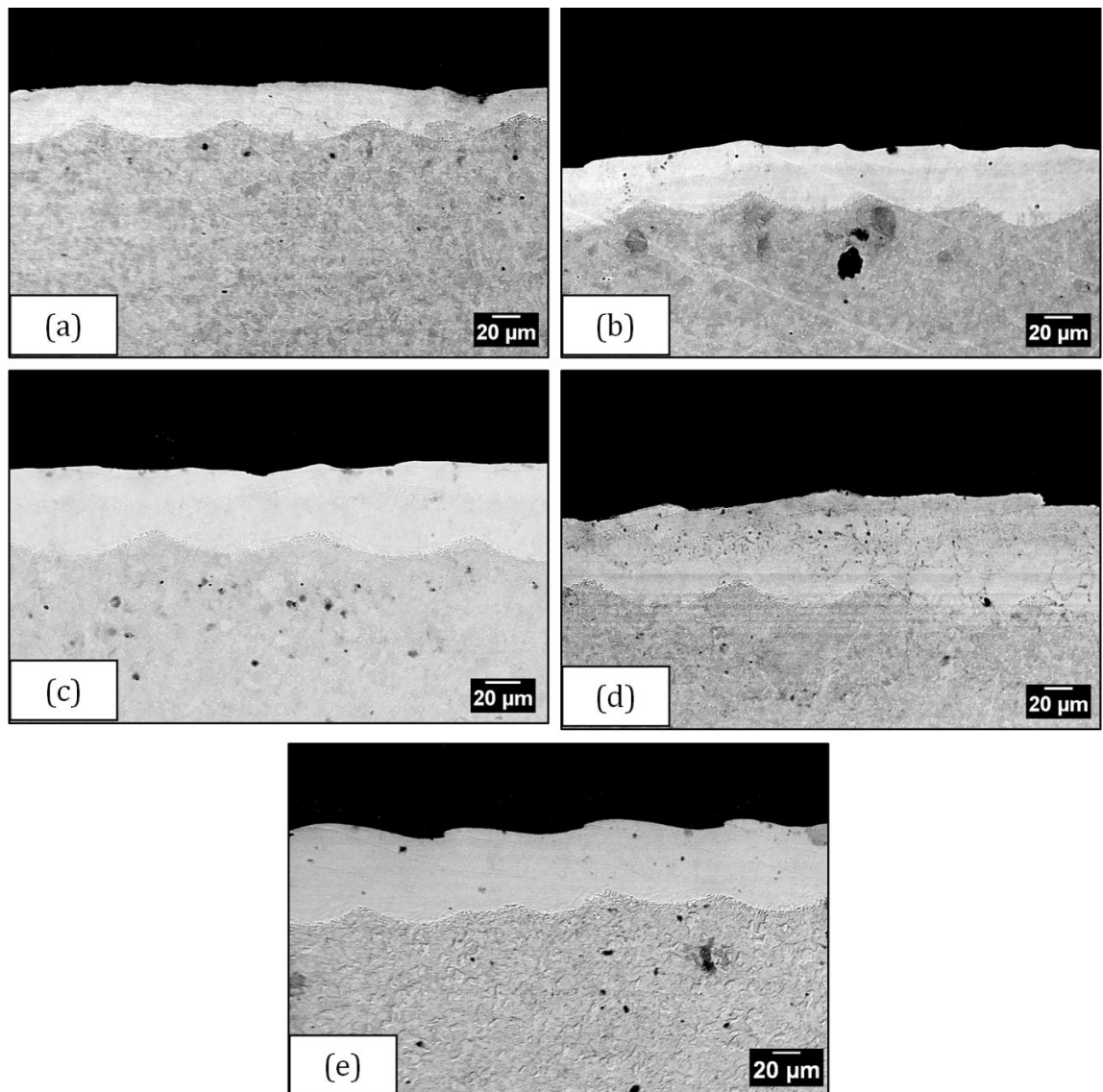


Figure 4.28: Micrographs of DOE5 samples processed at 0.10 J pulse energy and residence time of (a) 0.06 (sample F6), (b) 0.07 (sample F8), (c) 0.08 (sample F13), (d) 0.11 (sample F5) and (e) 0.14 ms (sample F7).

Further decrease of pulse energy to 0.08 J decreased the modified surface depth but also reduced the modified surface layer roughness and waviness geometry. The micrograph in Figure 4.29 (a) shows the sample processed at 1515 W peak power and 0% overlap. At this highest peak power, the waviness effect was reduced for an overlap of 0% compared to an overlap of 10%. A noticeable effect of overlap was observed again in Figure 4.29 (b) and (c) where the modified surface depth increased at 10% overlap compared to 0% overlap. The sample processed by peak power of 760 W and without overlap but increased residence time shown in Figure 4.29 (d), still presented an undulating surface geometry.

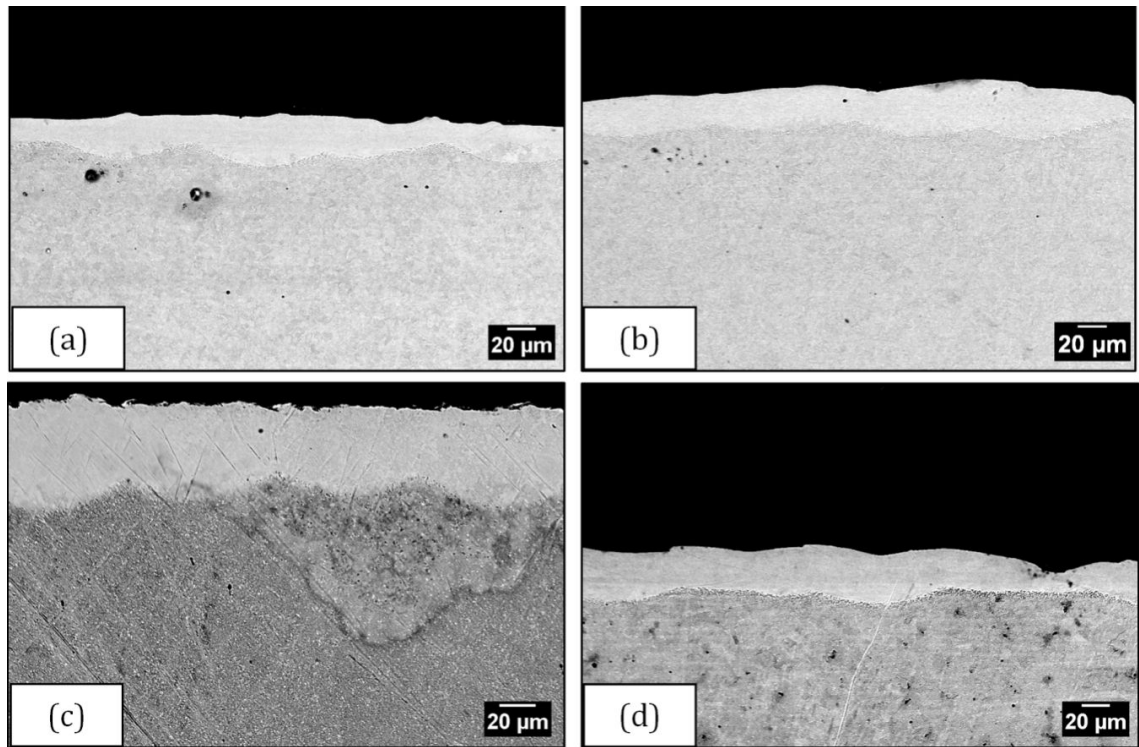


Figure 4.29: Micrographs of DOE5 samples processed at 0.08 J pulse energy and residence time of (a) 0.05 (sample F4), (b) 0.06 (sample F10), (c) 0.08 (sample F12) and (d) 0.10 ms (sample F3).

Statistical Analysis

(a) Modified Surface Depth

Analysis of variance (ANOVA) carried out for the modified surface depth response is given in Table 4.9. The quadratic model was used for analysis of modified surface depth. However, several terms like BC, AC, A^2 and C^2 were insignificant for modified surface depth response which were identified by p-values greater than 0.1000. The insignificant terms were removed using stepwise elimination process. The reduced model is shown in Table 4.10.

Table 4.9: ANOVA results for modified surface depth response using quadratic model.

Source	Sum of squares	Df	Mean square	F value	p-value prob > F	Remarks
Model	10526.16	9	1169.57	6.66	0.0103	Significant
A-Power	1912.71	1	1912.71	10.89	0.0131	
B-PRF	4550.58	1	4550.58	25.90	0.0014	
C-Overlaps	708.76	1	708.76	4.03	0.0846	
AB	936.36	1	936.36	5.33	0.0543	
AC	44.22	1	44.22	0.25	0.6313	
BC	36.00	1	36.00	0.20	0.6645	
A ²	408.72	1	408.72	2.33	0.1710	
B ²	1791.55	1	1791.55	10.20	0.0152	
C ²	96.91	1	96.91	0.55	0.4819	
Residual	1229.93	7	175.70			
Lack of fit	1216.54	3	405.51	121.16	0.0002	
Pure Error	13.39	4	3.35			
Cor Total	11756.09	16				
	Std. Dev.	13.26		R ²	0.8954	
	Mean	59.61		Adjusted R ²	0.7609	
	C.V. %	22.24		Adequate Precision	9.992	

The models adequacy was validated by examining the statistical properties which are lack of fit, R², adjusted R² and adequate precision. In the reduced model, see Table 4.10, though the lack of fit was significant; however R² and adjusted R² values were 84.7% and 77.8% respectively which indicates a good relationship between the factors and the modified surface depth response from the regression model. This model was generated after the insignificant terms were removed. F-value is a measure of how different the means are relative to the variability within each sample. The F-value of 361.85 implies that the model is significant with only a 0.01% chance that an F-value this large could occur due to noise. Terms with values of the probability less than 0.05 were taken as significant. These included A, B, C, AB and B² model terms. The final response equation for the modified surface depth after removing the insignificant terms is given in Equation 4.2.

Table 4.10: ANOVA results for modified surface depth response (after stepwise elimination).

Source	Sum of squares	Df	Mean square	F value	p-value Prob > F	Remarks
Model	9959.91	11	1067.39	361.85	< 0.0001	Significant
A-Power	1912.71	1	1912.71	11.71	0.0057	
B-PRF	4550.58	1	4550.58	27.87	0.0003	
C-Overlaps	708.76	1	708.76	4.34	0.0613	
AB	936.36	1	936.36	5.73	0.0356	
B ²	1851.49	1	1851.49	11.34	0.0063	
Residual	1796.18	11	163.29			
Lack of Fit	1782.79	7	254.68	76.09	0.0004	
Pure Error	13.39	4	3.35			
Cor Total	11756.09	16				
	Std. Dev.	12.78		R ²	0.8472	
	Mean	59.61		Adjusted R ²	0.7778	
	C.V. %	21.44		Adequate Precision	13.225	

Modified surface depth

Equation 4.2

$$=49.77 - 15.46A - 23.85B + 9.41C + 15.30AB + 20.91B^2$$

where A represents Power, B represents PRF and C represents % overlap. Figure 4.30 shows the normal probability plot of the residuals for modified surface depth where the studentized residuals are in a straight line. In Figure 4.31, the observed values were compared with the predicted values calculated from the model. The regression model can be seen to have fitted very well with the observed values.

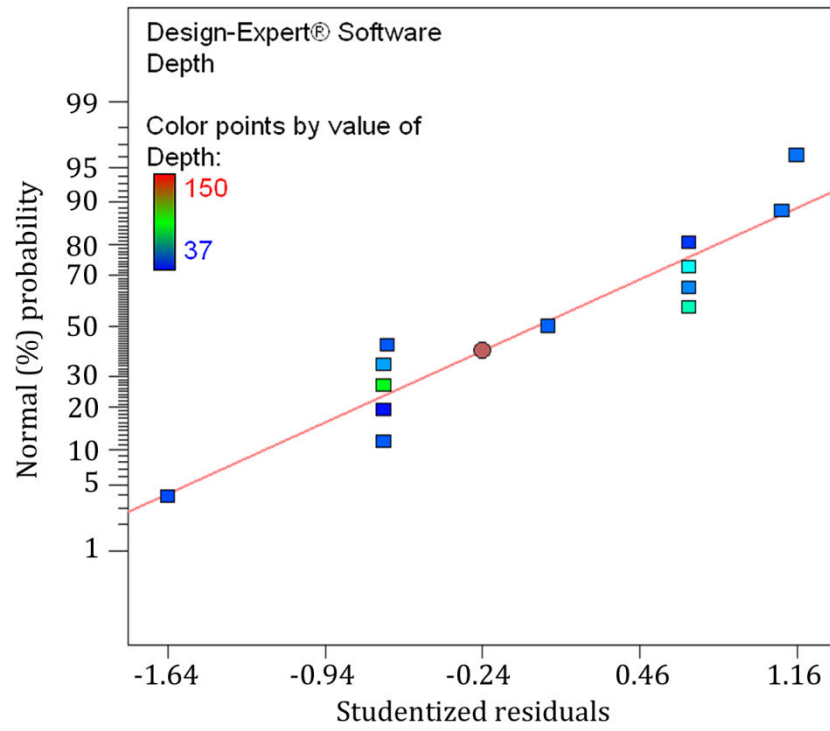


Figure 4.30: Normal probability plot of the studentized residuals for the modified surface depth response.

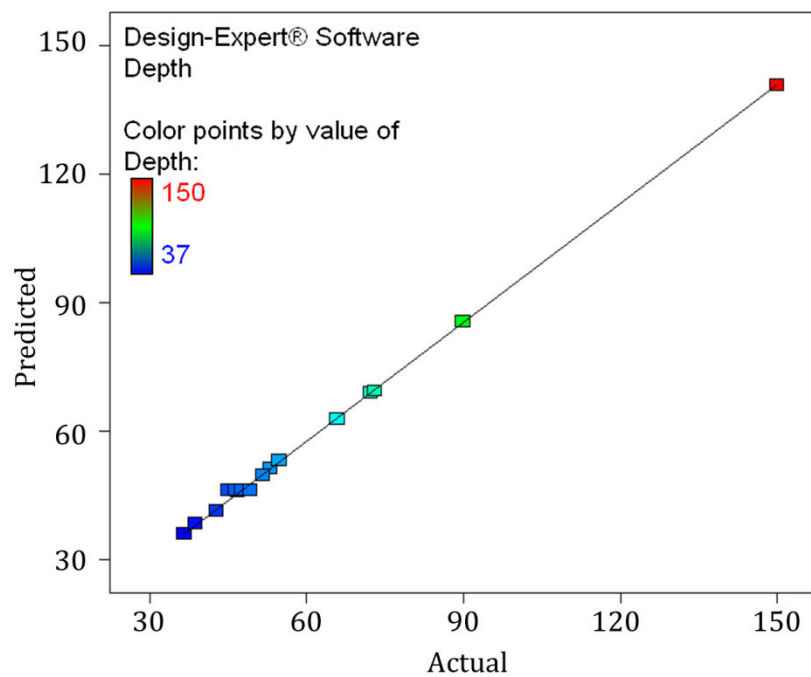


Figure 4.31: Predicted against actual plot of modified surface depth response.

Variations of modified layer depth corresponding to PRF and peak power factors are shown in Figure 4.32. The resulting laser modified layer maximum depth for all PRF and power settings and for 0% overlap was between 55 and 131 μm . At 760 W peak power and 0% overlap, the resulting modified layer range was between 131 and 150 μm . The maximum and minimum layer depths were both measured at 0% overlap. From the model, the highest layer depth was produced on samples processed within the 760-850 W peak power and 2300-2400 Hz PRF range while the minimum layer depth was predicted to be from the sample processed at the PRF of 2600 Hz and for 1326 W peak power.

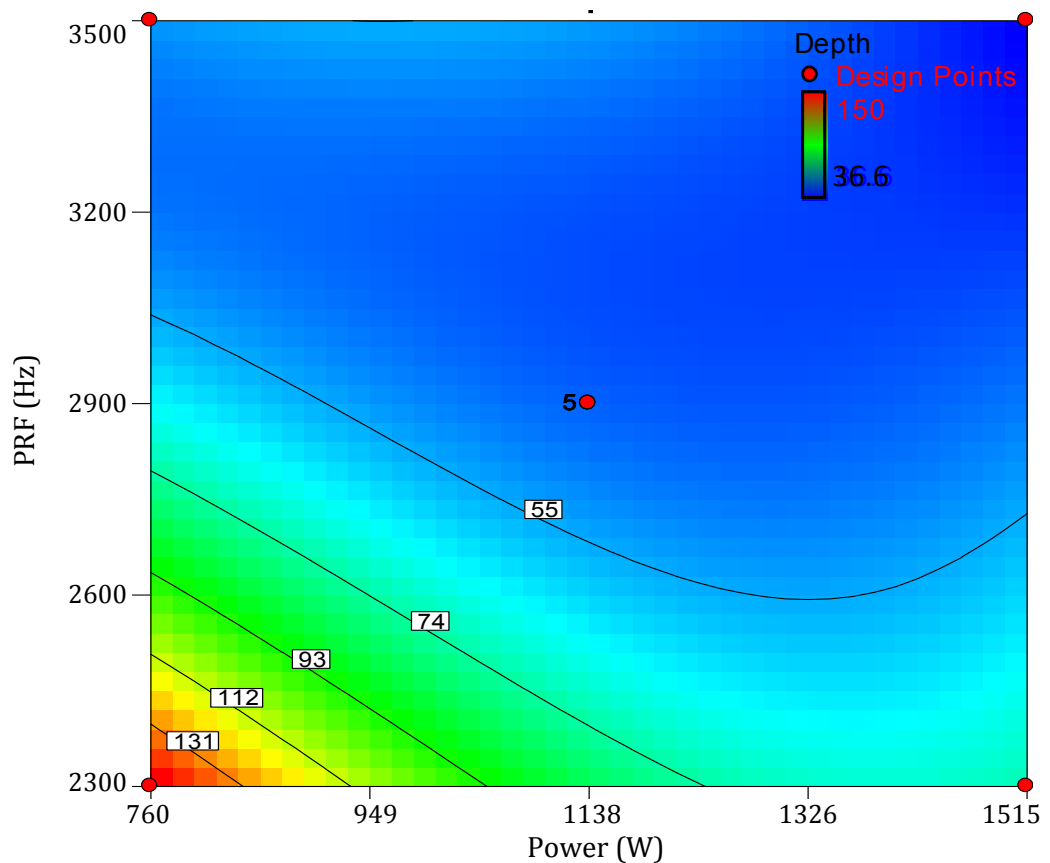


Figure 4.32: Contour plot for DOE5 samples (F1, F3, F15, F2 and F4) modified layer depth corresponds to PRF and power settings at 0% overlap.

Figure 4.33 shows the contour plot of modified layer depths corresponding to the overlap and power settings at constant PRF of 2300 Hz. At these parameter settings, the corresponding modified layer depth range was 72 to 144 μm . The modified layer depth increased with decreasing power and increasing overlap percentage. At less than 5% overlap and power range of 1075 to 1515 W, the measured depth was approximately 72 μm . The model also indicates that the maximum achievable modified layer depth at 2300 Hz PRF was approximately 144 μm . The maximum modified layer depths obtained at 2900

Hz and 3500 Hz PRF were 66 and 54 μm respectively (see Appendix E1). The depth range decreased at higher PRF settings due to corresponding lower pulse energies produced.

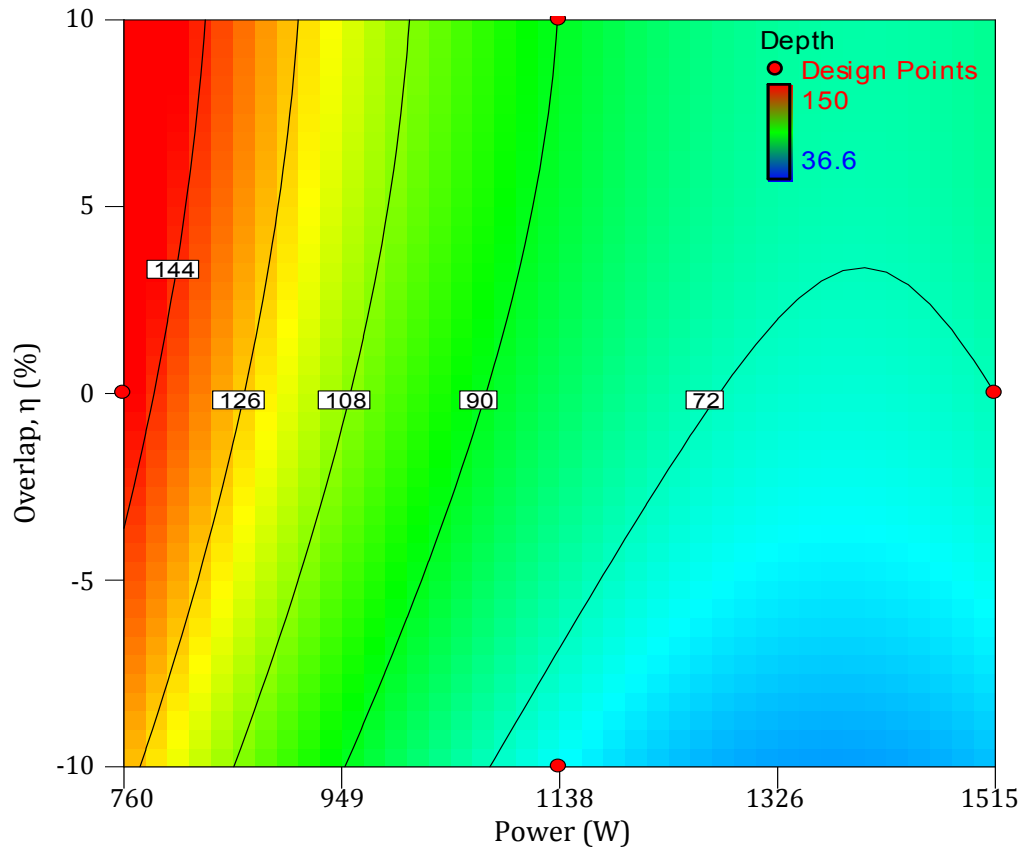


Figure 4.33: Contour plot of modified layer depths for DOE5 samples (F1, F9, F11 and F2) corresponding to overlap and power settings at 2300 Hz PRF.

Figure 4.34 shows the relationship between overlap and PRF at 760 W and the modified layer depth. The maximum and minimum modified layer depths were 140 and 54 μm respectively. The modified layer depth range measured at 1138 W power was from 42 to 80 μm whereas at 1515 W power, the range was between 36 and 69 μm (see Appendix E2(b)). At low power of 760 W, the depth range was higher as the duty cycle was 36% compared to 24% and 18% for 1138 W and 1515 W power settings respectively. Lower depth range measured at the high power settings was caused by the shorter pulse widths where the pulse width was limited by the duty cycle setting.

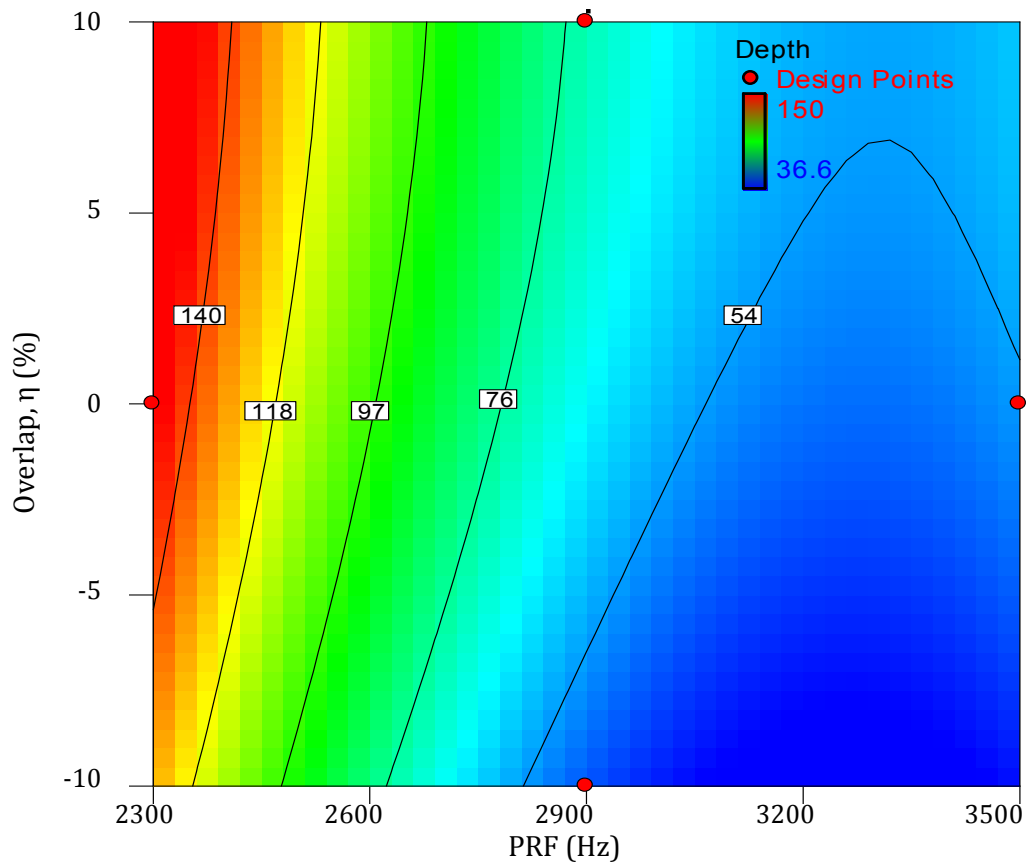


Figure 4.34: Contour plot of modified layer depths for DOE5 samples (F1, F5, F7 and F3) corresponding to overlap and PRF settings at 760 W peak power.

(b) Hardness Properties

The variance analysis for hardness response is tabulated in Table 4.11 where a quadratic model fit was used. The model F-value of 67.90, with p-value less than 0.0001, indicates the model is significant. In this model the terms B, C, AB, AC, BC, A² and C² were significant. Peak power (A) and second order of PRF (B²) were not significant. The predicted R² and adjusted R² were 95.06% and 97.41% respectively. Adequate signal precision of 32.65 was revealed from the model. The final response surface equation for the quadratic model of micro-hardness is shown in Equation 4.3.

Table 4.11: ANOVA results for hardness properties response using quadratic model.

Source	Sum of squares	df	Mean square	F value at 95% CI	p-value Prob > F	Remarks	
Model	29809.02	9	3312.11	67.90	< 0.0001	significant	
A-Power	4.50	1	4.50	0.092	0.7702		
B-PRF	15225.13	1	15225.13	312.13	< 0.0001		
C-Overlaps	4950.13	1	4950.13	101.48	< 0.0001		
AB	1260.25	1	1260.25	25.84	0.0014		
AC	5402.25	1	5402.25	110.75	< 0.0001		
BC	1681.00	1	1681.00	34.46	0.0006		
A ²	637.01	1	637.01	13.06	0.0086		
B ²	10.12	1	10.12	0.21	0.6626		
C ²	706.12	1	706.12	14.48	0.0067		
Residual	341.45	7	48.78				
Lack of Fit	66.25	3	22.08	0.32	0.8112		not significant
Pure Error	275.20	4	68.80				
Cor Total	30150.47	16					
	Std. Dev.	6.98	R ²	0.9887			
	Mean	831.82	Adjusted R ²	0.9741			
	C.V.%	0.84	Predicted R ²	0.9506			
	PRESS	1490.0	Adequate Precision	32.647			
		0					

*Predicted residual error of sum of squares (PRESS)

Micro-hardness

$$= 831.40 - 0.75A - 43.63B + 24.88C - 17.75AB - 36.75AC + 20.50BC + 12.30A^2 + 1.55B^2 - 12.95C^2 \quad \text{Equation 4.3}$$

Figure 4.35 shows the normal probability plot of the residuals for hardness properties with studentized residuals fall in a straight line. The observed values were compared with the predicted values calculated from the model where the regression model fitted well with the observed values as shown in Figure 4.36.

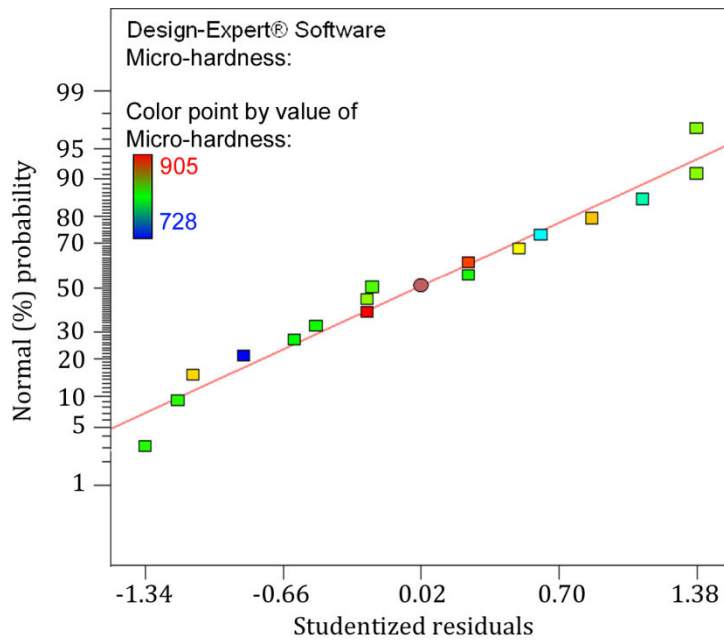


Figure 4.35: Normal probability plot of the studentized residuals for hardness properties response.

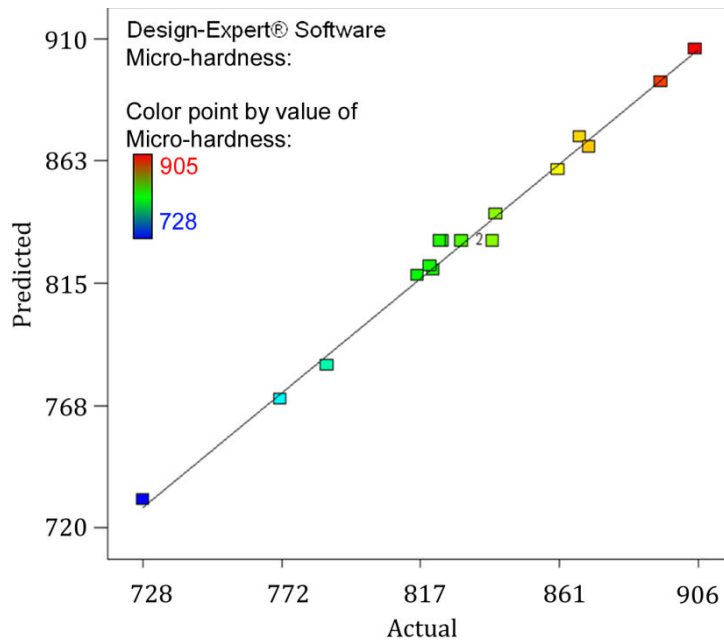


Figure 4.36 Predicted against actual plot for hardness properties response.

The hardness properties of DOE5 samples at different parameter setting are shown by contour graphs in Figure 4.37, Figure 4.38 and Figure 4.39. Figure 4.37 indicates the relationship of PRF and power with hardness at minus 10% overlap. The maximum hardness achieved was 892 HV_{0.1} while the minimum was 758 HV_{0.1}. Hardness values increased as the power increased and PRF decreased. The maximum hardness range decreased with increasing overlap. At 0% overlap, the hardness range was between 803

and 885 HV_{0.1}, see Appendix E3(a) with maximum measurement recorded at the high power setting of 1515 W and low PRF of 2300 Hz. In samples processed at 10% overlap, the maximum hardness of 880 HV_{0.1} measured was at the low power setting of 760 W and the minimum hardness of 799 HV_{0.1} measured at the high power setting of 1515 W, see Appendix E3(b).

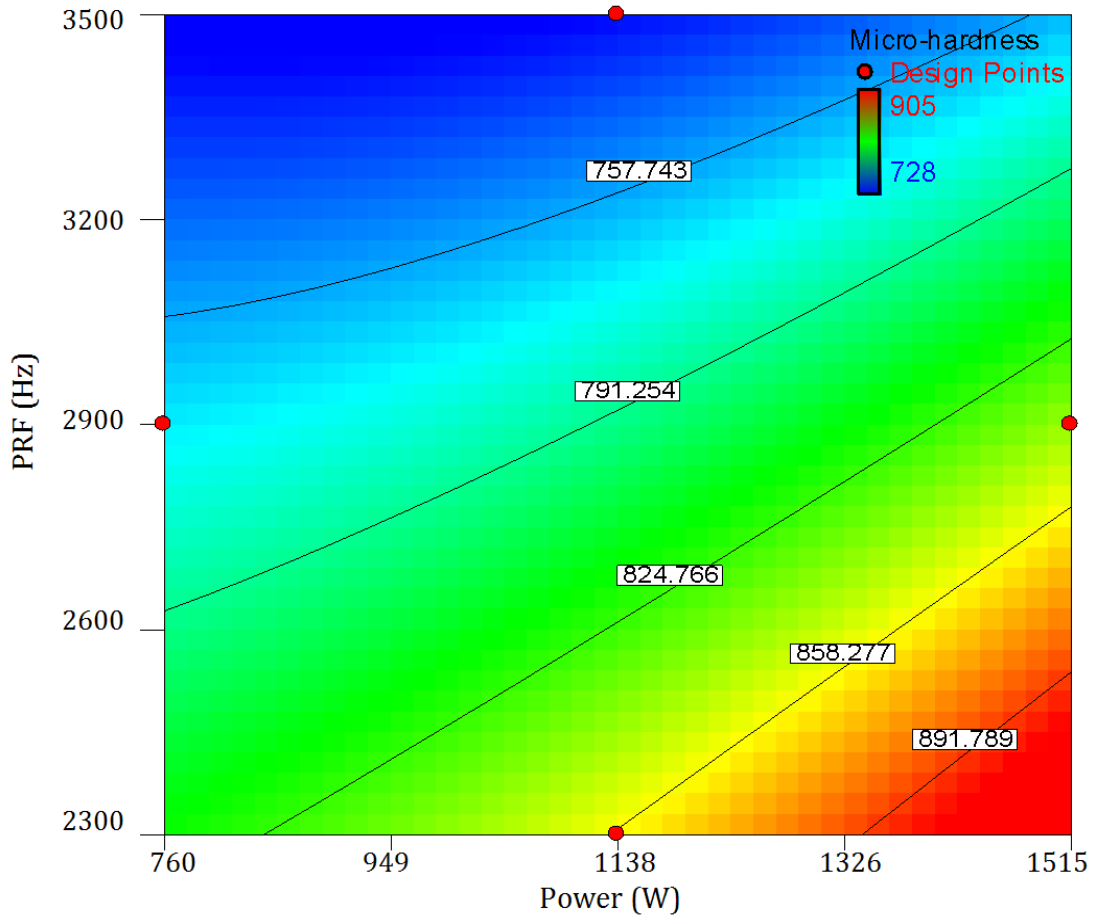


Figure 4.37: Contour plot of PRF and power effect on hardness at minus 10% overlap.
Design points shown are for sample F5, F9, F10 and F6.

The effect of overlap and power on hardness properties investigated at constant 2300 Hz PRF setting is shown in contour plot Figure 4.38. The maximum hardness is recorded at low PRF of 2300 Hz in the region of 907 HV_{0.1}. A hardness of 892 HV_{0.1} was measured between minus 10% and 0% overlap with power settings between 1420 W and 1515 W. The maximum hardness properties measured at 2900 and 3500 Hz were 873 and 862 HV_{0.1} respectively (see Appendix E4).

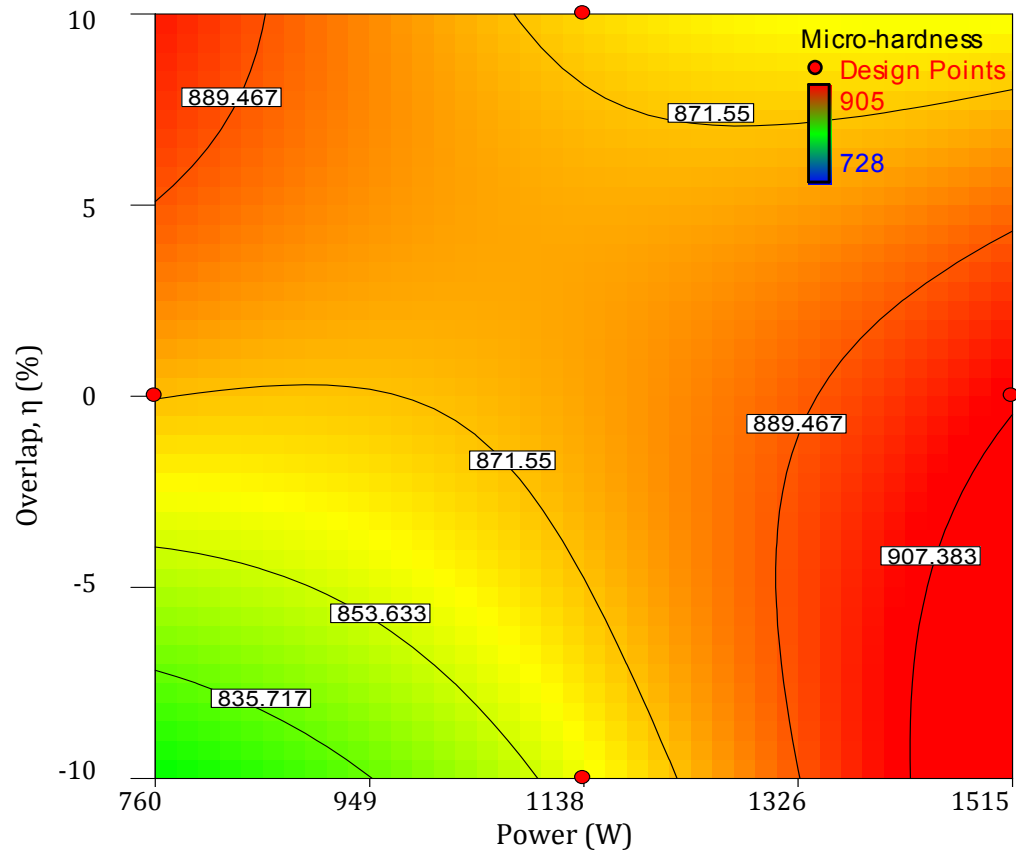


Figure 4.38: Contour plot of overlap and power effect on hardness at 2300 Hz PRF. Design points shown are for samples F1, F9, F11 and F2.

Investigation on overlap and PRF effect on hardness at 1515 W is presented in Figure 4.39. The maximum hardness of 898 HV_{0.1} was measured at low PRF and overlap settings. At highest PRF, the measured hardness was 789 HV_{0.1}. The maximum hardness decreased to 853 HV_{0.1} at 1138 W power, see Appendix E5(b).

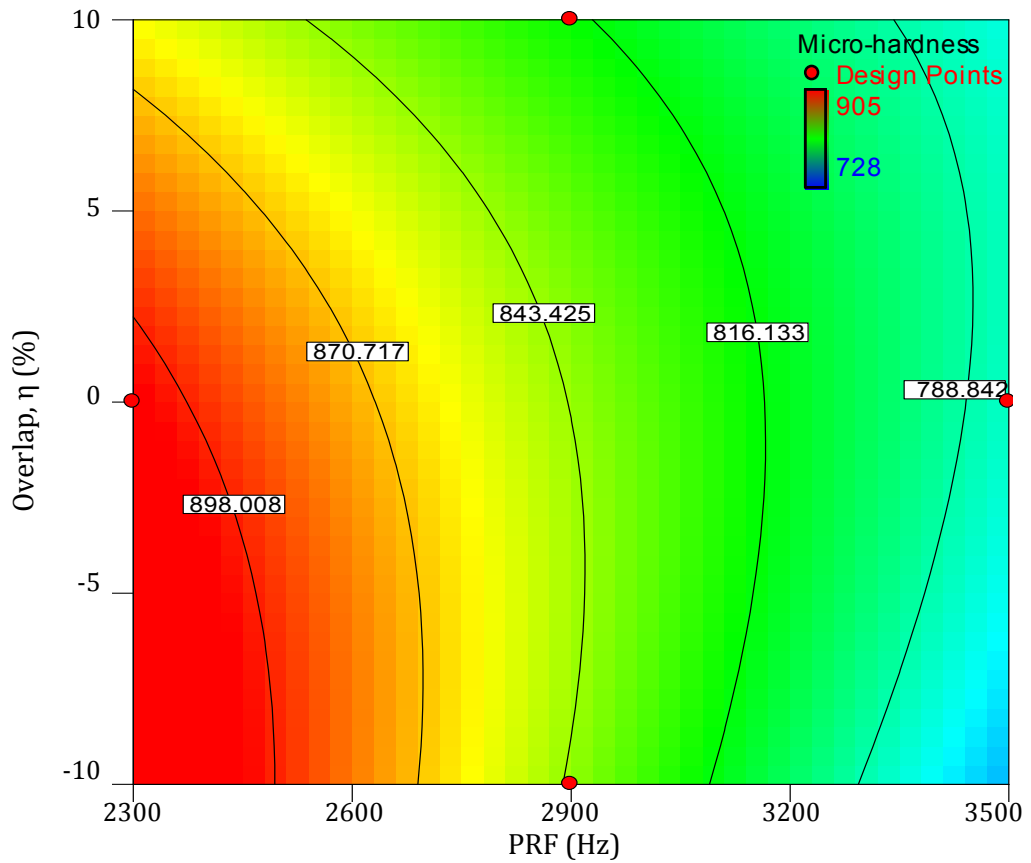


Figure 4.39: Contour plot of overlap and PRF effect on hardness at 1515 W power. Design points shown are for samples F2, F6, F8 and F4.

(c) Surface Roughness

In Table 4.12, the variance analysis for surface roughness response with cubic model is presented. The model F-value of 244.95 and p-value of 0.0001 imply the model is significant with related terms of A, B, AB, A^2 , B^2 , C^2 , A^2B and AB^2 . The overlap (C) and second order of PRF (B^2) were not significant in the model. The predicted R^2 and adjusted R^2 were 99.59% and 99.19% respectively. The final response surface equation for the cubic model of surface roughness is given by Equation 4.4.

Table 4.12: ANOVA results for surface roughness response using cubic model (after stepwise elimination).

Source	Sum of Squares	df	Mean Square	F Value	p-value Prob > F	Remarks
Model	365.94	8	45.74	244.95	< 0.0001	significant
A-Power	5.59	1	5.59	29.93	0.0006	
B-PRF	2.74	1	2.74	14.68	0.0050	
AB	76.28	1	76.28	408.50	< 0.0001	
A ²	47.72	1	47.72	255.55	< 0.0001	
B ²	12.98	1	12.98	69.48	< 0.0001	
C ²	8.92	1	8.92	47.79	0.0001	
A ² B	50.51	1	50.51	270.48	< 0.0001	
AB ²	19.81	1	19.81	106.10	< 0.0001	
Residual	1.49	8	0.19			
Lack of Fit	0.95	4	0.24	1.76	0.2984	not significant
Pure Error	0.54	4	0.14			
Cor Total	367.43	16				
	Std. Dev.	0.43		R ²	0.9959	
	Mean	4.45		Adjusted R ²	0.9919	
	C.V. %	9.70		Predicted R ²	N/A	
				Adequate Precision	65.009	

Surface roughness

$$= 2.73 - 1.18A - 0.83B + 4.37AB + 3.37A^2 + 1.76B^2 - 1.46C^2 - 5.03A^2B - 3.15AB^2 \quad \text{Equation 4.4}$$

Figure 4.40 shows the normal probability plot of the residuals for surface roughness response where studentized residuals fall in a straight line. The observed values were compared with the predicted values calculated from the model where the regression model fitted well with the observed values as shown in Figure 4.41.

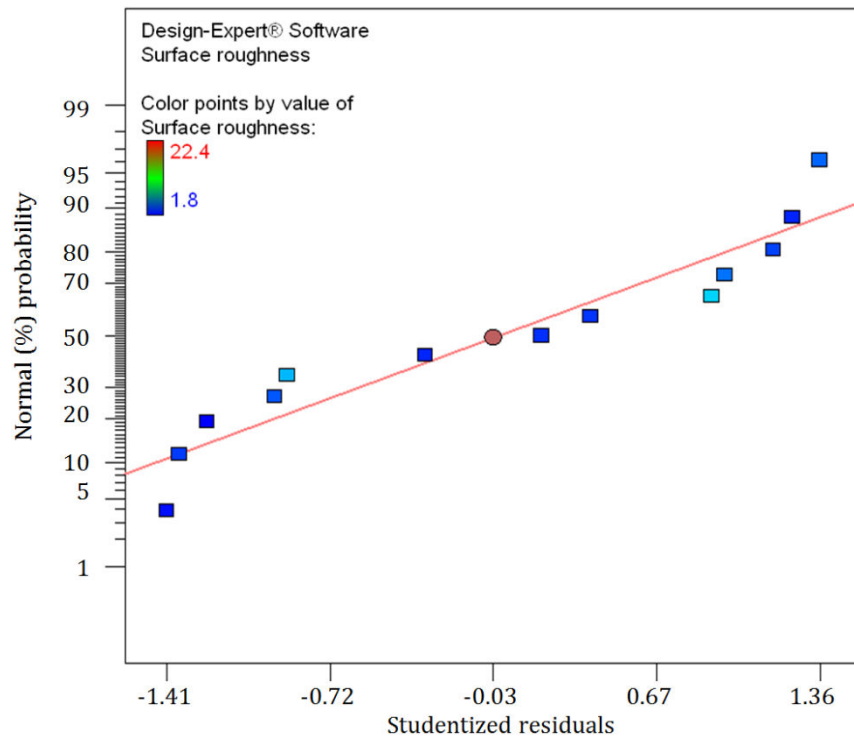


Figure 4.40: Normal probability plot of the studentized residuals for surface roughness response.

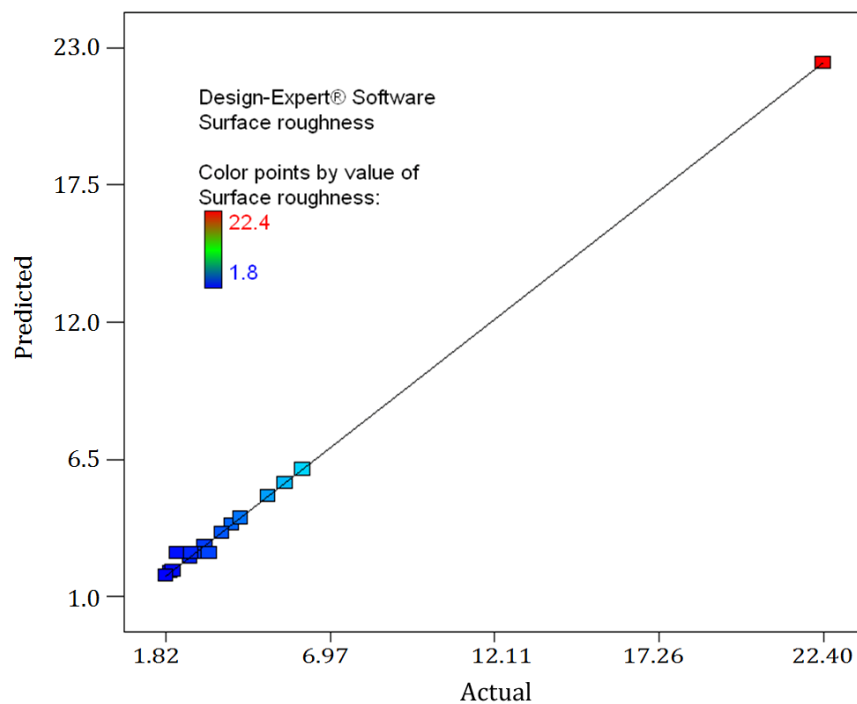


Figure 4.41: Predicted against actual plot for surface roughness response.

The average surface roughness is given in Appendix E6 with four measurements for each sample. There were 13 samples measured with a R_a of 5.0 μm and less. The minimum R_a of

1.8 μm was measured at minus 10 % overlap, 1138 W peak power and 3500 Hz PRF (see Appendix E6, sample F10).

In the reduced model, a significant interaction term was that between PRF and the peak power. The average surface roughness, R_a , measured from laser modified samples was plotted on a contour graph corresponding to peak power and PRF settings at minus 10 % overlap as shown in Figure 4.42. The R_a ranged mostly between 3.6 and 17.7 μm as shown in Figure 4.42. At low power of 760 W, the R_a values were as high as 17.7 μm due to prolonged laser-material interaction time which increased the molten pool thickness. The lowest R_a measured from the model at 0% and 10% overlap was respectively 5.4 and 3.7 μm (see Appendix E7).

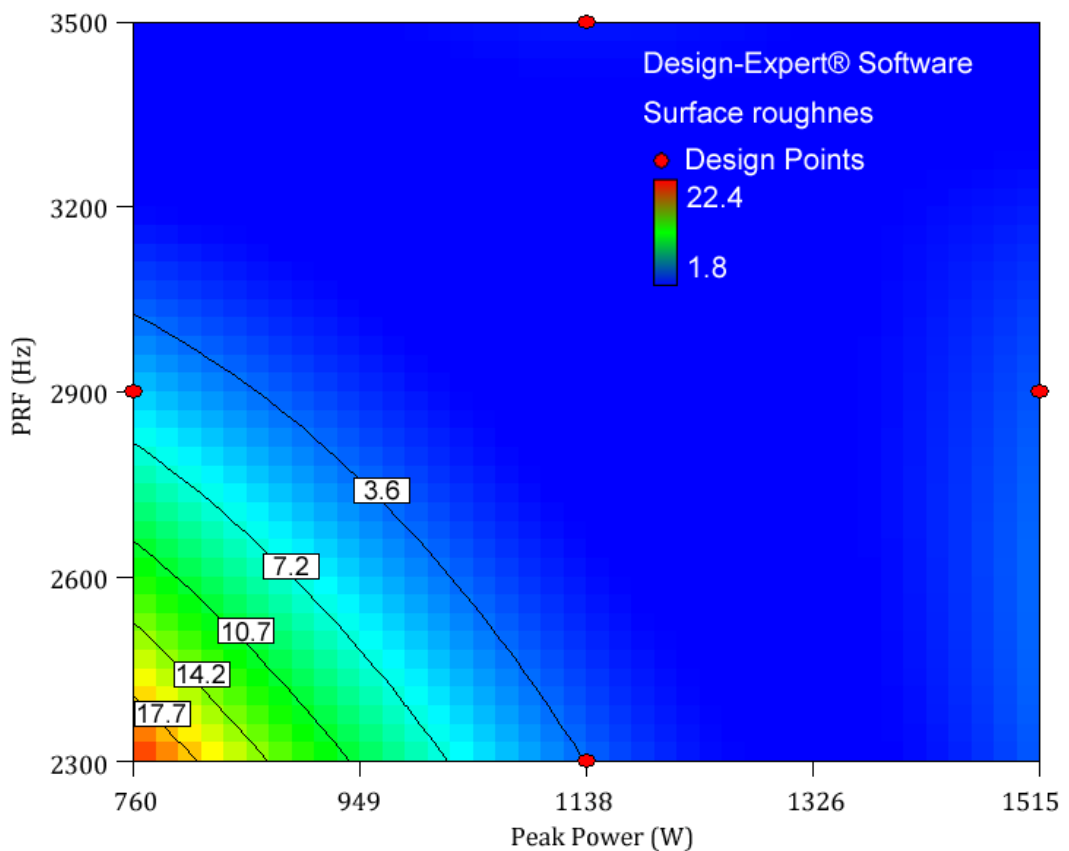


Figure 4.42: Contour plot of PRF, peak power and surface roughness relationship at minus 10% overlap. Design points are shown for samples F5, F9, F10 and F6.

The effect of overlap and power settings on surface roughness at the high PRF setting of 3500 Hz is shown by Figure 4.43. This interaction was acquired from the initial model. The resulting R_a range was between 0.7 and 3.1 μm . However, at the lower PRF of 2300 Hz, the R_a values increased where the minimum measurement was at 4.7 μm and maximum was

18.9 μm (see Appendix E8 (a)). Samples processed at 2900 Hz exhibited R_a values in the range of 1.9 to 6.2 μm , see Appendix E8 (b).

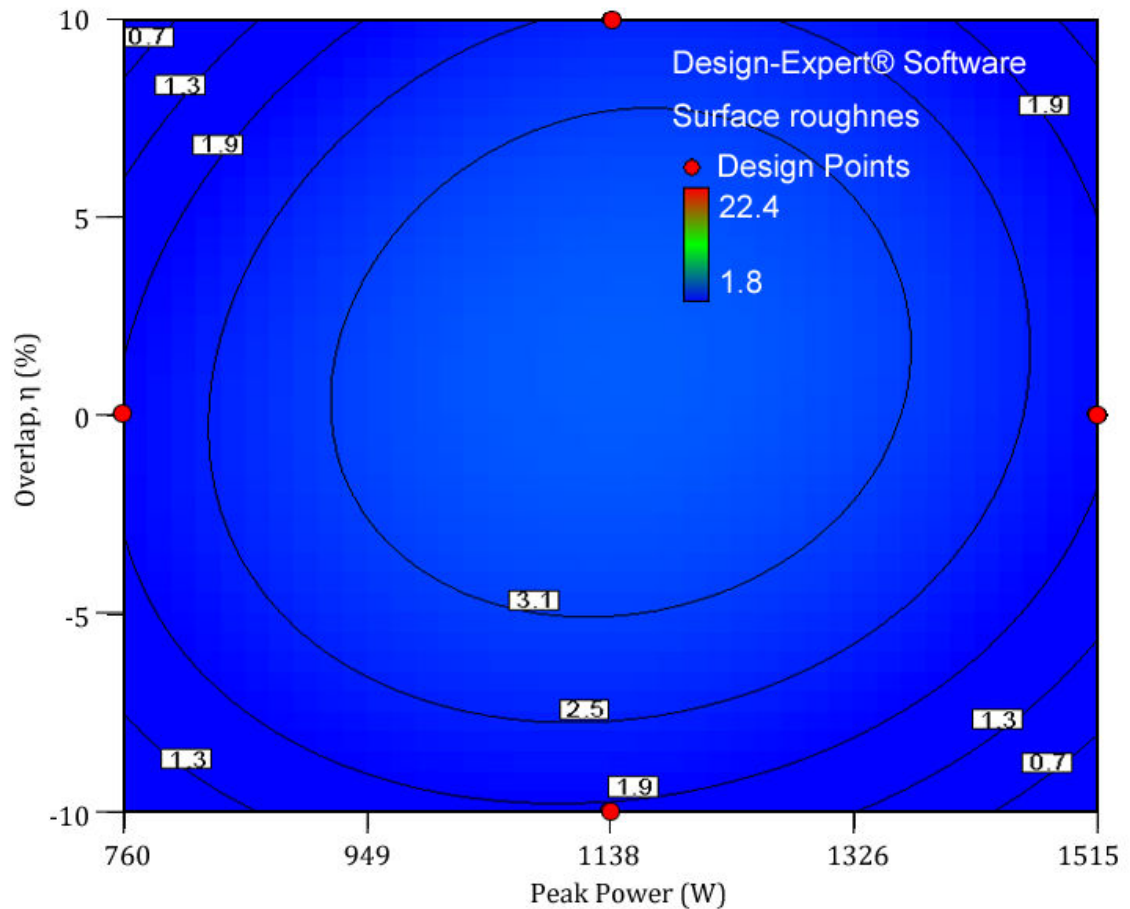


Figure 4.43: Contour plot of the insignificant effect of overlap and peak power on surface roughness response at 3500 Hz PRF. Design points are shown for samples F3, F10, F12 and F4.

Design Optimisation

Process optimisation was calculated within the constraints and range given in Table 4.13. Peak power, PRF and overlap ranges were as outlined between 760 and 1387 W; 2300 and 3500 Hz; and minus 10 and plus 10% respectively. Design solutions calculated are given in Table 4.14 where the optimised parameters are within the range of experimentally achieved hardness and modified surface depth results, but with a goal of minimising surface roughness. The highest and lowest desirability factors obtained were 1.000 and 0.940. The minimum surface roughness predicted was 1.3 μm R_a with 52 and 53 μm modified surface depth and hardness of 842 and 843 $\text{HV}_{0.1}$ (solution 22 and 14). The maximum achievable predicted modified layer depth was 70 μm , with 1.7 μm surface roughness and 857 $\text{HV}_{0.1}$ hardness (solution 24). The average hardness, surface roughness

and modified layer depth achieved from all of the 30 solutions were 861 HV_{0.1}, 1.7 µm and 53 µm.

Table 4.13: Constraints in design optimisation with hardness and modified layer depth were in range and surface roughness was minimised

Name	Goal	Lower Limit	Upper Limit	Importance
Power (W)	is in range	760	1515	3
PRF (Hz)	is in range	2300	3500	3
Overlap (%)	is in range	0.9	1.1	3
Hardness (HV0.1)	is in range	728	905	3
Surface roughness (µm)	minimize	1.82	3.50	5
Modified layer depth (µm)	is in range	50	150	3

Table 4.14: Design solutions in DOE5 to minimise surface roughness with range of hardness and modified layer depth.

Solution	Power (W)	PRF (Hz)	η (%)	Micro-hardness (HV) _{0.1}	Surface roughness, R _a (µm)	Modified layer depth (µm)	Desirability
1	760.06	3499.85	1.03	844.28	1.8	56	1.000
2	998.50	3386.91	1.09	842.89	1.8	54	1.000
3	1153.85	2844.67	1.09	844.96	1.5	53	1.000
4	865.99	3222.09	1.09	867.97	1.7	54	1.000
5	947.42	3144.69	1.09	857.72	1.7	53	1.000
6	834.07	3488.00	1.09	865.51	1.5	58	1.000
7	766.33	3436.84	1.05	855.28	1.8	55	1.000
8	1290.50	2759.99	1.10	838.91	1.4	54	1.000
9	1260.99	2582.08	1.09	851.70	1.8	62	1.000
10	989.92	3233.14	1.08	846.44	1.8	51	1.000
11	1004.73	3196.93	1.09	847.59	1.6	51	1.000
12	1284.79	2314.26	0.90	880.31	1.8	56	1.000
13	1165.57	2953.78	1.08	838.99	1.7	50	1.000
14	1167.34	2856.45	1.10	843.12	1.3	53	1.000
15	1306.15	2871.46	1.09	833.92	1.8	50	1.000
16	1277.15	2334.08	0.90	876.28	1.7	54	1.000
17	827.81	3457.65	1.07	860.26	1.7	57	1.000
18	1016.44	3230.86	1.09	844.58	1.7	51	1.000
19	1284.50	2704.33	1.09	842.70	1.5	56	1.000
20	1305.27	2345.22	0.91	880.66	1.8	54	1.000
21	1312.05	2471.26	1.10	853.40	1.6	66	1.000
22	1167.12	2889.78	1.10	841.80	1.3	52	1.000
23	1289.27	2399.69	0.90	871.36	1.7	51	1.000
24	1335.82	2390.93	1.10	856.84	1.7	70	1.000
25	1214.12	2915.52	1.09	837.22	1.5	50	1.000
26	1356.25	2403.22	0.90	881.86	1.8	50	1.000
27	1337.53	2784.47	1.10	834.43	1.6	53	1.000
28	1310.36	2315.18	0.91	885.02	1.8	56	1.000
29	760.00	3500.00	0.98	804.44	1.9	51	0.942
30	1215.96	2441.27	0.90	854.33	1.9	50	0.940

The design goal was next set as to maximise the modified surface depth and hardness and to minimise the surface roughness. The parameter limits and importance levels in Table 4.15 were set at the same values and levels as in Table 4.13. Changing the parameter goals resulted in new desirable solutions. From a set of 17 design solutions found, the highest and lowest desirability factors obtained were 0.661 and 0.427 respectively, see Table 4.16. Comparing to the design solutions in Table 4.14, a lower surface roughness of 0.7 μm R_a was predicted with higher modified layer depth and hardness of 58 μm and 886 $\text{HV}_{0.1}$ respectively (solution 10). The maximum achievable modified layer depth of 79 μm was also higher than was achieved in Table 4.14 with 1.8 μm surface roughness and 863 $\text{HV}_{0.1}$ hardness (solution 1). The average hardness, surface roughness and modified layer depth achieved from all the 17 solutions were 876 $\text{HV}_{0.1}$, 1.4 μm and 66 μm . Changing the parameter importance level reduced the number of solutions and desirable factor range, see Appendix F1 and F2.

Table 4.15: Constraints in design optimisation with hardness and modified layer depth were maximised and surface roughness was minimised.

Name	Goal	Lower Limit	Upper Limit	Importance
Power (W)	is in range	760	1515	3
PRF (Hz)	is in range	2300	3500	3
Overlap (%)	is in range	0.9	1.1	3
Hardness ($\text{HV}_{0.1}$)	maximise	728	905	3
Surface roughness (μm)	minimise	1.82	3.50	5
Modified layer depth (μm)	maximise	50	150	3

Table 4.16: Design solutions in DOE5 to minimise surface roughness with maximising hardness and modified layer depth.

Solution	Power (W)	PRF (Hz)	η (%)	Hardness ($\text{HV}_{0.1}$)	Surface roughness, R_a (μm)	Modified layer depth (μm)	Desirability
1	1272.43	2300.00	1.10	862.52	1.8	79	0.661
2	1278.88	2300.00	1.10	862.87	1.8	78	0.659
3	1287.60	2300.00	1.10	863.28	1.8	78	0.657
4	1291.39	2300.00	1.10	863.44	1.8	78	0.656
5	1307.90	2300.00	1.09	864.65	1.9	77	0.643
6	1335.24	2300.38	1.10	861.01	1.6	76	0.641
7	1366.32	2300.00	1.09	862.87	1.8	75	0.637
8	795.03	3500.00	1.10	882.00	0.8	59	0.492
9	789.15	3500.00	1.10	883.21	0.8	58	0.492
10	777.92	3500.00	1.10	885.51	0.7	58	0.491
11	811.69	3499.56	1.10	878.60	0.9	59	0.491
12	798.16	3500.00	1.10	880.57	0.9	59	0.491
13	771.98	3500.00	1.09	882.52	0.8	58	0.487
14	1313.80	2300.00	0.91	888.29	1.9	57	0.463
15	760.00	3213.48	1.10	890.73	1.8	56	0.451
16	760.00	3354.42	1.10	889.94	0.9	55	0.427
17	760.00	3293.78	1.10	889.56	1.3	55	0.425

Validation of this design was not conducted as laser irradiance range produced a planar response surface with high repeatability within the low range used (0.12 and 0.26 MW/mm²). At this low range of irradiance, the effect of the laser parameters on surface was such that only surface melting took place. Therefore, the resulted model can be assumed to produce the expected properties within the investigated range.

4.2.6 EDXS Analysis

The chemical composition of H13 tool steel substrate analysed using EDXS is given in Table 4.17. In Table 4.17, ten elements were detected from the H13 tool steel substrate; carbon (C), silicon (Si), sulphur (S), vanadium (V), chromium (Cr), manganese (Mn), iron (Fe), nickel (Ni), copper (Cu) and molybdenum (Mo). Figure 4.44 shows the selected area in the H13 tool steel substrate used for compositional area analysis. The elements distribution in the selected area of the H13 tool steel substrate is shown by micrographs in Figure 4.45. The EDXS qualitative analysis spectrums of phases detected in the selected area is given in Figure 4.46.

Table 4.17: Chemical composition of the H13 tool steel substrate analysed from selected area.

Elements (wt.%)	C	Si	S	V	Cr	Mn	Fe	Ni	Cu	Mo
Spectrum	1.56	1.13	0.47	1.10	5.01	0.42	88.41	0.18	0.21	1.51

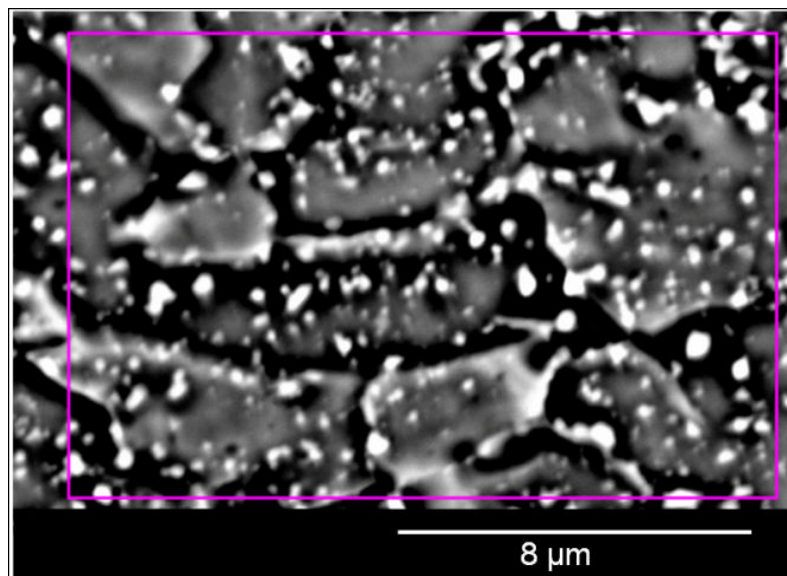


Figure 4.44: Selected area in H13 tool steel substrate.

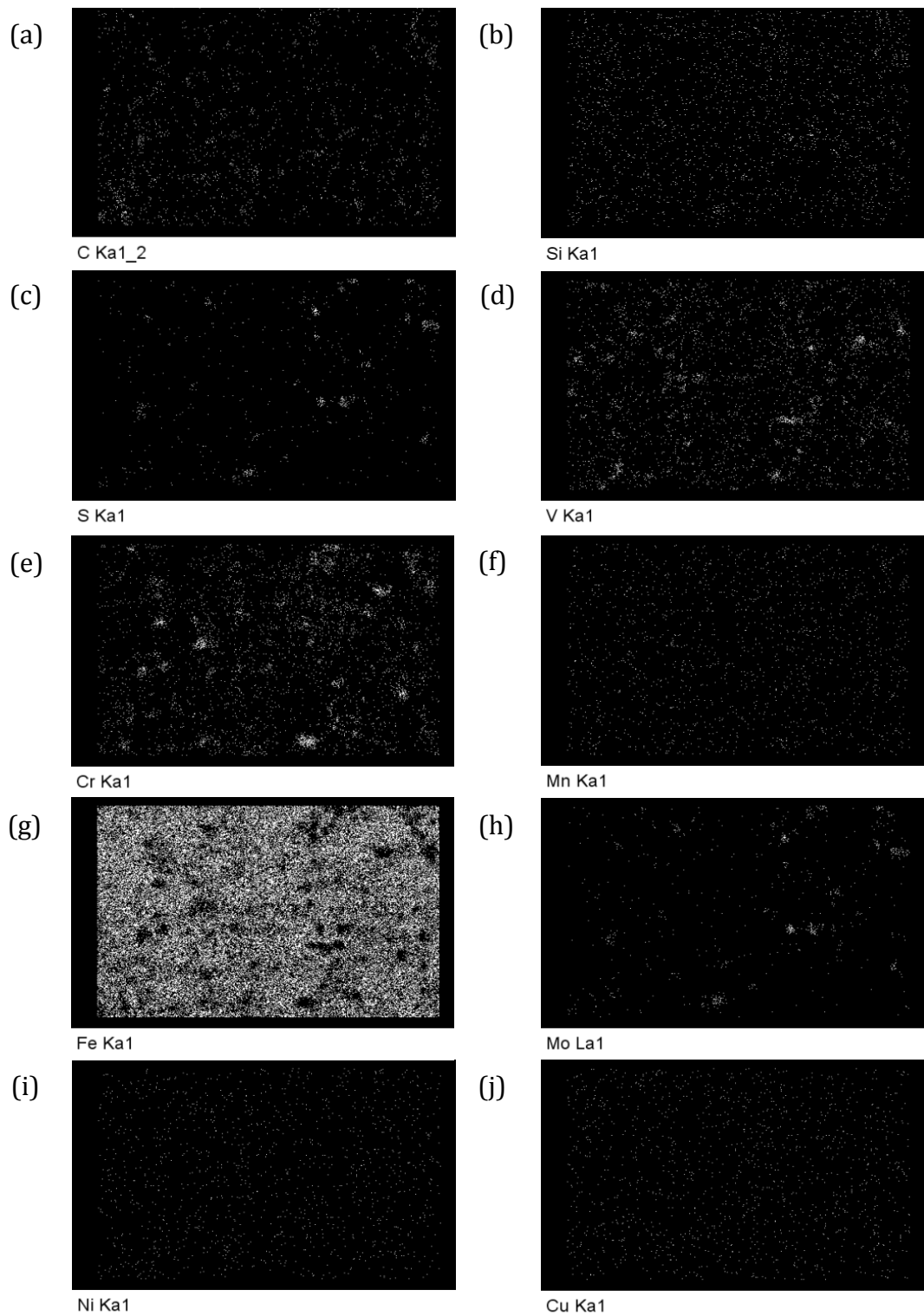


Figure 4.45: EDXS area analysis in H13 tool steel substrate with elements distribution (as-labeled).

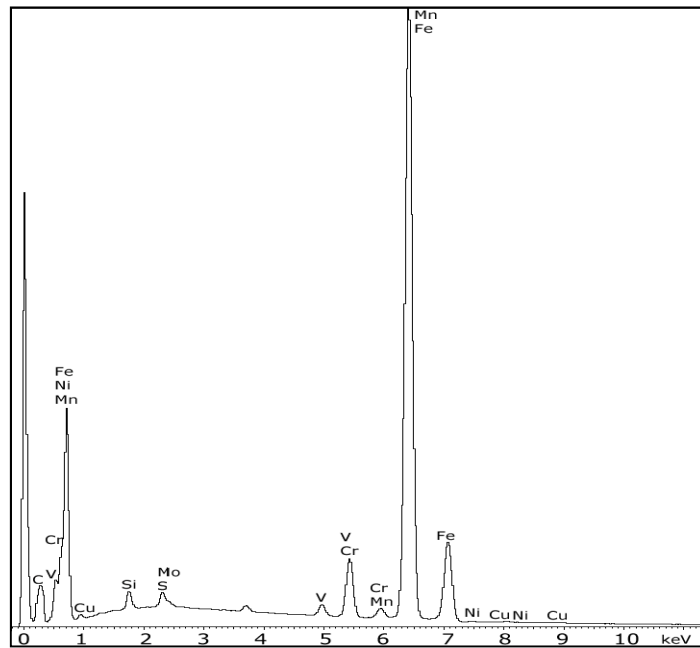


Figure 4.46: EDXS qualitative analysis spectrum of phases for H13 tool steel substrate.

The chemical composition of laser processed H13 tool steel samples was compared with the H13 tool steel substrate. The modified samples from DOE2 and DOE5 were analysed for their chemical composition. Table 4.18 shows the resulting analysis conducted for sample E8 (DOE2). The analysis for E8 sample was conducted using a single spectrum where the chemical composition was measured from the area selected as shown in Figure 4.47 (a). In Figure 4.47 (b) to (i), the presence of manganese (Mn), chromium (Cr), iron (Fe), nickel (Ni), molybdenum (Mo), silicon (Si), carbon (C) and sulphur (V) elements were seen as white shade in the selected area. From observation, distribution of elements like Ni, Mo and V resembled the grain boundaries geometries. A larger image of Ni distribution that shows its presence in grain boundaries is given in Figure 4.48. Figure 4.49 shows the spectrum of phases detected for sample E8.

Table 4.18: Chemical composition of sample E8 from selected area analysis.

Elements (wt.%)	C	Si	V	Cr	Mn	Fe	Ni	Mo
Spectrum	5.47	1.12	0.94	4.98	0.46	85.35	0.22	1.46

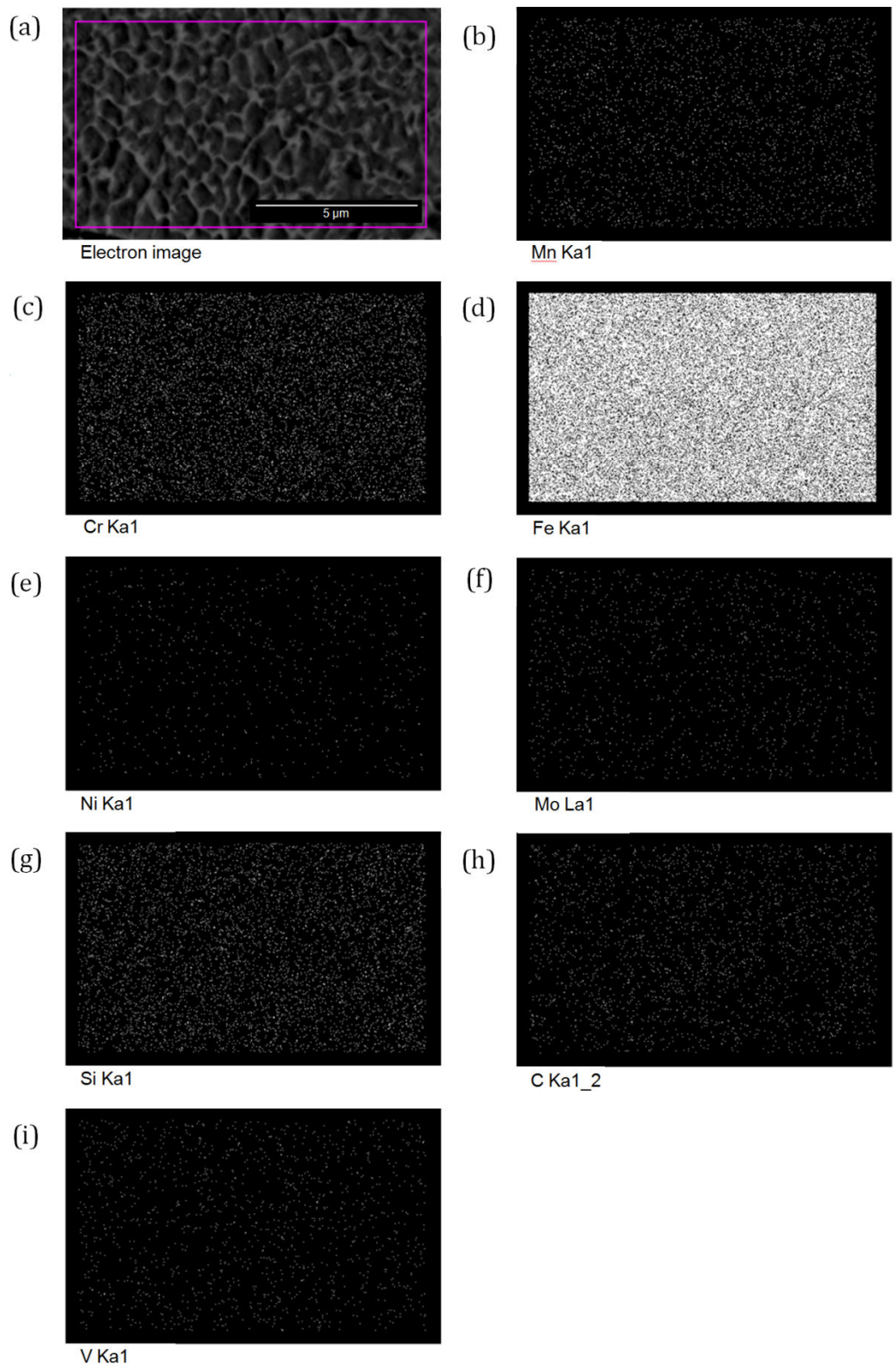


Figure 4.47: EDXS area analysis in sample E8 with elements distribution (as labeled).

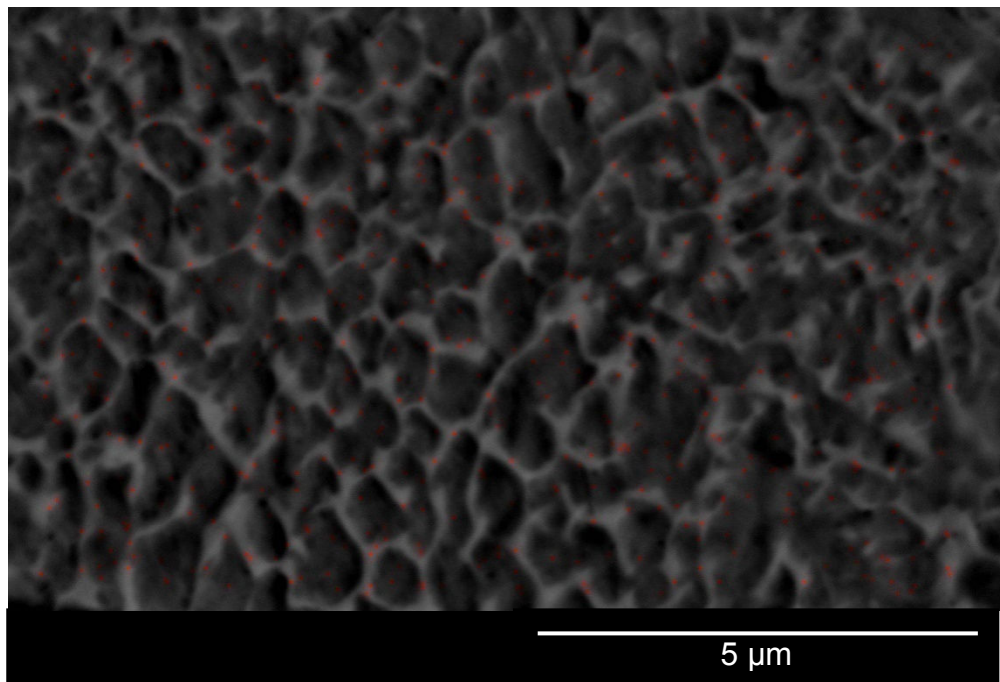


Figure 4.48: Nickel elements distribution in sample E8.

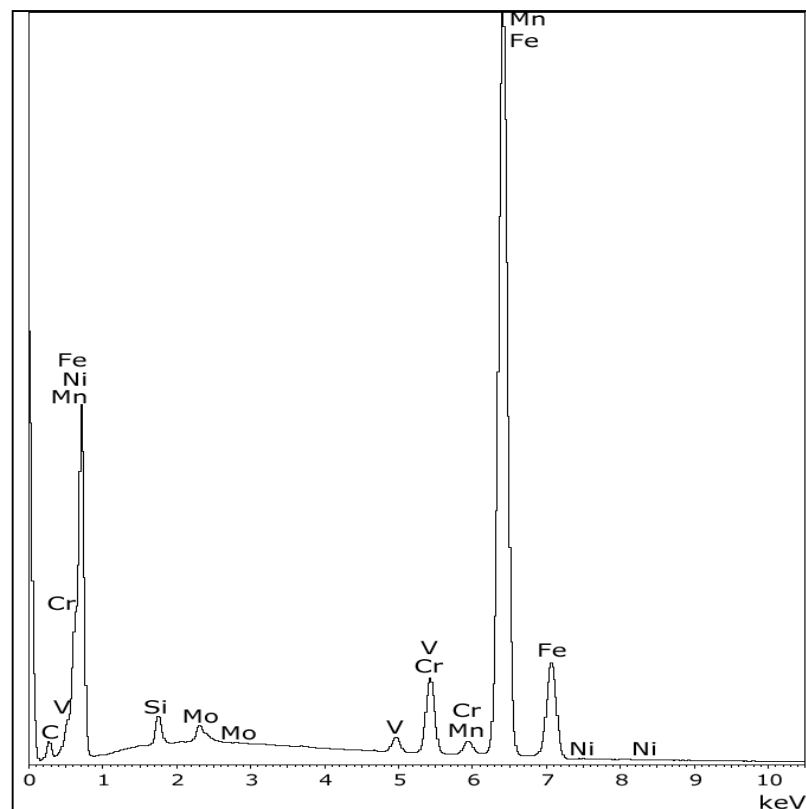


Figure 4.49: EDXS qualitative analysis spectrum of phases for sample E8.

Sample E15 and E27 were analysed using line spectra. The resulting chemical composition of the modified layers is given in Table 4.19. Figure 4.50 (a) and (b) show the measurements conducted in the modified layer of sample E27 and the resulting spectrum of phases detected respectively. The presence of eight elements in sample E27 was detected while in sample E15, nine elements were identified. In sample E15, the content of C was higher; while Cr content was lower when compared with sample E27. Cu was detected in sample E15 at 0.24 wt% which was absent in sample E8 and E27. In sample E8, Mo was detected at 1.46 wt%. Cr was recorded at is the highest level in sample E27 among the three samples. Variations of elements composition were observed in Table 4.19, where the samples were processed at different overlap, PRF and pulse energy. The maximum range of C in sample E15 was higher than the maximum level detected in sample E27.

Table 4.19: Chemical composition of modified layer in DOE2 samples cross section.

Sample		E15	E27
Processing parameters	η (%)	30	50
	PRF (Hz)	3810	4000
	E_p (J)	0.20	0.19
Elements (wt.%)	C	7.05-12.11	5.31-9.05
	Si	0.87-1.21	0.94-1.33
	S	0.35-0.44	0.35-0.89
	V	0.80-0.95	0.77-1.33
	Cr	4.59-4.93	4.44-6.23
	Mn	0.42-0.49	0.44-0.62
	Fe	81.19-84.99	82.85-86.77
	Ni	0.20-0.22	0.26-0.31
	Cu	0.24	-

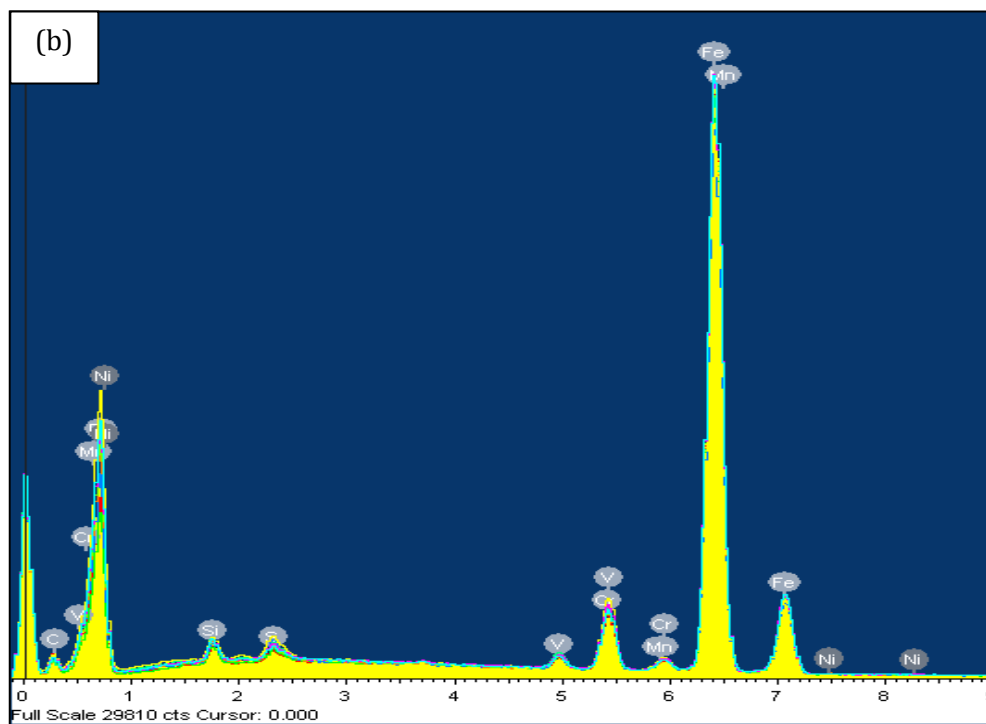
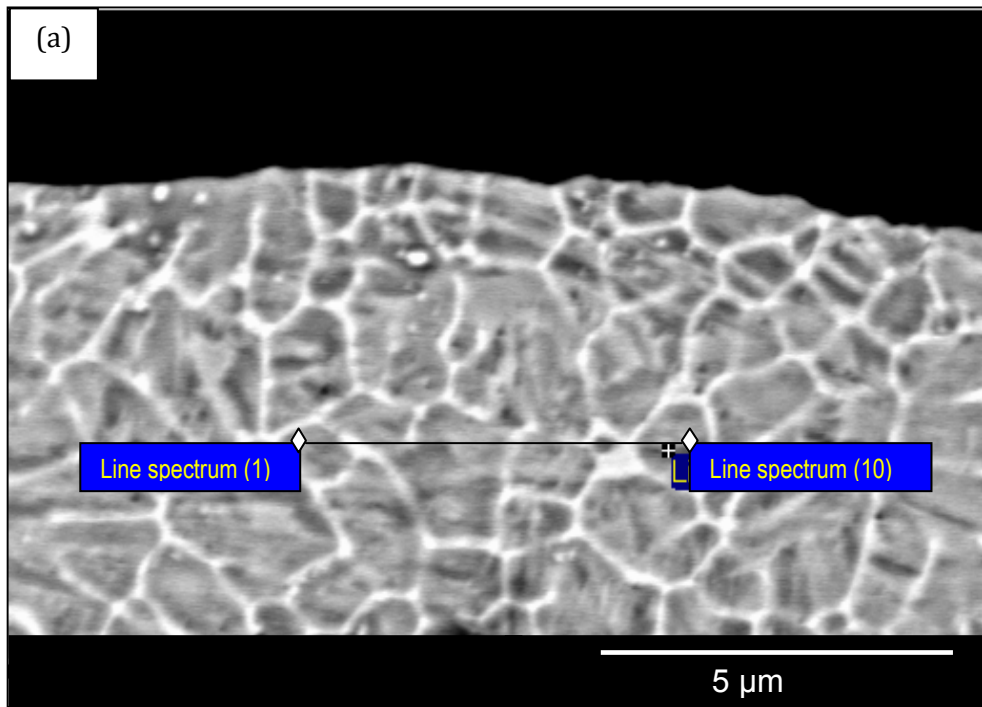


Figure 4.50: (a) Micrograph shows line spectrum measurements across sample E27 cross section and (b) EDXS qualitative spectrum analysis of phases indicates presence of primarily eight elements in sample E27.

From DOE5, four samples were analysed (F1, F11, F8 and F3) using line spectra. The chemical composition of each sample is given in Table 4.20. In F1 and F8 samples seven elements were detected, while eight elements were analysed in F11 and F3 samples. Micrograph in Figure 4.51 (a) shows eight line spectra across the modified layer and H13 tool steel substrate. EDXS qualitative analysis spectrums of phases in sample F11 is shown in Figure 4.51 (b) with C, V, Cr, Mn, Fe, Si, S and Mo detected. Two elements, Cu and Ni, were absent in these four samples. The processing parameter seemed to vary the elements composition where S was detected in sample F11 and F3 but was none in sample F1 and F8. Cr and Mo composition was the highest in sample F8 compared to other samples observed.

Table 4.20: Chemical composition comparison for DOE5 samples at different processing parameters.

Sample		F1	F11	F8	F3
Processing parameters	P _p (W)	760	1138	1515	760
	PRF (Hz)	2300	2300	2900	3500
	E _p (J)	0.12	0.12	0.10	0.08
	T _R (ms)	0.16	0.12	0.07	0.10
Elements (wt.%)	C	0.01-4.67	0.33-4.97	1.25	0.3-6.76
	Si	1.24-1.41	1.11-1.29	1.24-1.27	1.13-1.22
	S	-	0.48-0.52	-	0.49-0.50
	V	0.95-1.45	0.82-1.04	0.97-1.27	0.89-0.99
	Cr	4.98-5.53	4.99-5.44	5.27-6.23	4.69-5.26
	Mn	0.46-0.48	0.44-0.46	0.46-0.48	0.42-0.48
	Fe	87.35-89.72	87.15-91.03	88.58-92.02	85.80-90.90
	Mo	1.73-1.79	1.52	1.50-2.18	1.46

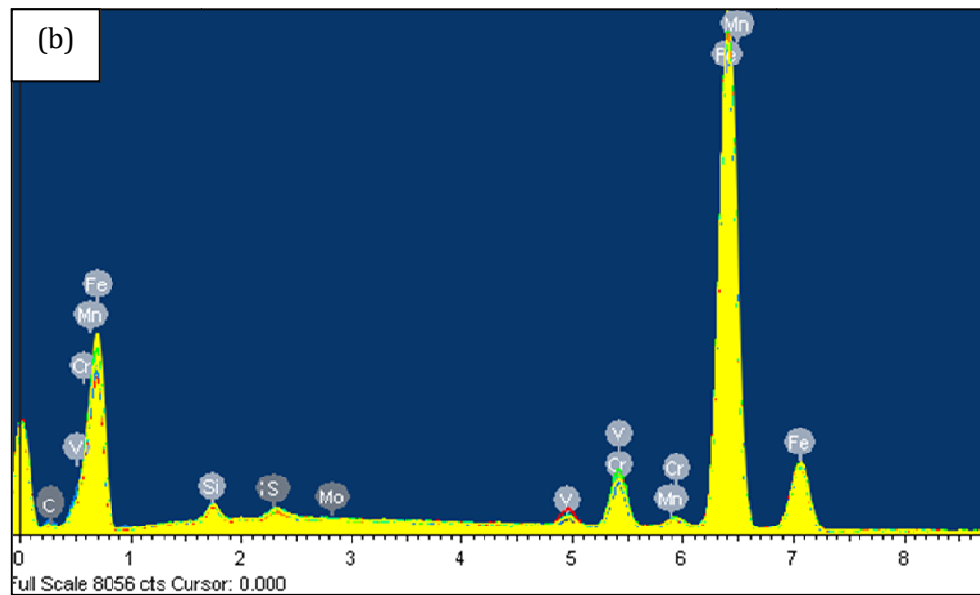
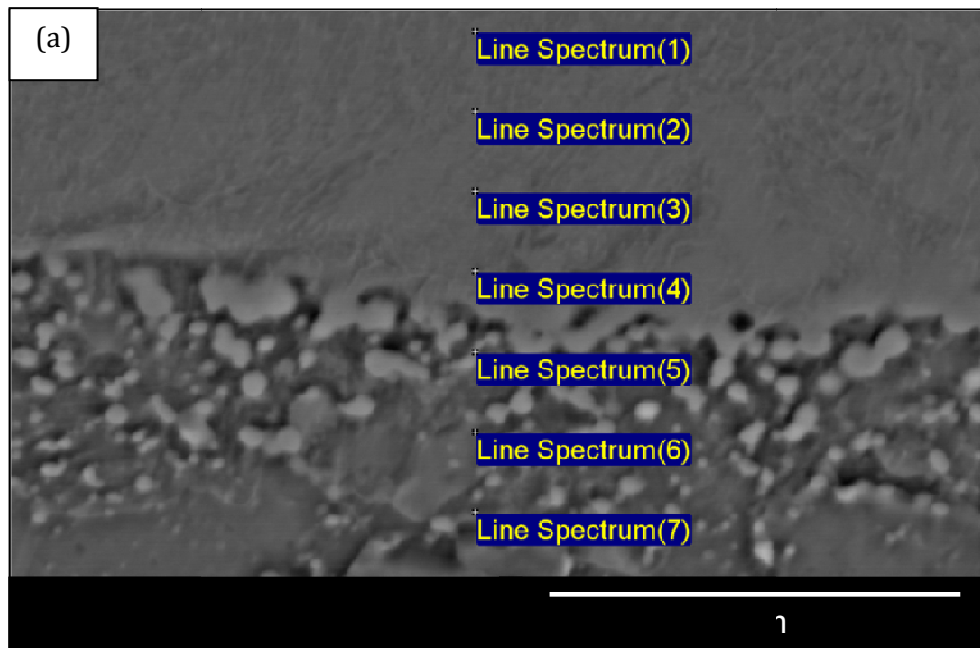


Figure 4.51: (a) Micrograph shows line spectrum measurements and (b) EDXS qualitative analysis spectrum of phases indicates presence of eight elements in sample F11 cross section.

4.2.7 XRD Analysis

The laser modified surface H13 was analysed for surface crystallinity and compared with the diffraction pattern of the as-received H13 steel. In Figure 4.52, the diffraction peaks of as-received H13 steel surface were characterised by distinct reflections of α -Fe (110), (200), (211) and (220) phase at 44.6°, 64.8°, 82.1° and 98.6° Bragg's angles (2 theta) respectively. The peaks intensity distribution was similar with the α -Fe phase (06-0696) peaks listed in the Joint Committee on Powder Diffraction Standards (JCPDS) database.

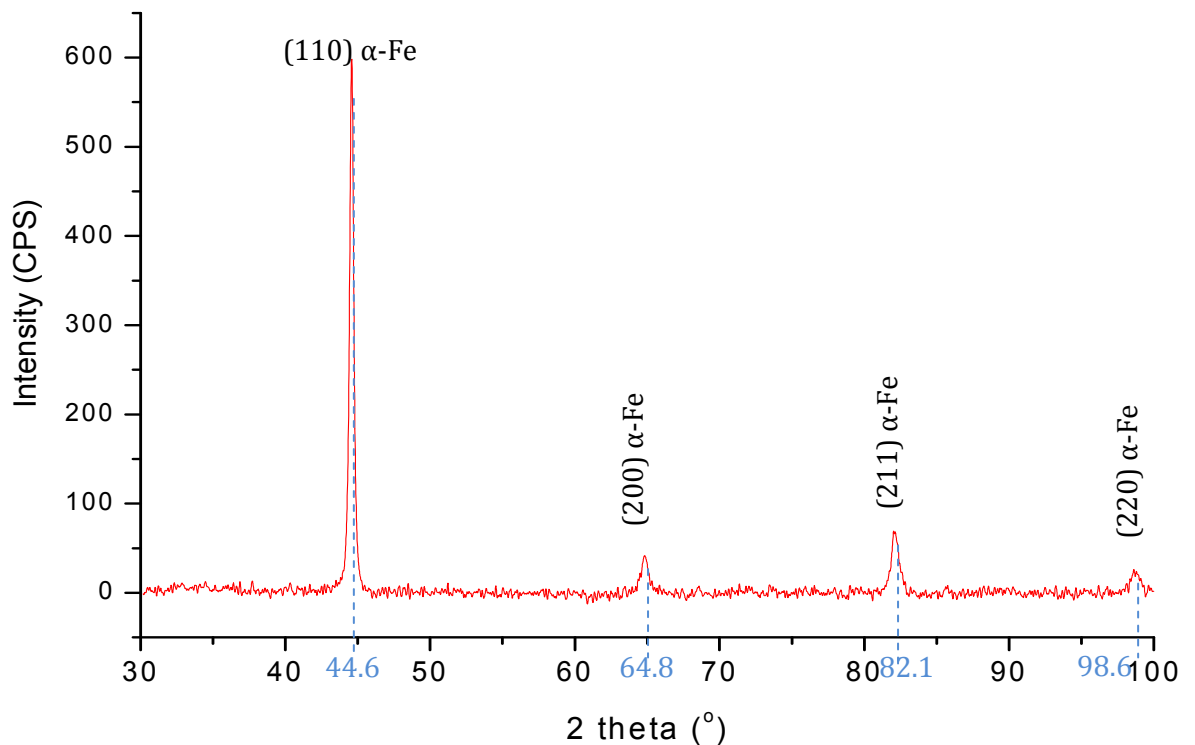


Figure 4.52: X-ray diffraction pattern of as received H13 tool steel.

The x-ray diffraction patterns produced by samples processed at 0.4 mm, 0.2 mm and 0.09 mm spot size are shown in Figure 4.53, Figure 4.54 and Figure 4.55 respectively. The peaks detected from Figure 4.53 (a) were (211) martensite, (110) and (200) α -Fe. Whereas in Figure 4.53 (b), the (200) α -Fe peak became less distinct and suppressed. At 0.4 mm spot size, the (110) α -Fe phase peak in Figure 4.53 (a) decreased as much as 66 % compared to the as-received H13 steel surface peak reflection, see Figure 4.52. Presence of (211) martensite peak was detected at 35.45° Bragg's angle, see Figure 4.53. The (211) martensite structure is body-centred-cubic in contrast with as-quenched martensite body-centred-tetragonal structure.

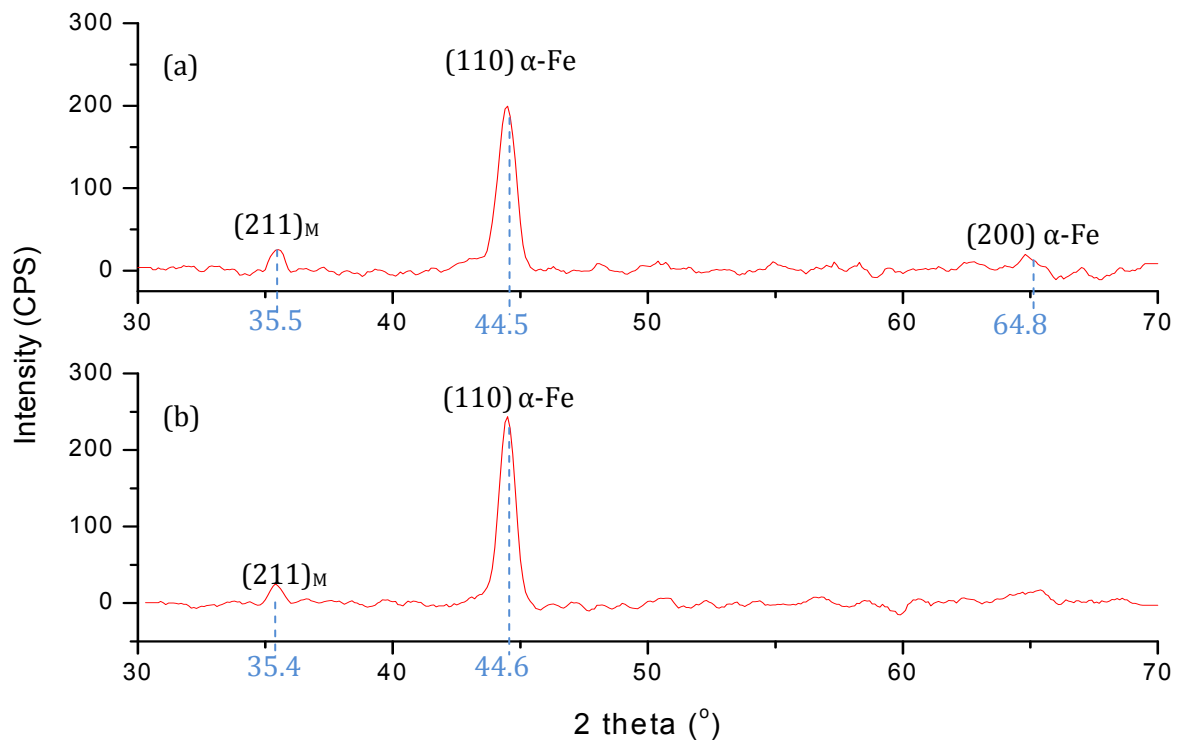


Figure 4.53: X-ray diffraction patterns of (a) E15 and (b) E8 sample from DOE2 processed at 0.4 mm spot size.

In Figure 4.54 (a) and (b), samples processed at 0.2 mm spot size produced (110) α -Fe peaks at a 60 % lower intensity than the as-received H13. The (200) α -Fe peak for samples in Figure 4.54 was decreased to 48 % and 84 % respectively compared to the as-received H13 tool steel.

Further (110) α -Fe peak reduction was observed on diffraction patterns of samples processed at a 0.09 mm spot size as shown in Figure 4.55 (a) and (b). The peak intensity of (110) α -Fe resulted from an as-received H13 sample was more than four times stronger compared to samples in Figure 4.55. A broadening effect of (200) α -Fe peak was found in the sample of Figure 4.55 (b)

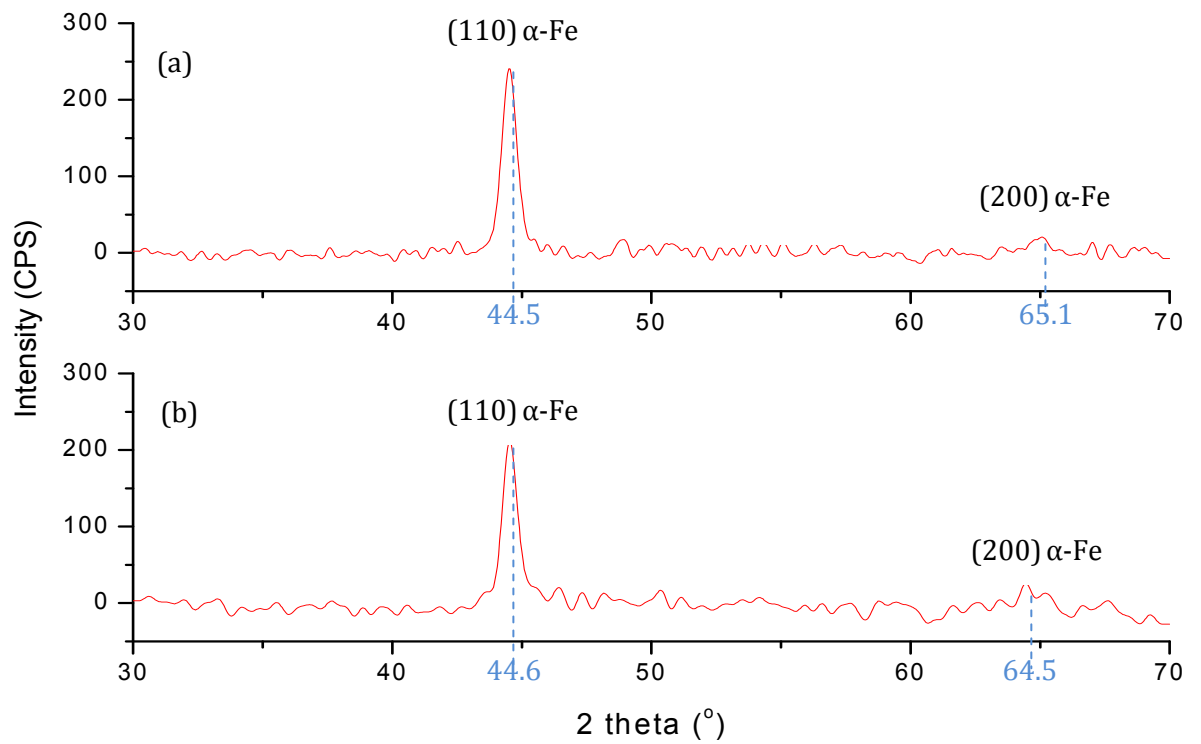


Figure 4.54: X-ray diffraction patterns of (a) N4 and (b) N12 sample of DOE3 processed at 0.2 mm spot size.

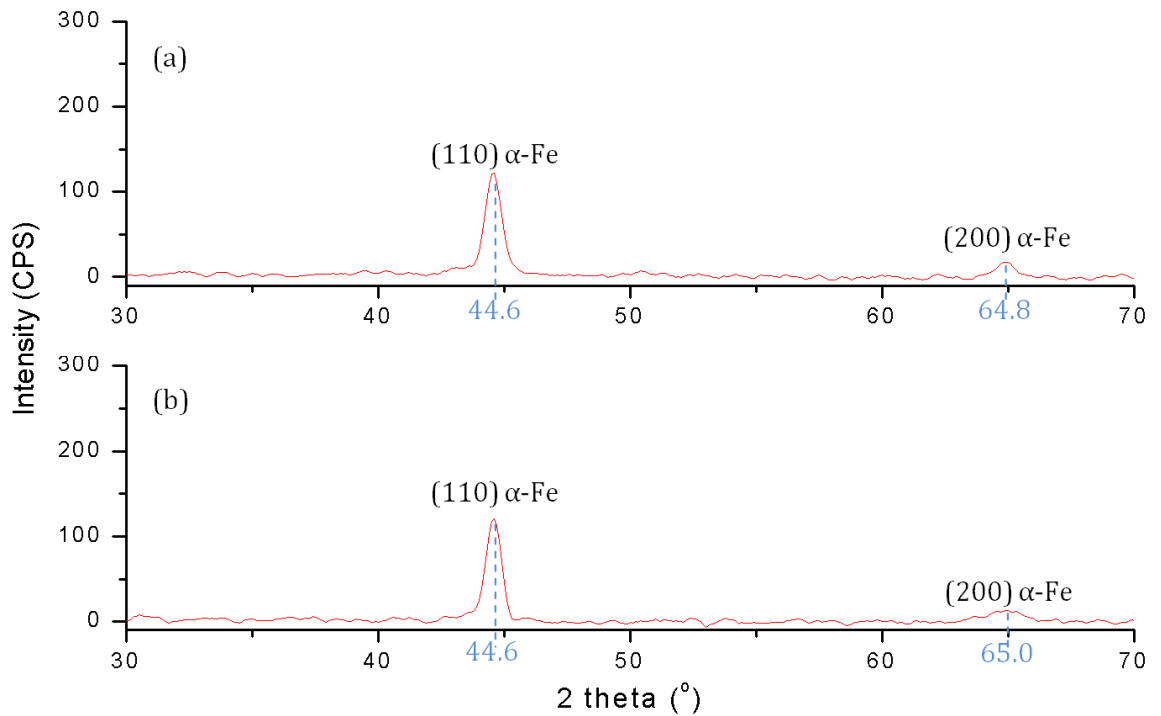


Figure 4.55: X-ray diffraction patterns of (a) X5 and (b) X2 sample from DOE4 processed at 0.09 mm spot size.

The crystallinity of the laser modified H13 tool steel sample surfaces were different from the as-received H13 steel in terms of relative strength ratio, I/I_1 , of diffraction peaks. Table 4.21 indicates a comparison of x-ray diffraction values for characterised angle measured from the samples scanning patterns and the standard peaks of α -Fe from the JCPDS database. The peaks' angles associated with as-received H13 steel surface were compared with the modified samples. All of the peaks detected on modified samples were at similar angles of reflection as the as-received H13 sample. The inter-planar spacing, d of the modified samples was retained while the relative intensity strengths differed. Referring to α -Fe (06-0696) from the JCPDS database, the relative strength ratio of the peaks at the four different angles were 100, 20, 30 and 10. The (200) α -Fe peak was diminished in sample E8 while it became more distinct in sample N12. Sample E8 processed at 0.4 mm spot size produced (211) martensite peak at 35.4° with at least 10 % of the relative strength ratio. The relative strength ratio of (211) α -Fe peak in sample X2 and X5 was higher than the as-received H13 steel (see Table 4.21). The FWHM values of (110) α -Fe peak in samples E8, E15, N4 and N12 increased at least 2.5 times higher than in as-received H13 steel. In sample X5, the increment was 2.7 times. A broadening of 1.045° was analysed on (200) α -Fe peak of sample X2 which was three times that of the as-received H13 peak.

Table 4.21: Contrast of x-ray diffraction values for as-received H13 steel and laser modified H13 steel surface.

Sample/spot size (mm)	Measured values					Data from JCPDS (α -Fe: 06-0696)		
	2θ ($^\circ$)	Max. intensity (CPS)	d (nm)	I/I_1	FWHM (2θ)	d (nm)	I/I_1	Plane (hkl)
As-received H13	44.6	591.0	0.2031	100	0.342	0.2027	100	110
	64.8	43.2	0.1437	7	0.584	0.1433	20	200
	82.1	72.8	0.1173	12	0.598	0.1170	30	211
	98.6	25.3	0.1016	4	1.003	0.1013	10	220
E15/0.4	35.5	24.6	0.2530	12	0.607			
	44.5	199.4	0.2035	100	0.854			
	64.8	19.7	0.1438	10	0.692			
E8/0.4	35.4	25.4	0.2530	10	0.601			
	44.6	243.6	0.2036	100	0.861			
N12/0.2	44.5	233.4	0.2033	100	0.849			
	65.1	20.6	0.1431	9	1.962			
N4/0.2	44.6	233.0	0.2033	100	0.925			
	64.5	36.5	0.1443	16	1.969			
X5/0.09	44.6	123.0	0.2032	100	0.940			
	64.8	12.3	0.1438	10	n/a			
	82.2	30.8	0.1172	25	n/a			
X2/0.09	44.6	131.0	0.2031	100	1.045			
	64.3	12.3	0.1448	9	n/a			
	82.2	26.9	0.1172	21	n/a			

Formation of Martensite and Meta-Stable Phases

Additional peaks were examined from the diffraction pattern. Apart from the α -Fe peaks reflected on the laser modified surface, samples processed with 0.4 mm spot size exhibited additional peak at 35.5° Bragg's angle. The peak was identified as (211) martensite peak as shown in Figure 4.56 (a), (b) (c) and (d). Figure 4.56 (b) reflected a more distinct (211) martensite peak compared to the other three samples.

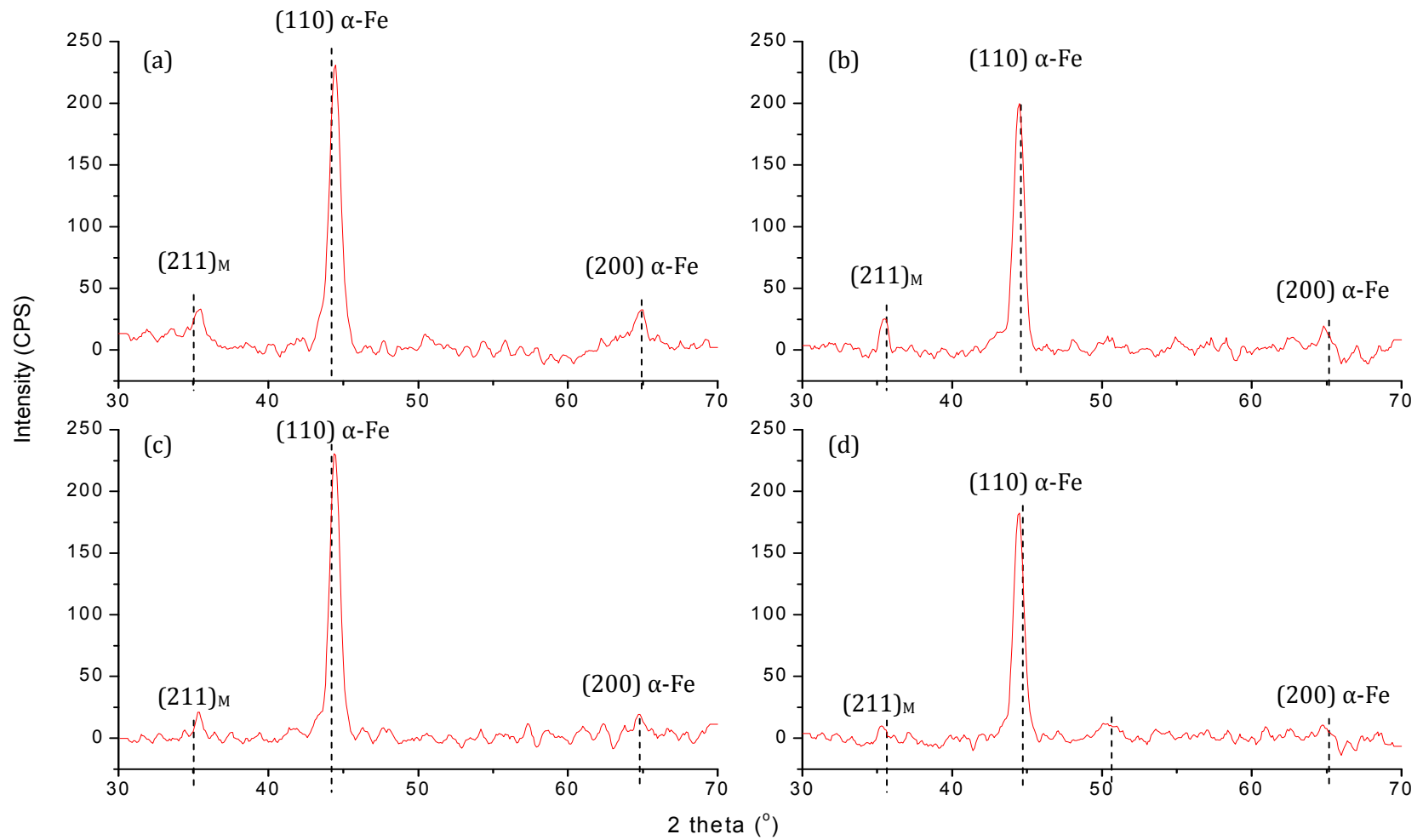


Figure 4.56: Reflection of martensite phase in (a) E18, (b) E15, (c) E21 and (d) E27 sample of DOE2 processed at 0.4 mm spot size.

The development of metastable phases was investigated on the laser modified samples processed at 0.09 mm spot size. Figure 4.57 (a) shows the reflection of (110) α -Fe peak on as-received H13 surface where a smooth peak outline was detected. However, in Figure 4.58 (a), (b) and (c), anomalous crystalline metastable phase peaks were reflected at different Bragg's angles. In Figure 4.58 (a), the peaks were reflected at 44.1 and 45.1° Bragg's angle while sample in Figure 4.58 (b) produced a sharp peak at 44.7°. Smaller peaks were reflected at 44.15, 44.65 and 45.25 ° in Figure 4.58 (b). Sample in Figure 4.58 (c) produced more peaks which were traced at Bragg's angles of 44.08, 44.11, 44.18, 44.28, 44.32, 44.44, 44.48, 44.52, 44.66, 44.7, 44.82, 44.87, 44.96 and 45.01°. Referring to the laser processing, the pulse energies used to modify samples in Figure 4.58 (a), (b) and (c) were 0.12 J, 0.10 J and 0.08 J respectively. At the lower pulse energy of 0.078 J, more than 10 metastable phase peaks were detected on the sample F10, Figure 4.58 (c). At the higher pulse energy of 0.12 J, only two anomalous peaks were reflected on sample of Figure 4.58 (a).

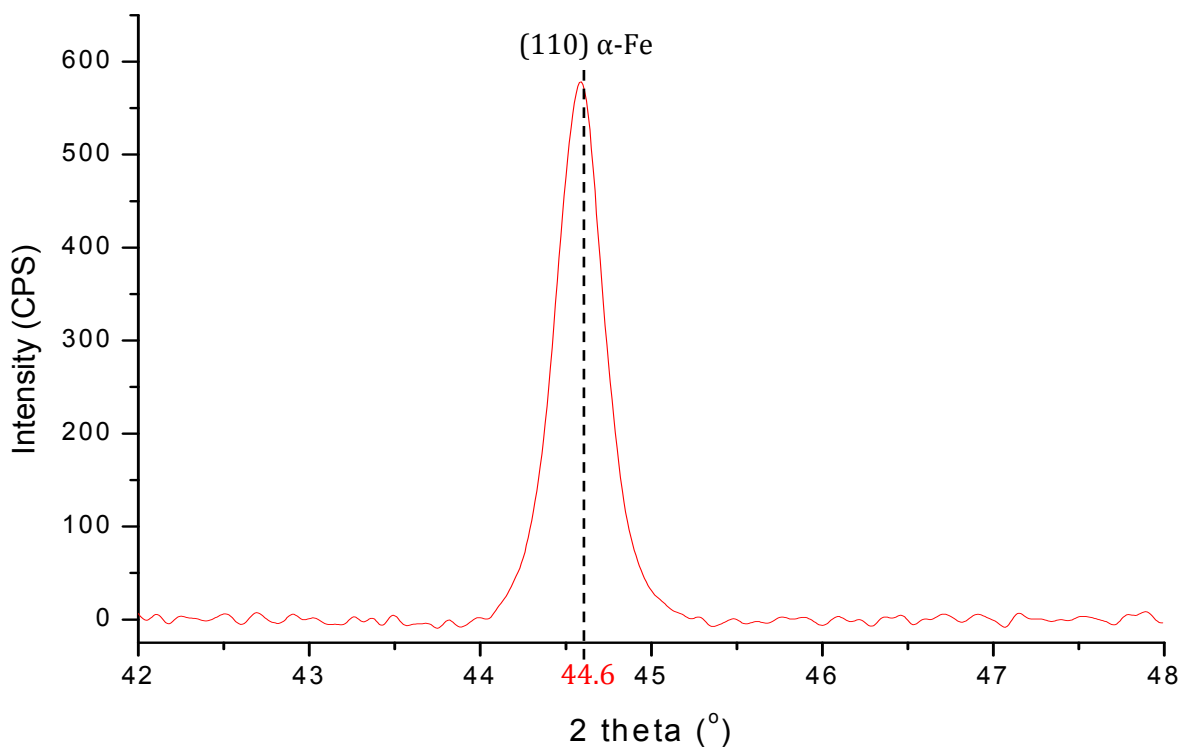


Figure 4.57: A close up of (110) α -Fe peak reflected from as-received H13 surface.

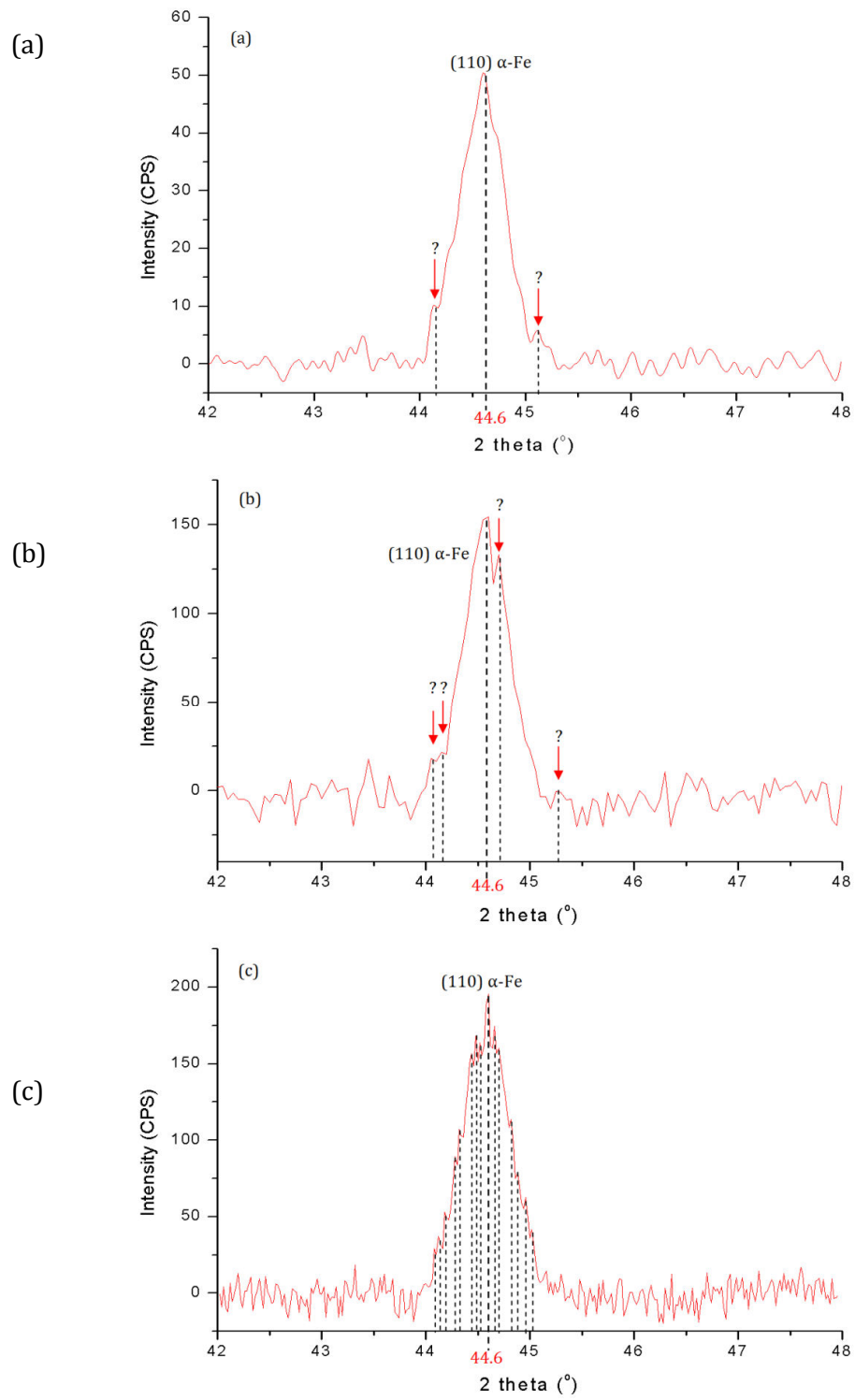


Figure 4.58: Metastable phase peaks reflected from sample (a) F1, (b) F6 and (c) F10.

4.3 Thermal Modelling Simulations of Laser Surface Modification of H13 Tool Steel

4.3.1 Temperature Distribution in Modified Surface

Thermal profiles of laser surface modification were simulated with the model as described in §3.4 with input laser parameters, surface absorptance factor and thermal properties of H13 steel at several Z values, as shown in Figure 4.59. In Figure 4.59 (a) to (e), the thermal model simulations indicate reducing temperature as expected for each subsequently deeper Z (depth) plane value upon progressing further into the substrate. Figure 4.59 (a) shows that when the thermal model was simulated at $Z = 0 \mu\text{m}$, the maximum temperature achieved is represented at a nominal value of 1. At $80 \mu\text{m}$ depth, the maximum nominal temperature achieved was 0.62 as shown in Figure 4.59 (c). In Figure 4.59 (d) and (e), the maximum nominal temperatures of 0.28 and 0.13 were recorded at $100 \mu\text{m}$ and $120 \mu\text{m}$ depth respectively. The temperature distribution plots from simulation allowed for the heating and cooling rates of any particular point within the modified surface to be calculated.

Figure 4.60 shows the cross section of the modified surface of sample F13 in the Y and Z axis. The dimension of the melted region, which is required for surface modification to occur, was limited by the volume of material for which the energy provided could raise the metal temperature to the material melt temperature, 1454°C . In Figure 4.59, the maximum modified layer depth simulated using the experimental laser processing parameters was approximately $100 \mu\text{m}$. However, the micrograph of Figure 4.60 shows that, using the similar parameter settings as in the simulation, the region where the temperature was raised to the melt temperature was only approximately $49 \mu\text{m}$ deep.

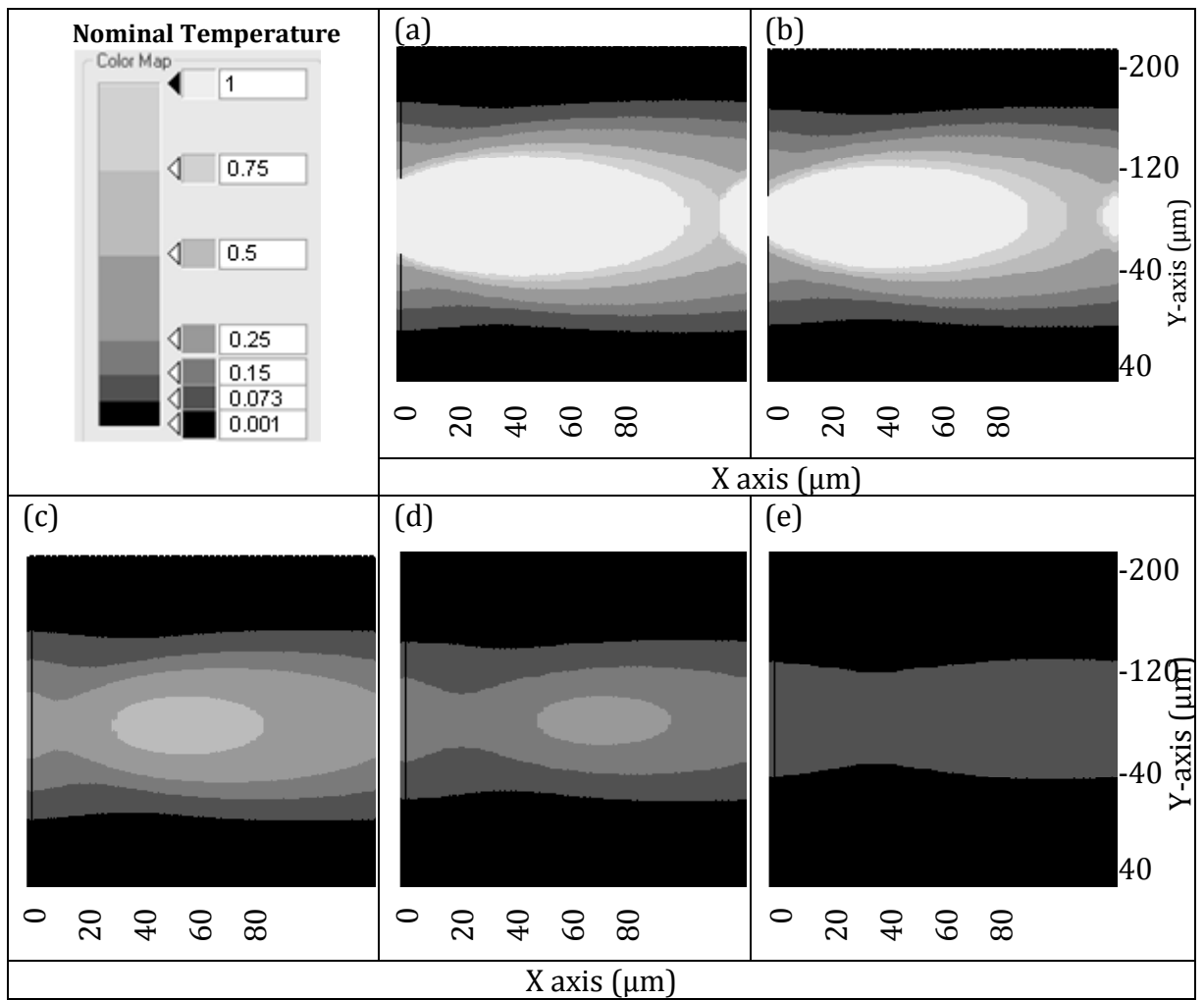


Figure 4.59: Nominal temperature distribution simulation in modified surface of sample X2 along depth, at (a) $Z = 20 \mu\text{m}$, (b) $Z = 40 \mu\text{m}$, (c) $Z = 80 \mu\text{m}$, (d) $Z = 100 \mu\text{m}$ and (e) $Z = 120 \mu\text{m}$.

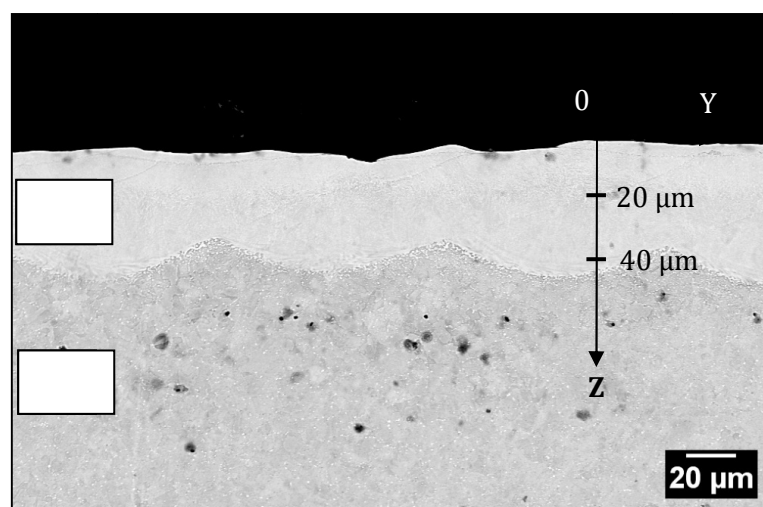


Figure 4.60: Modified layer [A] formed on substrate [B] after laser surface modification in sample F13.

4.3.2 Effect of Heating and Cooling Rate on Hardness Properties

Heating and cooling profiles from the model are shown in Figure 4.61. In Figure 4.61, the nominal temperature as a function of time was modelled for the H13 sample F13 processed at 1138 W power, 24% duty cycle, and 261 mm/s traverse speed. At 2900 Hz, the time needed for a complete pulse was 0.35 ms. At a specific point of $Y = 70.6 \mu\text{m}$, the nominal temperature distribution along the molten pool depth was plotted. The time needed to reach the maximum nominal temperature at the surface (where $Z = 0$), was 0.121 ms. The initial and maximum temperature achieved decreased with increasing depth. The time duration to reach these temperatures at deeper Z positions was also longer relative to shallower regions. Cooling rates recorded at the centre of the melt pool were twenty times higher than the cooling rate at a distance of 100 μm from the centre in Y direction, for six Z positions (0, 20, 40, 60, 80 and 100 μm).

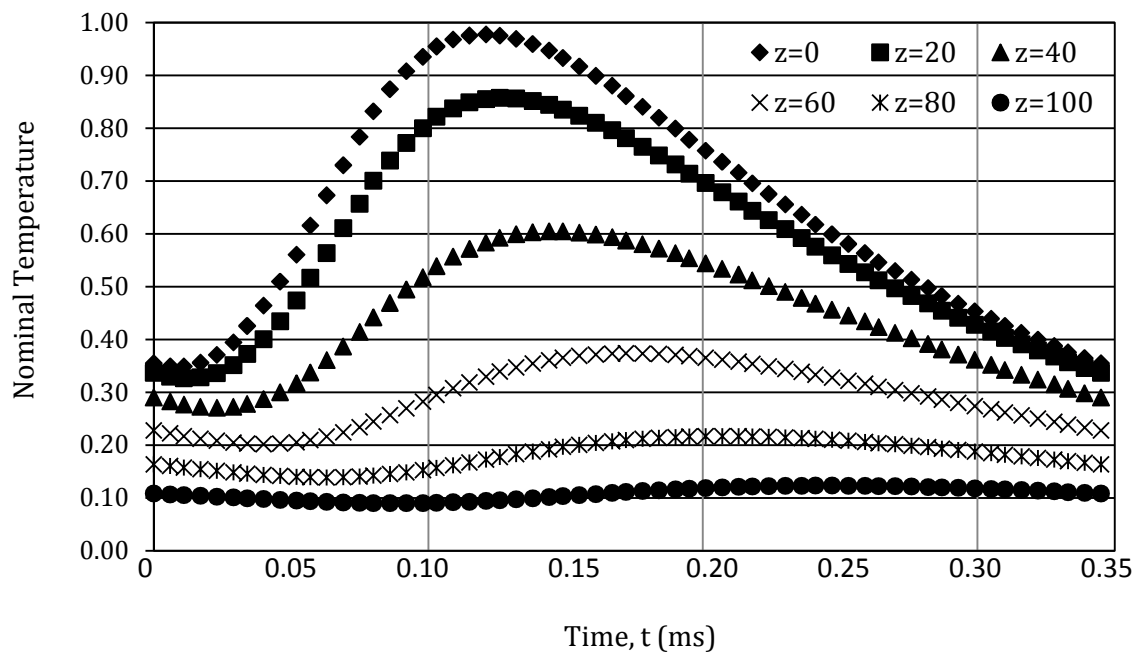


Figure 4.61: Nominal temperature as a function of time at $Y = 70.6 \mu\text{m}$ position for various depths.

The simulation of temperature profile in the modified surface was indirectly examined experimentally. The processing was conducted using similar laser parameter settings and sample surface absorptivity level to achieve maximum hardness. Seven sets of parameter settings were examined. These included 1138 W peak power, 2900 Hz PRF, 0.083 ms pulse width, 261 mm/s traverse speed, $5.35 \times 10^{-6} \text{ m}^2/\text{s}$ H13 tool steel thermal diffusivity, 28.6 W/m $^{\circ}\text{C}$ H13 tool steel thermal conductivity and 0.6 absorptivity factor, presented here.

The micro-hardness values measured at different distances within the processed surface is presented in Figure 4.62. The maximum hardness of 824 HV_{0.1} resulted from 2377 s⁻¹ nominal cooling rate and 4618 s⁻¹ nominal heating rate, at a 20 μm modified surface depth. At 724 and 572 HV_{0.1} micro-hardness, the nominal heating to cooling rate ratio was 1.76 and 1.54 respectively. As the heating to cooling rate ratio decreased, the micro-hardness also decreased.

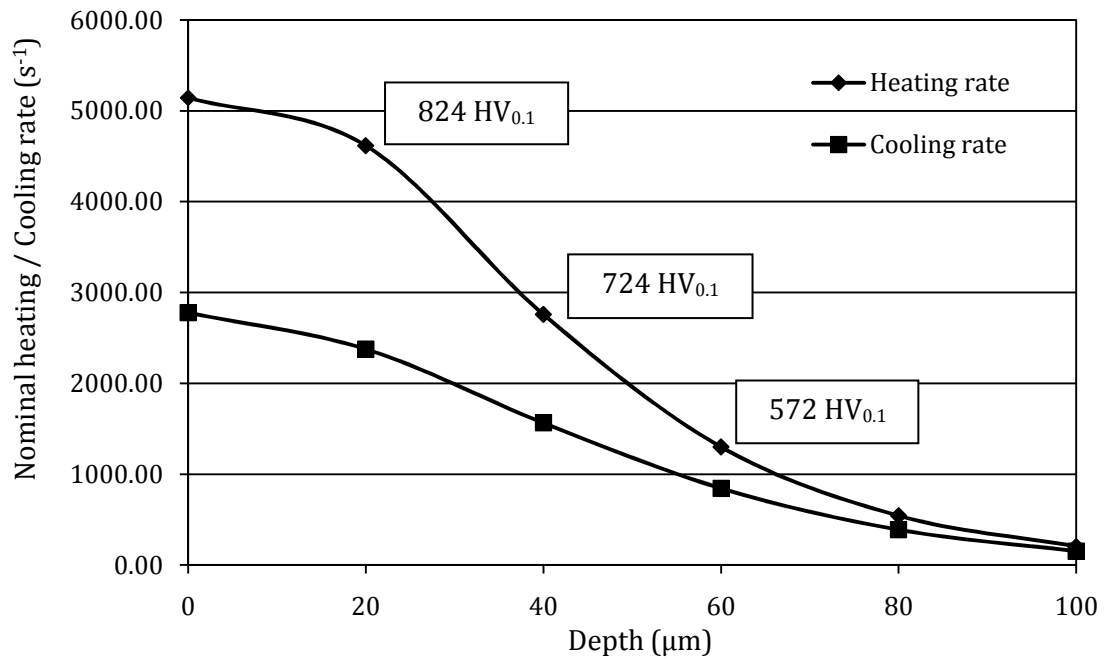


Figure 4.62: Micro-hardness of the modified surface corresponding to nominal heating and cooling rate of molten pool in the modified surface of sample F13 along the depth.

CHAPTER 5

Discussion

5.1 Introduction

The results discussion presented in this chapter is outlined in Figure 5.1. The characterisation results of laser surface modified H13 tool steel are discussed according to the characterisation methods. From the metallographic study, the effects of processing parameters on the surface absorptance, grain size and melt pool geometry are discussed and elaborated from each design of experiment. The hardness properties are discussed based on different hardening mechanisms in the samples. A review of the effects of processing parameters in each design of experiments on the surface profile and roughness is presented. In the XRD analysis section, discussion on metastable phase formation in the modified samples is presented. Temperature distribution during the surface processing, and heating and cooling rate effects on hardness properties are discussed in the thermal modelling section. The overall results from each DOE are presented in Table 5.1.

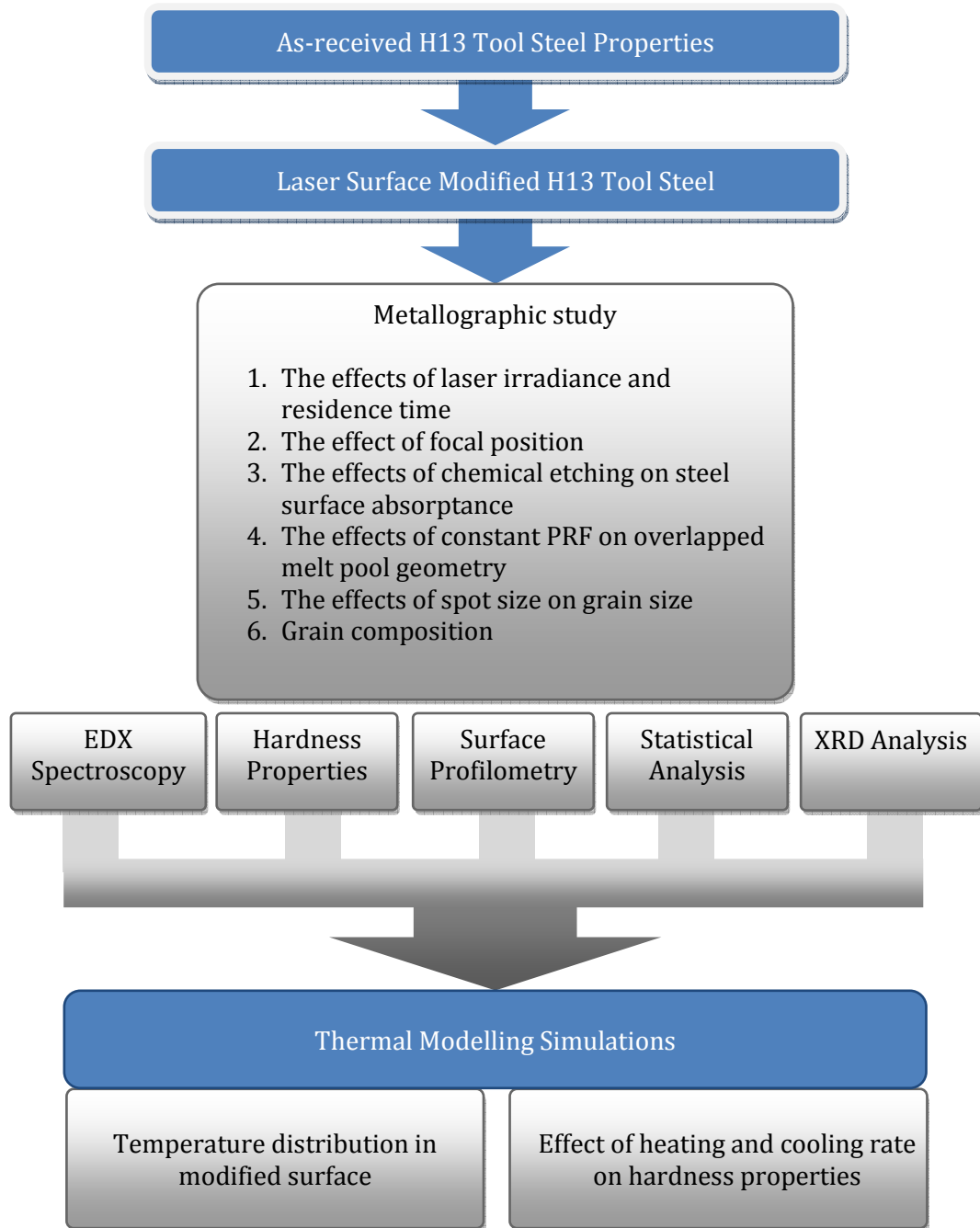


Figure 5.1: Outline of order of results discussion presented in this chapter.

Table 5.1: Summary of laser parameters setting ranges and characterisation results for the laser modified H13 tool steel samples.

DOE	Set parameters					Outcome parameters				Results			
	P _P (W)	P _A (W)	DC (%)	η (%)	PRF (Hz)	τ (ms)	E _P (J)	T _R (ms)	I (W/mm ²)	Depth (μm)	Hardness (HV _{0.1})	R _a (μm)	Minimum intensity of (110) α-Fe peak from XRD scan (cps)
DOE1	760	532	70	10	2857	0.14	0.11	0.22	3,872	0-29	-	-	-
		646	85	30	to	to	to	to					
		760	100	50	5000	0.35	0.27	0.38	5,576				
DOE2	760	646	85	10	2857	0.20	0.15	0.29	3,569	46-180	724-1017	3.5-38.2	199.4
		760	100	30	to	to	to	to					
		760	100	50	5000	0.35	0.27	0.38	5,592				
DOE3	507	249	49	10	2900	0.17	0.09	0.12	10,930	48-80	435-996	3.1-7.9	233.0
	760	274	36	50		0.12	0.10	to	to				
	1313	305	23	50		0.08	0.11	0.25	28,184				
DOE4	760	274	36	0	2900	0.06	0.10	0.06	91,943	42-88	670-976	3.2-9.5	123.0
	1138		24	10		to		to					
	1515		18	30		0.12		0.16	23,8087				
DOE5	760	274	36	-10	2300	0.05 to 0.16	0.08 0.10 0.12	0.05	108,582	37-150	728-905	1.8-22.4	50.0
	1138		24	0	2900			to	to				
	1515		18	10	3500			0.16	0.16				

5.1.1 As-received H13 Tool Steel

The as-received H13 tool steel had an average hardness of 280 HV_{0.1} (approximately 28 HRC) contributed to by homogenous ferritic matrix and spheroidal carbides. Samples were in the annealed condition which allowed machining to be performed. For die application, H13 tool steel is heat treated to achieve hardness in the range of 484 to 544 HV (48 to 52 HRC) [154]. The hardening mechanisms are different in as-quenched and fully heat treated tool steels. In the as-quenched tool work-hardening and solid solution hardening occur and the steel hardness is contributed to by carbon content in the solid solution. The fully heat treated tool steels hardness is affected by precipitates that cause precipitation hardening and solid solution hardening [168].

5.2 Laser Surface Modified H13 Tool Steel

Significant undercooling of the melt during laser processing leads to metastable effects with resulting enhanced surface properties. Pulse processing mode was selected to limit the material-laser interaction time and control the material's surface temperature. Appropriate selection of PRF and pulse width has been seen in previous specific cases to produce defect free modified surfaces [7, 8].

5.2.1 Metallographic Study

The Effects of Laser Irradiance and Residence Time

The measured modified surface depth in DOE1 was between 0 to 29 μm due to low energy absorbance. The micrographs of DOE1 samples indicate inefficiently processed H13 tool steel surface due to the laser spot focal position, surface reflectivity at the CO₂ laser wavelength, and the low laser irradiance which resulted from a defocused beam diameter. Although focusing the laser spot both above and below the surface position can produce a 0.4 mm spot diameter, focusing above the surface results in less energy absorption into the materials surface during processing [40, 53]. The reflectivity of metals' surfaces at the CO₂ laser wavelength is a problem in surface processing. Theoretically, a steel surface would normally absorb less than 15% energy when processed with CO₂ laser [62]. The irradiance was small due to the defocused beam diameter of 0.4 mm in DOE1. These factors explain why a non-melted surface resulted in samples processed at residence time of less than 0.31 ms.

The Effects of Focal Position

In DOE1, the findings indicating that the focal position affects the efficiency of material-laser interaction was also found in previous work [53]. Though the modified layer depth surface morphology was non-uniform, the modified layer formation indicated surface melting was improved when the focal position was below the surface. Reduced energy absorption by focusing above the surface caused broad and shallow melt pool formation. This finding is in general agreement with that of other workers [40, 53]. The findings from the work presented in this thesis indicate that residence time is the main factor controlling the energy loss factors and modified surface depth within the investigated irradiance range of 3000 to 5000 W/mm².

The Effects of Chemical Etching and Surface Roughening

Samples processed in DOE2 at 10% overlap produced regions with different surface depths due to the Gaussian beam profile used in the processing. Referring to Dickey et al., the irradiation effect of a Gaussian beam gives by Region I where the material can be processed, see Figure 5.2 (a), while Region II and Region III may not have sufficient irradiance for surface modification [169]. During processing, approximately 80% of the spot diameter was taken as the region of processing with the required beam intensity. Thus, the expected size of molten pool was 0.32 mm for the 0.4 mm laser beam spot size. However, the average molten pool width measurement was 0.23 mm which corresponds to an average effective beam diameter of 57% of the focused spot size. Existence of gaps between molten pools set with 10% overlap indicates the effective overlap percentage for both circumferential and linear translation should be set at a minimum of 30% for the 0.4 mm spot size and 5510, 5548 and 5592 W/mm² laser irradiance, 0.32, 0.34 and 0.38 ms residence time and, 2857 and 3200 Hz PRF settings, see Table 3.6. At 30% overlap, the pulses were overlapped within Region II and III. Figure 5.2 (a) and (b) from sample E8 show the corresponding Gaussian beam effect on the molten pool dimension where the deepest region was developed within Region I. The molten pool depth reduced within Region II and III.

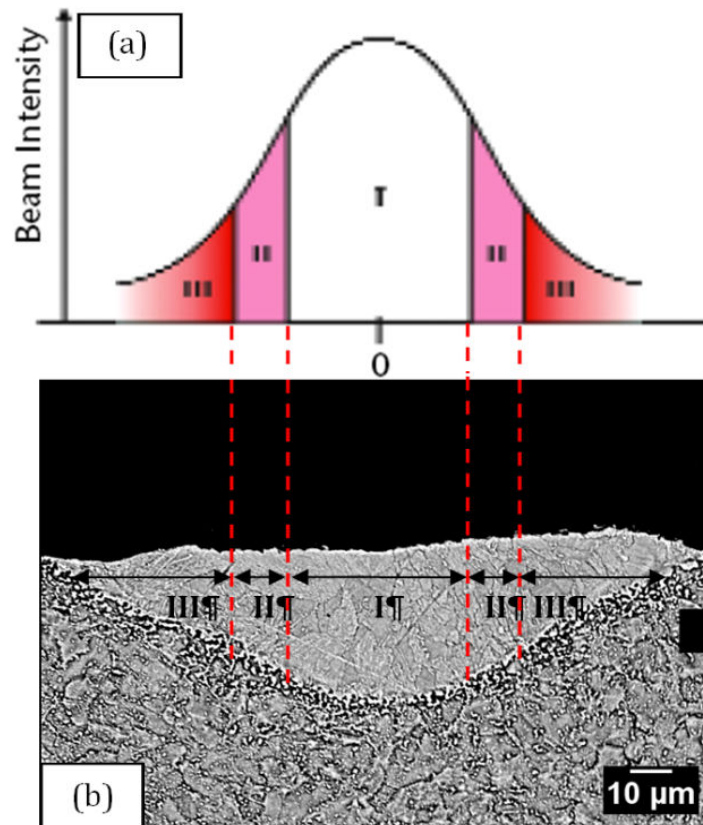


Figure 5.2: (a) Theoretical [169] and (b) experimental division of a Gaussian beam into regions on sample E8 modified surface cross section.

An increase of modified surface depth in DOE2 occurred due to enhanced surface absorptance from surface chemical etching pre-treatment. The findings from DOE2 informed the amount of laser energy required in the surface modification process of H13 tool steel. In DOE2, to produce more overlaps, PRF was increased. In this processing design, increasing pulse energy at higher overlap percentage required higher PRF settings in order to control the surface temperature. PRF settings above 5,000 Hz produced a continuous processing mode effect which creates defects in the surface. Low pulse energy (0.23 J) at high PRF (5000 Hz) failed to produce overlapped pulses as shown in the micrograph in Figure 4.10 (a). At high pulse energy and residence time, the sample temperature raises and sample surface reflectivity decreases [62, 63]. The surface absorptance increases, but molten pool profile on the upper surface was irregular for most samples produced in DOE2. This resulted from a high pulse energy and residence time combination where the liquid accumulated above the surface and left the pool edges during solidification as shown in Figure 4.10 (b). Chemically altered H13 tool steel surface became less reflective and absorbed more energy into the surface. The melt pool geometry formed at high pulse energy was shallow due to heat loss during processing. At high pulse energy processing, samples experienced vaporisation and it was revealed that heat loss due to element vaporisation reduced the heat input to the sample surface [170]. Variations

in molten pool depth and modified layer thickness indicate that the laser parameter settings and sample traverse speed could be set within a wide range of processing parameters to minimise the surface superheat temperature.

Surface roughened samples in DOE3 were processed at lower pulse energy as surface absorptance was further improved by roughening in addition to the etching pre-treatment. The increase of heat input into surface was due to the increased absorption of the laser beam energy on specimen surface. Similar results were found by other workers [53]. Compared to smooth surfaces, an increase in average surface roughness to approximately 3.0 μm for H13 tool steel has been seen to significantly increase absorptivity at the CO₂ laser wavelength by as much as 60% [66, 68]. Using a 0.2 mm spot size, the resultant molten pool diameter was approximately 0.25 mm which allowed use of 10% overlap between pulses. Lower percentages of overlapped pulses provided decreased residence time and reduced the modified surface roughness.

The Effects of Constant PRF Setting on Overlapped Melt Pool Geometry

In DOE3, overlap was possible either by increasing the PRF to gain more pulses and overlaps, or by keeping the PRF constant (2900 Hz) and varying the residence time via alterations to duty cycle. In previous work, overlap was achieved by increasing the PRF [9]. No previous studies have presented an investigation of alteration of duty cycle and related variation in the melt pool geometries during surface modification. From DOE2 and DOE3 sample observations, both settings resulted in overlapped geometries, but different surface properties were achieved. At constant PRF of 2900 Hz (of sample N10 and N24), the pulse width and pulse energy remained constant at 0.12 ms and 0.10 J respectively though the overlap was changed, see Table 4.4. The residence time increased when the overlap was increased. At 0% overlap the residence time is equivalent to the pulse width. With improved surface absorptance, a lower overlap percentage than 30% was possible as the surface covered by Region II and III in the Gaussian beam also melted. For longer residence time with 50% overlap the sample surface temperature increased and prolonged surface melting occurred. Lower percentages of overlap are preferable in the pulse laser surface modification process as the surface defects tend to develop in the higher overlap designs. This was also noted by other workers [28, 53]. The constant PRF setting also allowed the investigation of peak power effect exclusively on the modified surface depth.

The Effect of Peak Power on Modified Surface Depth

In DOE4, low peak power of 760 W produced bulging geometry at three different overlaps due to pulse width setting of 0.125 ms which was longer than set for the other two peak powers. Pulse width determines the laser-material interaction time or residence time at 0% overlap. Increasing pulse width decreased the heat penetration depth [70]. Low duty cycle allows short pulse duration which limits the energy penetration into sample surface. Though maximum modified surface depth was achieved at longer pulse width, this resulted in bulging surface geometry after every four pulses due to retained surface temperature. The bulging geometry occurrence leads to a conclusion that the molten surface was dragged along the translation direction, mounted up and only fully solidified after four cycles of pulse. At 36% duty cycle, the laser 'off' state of 64% was insufficient to cool down the surface [14]. While, higher peak power settings of 1138 and 1515 W were investigated at shorter pulse widths of 0.08 and 0.06 ms respectively; this allowed immediate solidification after each pulse hit as the laser off state/ cooling period (calculated using Equation 3.10) was 76% from the duty cycle or more. The penetration depth was deeper due to a combination of higher peak power and residence time. When the pulse energy was constant, peak power together with residence time determined the temperature profile. The observed modified surface indicates the significance of laser peak power and pulse width on surface property variations.

The Effects of Laser Spot Size on Modified Surface Properties

Table 5.2 shows the processing parameters used in the comparison of laser spot size effect. The effect of beam size on grain size of modified surface is shown by micrographs in Figure 5.3. Micrographs (a) to (c) in Figure 5.3 depict the grain size observation at high magnification corresponding to the specific laser irradiance and residence time settings indicated. At 0.09 mm spot size processing, the laser irradiance ranged from 108 to 264 kW/mm² and residence times were between 0.06 ms and 0.16 ms. The irradiance range for 0.2 mm and 0.4 mm spot size processing was between 3.9 and 28.0 kW/mm² with a residence time range of 0.12 to 0.38 ms. Grain size of modified layer in micrograph (a), (b) and (c) of Figure 5.3 was smaller compared to the as-received H13 tool steel grain size in Figure 4.1. The grain diameter linearly decreased with decreasing laser spot size.

Table 5.2: Processing parameters for H13 tool steel samples at three beam spot sizes.

Beam spot size (mm)	Sample	P_p (W)	DC (%)	η (%)	I (W/mm ²)	T_R (ms)
0.4	E8	760	85	10	5,548	0.32
	E9		100		5,592	0.38
	E14		85	30	4,618	0.29
	E15		100		4,631	0.34
	E26		85	50	3,971	0.32
	E27		100		3,971	0.38
0.2	N4	507	49	50	10,930	0.25
	N24	760	36		16,388	0.19
	N12	1313	23		28,184	0.12
0.09	F5	760	36	-10	132,686	0.11
	F6	1515	18		264,499	0.06
	F1	760	36	0	119,297	0.16
	F2	1515	18		237,809	0.08
	F7	760	36	10	108,582	0.14
	F8	1515	18		216,449	0.07

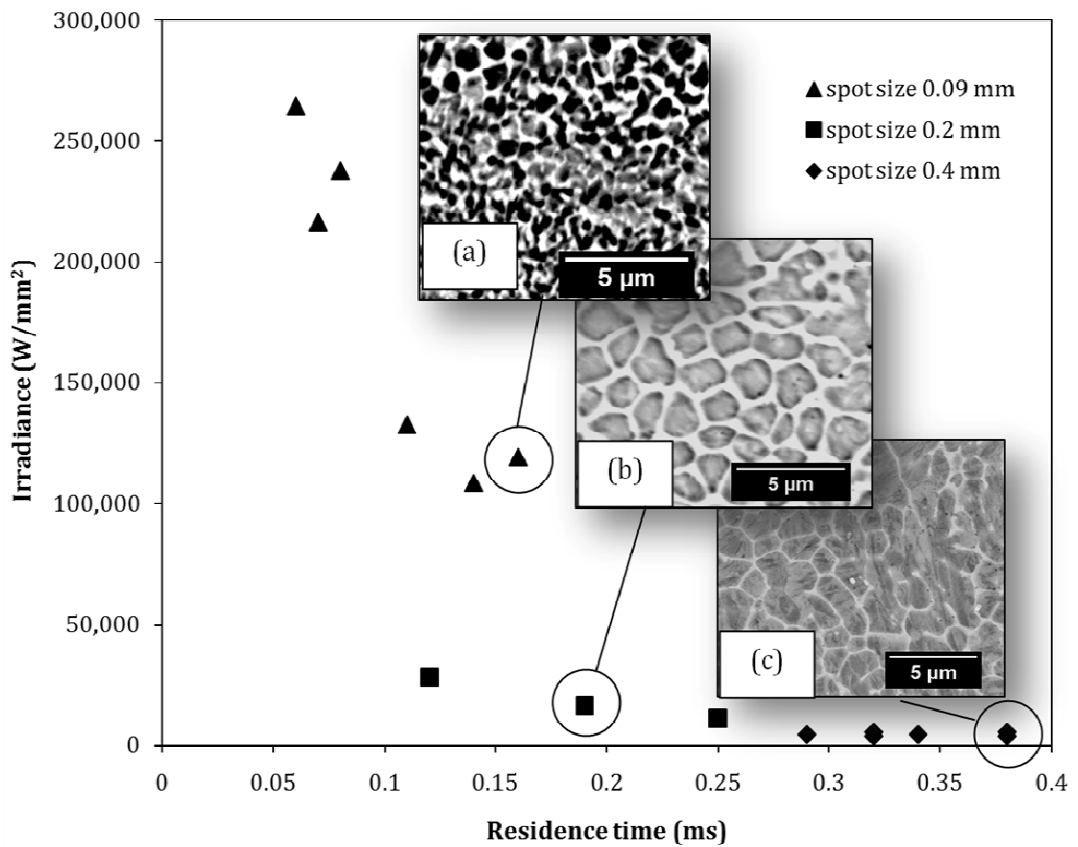


Figure 5.3: Micrographs of laser modified H13 samples processed at (a) 0.09, (b) 0.2 and (c) 0.4 mm spot size corresponding to the laser irradiance and residence time settings.

Decreasing spot size in processing H13 steel influenced the sample surface morphology. The resulting surface morphology of the laser processed samples at different beam sizes is shown in the micrographs of Figure 5.4. Micrographs (a) (c) and (e) in Figure 5.4 show the surface of the sample E26, N12 and F8 processed at 0.4, 0.2 and 0.09 mm spot size respectively. Figure 5.4 (b) shows varying molten pool depths of the sample processed with 0.4 mm spot size; where the maximum depth ranged from 135 to 205 μm . Micrographs in Figure 5.4 (d) and (f) depict consistent modified layer depths in the range of 70 μm to 80 μm produced by samples processed at 0.2 and 0.09 mm spot size. The molten pool geometrical pattern on the sample surface of Figure 5.4 (a) was not consistent and not measurable in a similar manner to other samples. The molten pool width measured from the sample processed at 0.2 mm spot size, Figure 5.4 (c), was 245 μm , while at 0.09 mm spot size, Figure 5.4 (e), the width was 286 μm . Bulging solidified molten pool geometries were observed in the micrographs of Figure 5.4 (b) and (d) while a relatively flat surface was formed for sample F8, as shown in Figure 5.4 (f).

The grain size was measured using Image J software on samples processed at 0.4 mm, 0.2 mm and 0.09 mm spot size as shown in Figure 5.5. Figure 5.5 (a) and (b) respectively show the micrograph layout used in the analysis at required image selection and adjusted threshold stages of image analysis. The range and distribution of grain sizes measured based on the Feret's diameter, are given in Table 5.3 and Figure 5.6. The Feret's diameter is the greatest straight line distance possible between any two points along the boundary of a region of interest [165, 166]. The grain size of samples produced with the 0.4 mm spot size ranged from 2.54 to 5.99 μm which was a large range when referred to the overall grain size distribution in Figure 5.6. At smaller spot size of 0.2 mm and 0.09 mm, the range of grain sizes decreased and produced a more consistent grain size in the modified surface.

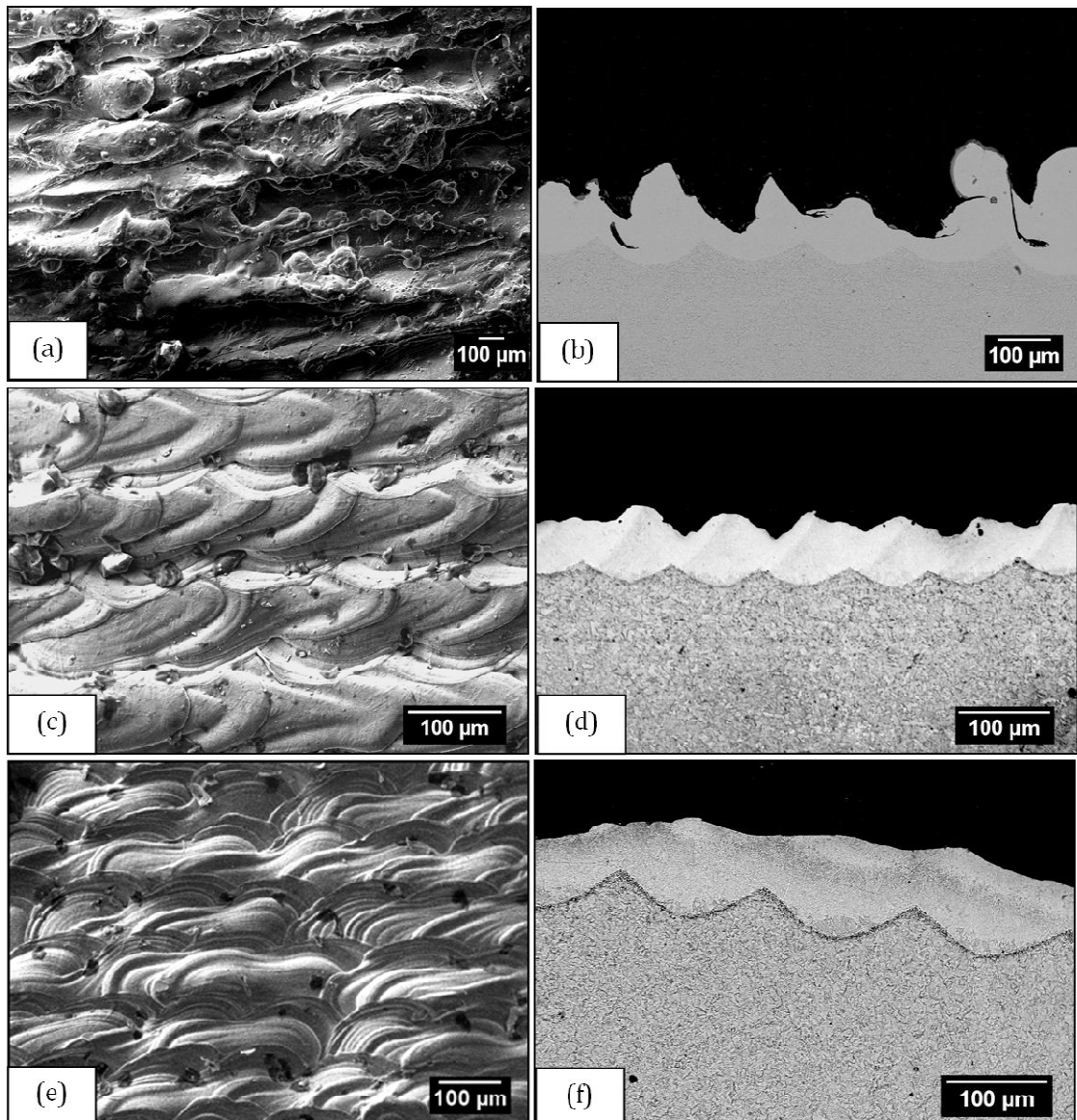


Figure 5.4: Molten pool width and thickness of samples processed at 0.4 mm (a), (b) and 0.2 mm (c), (d) and 0.09 mm (e), (f) spot size. Micrographs (a), (b) represent sample E26; (c), (d) represent sample N12; and (e), (f) represent sample F8.

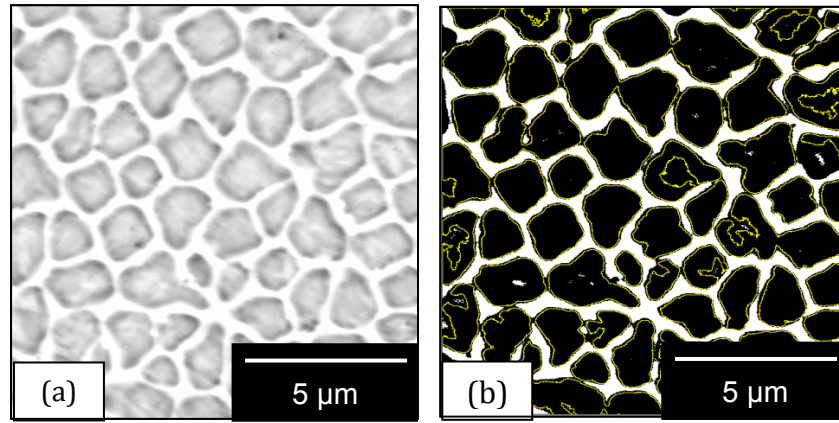


Figure 5.5: Grain measurement layout at (a) required selection and (b) threshold adjustment stages of analysis using Image J software. This micrograph was captured from the sample processed with a 0.2 mm spot size, N12.

Table 5.3: Range of modified H13 grain size processed at three beam spot sizes.

Laser spot diameter (mm)	Range of Feret diameter (μm)
0.40	2.54 – 5.99
0.20	1.60 – 2.83
0.09	0.51 – 1.09

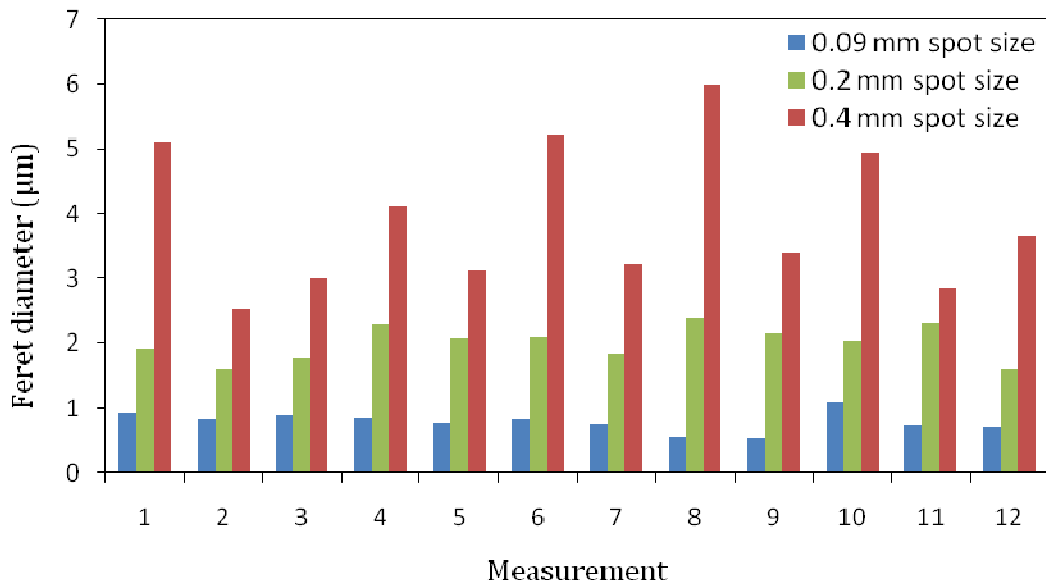


Figure 5.6: Average Feret's diameter distribution for 12 different samples processed at three different spot sizes

Samples processed using 0.4 mm spot size produced a deeper modified surface due to higher duty cycle settings. In DOE2, the irradiance was lower compared to the other DOEs. Therefore, pulse width was set between 0.20 and 0.35 ms regardless of the constant peak power. At smaller spot sizes of 0.2 and 0.09 mm, the laser irradiance was higher due to the

smaller affected area. In DOE3, the duty cycle was varied between 23 and 49% for different peak powers ranging between 507 and 1313 W. From the duty cycle setting, the resulting pulse width range was 0.125 to 0.080 ms to limit the high irradiance interaction time with the surface. Samples of DOE4 were processed at a higher range of peak power from 760 to 1515 W and at duty cycles of 18 to 36% to produce pulse widths ranging from 0.125 to 0.083 ms. Both DOEs yielded similar ranges of average modified surface depth (between 42 and 80 μm) due to the similar range of pulse width and the constant PRF of 2900 Hz used in both DOEs.

Low irradiances which were used with longer pulse widths roughened the modified surface due to longer residence times. The energy produced by the higher laser irradiances penetrated deep into the sample surface and formed definite solidified molten pools geometries. The samples processed with spot sizes of 0.2 mm and 0.09 mm resulted in molten pool diameters which were multiples of the laser beam spot diameter due to the corresponding high irradiance levels.

Decreasing the laser spot size increased the heating and cooling rates. Change of heating and cooling rate was evidenced by resulting observed different grain size ranges in the modified surface. Nano and ultrafine-grain size structures were developed in modified surface due to the large undercoolings produced from 0.09 mm spot size processing. Figure 5.7 shows a schematic image of a nano-crystalline material where the grain-boundary atoms are white and are not clearly associated with crystalline symmetry [171]. The micrographs of samples processed at 0.2 mm and 0.09 mm spot size in Figure 5.3 (a) and (b) clearly resemble the nano-crystalline structure. Nano-crystalline materials are characterized by a large volume fraction of grain boundaries and grain sizes have been observed to range between 10 and 300 nm [87]. The grain size range was found to vary greatly in this work with processing at a 0.4 mm spot size since the prolonged melting duration caused energy accumulation on the surface and recalescence. The local heat field and the local surface cooling rate can be varied greatly allowing control of grain formation through the surface layers. The smaller spot size of 0.09 and 0.2 mm resulted in a more controlled surface temperature gradient range due to the short residence time. The 'off' state in the laser pulse produced in these cases a sufficient time for development of undercooled austenite after each pulse and transformation to ultrafine-sized ferrite ranging from 0 to 3 μm . This is comparable with the austenite to ultrafine ferrite transformation obtained by thermo-mechanical controlled processing [111].

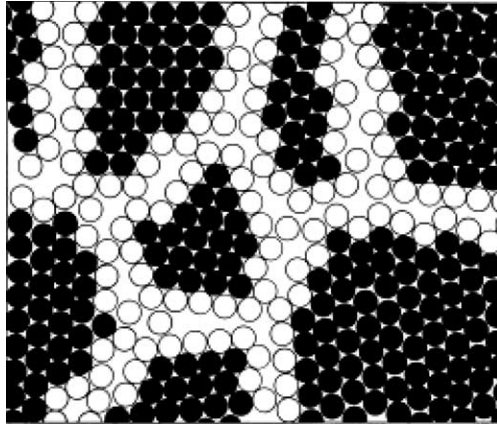


Figure 5.7: Two-dimensional model of a nano-structured material. The atoms in the centres of the crystals are indicated in black [171].

Consistent grain size distribution in the modified surface of samples processed with 0.09 and 0.20 mm spot size was possibly due to the large amount of grain boundary in the initial austenite phase. Similar trends have been previously recorded [172]. Initial austenite grain size was found from review to have a significant effect on the ferrite characteristics. The ferrite grain size distribution tends to be more uniform for a fine initial austenite grain size when compared to an initial coarse austenite grain size [111]. On the other hand, at large undercoolings, the austenite grain size becomes less deterministic for final grain structure [173].

Grain Morphology

Grain refinement in the modified surface and heat affected zone was found to be due to a steep temperature gradient and high cooling rate. The steep temperature gradient resulted in phase transformation, and supercooled/undercooled austenite which increased the number of nucleation sites for ferrite and lead to ferrite grain refinement [96, 98, 99]. In $Fe_{70}Co_{30}$ alloy, quenching without undercooling results in long elongated dendritic growth of the stable austenite phase [174]. In DOE2, ferrite transformation occurred at very low undercooling where martensite phase presence was also observed among the ferrite phase. The martensite phase in the modified surface resulted from solubility extension of the solute atoms at high cooling rate [94, 102]. Previous work also found that for laser processed Fe-based alloys, rapid austenizing followed by quenching can develop a unique microstructure consisting of ultrafine-grained martensite [99]. The martensitic transformation in Fe-Cr alloy begins in the grain boundary areas of significant Cr-depletion, where the chemical driving force is the main driving force [107].

The presence of α -Fe and martensite phases was accompanied with a small amount of carbides as found in previous work where carbides were detected at 45 μm below the

laser processed surface [32]. When austenite decomposes into ferrite, carbon must diffuse across the boundary between the two phases and away through the γ lattice [114]. However, as the solubility of carbon in ferrite at 723°C is only 0.02 wt%, a large amount of carbon still remains in the modified surface of H13 tool steel. During rapid quenching of Fe-based alloy, undercooled austenite caused incomplete carbon diffusion, nucleation and growth of carbide or $M_{23}(B,C)_6$ type crystalline phase [88]. However if the diffusion was allowed to complete, cementite phase will form.

The grain size is dependant to the undercooling where smaller sized grains were formed at high undercooling as the solidification process takes place in a short period of time. Variations of undercooling caused nano and ultrafine size grain formation near and within grain boundaries. Generally, ferrite forms as grain boundary allotriomorphs and nucleates at austenite grain boundaries above the eutectoid temperature. The allotriomorphic ferrite is usually lenticular in shape since it tends to grow preferentially along the grain boundary [114]. Indistinct grain boundaries could be due to recalescence effect in the steels during cooling. The temperature evolution from transformation heat causes recalescence and reduces the effective undercooling. Thus, at some large undercooling below the equilibrium temperature, the grain size achieved in practice is far greater than predicted theoretically [173].

In DOE3, similar phase transformation was observed due to undercoolings. Ultrafine grains with high volume fraction of grain boundaries were formed as a result of large undercoolings compared to DOE2 samples. The smallest ferrite grain size that can be achieved occurs when all of free energy for nucleation is used up in creating ferrite/ferrite grain boundaries [173]. Rapid heating and cooling rates from laser irradiation can yield nano-crystalline and/or amorphous structures [94, 175, 176]. Consequently, the number of grains increased in laser modified samples compared to the number of grains present within the same volume in the substrate. At the same time, grain growth was observed from coarse grains with faded grain boundaries due to recalescence and grain growth process in polycrystals [177]. Furthermore, solidification rate differed at different surface depths and overlapped areas due to thermal capacity and conduction of the substrate. In the overlapped regions, grain growth occurred, together with subgrains formation due to increased surface temperature and heat sink from the adjacent substrate.

In DOE4 and DOE5, high volume fraction of grain boundary, amorphous-like and quasi-crystalline phases were observed due to the large undercooling. The 'flower like' grains were also found in previous works of Rios et al. and Biswas et al. [101, 122]. In Fe-based alloys, the quench rate can be as high as 10^5 - 10^6 K/s to produce amorphous phase and is

limited to a maximum of 50% of Fe content composition [91]. In surface modification of H13 tool steel, the higher Fe composition necessitates a more rapid quench rate to produce amorphous phase. With the 0.09 mm laser spot size processing and duty cycles of 18 to 36%, the approximate cooling period range was 0.183 to 0.356 ms, see Table 4.7 and Table 4.8. At these cooling periods, the cooling rates calculated using Equation 3.11 were between 3.95×10^6 and 7.70×10^6 K/s. In order to develop metallic glass, the empirical rules are; that the alloy should contain more than three constituent elements, a large difference of more than 12% in the atomic size of the constituent elements, and the mixing enthalpy of the elements should be negative [178]. Due to the small weight percentage of each element in H13 tool steel relative to the Fe content, only amorphous-like phase formation was observed and randomly distributed within the ultrafine ferrite, even though the H13 tool steel pools were highly undercooled.

5.2.2 Hardness Properties

The laser parameter settings in DOE2, DOE3, DOE4 and DOE5 were designed to produce a range of heating and cooling rates, and resulted in different grain compositions and sizes. The hardness properties of laser modified samples correspond to different hardening mechanisms. Two major strengthening mechanisms identified from the metallographic study were grain refinement and metastable phase formation. In steels, ferrite grain size refinement is an important method for improving both the strength and toughness as ferrite is the stable phase at ambient temperature [173]. Ultrafine-grained materials exhibit excellent mechanical properties compared with conventional fine-grained materials or coarse-grained materials [6, 72, 115, 116, 168]. Table 5.4 shows the range of average hardness measured in the as-received and modified samples of four of the conducted DOEs.

Table 5.4: Hardness properties of as-received and laser modified H13 tool steels at a range of heating rate and cooling periods.

Sample	As-received H13	Laser modified H13 tool steel			
		DOE2	DOE3	DOE4	DOE5
Range of hardness ($HV_{0.1}$)	280	724-1017	435-996	690-922	728-905
Range of H_R (10^6 K/s)	-	3.69-4.81	5.61-11.80	8.68-22.50	8.94-27.20
Range of $t_{cooling}$ (ms)	-	≤ 0.026	0.094-0.226	0.183-0.282	0.183-0.363
Range of C_R (10^6 K/s)	-	≥ 54.69	6.21-14.90	4.97-7.67	3.95-7.70

Increment of hardness properties in DOE2 samples was contributed to by grain refinement along with martensite phase presence which is in agreement with previous

work [127]. The offset grain size, on microhardness, by changing from 30 μm (pre laser treatment) to 200 nm (post laser treatment) was found to be consistent with the Hall-Petch relationship. The Hall-Petch behaviour can be observed for low-carbon steel with grain changing from micron to submicron, independent of production method, and is valid for grain size changing over a range of two orders of magnitude [125]. The hardness properties of DOE2 samples correspond to varied duty cycles and overlaps, which indicates the dual effect of pulse energy and residence time. From the developed design model, a high hardness modified surface can be produced at high pulse energy of 0.23 J with less than 20% overlap and at lower duty cycles from DOE2 in the range of 85 to 88%, see Figure 4.15. While using lower pulse energy of 0.17 to 0.19 J necessitates high duty cycle of more than 97% and overlap of at least 35%, see Figure 4.15. The pulse energy and residence time combination determines the surface heating rate and quench rate of undercooled austenite. At 100% duty cycle, samples were cooled more slowly which caused heat accumulation on the surface and variations in undercooling rate and effect. The cooling rate at 85% duty cycle was sufficient at low overlap for large undercooling and the production of ultrafine ferrite. At high duty cycles of 98 to 100% the hardness was maximum at 40% and 50% overlap due to the lower laser irradiance used (by setting a higher PRF) which allowed for larger undercoolings. Lower irradiance resulted in a higher cooling rate caused by a higher degree of undercooling [137].

In DOE3, hardness enhancement occurred due to grain refinement and the presence of a high volume fraction of grain boundaries in the modified layer. The Hall-Petch relationship describes the increase of flow stress with decreasing grain size [179]. The smaller spot size of 0.2 mm compared to the 0.4 mm spot size yielded higher irradiance and retained stress during surface processing. Variation of average hardness in the modified layer was due to changes in both the peak and average power settings. Though high peak and average power resulted in high hardness properties, in pulse laser processing mode the average power should be constant. Changing the peak power and duty cycle at constant average power is sufficient to alter the resulting properties of the processed surface [59]. Low hardness in sample N4, see Table 4.5, processed at 0.09 J pulse energy was due to insufficient pulse energy for phase transformation. At a pulse energy of 0.10 J, lower hardness properties were measured in sample N10 processed at 10% overlap in contrast to sample N24 with 50% overlap due to insufficient residence time at this setting and the longer cooling period of 0.208 ms compared to 0.160 ms, see Table 4.4. Longer residence time at this setting allowed phase transformation to approach completion and formed finer grains during the shorter cooling period of 0.160 ms. The highest hardness measured in the sample processed at 0.11 J pulse energy indicates that a

finer grain size ferrite was transformed from undercooled austenite at this higher irradiance and shorter residence time setting, see sample N12 in Table 4.4 and Table 4.5.

Even though a lower irradiance needs a longer residence time for surface melting, however, for grain refinement, the grain size depends on the cooling period and the effect of both irradiance and residence time setting on the sample surface temporal temperature. Variations of hardness indicated that surface re-melting from overlapped pulses caused tempering of the previous laser irradiated surface and heat accumulation increased the average global surface temperature. The hardness decrease at a surface depth of approximately 80 μm (depending on the modified surface geometry) was due to the lower cooling rate as surface depth increased. Low hardness properties were recorded from heat affected zone (HAZ) where formation of ferrite and pearlite structure mostly found in the HAZ decreased the hardness properties [127]. Yet, the measurements recorded in the HAZ were still higher than measured in the substrate as refinement of ferrite occurred at low undercooling which is found to improve both strength and ductility of the steel [172]. A reduction in ferrite grain size to 1 μm will significantly strengthen Fe compared to other structural metals [111].

Hardness properties measured in DOE4 and DOE5 were contributed to by the ultrafine grain size generated and metastable phase formation detected in the SEM micrographs. In DOE4 and DOE5, the average power was constant at 274 W while peak power was varied at three levels which resulted in a mean hardness of 800 $\text{HV}_{0.1}$ for both DOEs. At the same pulse energy of 0.09 J in DOE 4, the change of average hardness corresponded to residence time variations regardless of the peak power settings.

5.2.3 Surface Roughness

Surface roughness results varied with pulse energy and laser spot size as given in Table 5.1. In DOE2 a range of average surface roughness (R_a) was achieved between 3.5 and 38.2 μm with the two significant factors identified as overlap and duty cycle, which are in agreement with previous work [53, 70]. The minimum surface roughness was achieved in samples processed at the minimum overlap of 10% and at a duty cycle of 85%. This which resulted from a lower number of pulses from 10% overlap compared to 30% overlap. Increasing both the number of pulses and the duty cycle increased the material-laser interaction time which leads to higher laser energy absorption [3, 50]. When more laser energy was absorbed the surface temperature increased and formed irregular geometries which increased the surface roughness [19, 74].

A lower range of surface roughness was recorded in DOE3 samples compared to DOE2 samples due to the smaller laser spot size of 0.2 mm used in sample processing. Although high irradiance settings at 0.2 mm spot size might cause an increase of surface roughness, the pulse energies and widths were reduced compared to samples processed in DOE2 [7, 19, 76]. Among the samples processed using 0.2 mm spot size, the surface roughness was lower in sample N4 where the pulse energy was lowest at 0.9 J, see Table 4.6. Higher surface temperature which resulted from a higher irradiance, improved the surface absorptance which promoted energy penetration and efficient surface melting. While increased overlap affected the residence time, 50% overlap setting increased the surface temperature compared to 10% overlap. The surface temperature was lower for processing with smaller pulse energy and improved surface topography resulted.

Higher laser irradiance was designed into sample processing conditions for the 0.09 mm spot size (DOE5), with three levels of peak power. A higher range of surface roughness was measured for these samples, between 1.8 and 22.4 μm , in comparison to measurements taken from samples processed with a 0.2 mm spot size. Increase of surface roughness for sample N24 from DOE3 was contributed to by the high duty cycle setting of 50% at the low peak power of 760 W. While duty cycle determines the pulse duration, an increase of overlapped pulses prolongs the laser-surface interaction time, both of which affect the surface temperature.

5.2.4 Statistical Analysis

(a) Modified Surface Depth

The cubic model selected for modified surface depth response was aliased. Some of the main interaction effects were insignificant. Using the stepwise elimination method, the model was reduced and the insignificant terms were automatically removed. Reducing the design model by removing the insignificant terms has been illustrated in previous work [161]. Though the initial model was aliased, the reduced model was significant and fitted well with the three key factors of peak power, overlap and PRF affecting the modified surface. The factor interactions were sufficient to achieve the design goal and were consistent with findings in DOE3 and DOE4.

The contour plot of PRF and overlap against peak power showed an elliptical shape which suggests factor interactions [180]. In DOE5, variation of pulse energy was investigated to obtain the optimised parameters for enhanced surface properties. Peak power settings remained as they were in DOE4, while the overlap range was reduced. The pulse energy resulting from PRF setting controlled the surface temperature. At higher pulse energy and

residence time, the sample temperature raised which increased sample surface absorptance [63]. Therefore, maximum modified surface depth, 150 μm , was formed at 2300 Hz PRF and 760 W peak power settings where the laser 'on' state was longer, for sample F1, see Table 3.9 and Table 4.8. The modified surface depth also increased with increasing overlap percentage due to increasing laser-material interaction time, see Figure 4.33. Longer laser-material interaction time/ residence time delayed surface cooling which is a disadvantage for enhanced surface morphology as shown in sample F1, see Figure 4.27 (d).

(b) Hardness Properties

A quadratic model was generated for the hardness response where the peak power was an insignificant factor for DOE5, see Figure 4.3. For the hardness response, the quadratic model was not aliased which allowed all interaction effects to be estimated. The insignificant terms were not removed as the original model was significant and well fitted. In this model, peak power was however insignificant as supercooling of austenite occurred within the irradiance and residence range. Supercooled austenite transformation to ultrafine grain refinement due to rapid laser pulse heating and cooling, yielded high hardness in the modified surface. Though the peak power term was insignificant, its interaction with other factors was significant in determination of the hardness properties.

The elliptical shape of contour plots for PRF and overlap against peak power, and overlap against PRF graphs suggested factor interactions with respect to the hardness response. The main cause of hardness variation was due to the three levels of pulse energy. The peak power and PRF interaction effect was significant. The maximum hardness achieved at minimum overlap of -10%, 1515 W peak power and 2300 Hz PRF was due to rapid solidification of supercooled austenite at a low duty cycle of 18%. The maximum hardness was resulted from the heating rate of 17.83×10^6 K/s at the highest pulse energy of 0.12 J and 0.08 ms residence time, see sample F2 in Table 4.8. The surface was solidified within a cooling period of 0.356 ms which was adequate to supercool the austenite phase and form ultrafine ferrite. The minimum hardness was measured from the sample processed at 0.08 J pulse energy and 0.06 ms residence time, see sample F10 in Table 4.8. The surface was melted at a heating rate of 22.67×10^6 K/s and consequently supercooled at a short cooling period of 0.195 ms. At this short cooling period, the austenite-ferrite transformation was interrupted and caused heat accumulation on the surface when subsequent pulses struck. Both heating rate and cooling time are significant parameters in laser surface modification in order to control the size of the microstructurally altered surface. The indentation marks in Figure 5.8 were observed on the sample cross section.

Smaller grain size in modified layer resulted in small indentation mark which exhibit higher hardness.

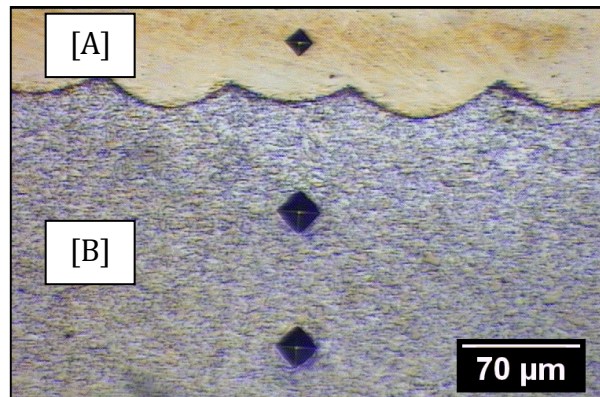


Figure 5.8: Increase of indentation mark diameter from modified surface [A] to substrate material [B] for sample F11.

The interaction of overlap and peak power shows high hardness was achieved at diagonal regions of the contour plot where the overlap and power was maximum, see Figure 4.38. Increasing the overlap at the lower power of 760 W was beneficial to increase the hardness. The changes in hardness were due to a balance interplay of residence time and pulse energy on the modified surface during processing. On the other hand, the mechanical properties were more homogenous at the 0% overlap [25].

The interaction of overlap and PRF setting indicates an increase of hardness properties with decreasing PRF due to larger supercooling during phase transformation. The overlap-PRF interaction effect on hardness properties was weak in contrast to the overlap-peak power interaction as both overlap and PRF were time based parameters. While peak power contributes to pulse energy, changes in overlap affect the residence time and consequently the surface cooling rate.

(c) Surface Roughness

The fit model for the DOE5 surface roughness response was cubic with eight significant terms. In this model, the overlap was an insignificant term as minimum surface roughness can be achieved at any overlap provided that the pulse energy and residence time were balanced to produce a supercooled surface. Many models work better as prediction equations without including the insignificant factors [181]. At 0.09 mm spot size, the laser irradiance was high which melted a large region allowing melt pool interaction from subsequent pulses for minus 10% overlap.

The range of surface roughness was broader in DOE5 compared to the other three DOEs due to the three levels of pulse energy used. Pulse energy setting has a significant effect for variation of surface roughness. In DOE5 the surface roughness decreased in samples processed at 0 % or -10 % overlap due to the short residence time. The residence time or material-laser interaction time at -10 % overlap was shorter than the time computed at 10 % overlap due to changes in the sample traverse speed. The residence time was computed from laser spot size, traverse speed and duty cycle, see Equation 4 in Appendix B. The resulting actual interaction time between the laser and material surface during processing was decreased as the overlap decreased at constant peak power and PRF. Low PRFs tend to produce high pulse energies which can roughen the surface at prolonged exposure to the laser energy [60, 74]. This explanation supports the surface roughness decrease with increasing PRF and decreasing residence time. Rapidly melted and solidified H13 surface by high pulse energy yields smaller grain size in the modified layer which exhibited higher hardness.

The contour plot of PRF against peak power indicates decreasing surface roughness with increasing peak power and PRF which explains the advantage of lower energy in laser surface processing, see Figure 4.42. In laser surface modification, high peak power setting was coupled with low duty cycle, while vice versa for low peak power, in order to obtain a similar proportion of the irradiance to residence time (I/T_R) setting.

The circular shape from the contour graph of overlap and peak power interaction suggests a level of interaction of these factor effects [180]. At high PRF, variation of overlaps and peak power to reduced surface roughness was insignificant due to the low pulse energy operation [19]. The overlap-power interaction was found significant at the lower PRFs of 2900 Hz or less.

Design Optimisation

The optimisation process involved combining the goals into the overall desirability function. A maximum desirability of one was set as the goal to be accomplished from the 28 parameter settings with high priority of minimising the surface roughness response. The hardness factor goal was set within a range of upper and lower limits because the results were already higher than found in previous works [3, 40, 55, 56, 65]. The modified surface depth range was less than found in some previous works. However in terms of hard surfacing or coating, the modified surface depth range coupled with high hardness achieved was applicable for wear resistant components. A thin and thick duplex coating system on H13 tool steel was previously presented between 3.0 ± 0.17 and 8.3 ± 0.16 μm respectively [182]. Other multilayer type of thin coatings found on die tools had a

thickness measurement of $2.875 \pm 0.074 \mu\text{m}$ [84]. Nevertheless, the laser modified surface is known to be well-bonded to the substrate and can fulfil the interfacial bonding strength requirement in coated surface [6]. The surface roughness response was minimised with high importance to meet die application requirement of less than $5.0 \mu\text{m Ra}$ [58]. In many engineering applications, minimum surface roughness is important to inhibit premature failure of components that generally initiate on the surface [77, 142, 183].

5.2.5 EDXS Analysis

The EDXS results showed that higher carbon percentage was detected in the as-received H13 tool steel when compared to the composition measured by spark light emission spectroscopy, see Table 3.1 in § 3.1. EDXS is commonly known however to produce C concentration results than are actually present due to the lack sensitivity of the lower mass elements. In the EDXS analysis, the untreated H13 tool steel cross section was measured from sample F10 substrate region. The high rate of heating and cooling during processing had possibly increased the percentage of C through diffusion. However, as the measurements were carried out deeper into the substrate, the cooling rate was much slower than the processed surface which explains the uniform distribution of elements in the selected area, see Figure 4.45 and Table 4.17.

The parameters used in modifying the H13 tool steel samples caused variation of elements composition. By heating the sample surface at its liquidus temperature of 1454°C the elements were redistributed. From the analysis conducted for DOE2 samples which were processed at pulse energies of 0.19, 0.20 and 0.23 J, the existence of the elements like Mo, Cu and Ni, and the range of the elements composition in the modified layer were determined. Diffusion of elements occurred during laser heating as the modified layer composition changed from that of the H13 tool steel substrate. Diffusion possibly occurred for C, Cr, Cu and S elements. The C diffusion was identified in the three samples (E8, E15 and E27) as the C content was higher when compared to the EDXS measurements of the H13 tool steel substrate. Increased pulse energy increased the sample temperature which increased the atomic diffusion rate. For sample E8, the high pulse energy of 0.23 J had resulted in a high diffusion rate in the molten surface. However under a high cooling rate, the rapid decrease of melt temperature trapped the atoms in their location. It seemed that the presence of elements in the modified layer was dependant on the energy, residence time and speed of undercooling during processing. The effect of higher laser scan speed on lowering the elements diffusion in molten region was also reported in previous works [46].

In DOE5 samples, the higher irradiance settings with 0.08, 0.10 and 0.12 J pulse energy had caused more diffused elements in the modified layer. In sample F1 and F8, with the range of cooling rates 5.06×10^6 to 5.09×10^6 K/s, sulfur diffusion occurred; see Table 4.20. Sulfur diffuses in steels at high temperatures (more than 1000°C). A similar finding was reported previously [184]. For all four DOE5 samples, Ni diffusion possibly occurred in the modified layer due to the higher irradiance used during processing compared to DOE2. In general, Ni diffusion in steel occurs at high temperature (over 1100°C) [185]. A Ni diffusion was observed in all four samples of DOE5 where the irradiances were between 119,297 and 216,449 W/mm^2 . These irradiances increased the sample surface temperature rapidly at shorter residence times compared to the lower irradiances and longer residence times in DOE2. The shorter residence time in sample F8 from DOE5 produced a higher composition of Cr and Mo elements in the modified layer when compared to other three samples. Shorter residence time increased the undercooling speed which possibly stopped the diffusion earlier than in other samples.

5.2.6 XRD Analysis

The peak reflection analysis of the modified samples conducted between 30 to 70° Bragg's angle was sufficient to investigate the phase crystallinity and broadening effect of the (110) α -Fe phase. The α -Fe phase expresses super saturation solid solution martensite and ferrite [186]. Peak reduction occurred in all laser modified samples with maximum reduction in samples X2 and X5 shown in Figure 4.55. Since sharp and strong peaks show a well-crystalline nature of α -Fe phase, the peak intensity reductions resulted from decreasing phase crystallinity [187]. The finding on decreasing phase crystallinity also supports the supercooled austenite transformation discussion earlier.

Referring to the processing parameter effects on samples in Table 4.21, the smaller spot size of 0.09 mm resulted in a more rapid heating rate compared to 0.2 and 0.4 mm spot size due to the combination of settings of high irradiance and short exposure time. Longer exposure times were necessary when processing samples at low laser irradiance to allow surface melting to take place. A low heating rate and small undercooling interplay in sample E8 and E15 to produce martensite phase during processing, see Figure 4.53. A similar peak traced at 35° angle position was referred to as structural transformation in water quenched Fe-Ga alloys after being heat treated at 1000°C [100]. At $4,600 \text{ W}/\text{mm}^2$ laser irradiance and 0.34 ms exposure time, the (110) and (200) α -Fe crystalline peaks intensity of sample E15 were reduced, see Figure 4.53 (a). A small increase of heating rate ($5,548 \text{ W}/\text{mm}^2$ laser irradiance and 0.32 ms exposure time) was adjusted for sample E8 which suppressed the (200) α -Fe peak, see Figure 4.53 (b).

In Table 4.21, the laser irradiances for sample N4 and N12 were 10,930 W/mm² and 28,184 W/mm² with residence times of 0.25 and 0.12 ms respectively. The martensite peak was absent in both samples N4 and N12. A noticeable change was the intensity of the (200) α -Fe peak decreased 10 % more in sample N12 in contrast to N4 due to higher laser irradiance. The samples processed at spot size of 0.09 mm indicated the presence of a small amount of randomly distributed nano-subgrains in the laser modified surface from the decrease of the crystalline peak intensity, see Figure 4.23. The findings show significant effect of heating rate where at low irradiance and longer exposure time combination, the martensitic transformation was initiated. Whereas, the large undercooling allowed for the martensitic transformation to be skipped and suppressed several long range order peaks.

The formation of nano size and ultra fine size grain structures in the modified layer corresponds to the diffraction peak intensities found in the XRD analysis. A small broadening effect occurred in the diffracted peaks of the modified surface due to an increase of grain boundaries from ultra-fine size sub-grain formations. In sample E15 and E8, one of the factors which caused grain refinement was the growth and evolution of martensite phase due to grain-subgrain boundaries and lattice structure changes under the specific variation in temperature [188, 189]. The broadening effect investigated is also correlated with the mechanical properties of steel where ultrafine grain exhibits high strength and good ductility in metallic materials [190, 191].

Formation of Martensite and Metastable Phases

As highlighted in the previous section, samples processed at 0.4 mm spot size underwent martensitic transformation with refined grains. The (211) martensite peak reflected was due to martensitic transformation from surface tempering. Grain refinement resulted from the laser energy which caused undercoolings and severe plastic deformation. The majority of nano-crystalline α' (bcc) resulted from the austenite to martensite ($\gamma \rightarrow \alpha'$) transformation during severe plastic transformation [117]. Generally, martensitic transformations are characterised by a diffusionless change in crystal structure. When the laser beam melted the surface at 0.4 mm spot size, the consequent rapid cooling rate caused martensitic transformation to occur. At the same time, the heat from processing increased the sample temperature which functioned to cause heat accumulation in the sample. Tempering effect then could take place on the martensitic structure due to the entrapped heat resulting in reduced cooling rates. In Fe-based alloys, the temperature dependant martensitic structure, α' was found at the grain-subgrain boundaries [188].

The anomalous phases are the most similar to quasicrystalline or metastable phases as referred to in previous works [102, 122]. Besides, metastability presents in grain refinement of undercooled melts [192]. The anomalous peaks were observed to split from the main (110) α -Fe peak due to formation of metastable phases during laser processing and could not be indexed on BCC or FCC symmetry. The peak splitting of X-ray diffraction is connected with the coexistence of rhombohedral and tetragonal phases and the presence of small-angle grains in the crystal [193-195]. However, the sharp peaks reflected were close to the characterisation of quasi-crystalline materials which contained non-periodic long range order featuring non-crystallographic symmetry [122]. The quasi-crystalline state is between the crystalline and amorphous phase [102]. The rapid heating and cooling rate during laser surface modification could yield the quasi crystalline phase. The preliminary results showed the metastable phases were affected by the pulse energy. The presence of metastable phase peaks were more reflected in the sample processed at the low pulse energy of 0.08 J, see Figure 4.58 (c). The findings are similar with those of previous works where formation and evolution of quasicrystalline phase can occur at either rapid or during conventional solidification from the melt [94, 102, 196]. In this way, novel materials can be developed by laser surface modification without being restricted by the equilibrium phase diagram [175].

5.3 Thermal Modelling Simulations of Laser Surface Modification of H13 Tool Steel

Temperature Distribution in Modified Surface

The analytical thermal model used to predict the temperature distribution of the pulsed laser surface modified H13 tool steel sample (F13) shows that the temperatures achieved were correlated with the micro-structural changes as determined from the metallographic study. Surface absorptance input was set as 60% of the pulse energy and simulation outputs were used to visualise the thermal field. The actual laser pulse energy absorbed depends on many factors including surface roughness, material type, laser wavelength and sample temperature. Therefore, nominal temperature values were used in this work instead of actual calculated temperature values. Heating and cooling rates are significant values in laser surface modification in order to control the size of the micro-structurally altered region after solidification. Prolonged heating rates results in heat accumulation in the surface and delays the solidification process which affects the grain size and hardness properties. The simulation considered constant thermal properties of H13 steel

throughout the process, therefore the modified layer shown by simulation was slightly deeper than that seen in the experimental results.

Effect of Heating and Cooling Rate on Hardness Properties

The simulations of temperature distribution in the pulse laser glazed surface can allow for prediction of the heating and cooling rate at specific points in the molten pool. Decreased cooling rate from the centre to the edge of the molten pool in the simulation was due to temperature drop at liquid-solid interface. The cooling rate at the liquid-solid transient boundary of the molten pool determines the solidification process and microstructure [197]. The heating and cooling rates were correlated with the hardness of the processed samples. The maximum hardness of 824 HV_{0.1} was achieved at a nominal heating to cooling rate ratio of 1.94. At higher Z values, lower heating and cooling rates occurred with corresponding reductions in the micro-hardness. In comparison to the substrate hardness of 280 HV_{0.1}, the laser surface modification produced an extremely hard surface which was at least three times higher than the substrate. There exists a strong relationship between reductions of micro-hardness and decreases of heating and cooling rate. The simulation findings can therefore be used to predict the hardness properties measured experimentally. This model was found to be useful and important for the provision of surface modification process maps for use with the pulse laser mode.

CHAPTER 6

Conclusion

6.1 Conclusion

The findings presented in this thesis can be concluded to several important points:

(a) DOE

Designs of experiment were developed to investigate the significance of each laser parameter on the surface properties and achieved optimised processing parameters. At the end of the parameter investigation it was found that, a deeper modified surface depth was developed by focusing the laser beam underneath the sample surface. By decreasing the laser spot size to process the samples, a definite size of molten pool developed from laser processing was achieved. Thus, overlap calculation was more precise which allowed generation of a continuous modified surface using pulsed laser processing.

Designing the overlap at constant PRF was successful to minimise the surface roughness properties. In order to process other sample geometries, the surface traverse speed at particular laser irradiance was found to be important factor to produce a specific surface roughness. The determined and investigated combinations of laser irradiance and residence time to process H13 tool steel samples were capable to produce supercooled surfaces with enhanced hardness properties.

(b) Metallographic Study

From the metallographic study, a significant effect of laser parameters on the modified surface depth, grain size and composition was determined. A summary of modified surface depth and grain size range, and grain composition of the as-received sample and samples from each DOE is given in Table 6.1. The overlapped pulses design and surface absorptance design developed in DOE3, DOE4 and DOE5 successfully produced a uniform modified surface with enhanced surface properties.

Table 6.1: Summary of metallographic study findings of as-received and laser modified H13 tool steel for the different DOE.

Sample characteristic	As-received	Laser modified H13 tool steel				
		DOE1	DOE2	DOE3	DOE4	DOE5
Average modified surface depth range (μm)	-	0-29	46-180	48-80	42-88	37-150
Feret grain size range (μm)	3.00-9.00	Not measured	2.54-5.99	1.60 -2.83	0.51-1.09	0.40-1.25
Grain composition	α -ferrite, martensite phase with M_{23}C_6 and M_7C_3 carbides (M=Cr, Fe)	Not measured	α -ferrite and lath martensite phase	α -ferrite and martensite phase at grain boundaries	α -ferrite and metastable phases-amorphous and quasi-crystalline	α -ferrite and metastable phases-amorphous and quasi-crystalline

(c) Hardness

The laser modified surface hardness properties were enhanced to greater than three times higher than the unmodified H13 tool steel substrate in the DOEs. Increase of hardness due to grain size decrease was in agreement with the Hall-Petch relationship. The laser irradiance and residence time variations at three different laser spot sizes used in the processing were suitable to enhance the surface hardness. In many previous works maximum hardness obtained in laser modified H13 tool steel was between 243 and 700 $\text{HV}_{0.1}$. In this research, the hardness achieved from design optimisation was from 435 to 996 $\text{HV}_{0.1}$ for all DOEs and from 728 to 905 $\text{HV}_{0.1}$ (61 to 67 HRC) from DOE5. Hardness properties are important in order to allow the laser modified surface to be used and developed for specific engineering applications.

(d) Surface roughness

Significant decrease of surface roughness with variation of laser parameter was achieved in laser surface modification of H13 tool steel. Component failure often initiates at the surface, the surface roughness requirement of $R_a < 5 \mu\text{m}$ commonly used for semi solid metal processing tooling applications. Table 6.2 shows the summarised results from four DOEs which indicate the minimum surface roughness achieved in the samples.

Table 6.2: Surface roughness of laser modified H13 tool steel from different DOE.

	DOE2	DOE3	DOE4	DOE5
Range of average surface roughness (μm)	3.5-38.2	3.1-7.9	3.2-9.5	1.8-22.4

(e) EDXS

Change of elements composition in the modified layer region was detected in DOE2 and DOE5 samples. The surface composition variation was due to the processing parameters: irradiance, pulse energy, residence time and the resulting heating and cooling rates. Heating the samples at high temperature allowed atomic diffusion to occur. The rapid drop of temperature which provided the stopped further atomic diffusion and then froze the present structure in place. Higher irradiances and shorter residence times in DOE5 caused a greater degree of element diffusion compared to DOE2.

(f) XRD

A significant decrease of α -Fe crystallinity and development of metastable phases were identified in the laser modified surface. Decreasing phase crystallinity and phase transformation variation in the laser modified surface were dependant on processing parameter settings, in particular the laser spot size. Processing the H13 tool steel samples using a laser spot size of 0.4 mm yielded martensite phase. Absence of martensite phase in samples processed at 0.2 and 0.09 mm laser spot size was due to the higher cooling rate on the sample surface. However, previous works indicate that the anomalous peaks developed in the samples processed at 0.2 and 0.09 mm laser spot size were possible to be identified in quasicrystalline phases. These findings reveal the phase source of the hardening mechanism and grain composition in the laser modified surface.

(g) Thermal modelling

In this work, an analytical thermal model was used to predict the temperature distribution of the pulsed laser modified samples. The temperatures achieved were correlated with the position of the microstructural changes as determined from the experimental work. The heating and cooling rates were correlated with hardness values achieved at various steps. This model was shown to be useful for the determination of laser parameters for surface hardening. The simulations of temperature distribution in pulse laser glazed surface can predict the heating and cooling rate at specific points in the molten pool. By evaluating these rates, the hardness of the processed samples can be determined. The hardness of 882 HV was achieved at nominal heating to cooling rate ratio of 1.94. At higher Z (surface depth) values, lower heating and cooling rates occurred with corresponding reductions in the micro-hardness. The findings are important for the provision of pulse laser surface modification process maps.

(h) Process optimisation

One set of optimised processing parameters were found at 1138 W peak power, 3500 Hz PRF and -10% overlap which produced a hardened surface of 728 HV_{0.1} with minimum average surface roughness of 1.8 µm and modified layer depth range between 42 and 50 µm. The R_a parameter was selected with minimum surface roughness as the highest desirability factor due to its importance in many engineering applications. The modified layer depth range at minimum surface roughness was also sufficient to act as a thermal barrier coating and protect the substrate. The hardness of sample processed at these parameters was 2.6 times higher than measured in the substrate. These findings are significant for the development of high hardness and smooth surface in many applications like dies, moulds and other toolings.

6.2 Future Work

Future works propose in this field include, analysis of surface cooling and heating rate using high magnification and temperature thermal camera. A detail study on molten pool properties of modified surface is crucial to create quasicrystal or amorphous surface in high %Fe content alloys. Amorphous alloys have been commercialised in many wear resistant applications due to their unique properties, however little information is available in the literature on developing amorphous surface on Fe-based alloy substrates.

Investigation of laser modified phase using transmission electron microscope (TEM) is important to study the presence of quasicrystalline phases and their properties. Supercooled surfaces contain superior properties compared to the substrate due to grain refinement and phase transformations. In many alloys especially Fe based, quasicrystals have not been properly characterised. Thus, by revealing the phase properties and stability, laser modified Fe-based alloy surfaces could be exploited in many interesting applications especially where application at elevated temperature (more than 1000°C) is required.

As the laser glazed surface has a reduced coefficient of thermal expansion compared to the substrate; ceramic coating of the glazed surface should be investigated to examine the potential benefits from functional grading of the thermal expansion coefficients and hence better adhesion and life time from the coating.

Bibliography

- [1] Klobčar D, Tušek J, Taljat B. Thermal fatigue of materials for die-casting tooling. *Materials Science and Engineering: A*. 2008;472(1-2):198-207.
- [2] Shah SV, Dahotre NB. Laser surface-engineered vanadium carbide coating for extended die life. *Journal of Materials Processing Technology*. 2002;124(1-2):105-112.
- [3] Jiang W, Molian P. Nanocrystalline TiC powder alloying and glazing of H13 steel using a CO₂ laser for improved life of die-casting dies. *Surface and Coatings Technology*. 2001;135(2-3):139-149.
- [4] Sjöström J, Bergström J. Thermal fatigue testing of chromium martensitic hot-work tool steel after different austenitizing treatments. *Journal of Materials Processing Technology*. 2004;153-154:1089-1096.
- [5] Matthews D.T.A, Ocelík V, deHosson J.T.M. Tribological and mechanical properties of high power laser surface-treated metallic glasses. *Materials Science and Engineering: A*. 2007;471(1-2):155-164.
- [6] DiMelfi RJ, Sanders PG, Hunter B, Eastman JA, Sawley KJ, Leong KH, et al. Mitigation of subsurface crack propagation in railroad rails by laser surface modification. *Surface and Coatings Technology*. 1998;106(1):30-43.
- [7] Pinkerton AJ, Li L. An investigation of the effect of pulse frequency in laser multiple-layer cladding of stainless steel. *Applied Surface Science*. 2003;208-209:405-410.
- [8] Tsai H.L., Tsai P.C. Performance of laser-glazed plasma-sprayed (ZrO₂-12wt.%Y₂O₃)/(Ni-22wt.%Cr-10wt.%Al-1wt.%Y) thermal barrier coatings in cyclic oxidation tests. *Surface and Coatings Technology*. 1995;71(1):53-59.
- [9] Kumar VC. Process parameters influencing melt profile and hardness of pulsed laser treated Ti-6Al-4V. *Surface and Coatings Technology*. 2006;201(6):3174-3180.
- [10] Mioković T, Schulze V, Vöhringer O, Löhe D. Influence of cyclic temperature changes on the microstructure of AISI 4140 after laser surface hardening. *Acta Materialia*. 2007;55(2):589-599.
- [11] Kalyon M, Yilbas BS. Laser pulse heating: a formulation of desired temperature at the surface. *Optics and Lasers in Engineering*. 2003;39(1):109-119.

- [12] Transient Heat Conduction in Semi-Infinite Solids Irradiated by a Moving Heat Source. Proceedings of the COMSOL Users Conference 2007: COMSOL; 2007.
- [13] Srivastava A, Joshi V, Shivpuri R. Computer modeling and prediction of thermal fatigue cracking in die-casting tooling. *Wear*. 2004;256(1-2):38-43.
- [14] Conde JC, Lusquiños F, González P, León B, Pérez-Amor M. Temperature distribution in a material heated by laser radiation: modelling and application. *Vacuum*. 2002;64(3-4):359-366.
- [15] Pereira A, Delaporte P, Sentis M, Cros A, Marine W, Basillais A, et al. Laser treatment of a steel surface in ambient air. *Thin Solid Films*. 2004;453-454:16-21.
- [16] Majumdar JD, Manna I. Laser processing of materials. *Sadhana*. 2003;28:495-562.
- [17] Xia Y, Liu W, Xue Q. Comparative study of the tribological properties of various modified mild steels under boundary lubrication condition. *Tribology International*. 2005;38(5):508-514.
- [18] Dadbin S. Surface modification of LDPE film by CO₂ pulsed laser irradiation. *European Polymer Journal*. 2002;38(12):2489-2495.
- [19] Panagopoulos CN, Markaki AE, Agathocleous PE. Excimer laser treatment of nickel-coated cast iron. *Materials Science and Engineering A*. 1998;241(1-2):226-232.
- [20] Shiner B. High-power fiber lasers gain market share. 2006;(Feb 2006).
- [21] Sánchez-Santana U, Rubio-González C, Gomez-Rosas G, Ocaña JL, Molpeceres C, Porro J, et al. Wear and friction of 6061-T6 aluminum alloy treated by laser shock processing. *Wear*. 2006;260(7-8):847-854.
- [22] Wang F, Yao Z, Deng Q. Experimental study on laser shock processing of brass. *Journal of University of Science and Technology Beijing, Mineral, Metallurgy, Material*. 2007;14(6):529-532.
- [23] Rana J, Goswami GL, Jha SK, Mishra PK, Prasad BVSSS. Experimental studies on the microstructure and hardness of laser-treated steel specimens. *Optics & Laser Technology*. 2007;39(2):385-393.
- [24] Wagner K, Putz A, Engel U. Improvement of tool life in cold forging by locally optimized surfaces. *Journal of Materials Processing Technology*. 2006;177(1-3):206-209.

- [25] Van Ingelgem Y, Vandendael I, Van den Broek D, Hubin A, Vereecken J. Influence of laser surface hardening on the corrosion resistance of martensitic stainless steel. *Electrochimica Acta*. 2007;52(27):7796-7801.
- [26] Xu Z, Leong KH, Reed CB. Nondestructive evaluation and real-time monitoring of laser surface hardening. *Journal of Materials Processing Technology*. 2008;206(1-3):120-125.
- [27] Real-Time Monitoring of Laser Transformation Surface Hardening of Ferrous Alloys. International Congress on Applications of Lasers and Electro-Optics; Nov. 15-18, 1999; ; 1999.
- [28] Yang Y, Song Y, Wu W, Wang M. Multi-pass overlapping laser glazing of FeCrPC and CoNiSiB alloys. *Thin Solid Films*. 1998;323(1-2):199-202.
- [29] Wear and porosity of electrodeposited gold contacts: the effect of laser glazing the substrate metal. *Electrical Contacts, 1989*, Proceedings of the Thirty Fifth Meeting of the IEEE Holm Conference on; 1989.
- [30] Aldajah SH, Ajayi OO, Fenske GR, Xu Z. Effect of Laser Surface Modifications Tribological Performance of 1080 Carbon Steel. *Journal of Tribology*. 2005;127(3):596-604.
- [31] Prakash B, Hiratsuka K. Sliding wear behaviour of some Fe-, Co- and Ni-based metallic glasses during rubbing against bearing steel. *Tribology Letters*. 2000;8(2):153-160.
- [32] Basu A, Chakraborty J, Shariff SM, Padmanabham G, Joshi SV, Sundararajan G, et al. Laser surface hardening of austempered (bainitic) ball bearing steel. *Scripta Materialia*. 2007;56(10):887-890.
- [33] Tondur S, Schnick T, Pawlowski L, Wielage B, Steinhäuser S, Sabatier L. Laser glazing of FeCr-TiC composite coatings. *Surface and Coatings Technology*. 2000;123(2-3):247-251.
- [34] Sreedhar C, Santhanakrishnan G, Gokularathnam CV, Krishnamurthy R. Effect of processing parameters on the laser glazing of plasma-sprayed alumina-titania ceramic. *Journal of Materials Processing Technology*. 2001;114(3):246-251.
- [35] Heitkemper M, Bohne C, Pyszalla A, Fischer A. Fatigue and fracture behaviour of a laser surface heat treated martensitic high-nitrogen tool steel. *International Journal of Fatigue*. 2003;25(2):101-106.

- [36] Colaço R, Gordo E, Ruiz-Navas EM, Otasevic M, Vilar R. A comparative study of the wear behaviour of sintered and laser surface melted AISI M42 high speed steel diluted with iron. *Wear*. 2006;260(9-10):949-956.
- [37] Liu Z, Chong PH, Skeldon P, Hilton PA, Spencer JT, Quayle B. Fundamental understanding of the corrosion performance of laser-melted metallic alloys. *Surface and Coatings Technology*. 2006;200(18-19):5514-5525.
- [38] Ryan P, Prangnell PB. Grain structure and homogeneity of pulsed laser treated surfaces on Al-aerospace alloys and FSWs. *Materials Science and Engineering: A*; In Press, Corrected Proof:1310.
- [39] Chuang Y, Lee S, Lin H. Effect of temperature on the sliding wear behavior of laser surface alloyed Ni-base on Al-Mg-Si alloy. *Applied Surface Science*. 2006;253(3):1404-1410.
- [40] Lee J, Jang J, Joo B, Son Y, Moon Y. Laser surface hardening of AISI H13 tool steel. *Transactions of Nonferrous Metals Society of China*. 2009;19(4):917-920.
- [41] Yue T.M., Yan L.J., Chan C.P., Dong C.F., Man H.C., Pang G.K.H., Excimer laser surface treatment of aluminum alloy AA7075 to improve corrosion resistance. *Surface and Coatings Technology*. 2004;179(2-3):158-164.
- [42] Olsen F.O., Alting L. Pulsed Laser Materials Processing, Nd-YAG versus CO₂ Lasers. *CIRP Annals - Manufacturing Technology*. 1995;44(1):141-145.
- [43] Mondal AK, Kumar S, Blawert C, Dahotre NB. Effect of laser surface treatment on corrosion and wear resistance of ACM720 Mg alloy. *Surface and Coatings Technology*. 2008;202(14):3187-3198.
- [44] Selvan JS, Subramanian K, Nath AK. Effect of laser surface hardening on EN18 (AISI 5135) steel. *Journal of Materials Processing Technology*. 1999;91(1-3):29-36.
- [45] Fan C, Zhang M. Some Fractal Structures in Rapidly Solidified Al-Mn Alloy. *Acta Metallurgica Sinica*. 1992;5(3):203-205.
- [46] S.-S. Deng and S.C. Wang, editor. Laser glazing study of Fe-based alloy and Co-based alloy. *Society of Photo-Optical Instrumentation Engineers (SPIE) Conference Series*; sep; ; 1996.

- [47] Deng S, Wang SC, editors. Research on Critical Factors of CW Laser glazing of Fe-C-Si-B Alloy. Laser Processing of Materials and Industrial Applications: SPIE; 1996.
- [48] Hetzner DW. Refining carbide size distributions in M1 high speed steel by processing and alloying. *Materials Characterization*. 2001;46(2-3):175-182.
- [49] Dallaire S, Cielo P. Pulsed laser glazing. *Thin Solid Films*. 1983;108(1):19-27.
- [50] Batista C, Portinha A, Ribeiro RM, Teixeira V, Costa MF, Oliveira CR. Surface laser-glazing of plasma-sprayed thermal barrier coatings. *Applied Surface Science*. 2005;247(1-4):313-319.
- [51] Alsultanny YA. Laser Beam Analysis Using Image Processing. *Journal of Computer Science*. 2006;2(1):109-113.
- [52] Han L, Liou FW. Numerical investigation of the influence of laser beam mode on melt pool. *International Journal of Heat and Mass Transfer*. 2004;47(19-20):4385-4402.
- [53] Shin HJ, Yoo YT. Microstructural and hardness investigation of hot-work tool steels by laser surface treatment. *Journal of Materials Processing Technology*. 2008;201(1-3):342-347.
- [54] Bordatchev EV, Nikumb SK. Effect of focus position on informational properties of acoustic emission generated by laser-material interactions. *Applied Surface Science*. 2006;253(3):1122-1129.
- [55] Brabazon D, Naher S, Biggs P. Glazing of tool dies for semi-solid steel forming. *International Journal of Material Forming*. 2008;1(0):985-988.
- [56] Brabazon D, Naher S, Biggs P. Laser surface modification of tool steel for semi-solid steel forming. *Solid State Phenomena*. 2008;141-143:255-260.
- [57] Nagai T, Hattori H, Utsunomiya T, Fujioka J, Uemura M. Relationship between the cooling rate and the formation of chilled microstructure for laser melting of cast Iron (Report1). *Quarterly Journal of the Japan Welding Society*. 2003;21:466-473.
- [58] Hamasaiid A, Dour G, Loulou T, Dargusch MS. A predictive model for the evolution of the thermal conductance at the casting-die interfaces in high pressure die casting. *International Journal of Thermal Sciences*. 2010;49(2):365-372.

- [59] Mahmoudi B, Torkamany MJ, Aghdam ARSR, Sabbaghzade J. Laser surface hardening of AISI 420 stainless steel treated by pulsed Nd:YAG laser. *Materials & Design*. 2010;31(5):2553-2560.
- [60] Issa A, Brabazon D, Hashmi MSJ. 3D transient thermal modelling of laser microchannel fabrication in lime-soda glass. *Journal of Materials Processing Technology*. 2008;207(1-3):307-314.
- [61] Hirogaki T, Nakagawa H, Hayamizu M, Kita Y, Kakino Y. In-situ heat treatment system for die steels using YAG laser with a machining center. *Precision Engineering*. 2001;25(3):212-217.
- [62] Steen WM. *Laser material processing*. 3rd ed. London;Berlin: Springer; 2003.
- [63] Fung C, Peng K, Doong J. Study of surface temperature on laser cutting and welding power absorption. *International Communications in Heat and Mass Transfer*. 1990;17(2):147-154.
- [64] Quintino L, Costa A, Miranda R, Yapp D, Kumar V, Kong CJ. Welding with high power fiber lasers – A preliminary study. *Materials & Design*. 2007;28(4):1231-1237.
- [65] Tobar MJ, Álvarez C, Amado JM, Ramil A, Saavedra E, Yáñez A. Laser transformation hardening of a tool steel: Simulation-based parameter optimization and experimental results. *Surface and Coatings Technology*. 2006;200(22-23):6362-6367.
- [66] Bergström D, Powell J, Kaplan AFH. The absorptance of steels to Nd:YLF and Nd:YAG laser light at room temperature. *Applied Surface Science*. 2007;253(11):5017-5028.
- [67] Abboud JH, Benyounis KY, Olabi AG, Hashmi MSJ. Laser surface treatments of iron-based substrates for automotive application. *Journal of Materials Processing Technology*. 2007;182(1-3):427-431.
- [68] Bhushan B, Gupta BK. *Handbook of tribology : materials, coatings, and surface treatments*. New York: McGraw-Hill; 1991.
- [69] Sabbaghzadeh J, Azizi M, Torkamany MJ. Numerical and experimental investigation of seam welding with a pulsed laser. *Optics & Laser Technology*. 2008;40(2):289-296.
- [70] Pinkerton AJ, Li L. The effect of laser pulse width on multiple-layer 316L steel clad microstructure and surface finish. *Applied Surface Science*. 2003;208-209:411-416.

- [71] Chiang K, Chen Y. Laser surface hardening of H13 steel in the melt case. *Materials Letters*. 2005;59(14-15):1919-1923.
- [72] SeDao, Hua M, Shao TM, Tam HY. Surface modification of DF-2 tool steel under the scan of a YAG laser in continuously moving mode. *Journal of Materials Processing Technology*. 2009;209(10):4689-4697.
- [73] Sun Y, Hanaki S, Yamashita M, Uchida H, Tsujii H. Fatigue behavior and fractography of laser-processed hot work tool steel. *Vacuum*. 2004;73(3-4):655.
- [74] Cabalín LM, Romero D, Baena JM, Laserna JJ. Effect of surface topography in the characterization of stainless steel using laser-induced breakdown spectrometry. *Surface and Interface Analysis*. 1999;27(9):805-810.
- [75] Tsai P, Lee J, Chang C. Improving the erosion resistance of plasma-sprayed zirconia thermal barrier coatings by laser glazing. *Surface and Coatings Technology*. 2007;202(4-7):719-724.
- [76] Li T, Lou Q, Dong J, Wei Y, Liu J. Modified surface morphology in surface ablation of cobalt-cemented tungsten carbide with pulsed UV laser radiation. *Applied Surface Science*. 2001;172(3-4):331-344.
- [77] Zhou H, Tong X, Zhang Z, Li X, Ren L. The thermal fatigue resistance of cast iron with biomimetic non-smooth surface processed by laser with different parameters. *Materials Science and Engineering: A*. 2006;428(1-2):141-147.
- [78] S.,Everitt; J.,Starink M.; T.,Pang H.; M.,Wilcock I.; B.,Henderson M.; S.,Reed P.A.. A comparison of high temperature fatigue crack propagation in various subsolvus heat treated turbine disc alloys. . 2007;23(12):1419; 5-1423.
- [79] Maillot V, Fissolo A, Degallaix G, Degallaix S. Thermal fatigue crack networks parameters and stability: an experimental study. *International Journal of Solids and Structures*. 2005;42(2):759-769.
- [80] Tong X, Li F, Liu M, Dai M, Zhou H. Thermal fatigue resistance of non-smooth cast iron treated by laser cladding with different self-fluxing alloys. *Optics & Laser Technology*. 2010;42(7):1154-1161.
- [81] Pellizzari M, Molinari A, Straffelini G. Thermal fatigue resistance of gas and plasma nitrided 41CrAlMo7 steel. *Materials Science and Engineering A*. 2003;352(1-2):186-194.

- [82] Klobčar D, Tušek J. Thermal stresses in aluminium alloy die casting dies. *Computational Materials Science*. 2008;43(4):1147-1154.
- [83] R., Perrone; D., Ugues; E., Torres; U., Regina; M., Rosso. Toughness and microstructure stability in hot-working tool steels subjected to washout in molten aluminium. . 2008; (2-3):231; 10; 296-240.
- [84] Rosso M, Ugues D, Torres E, Perucca M, Kapranos P. Performance enhancements of die casting tools through PVD nanocoatings. *International Journal of Material Forming*. 2008;1(0):1259-1262.
- [85] Zhou H, Zhang ZH, Ren LQ, Song QF, Chen L. Thermal fatigue behavior of medium carbon steel with striated non-smooth surface. *Surface and Coatings Technology*. 2006;200:6758.
- [86] Gilmore CJ, Bowen A. The Fine-Scale Microstructure Of Rapidly-Quenched Aluminium-Transition Metal Alloys. *Nondestructive Testing and Evaluation*. 1990;5(5):379.
- [87] Meyers MA, Mishra A, Benson DJ. Mechanical properties of nanocrystalline materials. *Progress in Materials Science*. 2006;51(4):427-556.
- [88] Hildal K, Sekido N, Perepezko JH. Critical cooling rate for Fe₄₈Cr₁₅Mo₁₄Y₂C₁₅B₆ bulk metallic glass formation. *Intermetallics*. 2006;14(8-9):898-902.
- [89] Miller MK, Liu CT, Wright JA, Tang W, Hildal K. APT characterization of some iron-based bulk metallic glasses. *Intermetallics*. 2006;14(8-9):1019-1026.
- [90] Lesz S, Kwapuliński P, Nowosielski R. Formation and physical properties of Fe-based bulk metallic glasses with Ni addition. *Journal of Achievements in Materials and Manufacturing Engineering*. 2008;31(1):35-40.
- [91] Yamamoto T, Yodoshi N, Bitoh T, Makino A, Inoue A. Soft Magnetic Fe-based Metallic Glasses Prepared by Fluxing and Water-Quenching. *Reviews on Advanced Materials Science*. 2008;18:126-130.
- [92] Wang SL, Li HX, Zhang XF, Yi S. Effects of Cr contents in Fe-based bulk metallic glasses on the glass forming ability and the corrosion resistance. *Materials Chemistry and Physics*. 2009;113(2-3):878-883.

- [93] Basu A, Samant AN, Harimkar SP, Majumdar JD, Manna I, Dahotre NB. Laser surface coating of Fe–Cr–Mo–Y–B–C bulk metallic glass composition on AISI 4140 steel. *Surface and Coatings Technology*. 2008;202(12):2623-2631.
- [94] Cui C, Hu J, Liu Y, Gao K, Guo Z. Formation of nano-crystalline and amorphous phases on the surface of stainless steel by Nd:YAG pulsed laser irradiation. *Applied Surface Science*. 2008;254(21):6779-6782.
- [95] Miao W, Liu XT, Tao K. Modification of surface mechanical properties of aluminum by high current Mo ion implantation using a MEVVA ion source. *Surface and Coatings Technology*. 2005;191(1):33-37.
- [96] Roy R, Gedevanishvili S, Breval E, Mistry P, Turchan M. Crystallinity destruction in metals by multiple pulsed lasers of different frequency. *Materials Letters*. 2000;46(1):30-34.
- [97] Dong H, Li XY, Bell T. Hardening response and tempering behaviour of electron beam surface melted Ti–8.5Si alloy. *Journal of Alloys and Compounds*. 1999;283(1-2):231-240.
- [98] Audebert F, Colaço R, Vilar R, Sirkin H. Production of glassy metallic layers by laser surface treatment. *Scripta Materialia*. 2003;48(3):281-286.
- [99] Li M, Wang Y, Han B, Zhao W, Han T. Microstructure and properties of high chrome steel roller after laser surface melting. *Applied Surface Science*. 2009;255(17):7574-7579.
- [100] Lograsso T.A, Ross AR, Schlagel DL, Clark AE, Wun-Fogle M. Structural transformations in quenched Fe–Ga alloys. *Journal of Alloys and Compounds*. 2003;350(1-2):95-101.
- [101] Rios CT, Bolfarini C, Botta F. WJ, Kiminami CS. Rapidly solidified Al₉₂Fe₃Cr₂Mn₃ alloy. *Materials Science and Engineering: A*. 2007;449-451:1057-1061.
- [102] de Medeiros SN, Cadore S, Pereira HA, Santos IA, Colucci CC, Paesano Jr. A. Quasicrystalline phase formation in the mechanically alloyed Al₇₀Cu₂₀Fe₁₀. *Hyperfine Interacts*. 2010;;213-217.
- [103] Va Åžerban ea. Fe-based bulk metallic glasses used for magnetic shielding. *Journal of Physics: Conference Series*. 2009;144(1):012037.
- [104] Yong X, Chang IT, Jones IP. Formation of a quasicrystalline phase in mechanically alloyed Al₆₅Cu₂₅Fe₁₅. *Journal of Alloys and Compounds*. 2005;387:128-133.

- [105] Clapp PC. How Would we Recognize a Martensitic Transformation if it Bumped into us on a Dark \& Austy Night ? J.Phys.IV France. 1995;05(C8):8-11-8-19.
- [106] Duerig TW, Albrecht J, Richter D, Fischer P. Formation and reversion of stress induced martensite in Ti-10V-2Fe-3Al. Acta Metallurgica. 1982;30(12):2161-2172.
- [107] Butler EP, Burke MG. Martensite formation at grain boundaries in sensitised 304 stainless steel. Journal de Physique. 1982;43:121-126.
- [108] Kajiwara S. Mechanism of isothermal martensitic transformation. Materials Transactions JIM. 1992;33(11):1027-1034.
- [109] Zhang M-, Kelly PM, Bekessy LK, Gates JD. Determination of retained austenite using an X-ray texture goniometer. Materials Characterization. 2000;45(1):39-49.
- [110] Magner SH, De Angelis RJ, Weins WN, Makinson JD. A historical review of retained austenite and its measurement by X-ray diffraction. JCPDS-International Centre for Diffraction Data 2002, Advances in X-ray Analysis. 2002;45:92-97.
- [111] Adachi Y, Wakita M, Beladi H, Hodgson PD. The formation of ultrafine ferrite through static transformation in low carbon steels. Acta Materialia. 2007;55(14):4925-4934.
- [112] Xiao F, Liao B, Shan Y, Yang K. Isothermal transformation of low-carbon microalloyed steels. Materials Characterization. 2005;54(4-5):417-422.
- [113] Kozeschnik E, Gamsjäger E. High-speed quenching dilatometer investigation of the austenite-to-ferrite transformation in a low to ultralow carbon steel. Metallurgical and Materials Transactions A. 2006;37(6):1791-1797.
- [114] John R. Lewis. Formation of deformation induced ferrite during mechanical testing. Canada: McGill University, Montréal, Canada; 1996.
- [115] Xu D, Duan G, Johnson WL, Garland C. Formation and properties of new Ni-based amorphous alloys with critical casting thickness up to 5 mm. Acta Materialia. 2004;52:3493-3497.
- [116] Shin DH, Kim I, Kim J, Park K. Grain refinement mechanism during equal-channel angular pressing of a low-carbon steel. Acta Materialia. 2001;49(7):1285-1292.

- [117] Wen C, Li W, Rong Y. Nanocrystallization and martensitic transformation in Fe-23.4Mn-6.5Si-5.1Cr (wt.%) alloy by surface mechanical attrition treatment. *Materials Science and Engineering: A*. 2008;481-482:484-488.
- [118] Lesuer D, Syn C, Sherby O. Nano-scale strengthening from grains, subgrains, and particles in Fe-based alloys. *Journal of Materials Science*. 2010;45(17):4889-4894.
- [119] Biju V, Sugathan N, Vrinda V, Salini S. Estimation of lattice strain in nanocrystalline silver from X-ray diffraction line broadening. *Journal of Materials Science*. 2008;43(4):1175-1179.
- [120] Lu JZ, Zhang L, Feng AX, Jiang YF, Cheng GG. Effects of laser shock processing on mechanical properties of Fe-Ni alloy. *Materials & Design*. 2009;30(9):3673-3678.
- [121] Gargarella P, Vilar R, Almeida A, Kiminami CS, Rios CT, Bolfarini C, et al. Laser remelting of Al₉₁Fe₄Cr₃Ti₂ quasicrystalline phase former alloy. *Journal of Alloys and Compounds*. 2010;495(2):646-649.
- [122] Biswas K, Galun R, Mordike BL, Chattopadhyay K. Laser Cladding of Quasi-Crystal-Forming Al-Cu-Fe-Bi on an Al-Si Alloy Substrate. . 2005;.
- [123] Hirata A, Hirotsu Y, Amiya K, Inoue A. Quasicrystal-like structure and its crystalline approximant in an Fe₄₈Cr₁₅Mo₁₄C₁₅B₆Tm₂ bulk metallic glass. *Journal of Alloys and Compounds*. 2010;504(Supplement 1):S186-S189.
- [124] Lim YY, Chaudhri MM. The influence of grain size on the indentation hardness of high-purity copper and aluminium. *Philosophical Magazine A*. 2002;82(10):2071.
- [125] Liu MY, Shi B, Wang C, Ji SK, Cai X, Song HW. Normal Hall-Petch behavior of mild steel with submicron grains. *Materials Letters*. 2003;57(19):2798-2802.
- [126] Zhang HW, Subhash G, Jing XN, Kecskes LJ, Dowding RJ. Evaluation of hardness-yield strength relationships for bulk metallic glasses. *Philosophical Magazine Letters*. 2006;86(5):333.
- [127] Eroglu M, Aksoy M. Effect of initial grain size on microstructure and toughness of intercritical heat-affected zone of a low carbon steel. *Materials Science and Engineering A*. 2000;286(2):289.

- [128] Yilbas BS, Arif AFM, Karatas C, Ahsan M. Cemented carbide cutting tool: Laser processing and thermal stress analysis. *Applied Surface Science*. 2007;253(12):5544-5552.
- [129] Singh J, Bhat BN, Poorman R, Kar A, Mazumder J. Laser glazing of vacuum plasma spray coated NARloy-Z. *Surface and Coatings Technology*. 1996;79(1-3):35-49.
- [130] Li JF, Li L, Stott FH. Thermal stresses and their implication on cracking during laser melting of ceramic materials. *Acta Materialia*. 2004;52(14):4385-4398.
- [131] Van Elsen M, Baelmans M, Mercelis P, Kruth J-. Solutions for modelling moving heat sources in a semi-infinite medium and applications to laser material processing. *International Journal of Heat and Mass Transfer*. 2007;50(23-24):4872-4882.
- [132] Peligrad AA, Zhou E, Morton D, Li L. A melt depth prediction model for quality control of laser surface glazing of inhomogeneous materials. *Optics & Laser Technology*. 2001;33(1):7-13.
- [133] Yilbas BS, Shuja SZ, Sami M. Pulsed laser heating of steel surfaces — Fourier and electron kinetic theory approaches. *International Communications in Heat and Mass Transfer*. 1998;25(6):843-852.
- [134] Yilbas BS, Al-Aqeeli N. Analytical investigation into laser pulse heating and thermal stresses. *Optics & Laser Technology*. 2009;41(2):132-139.
- [135] Shakeel Safdar ea. Numerical analysis of the effects of non-conventional laser beam geometries during laser melting of metallic materials. *Journal of Physics D: Applied Physics*. 2007;40(2):593.
- [136] Yilbas BS, Kalyon M. Analytical solution for multilayer assembly including heating and cooling cycles with laser pulse parameter variation. *Optics and Lasers in Engineering*. 2006;44(11):1219-1234.
- [137] Samant A.N, Dahotre N.B. Computational prediction of grain size during rapid laser surface modification of Al₂O₃ ceramic. *physica status solidi (RRL) ? Rapid Research Letters*. 2007;1(1):R4-R6.
- [138] Orazi L, Fortunato A, Cuccolini G, Tani G. An efficient model for laser surface hardening of hypo-eutectoid steels. *Applied Surface Science*. 2010;256(6):1913-1919.

- [139] Li W, Qu N. Study of high temperature wear resistance of hot work steel for magnesium alloy die casting. *Advanced Materials Research*. 2007;26-28:33-36.
- [140] Yan H, Hua J, Shivpuri R. Flow stress of AISI H13 die steel in hard machining. *Materials & Design*. 2007;28(1):272-277.
- [141] Lin Y, McHugh KM, Zhou Y, Lavernia EJ. Microstructure and hardness of spray-formed chromium-containing steel tooling. *Scripta Materialia*. 2006;55(7):581-584.
- [142] Kchaou M, Elleuch R, Desplanques Y, Boidin X, Degallaix G. Failure mechanisms of H13 die on relation to the forging process – A case study of brass gas valves. *Engineering Failure Analysis*. 2010;17(2):403-415.
- [143] Taktak S. Some mechanical properties of borided AISI H13 and 304 steels. *Materials & Design*. 2007;28(6):1836-1843.
- [144] McHugh KM, Lin Y, Zhou Y, Lavernia EJ. Influence of cooling rate on phase formation in spray-formed H13 tool steel. *Materials Science and Engineering: A*. 2008;477(1-2):50-57.
- [145] Venkata Ramana P, Madhusudhan Reddy G, Mohandas T, Gupta AVSSKS. Microstructure and residual stress distribution of similar and dissimilar electron beam welds-Maraging steel to medium alloy medium carbon steel. *Materials & Design*. 2010;31(2):749-760.
- [146] Umbrello D, Rizzuti S, Outeiro JC, Shivpuri R, M'Saoubi R. Hardness-based flow stress for numerical simulation of hard machining AISI H13 tool steel. *Journal of Materials Processing Technology*. 2008;199(1-3):64-73.
- [147] Reggiani B, Donati L, Zhou J, Tomesani L. The role of creep and fatigue in determining the high-temperature behaviour of AISI H11 tempered steel for aluminium extrusion dies. *Journal of Materials Processing Technology*. 2010;210(12):1613-1623.
- [148] Ukadgaonker VG, Bhat S, Jha M, Desai PB. Fatigue crack growth towards the weld interface of alloy and maraging steels. *International Journal of Fatigue*. 2008;30(4):689-705.
- [149] Joshi V, Srivastava A, Shivpuri R, Rolinski E. Investigating ion nitriding for the reduction of dissolution and soldering in die-casting shot sleeves. *Surface and Coatings Technology*. 2003;163-164:668-673.

- [150] Tyurin NF, Tursunov AV. Carburizing of die steels 3Kh2V8F and 5KhV2S. *Metal Science and Heat Treatment*. 1968;10(8):632-633.
- [151] Aghaie-Khafri M, Fazlalipour F. Vanadium carbide coatings on die steel deposited by the thermo-reactive diffusion technique. *Journal of Physics and Chemistry of Solids*. 2008;69(10):2465-2470.
- [152] Rodríguez-Baracaldo R, Benito JA, Puchi-Cabrera ES, Staia MH. High temperature wear resistance of (TiAl)N PVD coating on untreated and gas nitrided AISI H13 steel with different heat treatments. *Wear*. 2007;262(3-4):380-389.
- [153] Zeghni AE, Hashmi MSJ. The effect of coating and nitriding on the wear behaviour of tool steels. *Journal of Materials Processing Technology*. 2004;155-156:1918-1922.
- [154] Coldwell H, Woods R, Paul M, Koshy P, Dewes R, Aspinwall D. Rapid machining of hardened AISI H13 and D2 moulds, dies and press tools. *Journal of Materials Processing Technology*. 2003;135(2-3):301-311.
- [155] Tušek J, Taljat B, Klobčar D. *METALURGIJA*. 2007;46(1):67-71.
- [156] Mitterer C, Holler F, Üstel F, Heim D. Application of hard coatings in aluminium die casting-soldering, erosion and thermal fatigue behaviour. *Surface and Coatings Technology*. 2000;125(1-3):233-239.
- [157] Stasic J, Trtica M, Gakovic B, Petrovic S, Batani D, Desai T, et al. Surface modifications of AISI 1045 steel created by high intensity 1064 and 532 nm picosecond Nd:YAG laser pulses. *Applied Surface Science*. 2009;255(8):4474-4478.
- [158] Dobrzański LA, Piec M, Klimpel A, Trojanowa Z. Surface modification of hot work tool steel by high-power diode laser. *International Journal of Machine Tools and Manufacture*. 2007;47(5):773-778.
- [159] Tsai HL, Lin HS. The CO₂ laser hardfacing of mold steel. *Journal of Materials Processing Technology*. 1996;56(1-4):66-69.
- [160] Akgün OV, Ürgen M, Çakir AF. The effect of heat treatment on corrosion behavior of laser surface melted 304L stainless steel. *Materials Science and Engineering A*. 1995;203(1-2):324-331.

- [161] Kansal H.K, Singh S, Kumar P. Parametric optimization of powder mixed electrical discharge machining by response surface methodology. *Journal of Materials Processing Technology*. 2005;169(3):427-436.
- [162] Samant A.N, Du B, Paital SR, Kumar S, Dahotre NB. Pulsed laser surface treatment of magnesium alloy: Correlation between thermal model and experimental observations. *Journal of Materials Processing Technology*. 2009;209(11):5060-5067.
- [163] Raju K.S, Krishna MG, Padmanabhan KA, Muraleedharan K, Gurao NP, Wilde G. Grain size and grain boundary character distribution in ultra-fine grained (ECAP) nickel. *Materials Science and Engineering: A*. 2008;491(1-2):1-7.
- [164] Lee P.J, Ruess R, Larbalestier DC. Quantitative image analysis of filament coupling and grain size in iter Nb(Ti)[3]Sn strand manufactured by the internal Sn process. *IEEE transactions on applied superconductivity*. 1997;(2):1516-1519.
- [165] Walton WH. Feret's Statistical Diameter as a Measure of Particle Size. *Nature*. 1948;162:329-330.
- [166] Al-Thyabat S, Miles NJ. An improved estimation of size distribution from particle profile measurements. *Powder Technology*. 2006;166(3):152-160.
- [167] X D Hou ea. Study of the interaction between the indentation size effect and Hallâ€Petch effect with spherical indenters on annealed polycrystalline copper. *Journal of Physics D: Applied Physics*. 2008;41(7):074006.
- [168] Leskovsek V, Sustarsik B, Jutrisa G, Baksa D, Kopac J. Optimizing the vacuum heat treatment of hot-work tool steels by linear elastic fracture mechanics. *BHM Berg- und HÃ¼ttenmännische Monatshefte*. 2006;151(3):127-130.
- [169] Dickey F.M, Weichrnan LS, Shagam RN. *Laser Beam Shaping Techniques*. . 2000;.
- [170] Lei Y.P, Murakawa H, Shi YW, Li XY. Numerical analysis of the competitive influence of Marangoni flow and evaporation on heat surface temperature and molten pool shape in laser surface remelting. *Computational Materials Science*. 2001;21(3):276-290.
- [171] Gleiter H. Nanostructured materials: basic concepts and microstructure. *Acta Materialia*. 2000;48(1):1.

- [172] Hong SC, Lee KS. Influence of deformation induced ferrite transformation on grain refinement of dual phase steel. *Materials Science and Engineering A*. 2002;323(1-2):148-159.
- [173] Yokota T, García Mateo C, Bhadeshia HKDH. Formation of nanostructured steels by phase transformation. *Scripta Materialia*. 2004;51(8):767-770.
- [174] Hermann R, Löser W, Lindenkreuz G, Diefenbach A, Zahnow W, Dreier W, et al. Metastable phase formation in undercooled Fe-Co melts. *Materials Science and Engineering A*. 2004;375-377:507-511.
- [175] Yang J, Lian J, Dong Q, Guo Z. Nano-structured films formed on the AISI 329 stainless steel by Nd-YAG pulsed laser irradiation. *Applied Surface Science*. 2004;229(1-4):2-8.
- [176] Cui C, Hu J, Liu Y, Gao K, Guo Z. Morphological and structural characterizations of different oxides formed on the stainless steel by Nd:YAG pulsed laser irradiation. *Applied Surface Science*. 2008;254(20):6537-6542.
- [177] Fradkov V.E, Glicksman ME, Palmer M, Rajan K. Topological events in two-dimensional grain growth: Experiments and simulations. *Acta Metallurgica et Materialia*. 1994;42(8):2719.
- [178] Yokoyama M, Yamaura S, Kimura H, Inoue A. Production of metallic glassy bipolar plates for PEM fuel cells by hot pressing in the supercooled liquid state. *International Journal of Hydrogen Energy*. 2008;33(20):5678-5685.
- [179] Li Y.J, Zeng X.H, Blum W. Transition from strengthening to softening by grain boundaries in ultrafine-grained Cu. *Acta Materialia*. 2004;52(17):5009-5018.
- [180] Padmanaban G, Balasubramanian V. Optimization of laser beam welding process parameters to attain maximum tensile strength in AZ31B magnesium alloy. *Optics & Laser Technology*. 2010;42(8):1253-1260.
- [181] Lalwani D.I, Mehta N.K, Jain P.K. Experimental investigations of cutting parameters influence on cutting forces and surface roughness in finish hard turning of MDN250 steel. *Journal of Materials Processing Technology*. 2008;206(1-3):167-179.
- [182] Torres R.D, Soares Jr. P.C, Schmitz C, Siqueira C.J.M. Influence of the nitriding and TiAlN/TiN coating thickness on the sliding wear behavior of duplex treated AISI H13 steel. *Surface and Coatings Technology*; In Press, Corrected Proof.

- [183] Zhou L., Sun D, Liu C, Wu Q. Fatigue Behavior of High Speed Steel Roll Materials for Hot Rolling by Laser Impacting. *Journal of Iron and Steel Research, International*, 2006;13(6):49-52.
- [184] Zemskii SV, Gorodetskii VI, Emel'yanova LG. Diffusion and distribution of sulfur in steels St3 and 13Kh18N9. *Metal Science and Heat Treatment*. 1976;18(12):1072-1073.
- [185] Zamikhovskii VS, Pokhmurskii VI. Effect of chromium-nickel diffusion coatings on the mechanical properties of medium-carbon steel. *Metal Science and Heat Treatment*. 1973;15(3):262-264.
- [186] Yajiang L, Juan W, Bing Z, Tao F. XRD and TEM analysis of microstructure in the welding zone of 9Cr-1Mo-V-Nb heat-resisting steel. *Bulletin of Materials Science*. 2002;25(3):213-217.
- [187] Wang F, Shan A, Dong X, Wu J. Microstructure and oxidation resistance of laser-remelted Mo-Si-B alloy. *Scripta Materialia*, 2007;56(9):737-740.
- [188] Yasar E, Gungunes H, Akturk S, Durlu TN. New observations on the formation of athermal martensite in Fe-Ni-Mo alloys. *Journal of Alloys and Compounds*. 2007;428(1-2):125-129.
- [189] Suiker ASJ, Turteltaub S. Crystalline damage growth during martensitic phase transformations. *Philosophical Magazine*. 2007;87(32):5033.
- [190] Brezenitsky M, Moreh R, Dayan D, Kimmel G. Comparative study of steel alloys using STM and XRD. *Journal of Alloys and Compounds*. 1999;290(1-2):257-261.
- [191] Movaghar Garabagh M, Hossein Nedjad S, Nili Ahmadabadi M. X-ray diffraction study on a nanostructured 18Ni maraging steel prepared by equal-channel angular pressing. *Journal of Materials Science*. 2008;43(21):6840-6847.
- [192] Herlach D. Metastable Materials from Undercooled Melts. *Journal of Metastable and Nanocrystalline Materials*. 2004;20-21:435-442.
- [193] Fengbing S, Qiang L, Haisheng Z, Chunhong L, Shixi Z, Dezhong S. Phase formation and transitions in the lead magnesium niobate-lead titanate system. *Materials Chemistry and Physics*. 2004;83(1):135-139.
- [194] Lekston Z, Lagiewka E. X-ray diffraction studies of NiTi shape memory alloys. *Archives of Materials Science and Engineering*. 2007;28(11):665-672.

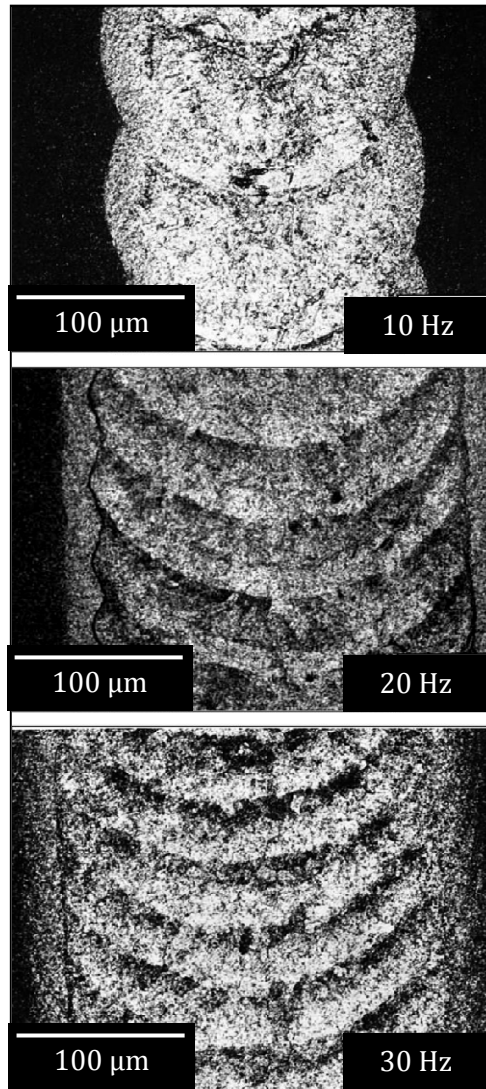
[195] S. O.R, Thomas H, Huang X, Michael D. X-ray diffraction measurement of doping induced lattice mismatch in n-type 4H-SiC epilayers grown on p-type substrates. 2003;83(10):1971; 3-1973.

[196] Yadav TP, Mukhopadhyay NK, Tiwari RS, Srivastava ON. On the evolution of quasicrystalline and crystalline phases in rapidly quenched Al-Co-Cu-Ni alloy. Materials Science and Engineering: A. 2007;449-451:1052.

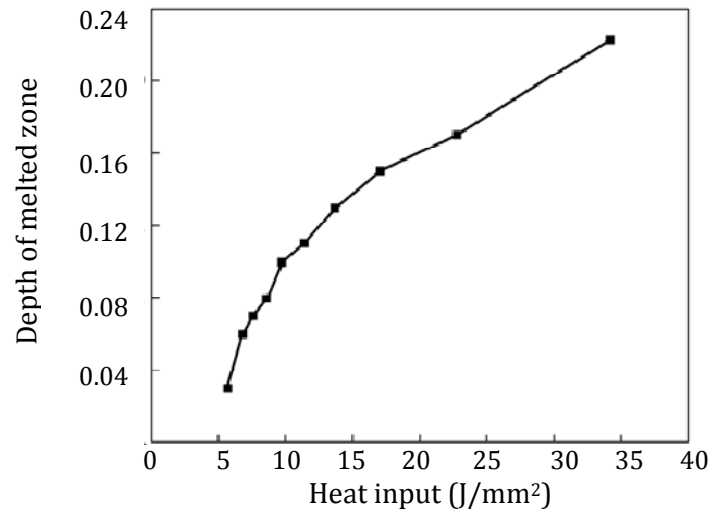
[197] Hu D, Kovacevic R. Modelling and measuring the thermal behaviour of the molten pool in closed-loop controlled laser-based additive manufacturing. Proceedings of the Institution of Mechanical Engineers, Part B: Journal of Engineering Manufacture. 2003;217(4):441-452.

APPENDICES

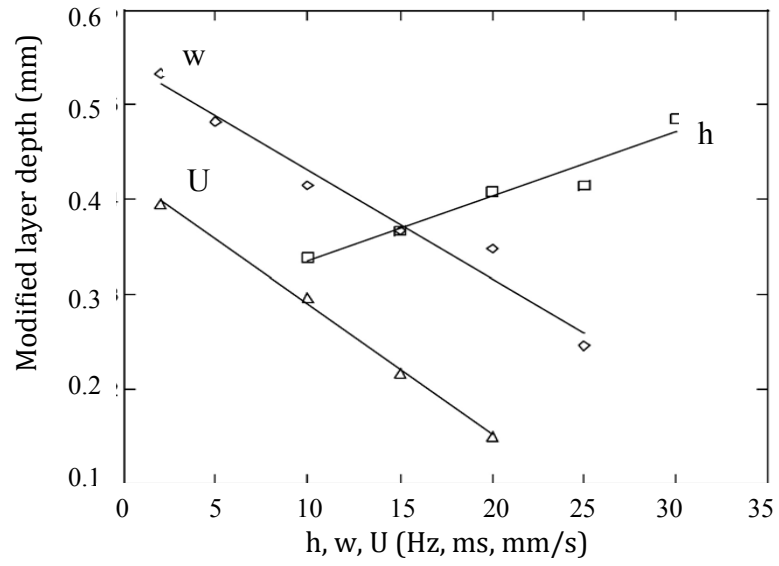
APPENDIX A1: Effect of pulsing frequency on overlapping with Ti-6Al-4V alloy [9].



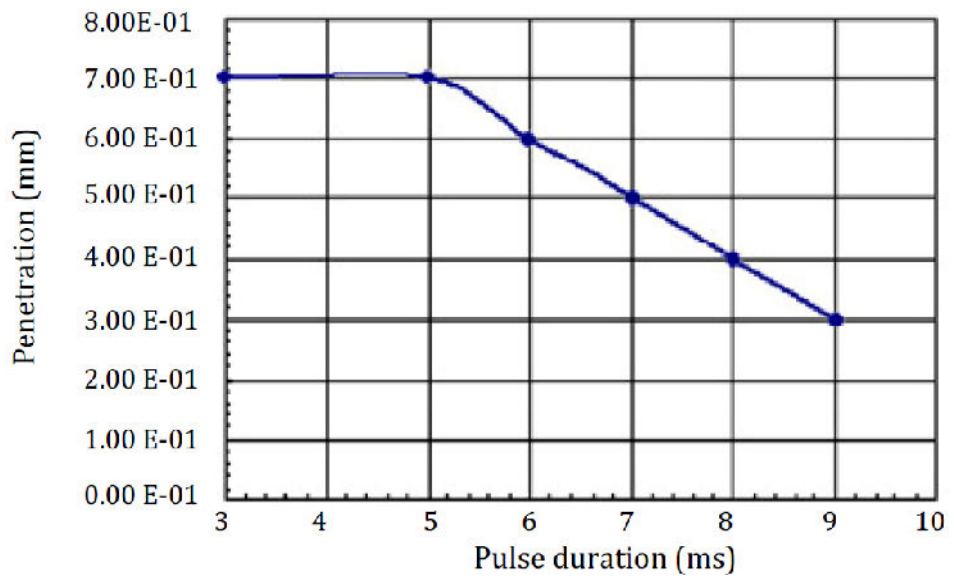
APPENDIX A2: Change of depth of melted zone with heat input rate in laser glazing of H13 tool steel using fiber laser system [40].



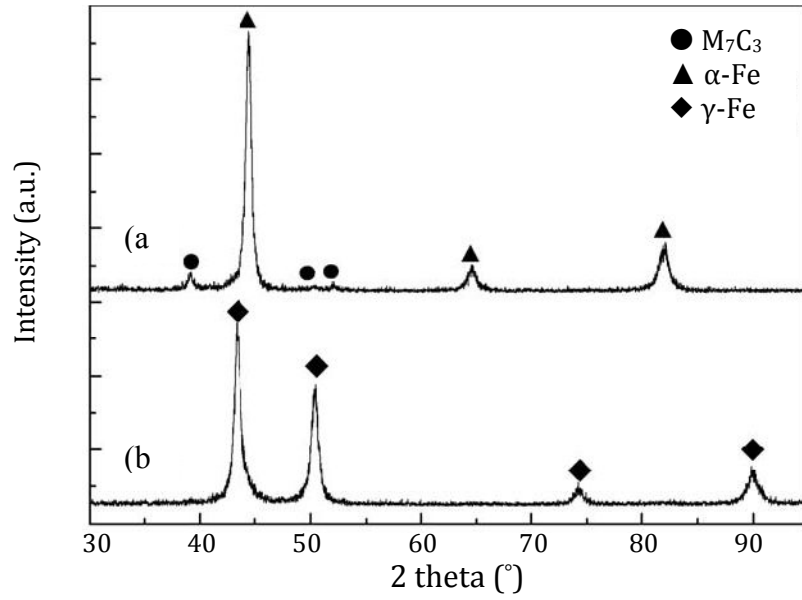
APPENDIX A3(a): Changes of modified layer depth with frequency, h, pulse width, w, and scan rate, U in Ti-6AL-4V using Nd:YAG laser system [9].



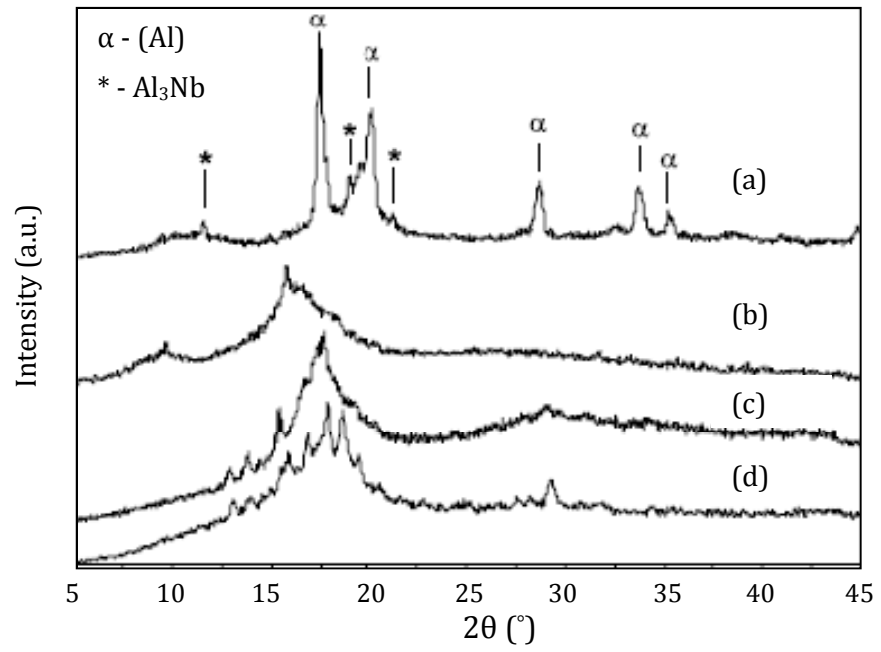
APPENDIX A3 (b): Variations of the heat penetration of the work piece relative to the pulse duration in st14 steel using Nd:YAG laser system [69].



APPENDIX A4(a): X-ray diffraction profiles of the top surface of the (a) as-received and (b) laser melted high chrome steel [99].



APPENDIX A4 (b): XRD patterns of the laser treated (a) Zr based, (b) Mg-based, and (c), (d) Al-based alloy samples using Mo-K α radiation [98].



APPENDIX B: Laser processing parameters

Peak Power, PP

Peak power is the maximum occurring optical power transmitted to the material's surface measured in Watts (W).

Duty Cycle, DC

Duty cycle is the division of time when the laser system is in 'active' or 'on' condition measured in percentage (%) during a laser pulse period. It affects the pulse width and imparted laser power by controlling the material-beam interaction time and the average power at the same time. Low duty cycles produce shorter pulse widths and reduce the materials-beam interaction time at the set maximum peak power.

Pulse Repetition Frequency, PRF

Pulse repetition frequency is defined as the number of emitted pulses per second, or the inverse temporal pulse spacing. The number of pulses produced by the laser system in one second is measured in Hertz (Hz). In different interpretation, PRF determines the laser speed which controls materials-laser interaction time when the laser system actively operates at 100 % duty cycle. For example, if PRF was set to 2500 Hz, the laser beam firing time was 0.4 ms for each pulse.

Pulse Period, T

Pulse period is the time duration for each pulse triggered from the laser head. In the pulse laser processing mode, pulse period is determined from the inverse value of pulse repetition frequency. For example, when the PRF was set to 2500 Hz, the resulted period for each pulse was 0.4 ms. Period of 0.4 ms is also the time frame for a pulse in both 'active' and 'inactive' or 'on' and 'off' condition as shown in Figure 2.41.

Pulse Width, τ

Pulse width refers to the time duration when the pulse was in 'active' or 'on' state as shown in Figure 2.41. The active condition is controlled by the duty cycle percentage and can be calculated using Equation 1. For example, at 35% duty cycle and 2500 Hz frequency, the pulse width is 0.14 ms.

$$\tau = \frac{1}{PRF} \times DC [mm/s] \quad \text{Equation 1}$$

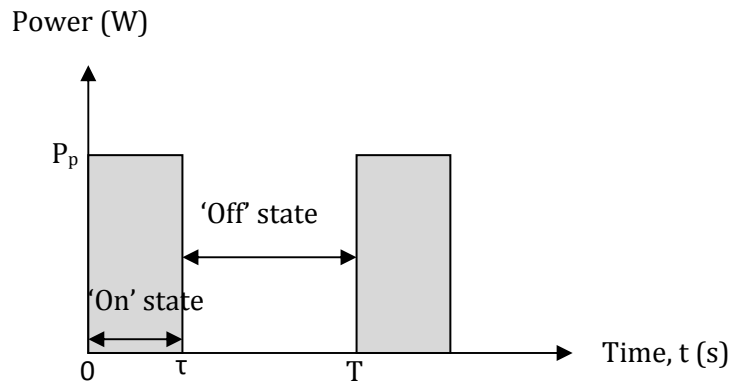


Figure 2.41: Power as a function of time in pulse processing mode.

Traverse Speed, S

Traverse speed is the sample movement velocity during processing measured in millimetre per second (mm/s). With the processing distance taken as the beam diameter, d , the traverse speed is given by Equation 2.

$$S = \frac{d}{t} [mm/s] \quad \text{Equation 2}$$

Circumferential Speed, ω

Circumferential speed is the sample speed at the rotational direction measured in revolutions per minute (rpm). Samples are rotated continuously to produce a rapid cooling rate during processing. To determine the circumferential speed, the traverse speed in Equation 2 is used. Taking the processing distance as the sample circumference, the circumferential speed, ω is given by Equation 3. The circumferential speed can then multiply by 60 to set controller inputs in unit of rpm.

$$\omega = \frac{S}{\text{sample circumference}} \left[\frac{rev}{s} \right] \quad \text{Equation 3}$$

Residence Time, T_R

Residence time is the materials-beam interaction time measured in millisecond (ms). The materials-beam interaction time depends on both laser speed and sample traverse speed. At zero overlap where the laser processing beam was set to continuous mode, the residence time relation is represented by Equation 2. However, in pulse mode, the

materials-laser interaction time is limited by the set duty cycle. The residence time calculation for pulse mode laser processing is given by Equation 4.

$$T_R = \frac{DC \times d}{S} \quad \text{Equation 4}$$

Average Power, P_{ave}

The average power during pulse mode indicates the effective laser power at a given duty cycle. When the peak power is set to a maximum value of 1520 W, at 50 % duty cycle, the average power is 760 W. Equation 5 shows the average laser power formula at a peak power, pulse width and pulse period.

$$P_{ave} = \frac{P_p \times \tau}{T} \quad \text{Equation 5}$$

Pulse Energy, E

Pulse energy is the amount of heat resulting from a given peak power and pulse width, measured in Joule (J). The pulse energy is calculated using Equation 6. The pulse energy determination is significant to estimate the total energy needed to raise the materials surface temperature and consequently melt the surface. Fluence or energy density, F, is calculated as pulse energy divided by laser beam spot area.

$$E = \frac{P_{ave}}{PRF} \quad \text{Equation 6}$$

Laser Irradiance, I

Laser irradiance is the laser power density measured in Watts per beam area (W/mm^2). Laser irradiance is determined from energy density, residence time and duty cycle and is calculated using Equation 7. At constant peak power, the laser irradiance increases as the beam size gets smaller.

$$I = \frac{F}{T_R} \times DC \quad \text{Equation 7}$$

APPENDIX C1: Average hardness of DOE2 samples

Sample	Hardness (HV _{0.1})			Mean	Std. Dev.	Std. Dev./√n	Interval	Lower range	Upper range
	1	2	3						
E6	772	765	780	772	7.5056	4.3333	18.6463	753	791
E8	1017	1016	1017	1017	0.5774	0.3333	1.4343	1016	1018
E9	946	950	942	946	4.0000	2.3094	9.9374	936	956
E12	865	882	898	882	16.5025	9.5277	40.9979	841	923
E14	960	946	932	946	14.0000	8.0829	34.7807	911	981
E15	1020	1012	1018	1017	4.1633	2.4037	10.3431	1007	1027
E18	875	880	890	882	7.6376	4.4096	18.9744	863	901
E21	950	928	960	946	16.3707	9.4516	40.6704	905	987
E26	725	720	728	724	4.0415	2.3333	10.0403	714	734
E27	1017	1015	1020	1017	2.5166	1.4530	6.2521	1011	1023

APPENDIX C2: Surface roughness of DOE2 samples with 95% CI

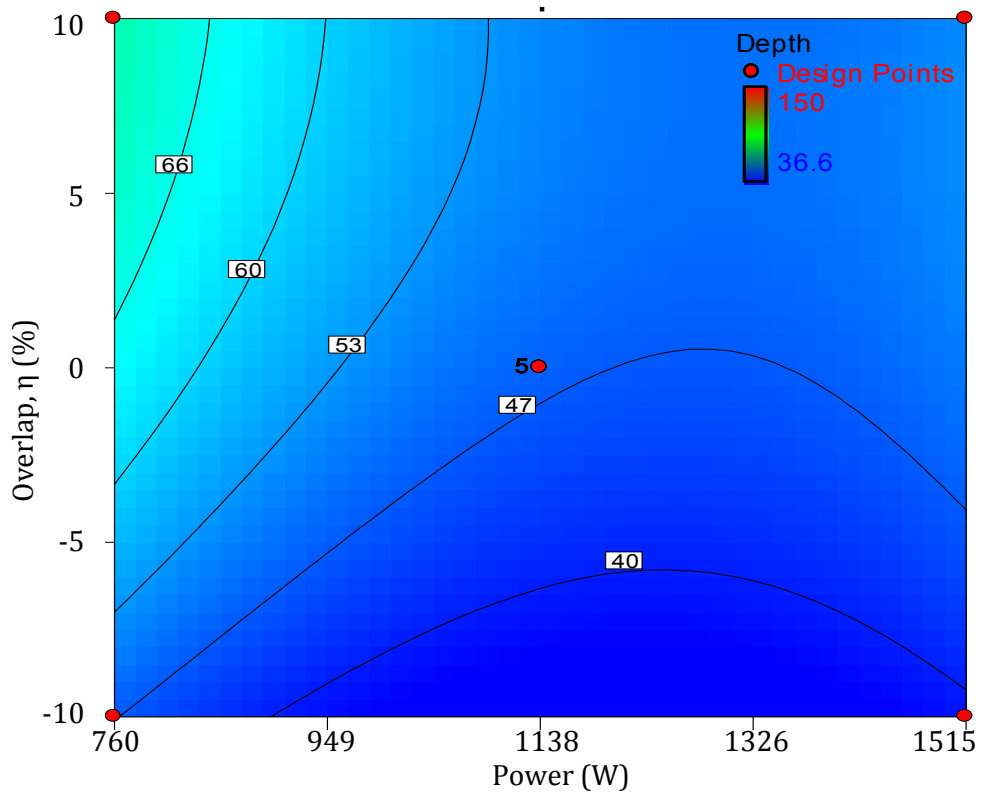
Sample	Surface roughness, Ra (μm)			Mean	Std. Dev.	Std. Dev./ \sqrt{n}	Interval	Lower range	Upper range
	1	2	3						
E6	21.4	20.5	22.5	21.5	1.0017	0.1113	0.478907	21.0	21.9
E8	3.6	3.5	3.4	3.5	0.1000	0.0111	0.047811	3.5	3.5
E9	30.9	31.4	29.8	30.7	0.8185	0.0909	0.391351	30.3	31.1
E12	28.2	29.4	28.6	28.7	0.6110	0.0679	0.292131	28.4	29.0
E14	7.7	8.1	7.4	7.7	0.3512	0.0390	0.167907	7.6	7.9
E15	33.2	33.9	34.1	33.7	0.4726	0.0525	0.225946	33.5	34.0
E18	37.0	38.7	39.0	38.2	1.0786	0.1198	0.515681	37.7	38.7
E21	25.4	24.3	25.9	25.2	0.8185	0.0909	0.391351	24.8	25.6
E24	29.5	28.9	29.2	29.2	0.3000	0.0333	0.143433	29.1	29.3
E26	21.9	20.9	23.1	22.0	1.1015	0.1224	0.526646	21.4	22.5
E27	30.1	29.5	30.4	30.0	0.4583	0.0509	0.219098	29.8	30.2

Df = 2, CI = 0.95, α = 0.025, t distribution = 4.303

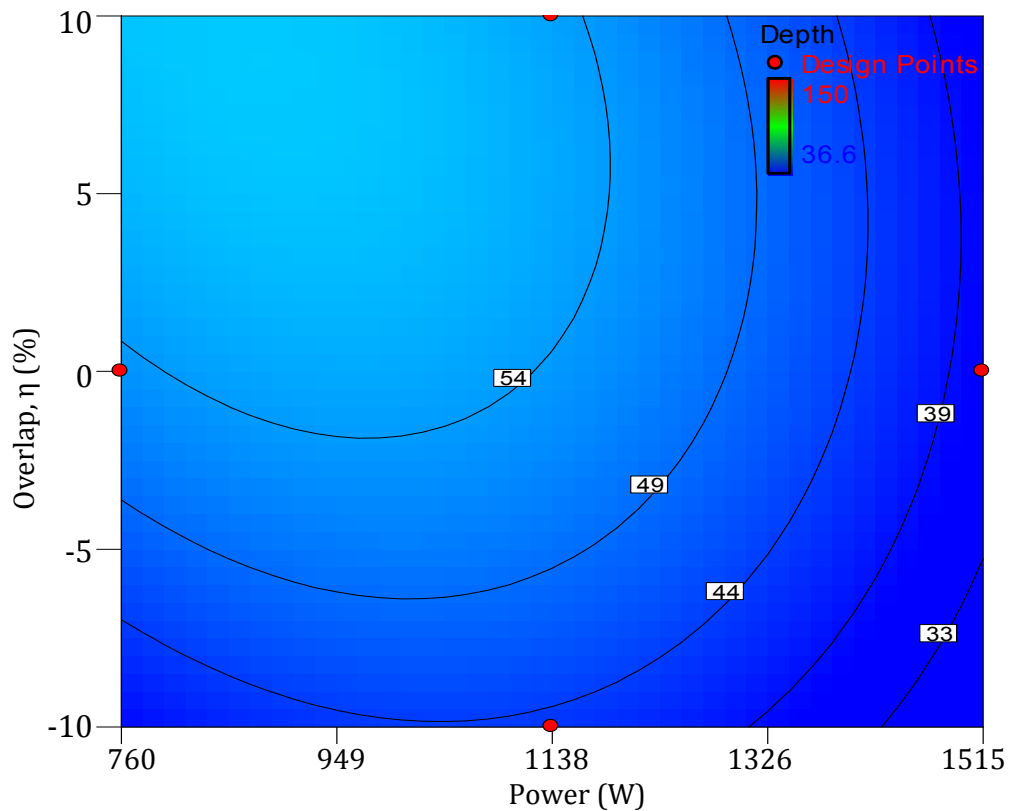
APPENDIX D1: Modified surface depth of DOE4 samples.

Sample	Modified layer depth (μm)			Mean	Std. Dev.	Std. Dev./ \sqrt{n}	Interval	Lower range	Upper range
X1	88.7	84.9	88.8	87.5	2.2097	1.2758	5.4896	82.0	93.0
X2	55.0	49.7	42.8	49.2	6.1350	3.5421	15.2415	33.9	64.4
X3	53.5	50.5	47.4	50.5	3.0642	1.7691	7.6126	42.8	58.1
X4	85.6	78.8	75.7	80.0	5.0931	2.9405	12.6529	67.4	92.7
X5	46.6	44.3	36.7	42.6	5.2075	3.0065	12.9371	29.6	55.5
X6	67.0	57.1	51.0	58.4	8.1035	4.6786	20.1318	38.2	78.5
X7	88.2	85.4	83.8	85.8	2.2048	1.2730	5.4775	80.3	91.3
X8	72.4	69.8	66.8	69.7	2.8024	1.6180	6.9621	62.7	76.6
X9	86.9	80.8	76.7	81.5	5.1256	2.9593	12.7337	68.7	94.2

APPENDIX E1: Contour plot of overlap, power and modified layer depth for DOE5 samples at (a) 2900 Hz and (b) 3500 Hz PRF

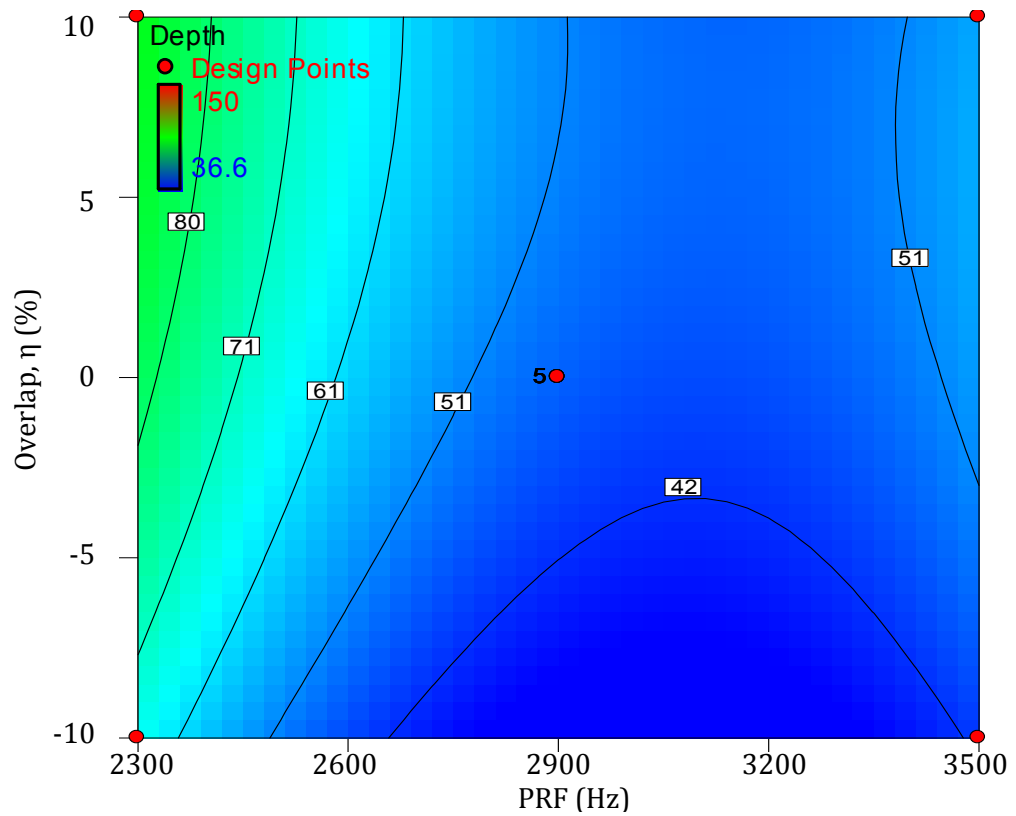


(a) 2900 Hz PRF

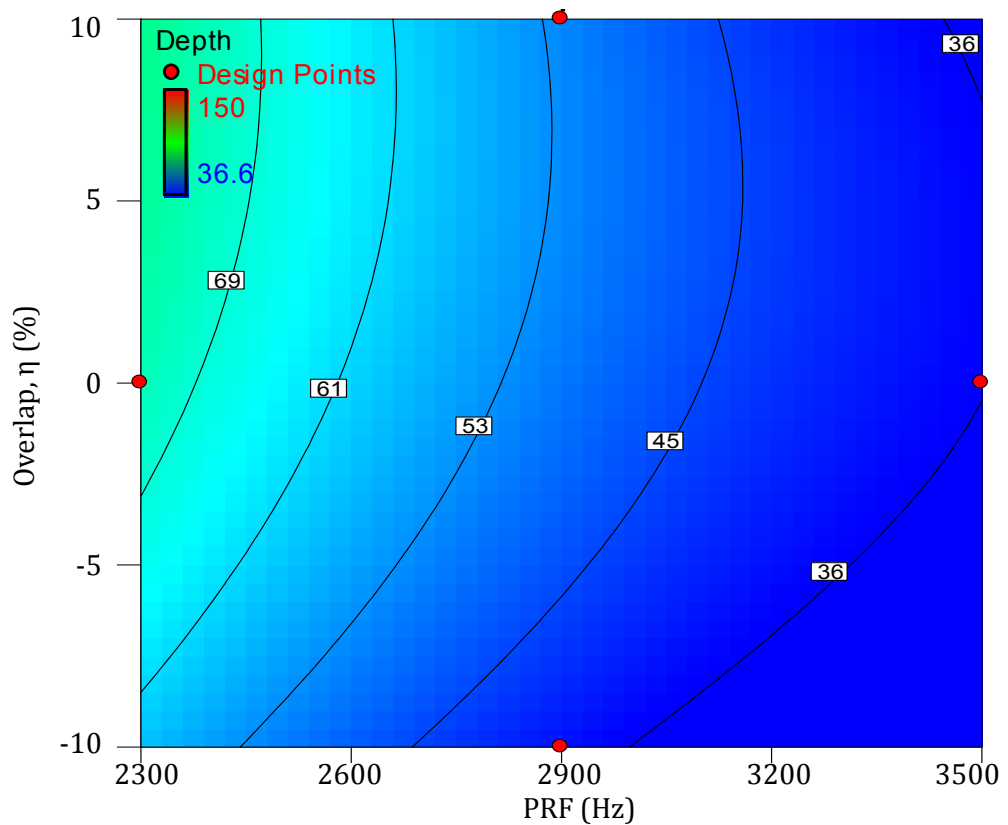


(a) 3500 Hz PRF

APPENDIX E2: Contour plot of overlap, PRF and modified layer depth for DOE5 samples at
 (a) 1138 W and (b) 1515 W power

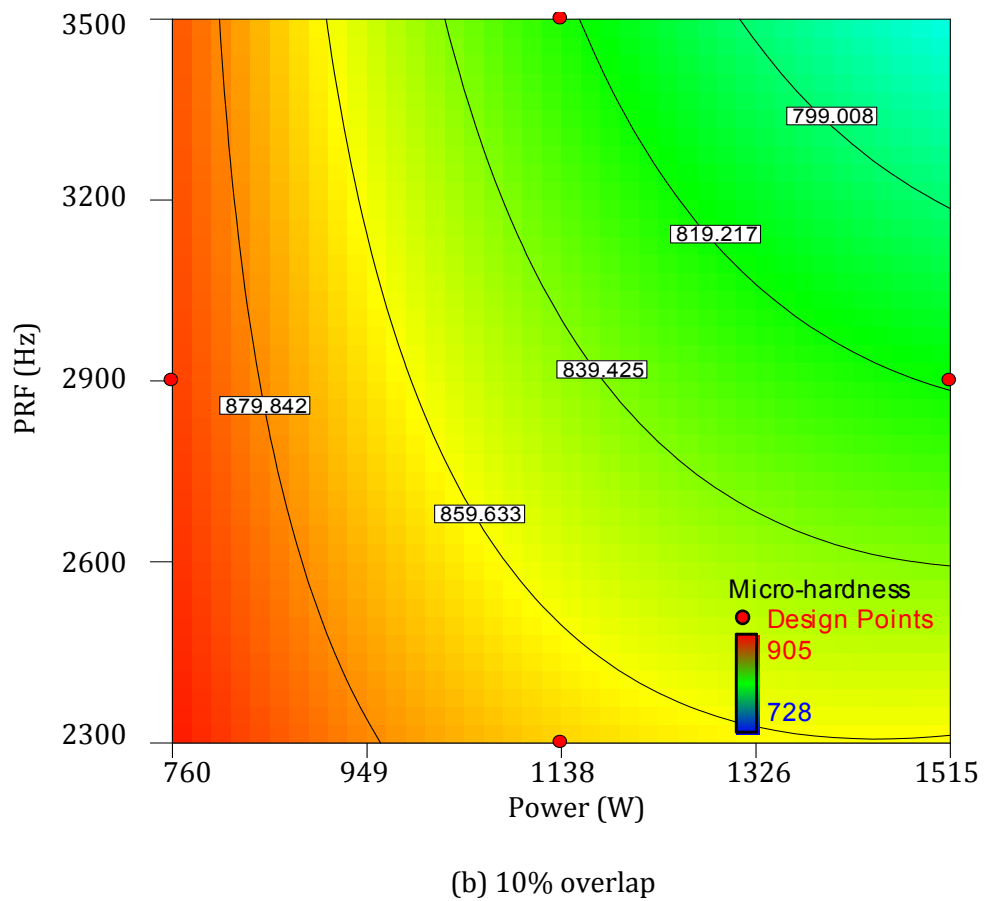
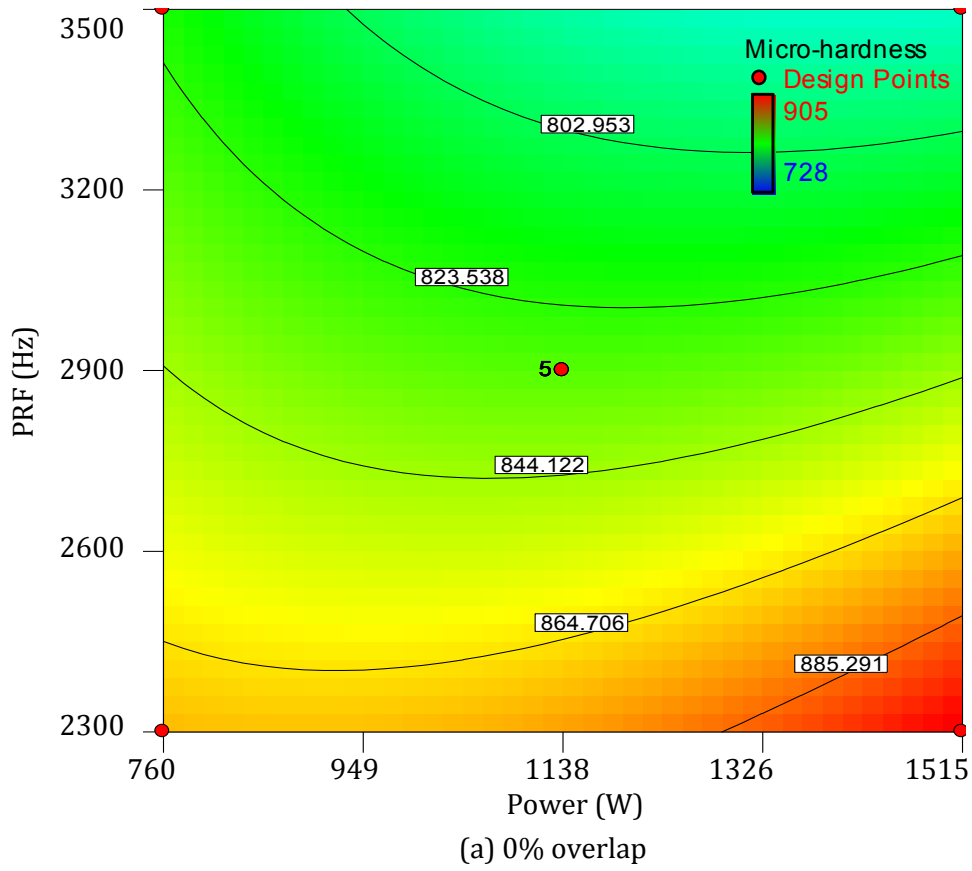


(a) 1138 W power

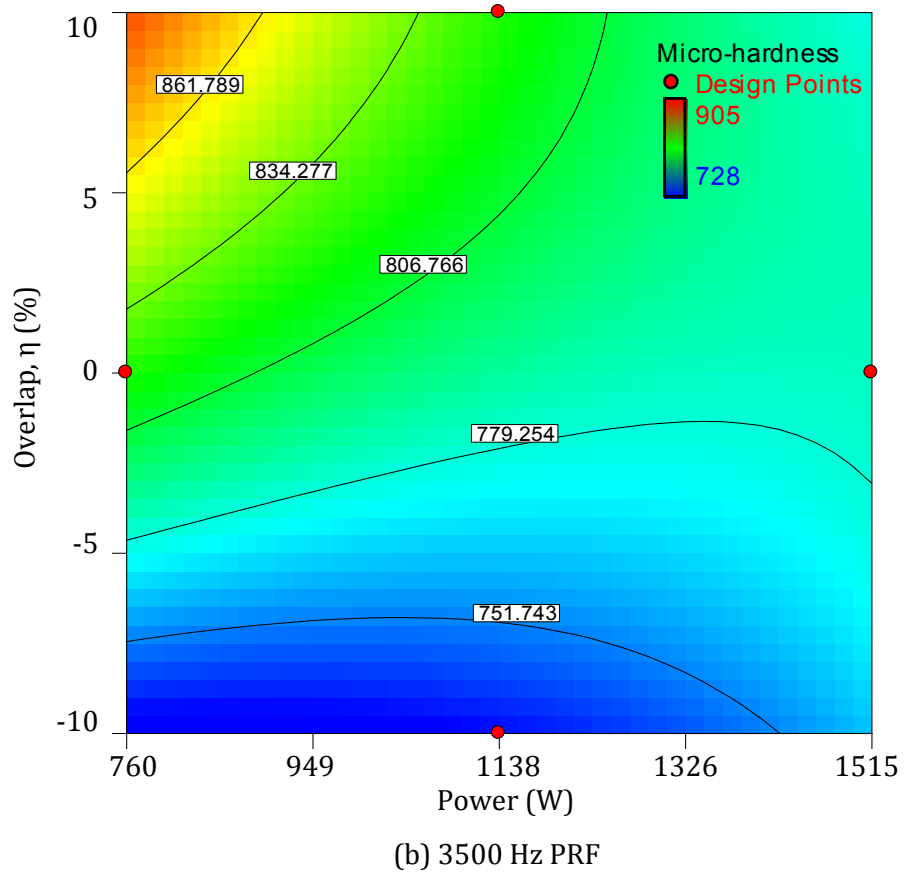
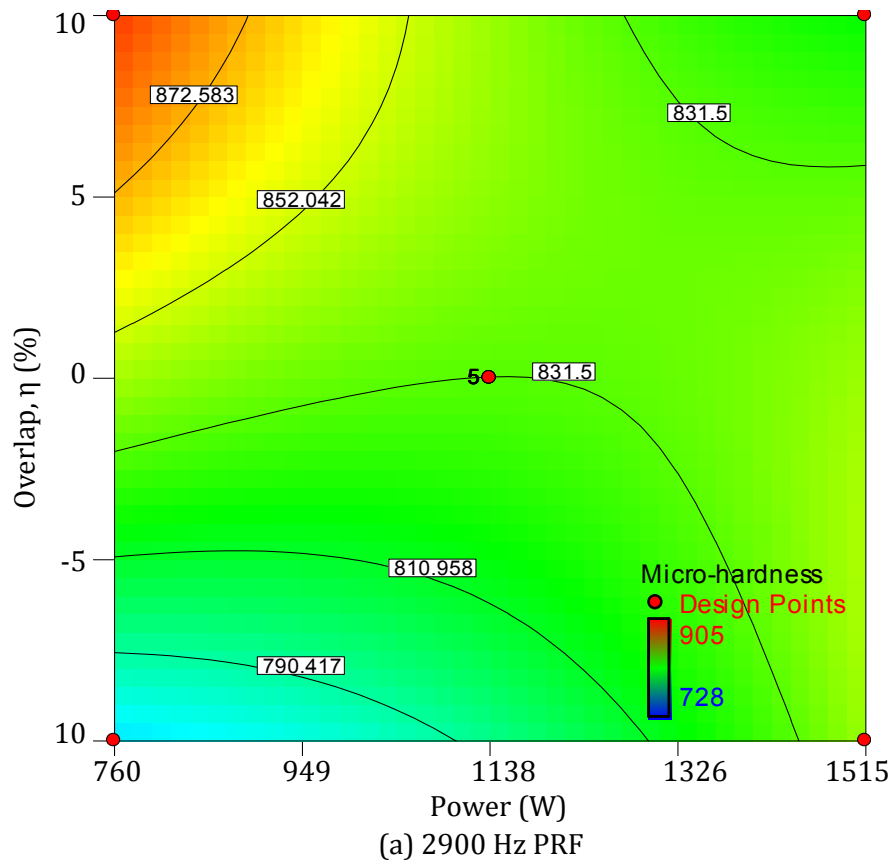


(b) 1515 W power

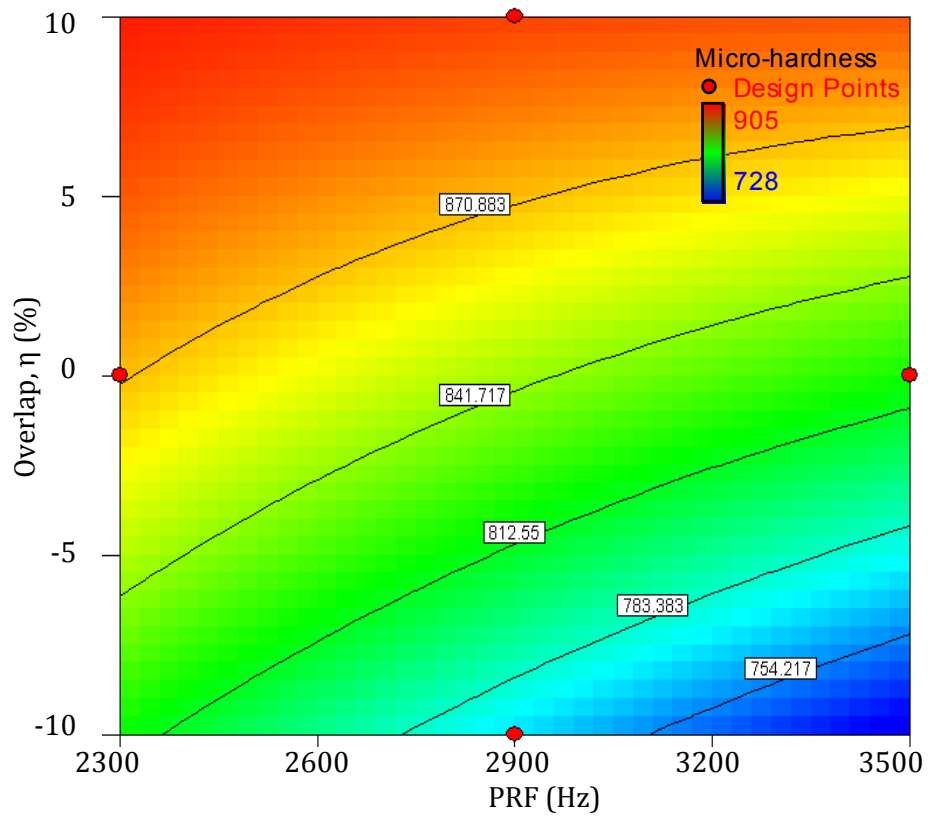
APPENDIX E3: Contour plot of PRF, power and hardness for DOE5 samples at (a) 0% and (b) 10% overlap



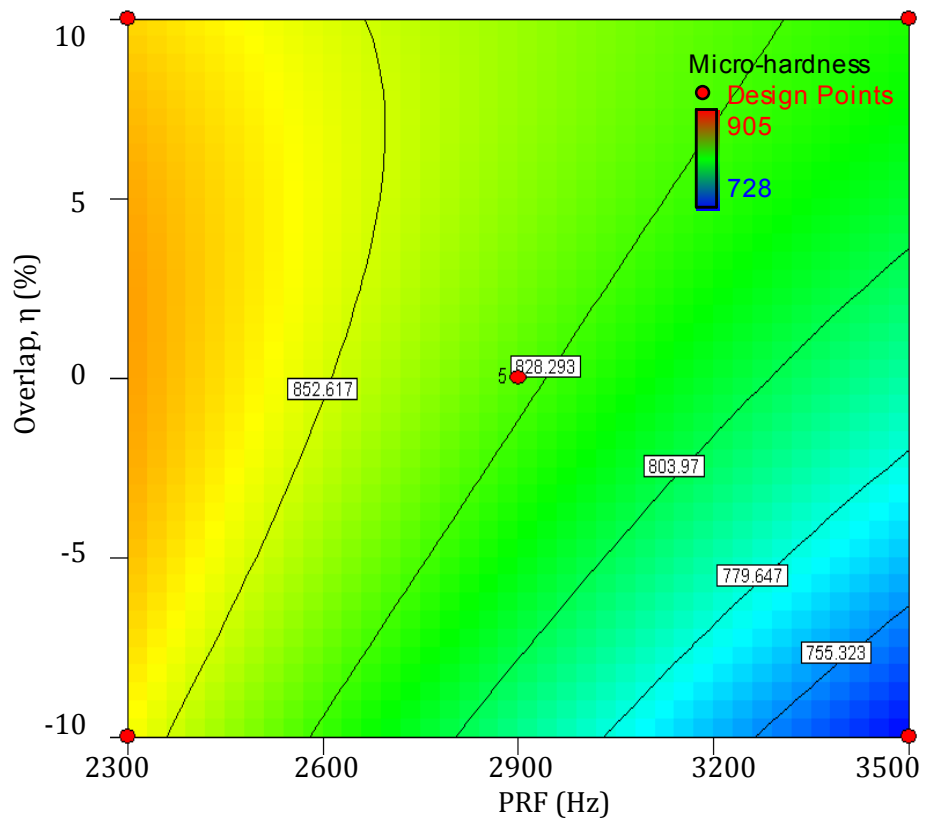
APPENDIX E4: Contour plot of overlap, power and hardness for DOE5 samples at (a) 2900 Hz and (b) 3500 Hz PRF



APPENDIX E5: Contour plot of PRF, overlap and hardness for DOE5 samples at (a) 760 W and (b) 1138 W peak power



(a) 760 W



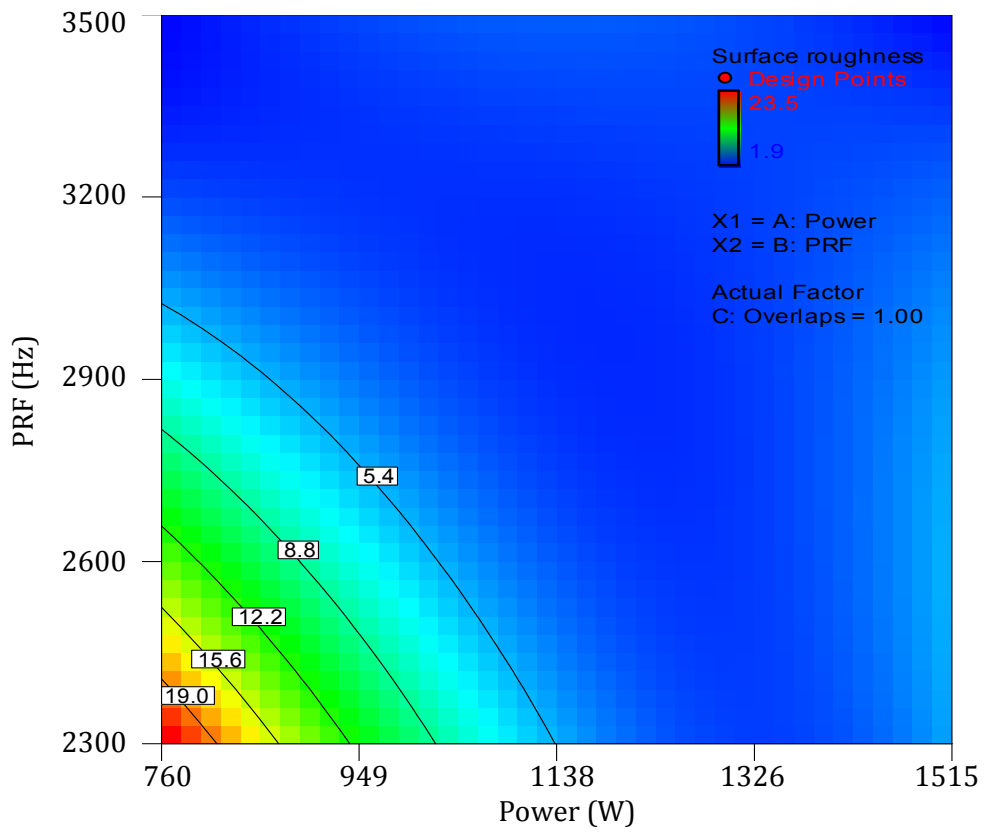
(b) 1138 W

APPENDIX E6: Average surface roughness of DOE5 samples with 95% CI.

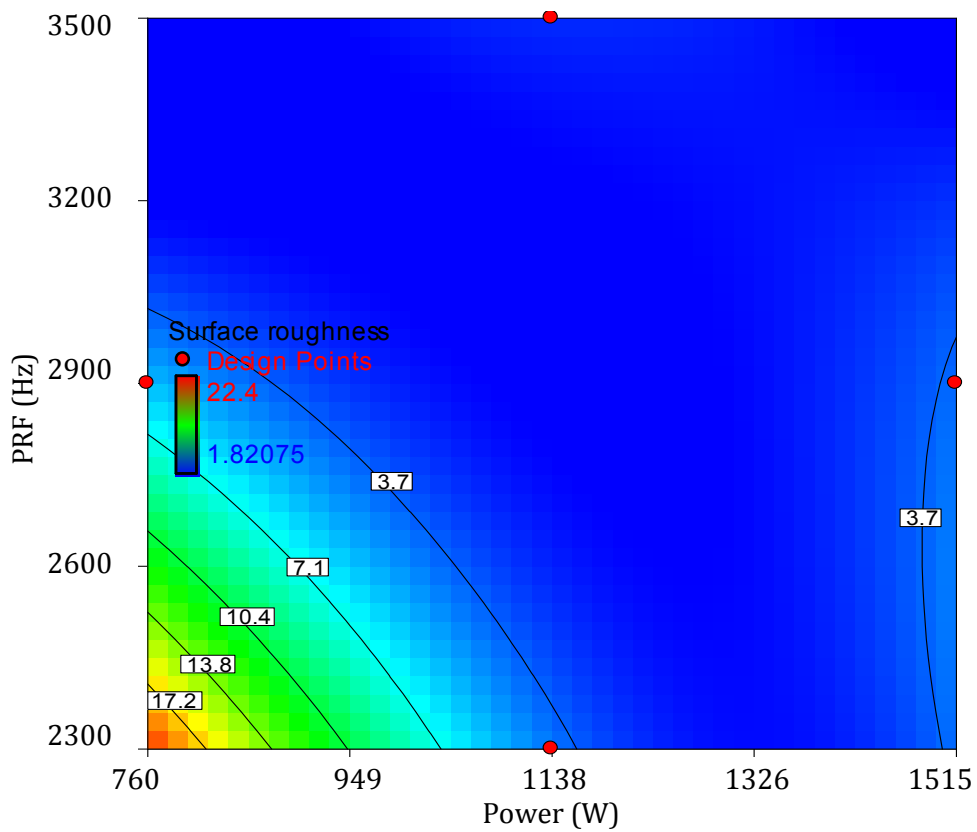
Sample	Average surface roughness, R_a (μm)				Mean	Std. Dev.	(Std. Dev./ \sqrt{n})	Interval	Lower range	Upper range
	1	2	3	4						
F1	23.2	16.7	25.5	24.2	22.4	3.915	0.24468	0.77858	21.62	23.18
F2	4.5	5.3	5.1	5.2	5.0	0.359	0.02246	0.07148	4.93	5.07
F3	1.8	1.9	2.0	2.1	2.0	0.129	0.00807	0.02567	1.97	2.03
F4	2.2	1.7	2.0	2.3	2.0	0.265	0.01654	0.05262	1.95	2.05
F5	6.9	8.1	5.1	4.2	6.1	1.756	0.10973	0.34917	5.75	6.45
F6	2.7	3.6	3.0	2.9	3.0	0.387	0.02421	0.07702	2.92	3.08
F7	6.5	5.8	5.9	4.0	5.5	1.079	0.06741	0.21450	5.29	5.71
F8	3.9	3.7	3.7	4.3	3.9	0.283	0.01768	0.05625	3.84	3.96
F9	4.3	3.2	3.2	3.5	3.6	0.520	0.03248	0.10334	3.50	3.70
F10	1.7	1.8	2.1	1.7	1.8	0.189	0.01183	0.03765	1.76	1.84
F11	4.0	3.5	4.5	4.5	4.1	0.479	0.02992	0.09520	4.00	4.20
F12	2.8	2.4	2.3	2.8	2.6	0.263	0.01644	0.05230	2.55	2.65
F13	1.9	2.3	2.3	2.3	2.2	0.200	0.01250	0.03978	2.16	2.24
F14	2.8	2.7	2.9	2.8	2.8	0.082	0.00510	0.01624	2.78	2.82
F15	3.0	2.7	2.8	3.0	2.9	0.150	0.00937	0.02983	2.87	2.93
F16	3.1	3.2	3.0	3.4	3.2	0.171	0.01067	0.03396	3.17	3.23
F17	2.7	2.8	2.6	2.4	2.6	0.171	0.01067	0.03396	2.57	2.63

**Df = 3, CI = 0.95, α = 0.025, t distribution = 3.182

Appendix E7: Contour plot of PRF, power and surface roughness for DOE5 samples at (a) 0% and (b) 10% overlap

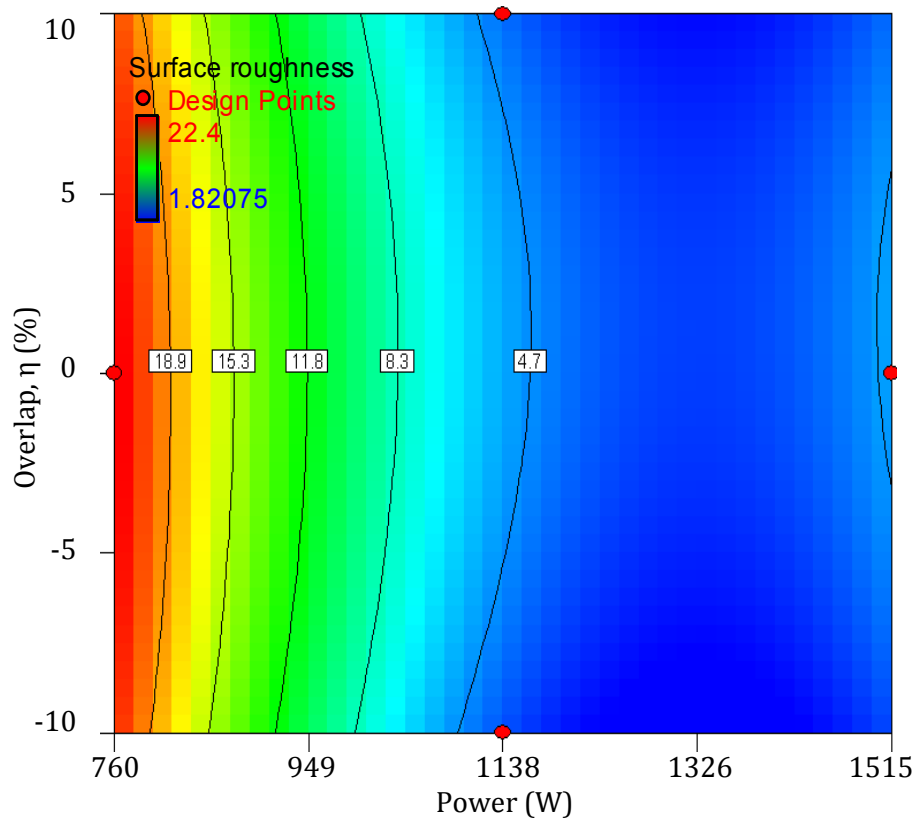


(a) 0% overlap

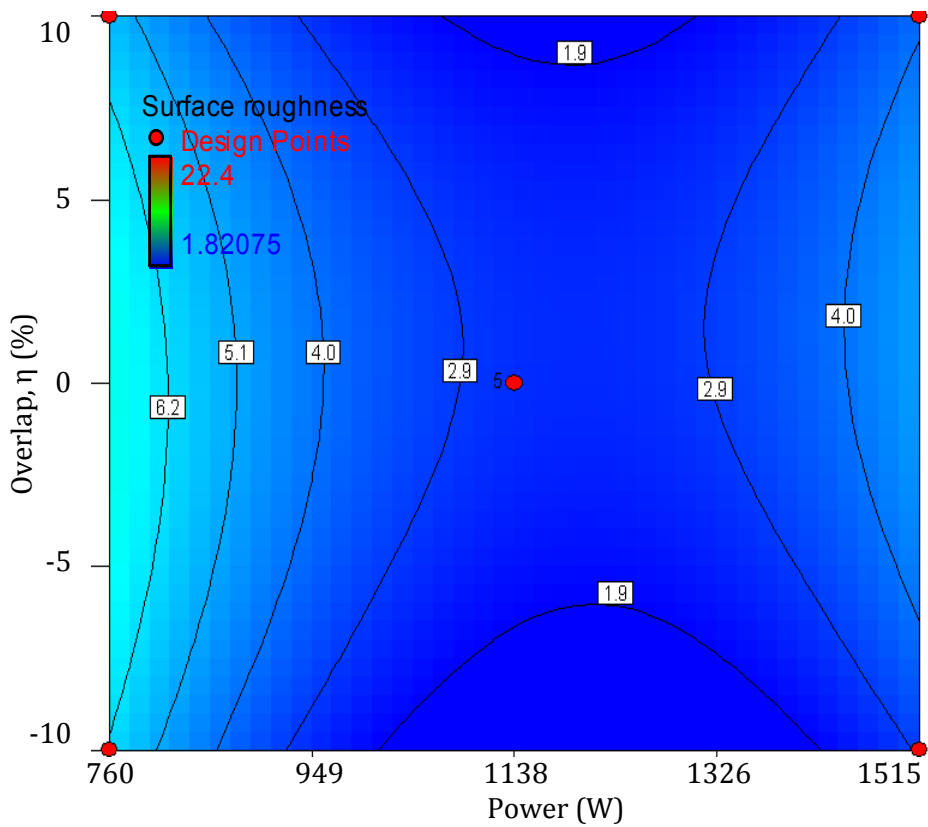


(b) 10% overlap

Appendix E8: Contour plot of overlap, power and surface roughness for DOE5 samples at
 (a) 2300 Hz and (b) 2900 Hz PRF



(a) 2300 Hz PRF



(b) 2900 Hz PRF

APPENDIX F1: Constraints in design optimisation with maximum rank of response importance

Name	Goal	Lower Limit	Upper Limit	Importance
Power (W)	is in range	760	1515	3
PRF (Hz)	is in range	2300	3500	3
Overlap (%)	is in range	0.9	1.1	3
Hardness (HV _{0.1})	maximise	728	905	5
Surface roughness (µm)	minimize	1.82	3.50	5
Modified layer depth (µm)	maximise	50	150	4

APPENDIX F2: Design solutions in DOE5 using maximum rank of response importance.

Solution	Power (W)	PRF (Hz)	η (%)	Micro-hardness (HV)_{0.1}	Surface roughness, R_a (μm)	Modified layer depth (μm)	Desirability
1	1272.32	2300.00	1.10	862.52	1.82	79	0.636
2	1287.52	2300.00	1.10	863.28	1.82	78	0.631
3	1286.34	2300.00	1.10	862.13	1.73	78	0.630
4	1296.55	2300.00	1.06	873.26	2.52	77	0.525
5	776.32	3500.00	1.10	885.87	0.65	58	0.471
6	782.71	3500.00	1.10	884.54	0.70	58	0.471
7	787.69	3500.00	1.10	883.51	0.74	58	0.471
8	764.92	3500.00	1.10	888.26	0.55	58	0.471
9	762.06	3500.00	1.10	888.86	0.52	58	0.471
10	777.98	3500.00	1.10	884.80	0.70	58	0.470
11	847.35	3500.00	1.10	871.48	1.19	59	0.465
12	1320.24	2300.00	0.92	890.14	2.14	59	0.450
13	1319.39	2300.00	0.91	889.50	1.99	58	0.448
14	1324.24	2300.00	0.93	891.29	2.34	60	0.447
15	1319.67	2300.00	0.94	890.92	2.49	62	0.440
16	760.00	3216.47	1.10	890.31	1.82	56	0.429